Annual Report 2020

CENTER FOR EXPERIMENTAL NUCLEAR PHYSICS AND ASTROPHYSICS

University of Washington

CENPA

Center for Experimental Nuclear Physics and Astrophysics

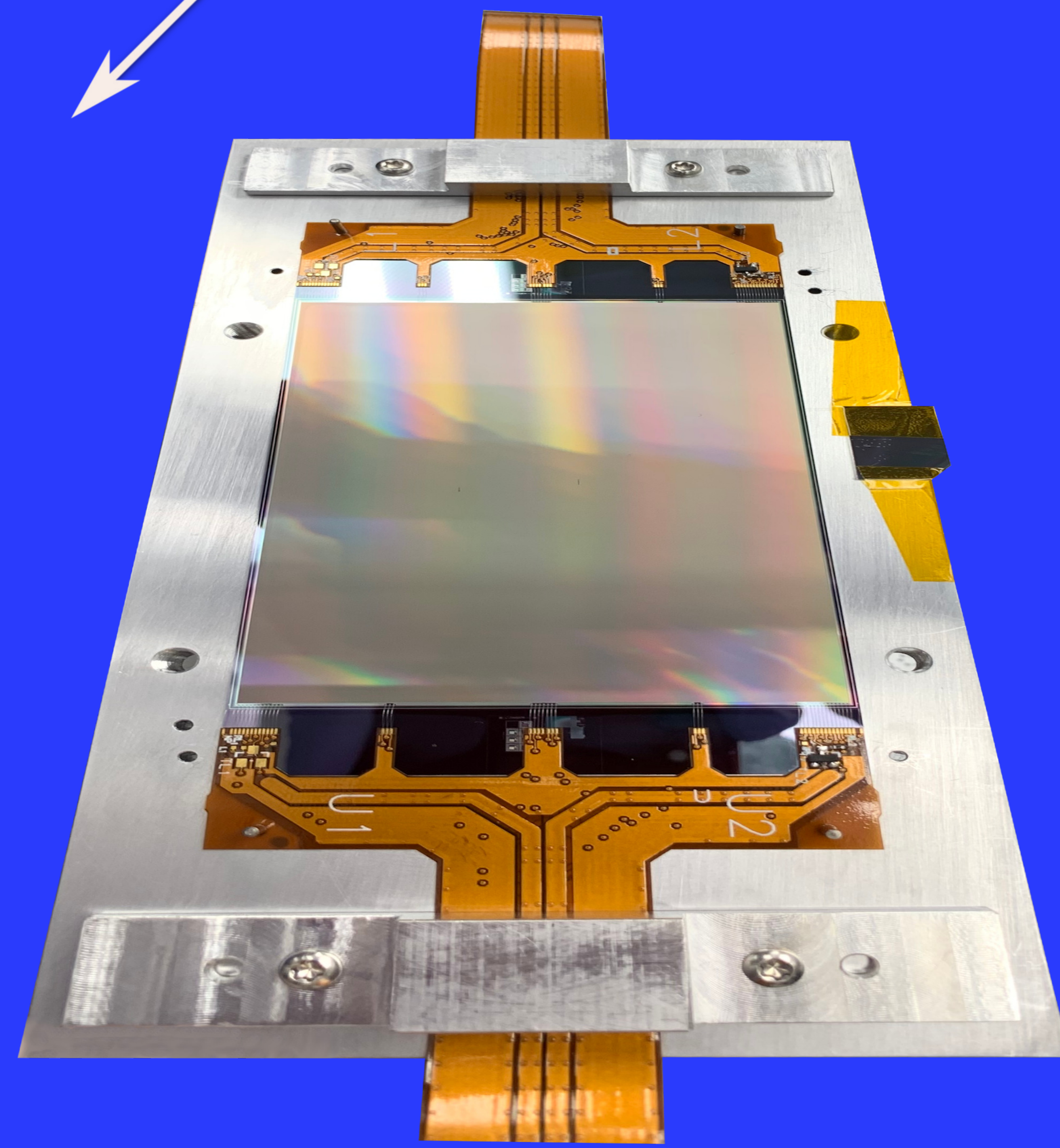

Annual Report 2020

University of Washington

ANNUAL REPORT

Center for Experimental Nuclear Physics and Astrophysics
University of Washington
June 1, 2020

Sponsored in part by the United States Department of Energy
under Grant #DE-FG02-97ER41020.

Cover design by Gary Holman. Cover front: The 6000 x 4000 pixel DAMIC-M CCD packaged at CENPA (Sec. 5.6). Cover back: *Top:* Clint Wiseman, Gulden Othman, Tim Mathew, and Keira Hansen working on the LEGEND Cage Cryostat (Sec. 1.20), *Middle:* Noah Hoppis behind ^{19}Ne SF_6 cold trap (Sec. 3.13), *Bottom:* Chelsea Bartram, Patrick Harrington, and Christian Boutan inspecting ADMX quantum amplifier package (Sec. 5.1).

FOREWORD

One can't help but to notice that this year's Annual Report back page reflects an interruption of the many decades tradition of the springtime outdoor group photo. Of course this is related to the ongoing COVID-19 crisis and the precautions we are taking with our Stay-Home, Stay-Healthy directives in the state of Washington. At this time, our hearts go out to the many critical workers who have maintained our health, our safety, our food supply, and our internet! Those of us working at CENPA, and in general throughout the physics community, are relatively lucky. Most of us are able to work, study, and teach profitably, even if inconveniently, while at home. Progress is being made on data analyses, paper preparations, experimental simulations, and instrument designs. However, almost all of our in-lab work has stalled. A notable exception is the ADMX axion search experiment, which continued to take data with minimal in-person efforts, mainly for cryogenic maintenance. Several CENPA technical staff members have been deemed essential workers by the University of Washington, which allows them to maintain the safety of critical systems and to carry out some work in isolation from others. Most work has slowed and some critical experimental efforts are on pause. The same is true of our external efforts; for example, the muon $g-2$ Run-3 at Fermilab was stopped when the accelerator complex went into standby mode.

At CENPA, Jens Gundlach, who leads the Gravity/LIGO group, also heads a separate, high-profile NIH program in DNA sequencing technology; this biophysics group is conducting research on the enzymes of SARS-CoV-2 to develop antiviral drugs. Their work – truly essential COVID-19 science – has gone on unabated, under very special safety rules. Beginning in March, Charlie Hagedorn was a key member of the team behind FindTheMasks.com, an open-data project mapping more than 4,000 healthcare institutions for personal-protective-equipment donations. The small numbers CENPA had in inventory were donated to local medical staff.

Our CENPA teaching faculty experienced an abrupt transition to all online-classes in the last 2 weeks of Winter quarter, followed by the entire online-only Spring quarter. This has been a significant challenge, leading to issues such as, how does one administer a remote introductory physics exam to 1000 students? Our lab has maintained weekly Monday Meetings, where students and postdocs give presentations on their research status. This important community-building event has gone on uninterrupted over Zoom, as have occasional seminars, General and Final Ph.D. exams, and group, staff, and faculty meetings. A number of CENPA members gave remote talks at the recent April APS meeting, and others at various online conferences and workshops.

It is late May when this Foreword is written, more than 2 months since the stay-at-home orders have been in place. Restrictions are beginning to lift, allowing limited on-campus research to restart under a new set of evolving rules. Peter Kammel is the Chair of the Physics Department Safety Committee. He has been working tirelessly in the past few weeks to establish protocols to permit researchers back into Physics and CENPA laboratories. By the time this Annual Report is printed, we expect that most of our onsite, experimental efforts will be running again, although not at full strength. For those of us who can work from home, we have been directed to do so for the indefinite future.

Let us all hope that a science-driven solution will emerge and that next year's CENPA annual photo will feature us once again in the sunshine, on the lawn of our campus. We wish you well and please enjoy this year's Annual Report.

– David Hertzog –

INTRODUCTION

The Center for Experimental Nuclear Physics and Astrophysics, CENPA, was established in 1998 at the University of Washington as the institutional home for a broad program of research in nuclear physics and related fields. Research activities — with an emphasis on fundamental symmetries and neutrinos — are conducted locally and at remote sites. In neutrino physics, CENPA is the lead US institution in the KATRIN tritium beta decay experiment, the supportive local tritium decay experiment TRIMS, the site for experimental work on Project 8, a collaborating institution in the MAJORANA ^{76}Ge and LEGEND-200 double beta decay experiments, and in the COHERENT neutrino-nucleus scattering experiment. The Muon Physics group developed and completed the MuSun experiment to measure muon capture in deuterium at the Paul Scherrer Institute in Switzerland. The muon group has a major leadership role in the measurement of the muon's anomalous magnetic moment at Fermilab, which aims to even higher precision than it is presently known from our previous work at Brookhaven. The fundamental symmetries program also includes "in-house" research on the search for a static electric dipole moment in ^{199}Hg, and an experiment using the local Tandem Van de Graaff accelerator to measure the electron-neutrino correlation and Fierz interference in ^{6}He decay. Looking to the future, we have a new program in next-generation $0\nu\beta\beta$ decay with the SELENA experiment.

In addition to the research directly supported by DOE's Office of Nuclear Physics through the CENPA core grant, other important programs are located at CENPA, forming a broader intellectual center with valuable synergies. The "Gravity" group carries out, with both DOE and NSF support, studies of the weak and strong Equivalence Principles, fundamental precepts of General Relativity, as well as searches for non-Newtonian forces such as those predicted by theories with extra dimensions. In addition, they participate in LIGO with unique instrumentation that aids the functioning and stabilization of the interferometers. The DOE Office of High Energy Physics supports the unique ADMX axion search experiment. The NSF supports the DAMIC experiment that looks for light dark matter.

CENPA is home to a large number of faculty, research faculty, postdoctoral scholars, graduate, and undergraduate students. The core professional engineering and technical staff provide diverse capabilities and skills such as state-of-the-art detector development, fabrication of custom electronics, large-scale computing, and design engineering. New advancements, capabilities, and ideas are regularly shared at seminars by CENPA members and visitors alike.

Transitions

This past year has been one with an enormous number of transitions as we have seen postdoctoral scholars move to more permanent research positions, many Ph.D. students complete theses, and various milestones and departures in the CENPA technical staff.

In the late summer of 2019, Research Assistant Professor Martin Fertl (Project 8 / Muon $g-2$) began a tenured Associate University Professor appointment at the Johannes Gutenberg

University Mainz, Germany. Martin has started a new group and continues to be involved in both projects.

In autumn 2019, postdoctoral scholar Kim Siang Khaw (Muon $g-2$) began a tenure-track Associate Professor position at the School of Physics and Astronomy (SPA), Shanghai Jiao Tong University (SJTU), with a joint a position as a T. D. Lee Fellow. Kim Siang is helping to lead the growing Shanghai group in many Muon $g-2$ efforts.

Postdoctoral scholar Walter Pettus was recently offered a tenure-track Assistant Professor position at Indiana University, which he has accepted. Walter will launch a new research group at IU and continue his involvement in Project 8 and LEGEND-200.

Senior postdoctoral scholar Krishna Venkateswara (LIGO) accepted a research position at Paroscientific Inc. in Redmond.

ADMX postdoctoral scholar Nicole Crisosto, an expert in low-temperature cryogenics, is now working in the Microsoft quantum group.

Postdoctoral scholar Menglei Sun, who contributed significantly to the first KATRIN analysis, has taken a position at Synopsys Inc. in Seattle.

PNNL postdoctoral scholar Ben LaRoque, who has been permanently stationed at CENPA on Project 8, accepted a staff position at PNNL and will be departing in the summer.

Junior Research Engineers Seth Kimes and Joben Pederson were both lured to Microsoft where they will provide their cryogenic skills to the developing quantum computing there.

Senior Engineer Doug Will celebrated more than 45 years of service to CENPA and continues to be a role model for junior engineers and a leader in our cryogenics efforts.

Mechanical Engineer John Amsbaugh retired in March, 2020 after more than 40 years of service to CENPA. John was central to the design and realization of many of the innovative detector systems and accelerator components over his career and he will be sorely missed.

We continue to train a large number of graduate students at CENPA. From April 2019 - March 2020, the following graduate students defended their CENPA-based Ph.D. theses:

- Rachel Ryan (MuSun), after a short post-defense extension with our group, accepted a research Fusion Scientist position at Helion Energy.
- Ian Guinn (Majorana Demonstrator), is presently a postdoctoral scholar at UNC Chapel Hill / TUNL working on LEGEND-200.
- Micah Buuck (Majorana Demonstrator), is presently a postdoctoral scholar at SLAC working on the LZ experiment.
- Yelena Bagdasarova (He-6) is a Research Scientist in the Dept. of Ophthalmology at the University of Washington.
- Rachel Osofsky (Muon $g-2$) has taken a position at the Johns Hopkins Applied Physics Institute.

- Ying-Ting Lin (TRIMS) returned to Taiwan to undertake his national service tour of duty there.

- John Lee (Gravity) defended his Ph.D. on the new $1/r^2$ gravity limit just as this report was being written. His future plans are developing.

Notable

We are in the last year of our three-year DOE Office of Nuclear Physics award to CENPA, which is supporting the bulk of the efforts described in this Annual Report. Owing to the COVID-19 crisis, we will be submitting an 18-month extension request to DOE per their recommendations.

The CENPA Seminar Series was jointly run by postdoctoral scholars Elise Novitski and Walter Pettus. This series has been enormously successful and well attended locally and remotely. Speakers, covering a wide range of topics of interest to the Center, are invited.

Research Highlights

- The KATRIN experiment has made the transition to nominal tritium operation, with data from the first 30 days resulting in a new neutrino mass limit of 1.1 eV, an improvement by a factor of approximately 2.

- A comprehensive analysis of the data from the TRIMS experiment has been carried out. The results are in strong contradiction to earlier experiments, and, in contrast, support the current theoretical model that is used to calculate the final-state spectrum in KATRIN for extracting neutrino mass. A paper on the HT data has been published in Phys. Rev. Lett., and another is in preparation on the T_2 data.

- The second phase of Project 8 is a “microtritium experiment” that has now completed a three-month-long run. Preliminary analysis shows the expected spectrum shape and extremely low backgrounds, one of the anticipated features of the Cyclotron Radiation Spectroscopy (CRES) method. This completes Phase II, and attention now focuses on the demonstrators required for the design of a research-scale Project 8 experiment.

- The first stage of an atomic-tritium source demonstrator for Project 8 has been completed and is undergoing commissioning. It includes a thermal dissociator for ‘cracking’ molecular hydrogen and a mass spectrometer for analyzing the beam. Studies of dissociation and cooling will be carried out with hydrogen and deuterium.

- The Majorana Demonstrator recently presented preliminary results on its background model, two-neutrino double-beta decay to excited states, and low-energy rare event searches. Soon, all enriched detectors will be removed and sent to LNGS for use in the LEGEND-200 apparatus.

- The LEGEND Collaboration has entered the construction phase for the LEGEND-200 apparatus at LNGS in Italy. Procurement of detectors, fabrication of hardware components, and software development are proceeding. Preparations continue to completing key design and critical R&D work for LEGEND-1000 prior to the DOE downselect process.

- The ^{21}Ne(p,γ) experiment was successfully run over 3 months during the summer of 2019. This involved setting up 12 Ge detectors for angular distribution measurements, switching the accelerator to run in terminal-ion source mode, a dedicated program to optimize implantation of ^{21}Ne targets, and a data-taking campaign with 24/7 running for 3 months. Data analysis is under progress.

- The data analysis on extraction of little-a from laser-trapped ^{6}He continued to completion during 2019. We are presently working on a publication.

- We are mounting the experiment to search for tensor currents using the CRES technique to search for little-b from ^{6}He, ^{19}Ne. We have installed the superconducting solenoid and built a helium recovery system using the ADMX compressor. The magnet was cooled down and biased successfully. We installed a cryocooler unit and set up the cooling distribution for our RF system. The daq system is running and presently undergoing tests of noise levels. Tests with an ^{83}Kr source are expected soon.

- We designed and tested production from a ^{19}Ne source built on the style of the Berkeley/Princeton design. While production is below expectations ($\approx 10^9$ instead of 10^{10} ^{19}Ne atoms/s), it is adequate for our needs.

- The Muon $g-2$ collaboration continues to analyze the Run-1 data set, with its very challenging features. In parallel, we completed Run-2 data taking in June 2019 and launched Run-3 in autumn. In total, we envision the statistical harvest of these three data sets to exceed that obtained by BNL E821 by at least a factor of 6. The experiment will continue for several more years.

- The lifetime results from the μ^+ datasets collected in MuSun were unblinded and compared with the free muon lifetime measured with high precision in our previous dedicated MuLan experiment. The good agreement found verifies essential aspects of MuSun's technique and is encouraging towards the ongoing final analysis of the ten-times higher statistics of the negative muon data, which determines the muon capture rate in deuterium.

- The ADMX G2 experiment increased its mass coverage in the search for the QCD Axion Dark Matter by fourfold.

- The ADMX G2 experiment achieved sensitivity to the "DFSZ" axion, a decades-long goal of the dark-matter axion community. ADMX is by far the only experiment with this sensitivity. Over the last year, ADMX increased its mass-scanning rate by fourfold in the most compelling axion-mass region. ADMX finally has the mass-reach and sensitivity reach to be able to detect dark-matter axions, and ADMX could find the axion at any time.

- DAMIC released world-leading exclusion limits on the scattering of dark matter particles with masses smaller than 5 MeV. Further analysis of the dark matter search data is ongoing, with results from the search for GeV-scale weakly-interacting massive particles (WIMPs) in preparation.

- The first prototype DAMIC-M charge-coupled device (CCD) sensors were successfully packaged and tested at CENPA. Single-electron response was demonstrated with a 24-megapixel CCD. This is the most-massive, lowest-noise CCD ever tested, a milestone for the DAMIC-M program.

- Selena completed the first experimental measurements with a single-pixel amorphous selenium sensor. The charge generation and transport properties of amorphous selenium were measured and results are being prepared for publication. We started collaboration with Berkeley Lab to interface amorphous selenium with the Topmetal-II CMOS sensor.

- The Eot-Wash "Gravity" group published a test of Newton's $1/r^2$ law at Yukawa ranges down to 39 micrometers. They are presently conducting a search for dark matter using a torsion balance.

- The CENPA LIGO Group deployed ground rotation sensors at LIGO that are detecting ground deformation due to wind and built a gravitational calibrator for LIGO.

As always, we encourage outside applications for the use of our facilities. As a convenient reference for potential users, the table on the following page lists the capabilities of our accelerators. For further information, please contact Gary Holman, Associate Director (holman@uw.edu) or Eric Smith, Research Engineer (esmith66@u.washington.edu) CENPA, Box 354290, University of Washington, Seattle, WA 98195; (206) 543 4080. Further information is also available on our web page: `http://www.npl.washington.edu`.

We close this introduction with a reminder that the articles in this report describe work in progress and are not to be regarded as publications nor to be quoted without permission of the authors. In each article the names of the investigators are listed alphabetically, with the primary author underlined in the case of multiple authors, to whom inquiries should be addressed.

David Hertzog, Director　　　　Gary Holman, Associate Director and Editor

Special thanks to David Hertzog, Hamish Robertson, Eric Smith, Erik Shaw, and Drew Byron for article technical review.

TANDEM VAN DE GRAAFF ACCELERATOR

Our Tandem accelerator facility is centered around a High Voltage Engineering Corporation Model FN purchased in 1966 with NSF funds, with operation funded primarily by the U.S. Department of Energy. See W. G. Weitkamp and F. H. Schmidt, "The University of Washington Three Stage Van de Graaff Accelerator," *Nucl. Instrum. Methods* **122**, 65 (1974). The Tandem was adapted in 1996 to an (optional) terminal ion source and a non-inclined tube #3, which enables the accelerator to produce high intensity beams of hydrogen and helium isotopes at energies from 100 keV to 7.5 MeV.

Some Available Energy Analyzed Beams

Ion	Max. Current (particle μA)	Max. Energy (MeV)	Ion Source
^{1}H or ^{2}H	50	18	DEIS or 860
^{3}He or ^{4}He	2	27	Double Charge-Exchange Source
^{3}He or ^{4}He	30	7.5	Tandem Terminal Source
^{6}Li or ^{7}Li	1	36	860
^{11}B	5	54	860
^{12}C or ^{13}C	10	63	860
*^{14}N	1	63	DEIS or 860
^{16}O or ^{18}O	10	72	DEIS or 860
F	10	72	DEIS or 860
* Ca	0.5	99	860
Ni	0.2	99	860
I	0.001	108	860

*Negative ion is the hydride, dihydride, or trihydride.

Several additional ion species are available including the following: Mg, Al, Si, P, S, Cl, Fe, Cu, Ge, Se, Br and Ag. Less common isotopes are generated from enriched material. We recently have been producing the positive ion beams of the noble gases He, Ne, Ar, and Kr at ion source energies from 10 keV to 100 keV for implantation, in particular the rare isotopes ^{21}Ne and ^{36}Ar. We have also produced a separated beam of 15-MeV ^{8}B at 6 particles/second.

Contents

1 Neutrino Research

KATRIN

1.1 Status of the KATRIN neutrino mass experiment

J. F. Amsbaugh, G. Bayarbaatar, A. Beglarian*, T. H. Burritt, P. J. Doe, S. Enomoto, J. A. Formaggio†, F. M. Fränkle*, M. Hanley, A. Vizcaya Hernández‡, L. Kippenbrock, A. Kopmann*, E. L. Martin§, D. S. Parno‡, D. A. Peterson, A. W. P. Poon¶, R. G. H. Robertson, S. Schmid*, M. Sun, D. Tcherniakhovski*, L. A. Thorne‡, T. D. Van Wechel, J. F. Wilkerson§, and S. Wüstling*

The year 2019 was a banner year for KATRIN with the transition from tritium commissioning activities to nominal tritium operation and significant publications, including the first neutrino mass result. Life now consists of a series of KATRIN Neutrino Mass measurements designated KNM1, KNM2... interspersed with systematic studies and routine maintenance. It is expected that four such cycles will be performed per year. KATRIN's final sensitivity will be reached when the statistical and systematic errors are roughly equal. To this end the focus is to ensure data quality, to maximize statistics and to understand and reduce the sources of systematic error, thereby charting the fastest course to the KATRIN design sensitivity of 0.2 eV or better.

KNM1, which took place over 28 days between April and May 2019 provided the input for the first physics result, establishing a new, direct kinematic limit of 1.1 eV (90% confidence level) on the neutrino mass. This result appeared in the November edition of Physical Review Letters as the Editors' Suggestion and adorned the cover of PRL.

Although KNM1 lasted only 28 days with a tritium source intensity a factor of 5 smaller than nominal, the 1.1 eV limit represents almost a factor of 2 improvement over earlier results. Fig. 1.1-1 shows the fit over a range of 90 eV surrounding the 18.57 keV endpoint of the tritium spectrum. Tritium scans were performed at a total of 27 spectrometer retarding potentials. The time spent at each retarding potential is chosen to optimize the determination of both the energy spectrum and the background and can be seen in Fig. 1.1-1.

In March 2020 a paper covering the very first tritium run appeared in the European Physical Journal C. This 13-day run at 0.5% source intensity provided the opportunity to test the analysis techniques which are described in detail in the paper. The physics analysis teams then applied the techniques and strategy to the KNM1 data with great success.

To accompany the physics papers an updated hardware paper is in preparation that describes the many hardware upgrades, including the new detector veto system supplied by

*Karlsruhe Institute of Technology, Karlsruhe, Germany.
†Massachusetts Institute of Technology, Cambridge, MA.
§University of North Carolina, Chapel Hill, NC.
‡Carnegie Mellon University, Chapel Pittsburgh, PA.
¶Lawrence Berkeley National Laboratory, Berkeley, CA.

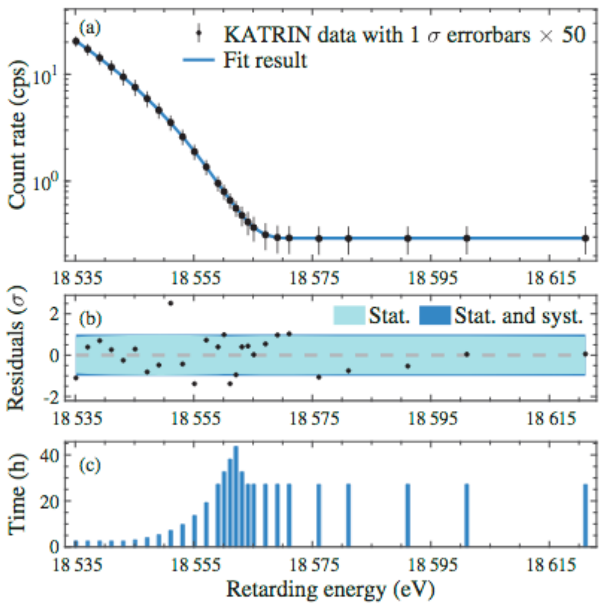

Figure 1.1-1. A fit to the region around the endpoint of the tritium spectrum based on 274 tritium scans at 27 different retarding potentials.

CENPA. Central to these upgrades is improvement to the liquid nitrogen cooled baffles that prevent radon from the non-evaporable-getter (NEG) pumps entering the sensitive volume of the spectrometer. During the first tritium run it was observed that the efficiency of the baffles was slowly decreasing. It was determined that this was due to a monolayer of water, from a poorly baked prespectrometer, forming on the surface of the baffle. Hardware has been installed that allows the baffle to operate at a lower temperature, restoring the original efficiency for blocking radon.

Two primary challenges remain, backgrounds in the spectrometer/detector system and possible instabilities in the plasma potential. The spectrometer background is currently a factor of approximately 25 times higher than the design goal of 0.01 Hz. This background has two main sources which contribute approximately equally, one of which is ^{219}Rn from the NEG pumps which enters the spectrometer and alpha decays to produce a trapped electron which subsequently produces further electrons by ionizing residual gas. The retarding potential then accelerates the electrons into the detector, constituting a background. Preliminary results indicate that the colder baffles will significantly reduce this background. The second source is caused by Rydberg atoms sputtered off the walls of the spectrometer by α decays of ^{210}Po, resulting from contamination by atmospheric radon during construction of the spectrometer. A number of ingenious solutions to this problem are being investigated but the simplest to implement is to move the analysis plane from the center of the spectrometer downstream towards the detector. Since the Rydberg atoms are distributed throughout the volume of the spectrometer, moving the analysis plane reduces the volume and hence the background by a factor of approximately 2 to ~ 0.12 Hz. This comes at the cost of reduced energy resolution, but the net result is improved sensitivity to the neutrino mass. The detector contribution to the total background will therefore increase from 5% to 10%. To counter this we are seeking to improve the energy resolution of future detector wafers, enabling the analysis “region of interest” to be reduced, hence reducing the detector related backgrounds. In addition we will use the improved veto to reduce natural backgrounds.

For the detector wafer used for KNM1 only 117 of the 148 pixels were used for analysis. Of the 31 unused pixels, 25 were lost due to apparent shadowing from upstream objects and 6 were lost due to sporadic noise. A new wafer was installed in February which provides 100% usable pixels and an average energy resolution of 2.4keV for the 60-keV γ from ^{241}Am.

The plasma potential of the tritium source is established by its contact to the rear wall that is held at a fixed potential. Analysis of KNM1 data indicated that there may be a radial dependence as well as a long-term drift of the plasma potential. To further investigate this it is planned to raise the source temperature from 30K to 80K, enabling the tritium to be “spiked” with ^{83m}Kr, allowing the Kr lines to be used to monitor source stability. The higher temperature operation will result in a lower source density and therefore event rate. Once the plasma instabilities are understood the aim would be to return to lower source temperatures and nominal source density.

The KNM3 program will begin once the current pandemic allows the return to normal staffing of the tritium laboratory and other critical infrastructure. Initial systematic studies will focus on the shifted analysis plane and plasma instabilities with the source at 80K. Based on the findings, KNM3 data will be taken with a shifted analysis plane and either at the higher source temperature and lower density or return to the nominal source conditions.

1.2 KATRIN data processing and analysis at CENPA

S. Enomoto

The neutrino mass measurements of KATRIN consist of retarding-potential scans across the tritium spectrum around the end-point. The analysis of the scan data is divided into two stages. The first stage is the event-level and time-series-level analysis, producing a highly reduced dataset called the Run Summary. Typical contents of the Run Summary include the rate of the Focal Plane Detector (FPD), retarding voltage, source gas activity, and source isotopologues, all with error estimations. Detailed models of the apparatus, such as the 3D magnetic fields of the spectrometer based on sensor readings and simulation calculations are also included. The second stage reads the Run Summary files and performs model fitting. During KATRIN data taking, all the raw data files are transferred to CENPA for the first-stage analysis and the resulting Run Summary files are distributed to the collaboration using the Intermediate Data Layer for Everyone (IDLE) platform, with various software components developed in CENPA (Fig. 1.2-1).

The majority of the first-stage analysis was developed by the UW KATRIN group, using the Building Elements for ANalysis Sequence (BEANS) analysis tool. This includes data cleaning for hardware troubles and misconfigurations, data quality analysis and filtering, event rate analysis, spectrometer condition analysis on slow-control data, and the integra-

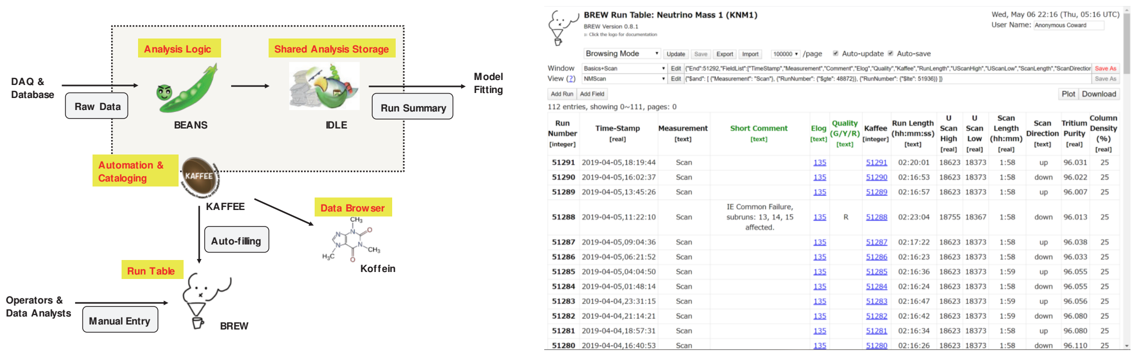

Figure 1.2-1. *Left*: KATRIN First-Stage Data Analysis Chain. All the software components in the figure were developed in CENPA. *Right*: Screenshot of the BREW Run Table web interface. Most of the entries are automatically filled according to run types, while operators and analysts can edit manually. There are links to e-log and Run Summary. Flexible queries on the stored values can generate run lists for various purposes.

tion of these elements. Running a chain of analysis programs is automated using the Katrin Automation Framework for Fpd Examination and Evaluation (KAFFEE) software, which recognizes run types and data contents, and determines which program to start next with what parameters etc., then runs it, collects results, and builds a catalog of analysis results. The results in KAFFEE catalog can be interactively explored with the Koffein data browser, and some numbers in the KAFFEE results go into a run database on Browsable Run Entry Workspace (BREW) system which serves as a single shared run list in the collaboration. BREW takes inputs not only from KAFFEE auto-filling, but also from manual editing by operators and analysts, as well as Excel-sheet exporting and importing, with history management and conflict handling. For the KNM1 and KNM2 period, 11794 KATRIN runs were processed in CENPA with a chain of typically 10 different analysis programs for each run.

1.3 Data quality

S. Enomoto and M. Sun

Data quality analysis is critically important for the operation efficiency and for a reliable certification of the recorded data. The quality of the KATRIN data is monitored using a software toolkit developed and maintained by the UW KATRIN group. The quality checker filters data based on the operating status of the experimental apparatus.

The status of the KATRIN hardware is monitored by thousands of sensors mounted on the apparatus or inside the experiment hall. Quality of each subsystem can be assured by requiring the values of the corresponding sensors to be within certain ranges. The ranges of *good* condition are determined by experts of the sub-system, based on the knowledge of the apparatus, based on past values, and/or based on influence to neutrino mass estimation. The set of criteria is stored in the KATRIN SQL database together with target run types and validity periods.

We define a range of normal operation for each sensor, and we compare the sensor readings with the criteria. Difficulty arises from non-ideal behavior of sensors, such as noise, glitches, missing readings, and time mis-synchronization. Validity of sensors and criticality of troubles depend on the sensor and the context: some sensors are redundant for backup, some sensors operate only for certain sensitivity ranges, and some sensors are temporarily replaced with something else. Given the importance of the quality criteria, we should have only one master document on the criteria in the collaboration, however, the database itself cannot be directly used for this purpose because not all hardware experts are familiar enough with the software. A committee of KATRIN made a decision that the master document must be Excel sheets, to be filled and checked by the experts. Data integrity between Excel files on PC and SQL database on the server is a challenge, even if all the criteria are somehow described in a way that can be stored in a SQL database.

Although a simple pair of upper and lower boundaries work for the majority of sensors, it cannot handle the complexity. Some sort of logic, or sequencer on readings, is clearly necessary. By applying the BEANS concept of "linear sequence for everything" to the common control system construction, we designed a system of "chain of time-series processors" to handle all the mentioned use cases. The minimal case is just one processor of ValueRangeTest, which converts time-series of analog inputs to time-series of *quality levels* (in KATRIN, these are currently Green', 'Yellow' or 'Red'), while a chain can consists of any number of other processors including moving average, differentiation, gap detection, interpolation, grace period, hysteresis, vector operations, FIR/IIR filters, Kalman filter, and user-made custom filters. Like BEANS, processor objects are serializable to the JSON format (or any equivalent), and the database stores the serialized text of the processor chain as a description of the quality criteria (Fig. 1.3-2, *top left*).

Commonly used processor structures and parameters are extracted from the JSON serialization and formatted in a table, while the rest are still described in JSON as extension. A Python script was written to convert the data between Excel files and JSON serialization. If a criterion is described only with the common part, which is the case for most of the

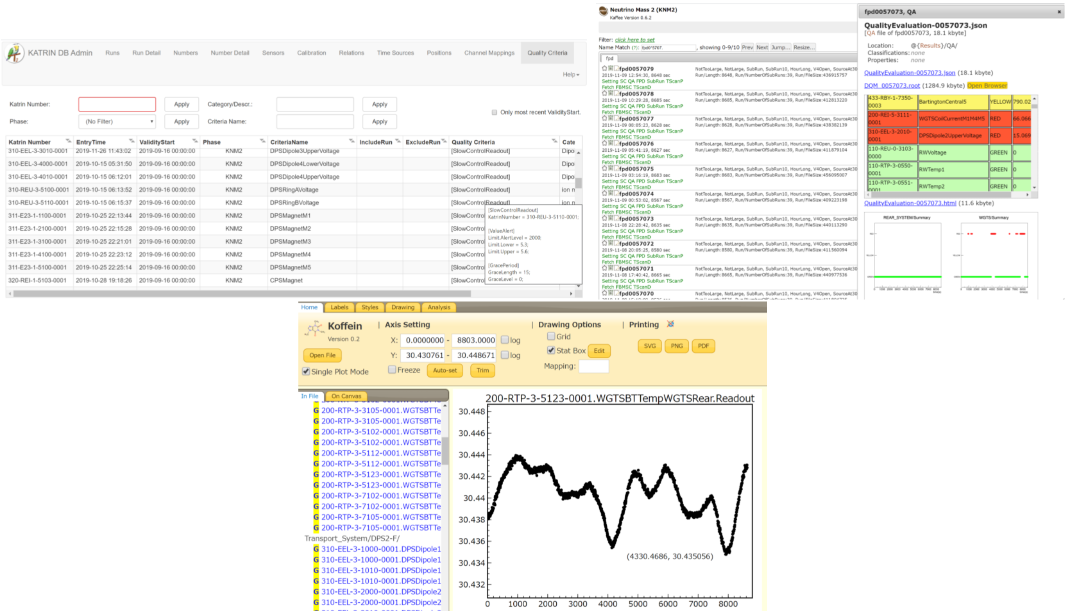

Figure 1.3-2. *Top Left*: Screenshot of Quality Criteria DB table. The pop-up box on the right shows a criteria description, a serialization of the processor chain in the INI format for readability in this example. *Top Right*: Screenshot of KAFFEE automation chain, showing a result of “QA” analysis. *Bottom*: Screenshot of Koffein interactive data browser on the QA analysis result.

sensors, then it fits into a simple Excel sheet with the *extension JSON* column empty. As the Python script can handle all the other structures such as comments and sections, it can generate a more human-readable summary document on-the-fly (this part is currently under development).

The chain of time-series processors is implemented as a BEANS element, therefore the quality analysis can be performed within the KATRIN standard data analysis framework (Fig. 1.2-1). BEANS automatically optimizes the data access to work with thousands of sensors for thousands of runs. KAFFEE automatically launches the quality analysis programs according to run types. The quality analysis results are summarized in KAFFEE catalog (Fig. 1.3-2, *top right*), and BREW has a column for quality flags for every run (Fig. 1.3-1, *bottom*). The Run Summary also has a section for the quality analysis summary.

1.4 FPD event level analysis

S. Enomoto

Despite the simple objective of FPD event analysis, counting arriving electrons, the analysis is not simple due to the discrepancy between the number of arrival electrons and the number of events recorded. The discrepancy, defined as (in)efficiency, is primarily determined by a cut on recorded energy to remove background events, but is also significantly influenced by other processes such as back-scattering on the Si detector, charge sharing among pixels, event pile-up, and readout dead-time. If the efficiency has dependence on the retarding potential of the spectrometer, or dependence on the rate itself, it will deform the shape of the integral spectrum (which is a spectrum constructed by FPD rates for various retarding potentials, used as input for spectrum shape fitting for the neutrino mass estimation) and thus become systematics on the neutrino mass estimation, if not corrected.

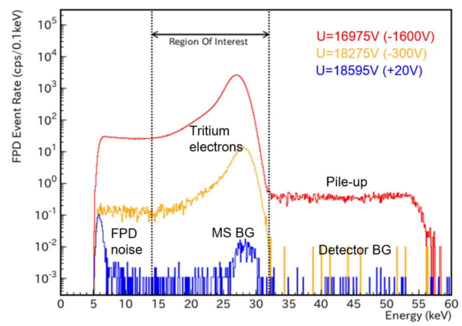

Figure 1.4-3. FPD Energy Spectra for several different retarding potential settings. Note that in KATRIN the energy measured by FPD is not directly used for spectroscopy of the tritium beta decay. The Region-Of-Interest (ROI) of FPD energy is defined to select beta electrons with reduced background events. The integral spectrum for beta spectroscopy is constructed from the FPD rates in the ROI for various retarding potential (U) settings. The FPD rate becomes higher for lower U settings because all the beta decay electrons with energy above U reach FPD. If U is set above the end-point of the beta decay, FPD sees only background events. In the figure, the energy above the end-point is indicated in the parenthesis.

Examples of FPD energy spectra for several retarding potentials are shown in Fig. 1.4-3. The events consist of not only the tritium decay electrons but also backgrounds from the spectrometer and the detector, with distinct spectrum shapes. The spectrum shape and peak position of the tritium electrons depend on the retarding potential as all electrons with an energy above the retarding potential reach the detector. The tail on the low-energy side is due to some complicated interplay of multiple effects and processes, including dead-layer of the detector, charge sharing among pixels, back-scattering, and reflection of the back-scattered electrons by the magnetic and electric fields back to the detector again. The low-energy tail has significant variation in the shapes caused by structures of the KATRIN field configuration and non-uniformity of the Si wafer. The high-energy side tail is due to the pile-up process, which varies according to the rate.

The KATRIN KNM1/KNM2 run data consist of tritium scans and a number of different calibrations. The tritium scan rates are typically very low at around 100 mcps/pixel, while source activity monitoring runs are taken at around 1 kcps/pixel, and some calibrations with an e-gun are taken at 30 kcps/pixel. While a higher electronics gain is preferred for low rate measurements for a better ADC resolution, lowered gain is necessary for high rate measurements to mitigate tail pile-up, which causes dead-time by baseline fluctuations moving out of ADC range. Using the Detector Readout Instrument and Pile-up Simulation (DRIPS) software developed at CENPA, the electronics gain was carefully adjusted for the KNM run plans, to keep the dead-time less than 0.05% for 50 kcps of 28-keV electrons, while the resolution degradation at low rates is smaller than the intrinsic detector resolution.

The event selection energy range, Region Of Interest (ROI), directly influences the detection efficiency and background rates. While a figure-of-merit optimization between the statistics and backgrounds resulted in a rather narrow window of few keV around the peak (Fig. 1.4-3), such an aggressive cut on a point where the spectrum slope is steep would increase susceptibility to apparatus instabilities and unknown systematics such as source potential fluctuations and FPD instability on gain and/or resolution. For KNM1 and KNM2, we adopted a rather broad ROI that extends from 14 keV to 32 keV in order to start from a safe side on systematics. Due to the unexpectedly high backgrounds from the spectrometer which has a spectrum shape almost identical to signal electrons, the increase of the total background for this broad ROI is small, at the several-percent level. By setting the lower bound of the energy cut at 14 keV (half of the incident electron energy), event triggering loss by charge splitting to another pixel cancels exactly with the additional triggering by charge splitting from another pixel. This canceling also applies to multiple events by a single incident electron caused by back-scattering on a pixel and reflection back to another pixel. The reduced dependence on peak width (FPD resolution) improves efficiency uniformity over pixels, making analysis of position dependent effects a lot easier.

For a fixed ROI, the detection efficiency varies depending on the retarding potential (U) setting, as all the beta decay electrons above the threshold reach the detector and therefore the energy distribution of electrons varies. Also the change of rates causes change of pile-up and thus causes change of detection efficiency. All these systematics were estimated by analyzing various measured spectrum shapes and simulations, and 0.1% level corrections were applied on the efficiencies. The error of the correction was estimated to be few tens ppm of the spectrum shape, small enough to be negligible to the KATRIN systematics budget.

The FPD event rates also provide rich information about the KATRIN apparatus status and stability, because the retarding potential is basically the difference of potentials between the tritium decay points and spectrometer, and changes of the potentials directly affect the FPD rates. Periodic rate measurements were performed with a lowered retarding potential at 300 eV below the beta decay end-point, which is very deep compared to the neutrino mass scale of $\sim$eV and therefore the statistics are high even for a short time. Possible drifts were searched for, which could be caused by work-function drift due to gradual contamination of the beam-tube surface, at $\sim$100 mV level sensitivity with a few minutes of data. Even for a stable mean value, over-dispersion of the rates compared to the pure Poissonian distribution was analyzed to estimate (or set an upper limit on) possible small time-scale fluctuations of the source plasma potential. Using a similar principle, we developed a method to detect 50 Hz ripple induced from the power-line grid onto the retarding potential, utilizing a kind of frequency lock-in technique. This method can detect 10 mV ripple on 18 kV voltage (<1 ppm!) in one hour, and has been used to test every KATRIN configuration.

1.5 FPD stability investigation

G. Bayarbaatar

To reduce the gap between KATRIN's systematic and statistical errors, it is becoming ever more important to ensure data quality of KNM2. Earlier this year, during the KNM2 FPD stability analysis, we noticed a gain jump of $\sim$400 eV in our tritium energy data, causing an efficiency jump of 0.066%. This small instability, which used to be considered negligible before, is now a subject of concern due to a recent detailed analysis on KATRIN's plasma investigation that requires the detector to be stable at this level.

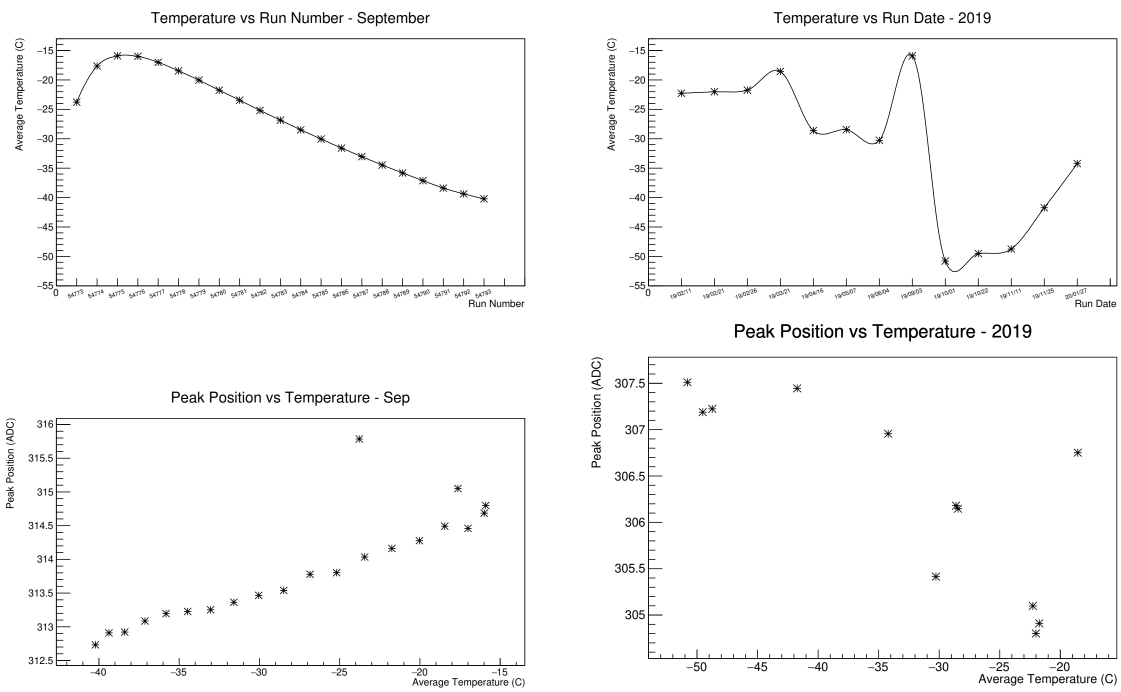

Figure 1.5-4. FPD Gain Stability. The top two graphs show the temperatures of the detector mounting *carousel* during our monthly ^{241}Am calibration runs. One plot point represents the average carousel temperature during a one hour long ^{241}Am calibration run. The left graph consists of consecutive runs taken on September 3rd, 2019, while the right graph consists of chosen runs from each month that a calibration was done in the year 2019. The bottom two graphs represent how the carousel temperature points taken from the top plots are related to the peak positions ($\approx$ gain) of the corresponding ^{241}Am calibration runs. Here, the peak positions seem to be dependent on the carousel temperature in the September plot (in a one month span); however, no clear dependence is observed in the 2019 plot or in a much longer one year time span.

This gain jump of $\sim$400 eV in the tritium spectrum scans was traced to instabilities of our bi-weekly FPD energy calibration with an ^{241}Am source. A thorough investigation of past ^{241}Am calibrations revealed dependence on various parameters, including wafer temperature, preamp temperature and ambient-air temperature. It turns out, the gain drift is not dependent on a single parameter, but on an interdependent combination of a few. The two plots in Fig. 1.5-4 show how peak positions of ^{241}Am-calibration runs change with carousel temperatures in a span of one month (September) and one year (2019), respectively. From this comparison, we have concluded that carousel temperature is a good indicator of peak position changes in the one month data - a shorter time span, but not for data accrued in a longer span, as in the one year data.

Since various processes in the system could be influencing this gain, we are targeting several temperature dependent processes to investigate further, these include:

- PIN diode electron/hole-pair production energy, and/or charge collection efficiency
- capacitance of the detector, if the detector is not fully depleted and if depletion changes
- capacitance of the capacitors in the preamp charge integrator near FET heat source
- gain of the optical driver used for optical transmission of analog signal

As of right now, April 2020, dedicated measurements are planned to test our hypotheses, and hardware upgrades are being made based on this finding. For example, thermometers are being placed near the optical fiber signal transmitters, giving much more accurate measurements of temperature that could be affecting optical output intensity as we suspect.

Using our findings and results from proposed measurements, we are constructing a gain drift model with multiple controlling parameters that could potentially explain the system process as a whole. Once established, we will not only have better understanding of our systematics, but also be able to optimize energy calibration frequency to increase the KATRIN live time for neutrino mass measurements.

1.6 Pile-up correction

S. Enomoto and M. Sun

Inelastic scattering in the source causes electrons to lose energy. Precise information on the energy loss can be achieved by a measurement of the energy differential scattering cross section near the endpoint of the tritium beta spectrum. Such a measurement can be performed using a monoenergetic electron source (e-gun) mounted at the rear wall of KATRIN. These electrons span a 50-eV wide range of surplus energy E − qU and pass through the molecular tritium source. The e-gun is operated at a rate of about 10^4 cps, which is 100 times higher than the nominal rate of tritium data taking. In addition, the e-gun will operate in a pulsed mode, where a large number of electrons get emitted at each pulse. At such a high rate, multiple electrons can arrive at the detector within a short time window and get identified as one electron due to the intrinsic deadtime of the detector. This effect is known as pile-up and can lead to an underestimation of the electron rate.

To correct for the energy distortion caused by the pile-up, an extension to the conventional trapezoidal filter was developed at CENPA. Here an additional trapezoidal stage provides another energy estimation, bipolar energy, which has tolerance to tail pile-up, and another time information, flat-top length, which can be used to resolve peak pile-up. (Fig. 1.6-5).

To fully utilize all the features of the pulse and increase the discriminating power be-

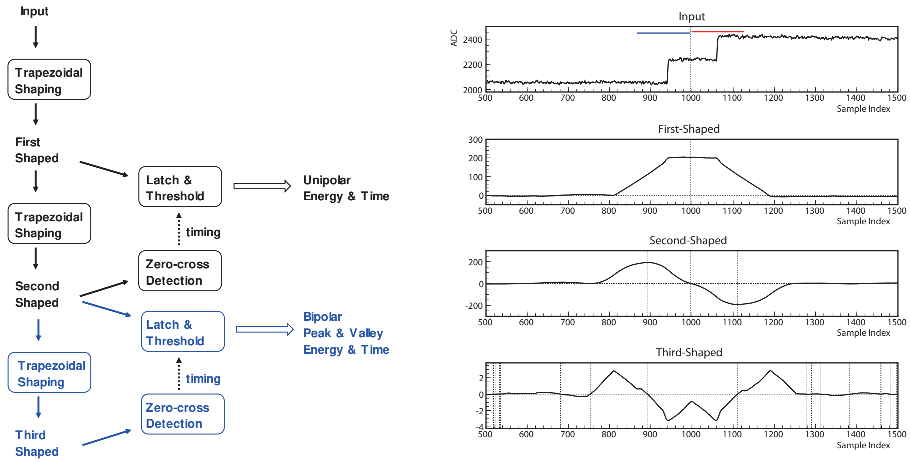

Figure 1.6-5. Outline of bipolar shaping trapezoidal filter (*left*) and DRIPS simulation of the filter behavior (*right*). This figure shows an example of pile-up of two electrons separated by an interval the same as the filter shaping length. The shaping process contains three trapezoidal filters, where the amplitude of the first one gives the unipolar energy. In the second shaping stage, the zero-crossing position is used as the trigger time. In the third shaping stage, zero-crossing points are corresponding to the peak and valley positions in second shaping, and their difference is called the flat-top width.

tween different multiplicities, we implemented a pile-up correction method based on gradient boosting decision trees. A decision tree is a tree-like model that contains a sequence of conditional control statements and decisions. One decision tree is prone to overfitting. To avoid overfitting and increase the accuracy of the model, multiple decision trees can be combined. The gradient boosted decision tree algorithm combines in series many sequentially connected weak decision trees, each tree attempting to minimize the errors of the previous tree, in order to form a strong model. In this study, we use the XGBoost python library to train and test our pile-up correction model.

Data used in this study is produced by the DRIPS simulation software which incorporates detailed detector responses. Electrons with a peak energy of 18.6 keV are simulated at an input rate of 10^4 cps. To better model the real data, the input distribution of the electron arrival time is obtained from previous e-gun data taking. For each surplus energy, a subset of data that contains 30 s of simulated events is generated.

The data used for training the boosted decision tree model is chosen to be a subset of simulated data with surplus energy of 3 eV. The following 6 features are used to construct the model:

- Unipolar energy: the reconstructed energy of the electron
- Bipolar peak time: the peak to zero-crossing time in bipolar mode
- Bipolar valley time: the valley to zero-crossing time in bipolar mode
- Bipolar peak energy: the amplitude of the bipolar peak
- Bipolar valley energy: the amplitude of the bipolar valley

The true values of the multiplicities are obtained by matching the incident electrons with triggered events. Since the multiplicity is a discrete variable, we use the multiclass classifier in the XGBoost to construct the classification model. The predicted results of applying such a model on testing data are probabilities for each multiplicity. There are two ways to use the predicted results: either sum over all possible multiplicities weighted by their probability or use the most probable multiplicity as the prediction. In the former case, an accuracy of 99.93% is achieved, while in the latter case the accuracy is 99.79%. An example of the prediction result is illustrated in Fig. 1.6-6.

To evaluate the uncertainty of the prediction accuracy caused by fluctuation in data, 100 sets of simulation data are generated and tested by the same model. The resulting uncertainty is 0.03%.

The electron rate is not a constant during the e-loss measurement, because of the different setting of surplus energy as well as fluctuations in column density of the source. To evaluate the changes in model performance, we generated 12 sets of testing dataset with a rate ranging from $6{\cdot}10^3$ cps to $1.2{\cdot}10^4$ cps. These data are tested by the same model that is trained at 10^4 cps, and the resulting performance shows negligible dependency on the electron rate, as shown in Fig. 1.6-6.

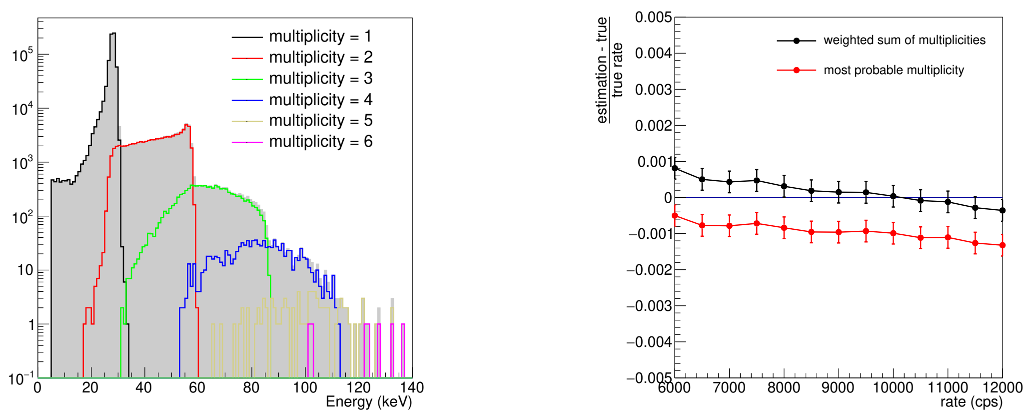

Figure 1.6-6. *Left*: Predicted energy spectrum of the simulation data. The filled area is the true energy distribution obtained from simulation, while the colored histograms are predicted results using the XGBoost model. *Right*: Mis-prediction rate as a function of the electron rate.

When surplus energy increases, the distribution of the time interval between consecutive events also changes, resulting in different multiplicity distributions in data. To study the possible model performance dependency on surplus energy, 20 sets of simulated data are generated with various surplus energy in the range [-3 V, 17 V]. The model is trained using a combined dataset with 3V, 7V and 12 V surplus energy, and is applied to all the 20 sets of testing data. The results show a 0.1% change in performance over all the testing data. Therefore, the prediction accuracy of the boosted decision tree model is robust against fluctuations in data. This method will be applied to e-loss measurements to mitigate the pileup effect.

TRIMS

1.7 TRIMS and the beta decay of molecular tritium

M. Kallander, Y.-T. Lin, E. Machado, D. S. Parno*, R. G. H. Robertson, and A. P. Vizcaya Hernández*

The Tritium Recoil Ion Mass Spectrometer (TRIMS) is a novel time-of-flight mass spectrometer designed to measure the branching ratio of the beta decay of molecular tritium to the many possible ionic final states. A final-state theory is needed to interpret neutrino mass experiments like KATRIN that use molecular T_2. One prediction of this theory is that 57% of the beta decays lead to the bound HeT^+ molecular ion (Saenz *et al*[1]). However, the only extant data on this branch come from two experiments with electromagnetic mass spectrometers in the 1950's[2,3]. The experiments were in good agreement with each other but in complete disagreement with theory: the branching ratio leading to the bound molecular ions was found to be 90 to 95% for both HT and T_2.

The heart of TRIMS is a 20-cm acceleration column made by NEC that has 60 kV applied across it. A uniform coaxial magnetic field of 0.237 T guides electrons and ions to Si detectors at either end (see Fig. 1.7-7). Molecular tritium is introduced into the chamber at

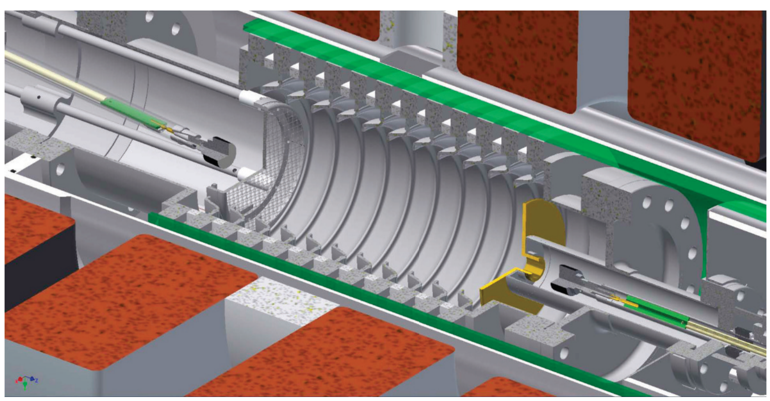

Figure 1.7-7. Cutaway view of the central part of the TRIMS apparatus, showing the acceleration column, two Si detectors on movable arms and the 4 magnet coils.

a pressure of a few 10^{-8} Torr. The gas supplied is predominantly T_2 but can be catalytically converted to HT by isotopic exchange on platinum-group filaments of vacuum gauges in a separate section, if desired. The data consist of delayed coincidence events between ions and electrons. From the ion energy and time of flight relative to the electron, a mass spectrum can be formed. Some decays lead to two ions or to a doubly charged He ion, and two electrons, so a charge spectrum is also calculated. The charge spectrum for HT is shown in Fig. 1.7-8. The figure shows singly charged groups of protons, He^+, HHe^+, and a weak mass-6 group

*Carnegie Mellon University, Pittsburgh, PA.

[1] A. Saenz, S. Jonsell and P. Froelich, Phys. Rev. Lett. **84**, 242 (2000).
[2] A. H. Snell, F. Pleasonton and H. E. Leming, J. Inorg. Nucl. Chem. **5**, 112 (1957).
[3] S. Wexler, J. Inorg. Nucl. Chem. **10**, 8 (1959).

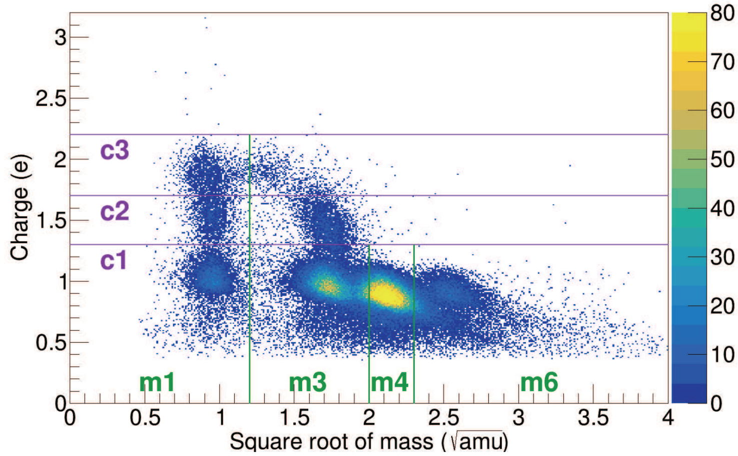

Figure 1.7-8. Coincidence data from TRIMS for HT grouped by charge and mass.

from residual T_2 that decays to THe^+. The charge-2 groups are He^{++} and H^++He^+. One can also see groups centered at charge 1.5, which arise when one of the electrons or one of the ions from a charge-2 decay is missed. Simply by inspection of this plot it is apparent that the branching ratio to the mass-4 group cannot be as large as 90 to 95%. A detailed analysis of the data has now been completed, with the conclusion that the branching ratio to HHe^+ is very consistent with the theoretical prediction.

The results for HT have been submitted for publication[1], and those for T_2 are being written up. The same theoretical treatment is used for both, and the initial focus on HT was motivated by practical considerations. With the heteronuclear parent, the final-state ions H^+ and He^+ are readily separated, while with T_2, the mass-3 ions T^+ and He^+ are indistinguishable. Furthermore, a substantial fraction of the mass-6 THe+ ions are produced in excited rotational and vibrational states that are energetically unbound but hindered by angular momentum from decaying. Those quasibound states may have appreciable lifetimes. In HT only 2% of the products are quasibound.

The data-taking phase of TRIMS is complete and results are being published. The apparatus is being kept in cold standby status pending completion of the papers.

[1] Y.-T. Lin *et al.*, Phys. Rev. Lett. **124**, 222502 (2020).

Project 8

1.8 Project 8

A. Ashtari Esfahani, C. Claessens*, P. J. Doe, M. Durand, M. Fertl*, J. Gort, J. Hartse, M. Huehn, M. Kallander, B. H. LaRoque‡, A. Lindman*, E. Machado, E. Novitski, W. Pettus, H. Robel, R. G. H. Robertson, G. Rybka, Y. Wang§, T. Weiss¶, S. Wilde, A. Ziegler‖, and The Project 8 Collaboration

Project 8 is an experimental program with the goal of applying a new technique in electron spectroscopy to the determination of neutrino mass. We have shown that the technique, Cyclotron Radiation Emission Spectroscopy (CRES) is indeed capable of precisely measuring the energies of single electrons[1]. This proof of concept, carried out with ^{83m}Kr, was Phase I of our staged program toward a final large-scale experiment.

In Phase II we have acquired the first tritium spectrum with CRES. As in Phase I, the apparatus is on the scale of a waveguide cell having an effective volume of only a few mm^3. A tritium-handling system that stores, meters, and dispenses tritium was built and has operated very successfully. The experiment is fully remotely operable with the exception of filling the superconducting magnet with cryogens. A method for dealing with the ^{3}He produced continuously was devised without the need for a permeator. A cylindrical waveguide cell replaced the rectangular one used in Phase I to increase the source volume, and 4 traps were implemented in the available uniform field region of the NMR magnet. The efficiency varies with frequency, because of TE11 reflections at the cell windows and a trapped TM01 mode in the cell, but could nevertheless be determined from a careful study of the signal-to-noise ratio. We expect that CRES offers the prospect of extremely low backgrounds, and that appears to be borne out. The planned 100-d run came to an end March 18, 2020, completing Phase II (papers aside).

Phase III, already in progress for some time, is focused on demonstrating several fundamental elements of a large-scale (Phase IV) neutrino mass experiment. A very attractive aspect of Project 8 is that an atomic tritium experiment appears to be possible. It would eliminate the 1-eV broadening associated with molecular degrees of freedom, and the associated theory for them. One of the two overarching concepts to demonstrate is the ability to detect CRES signals in the free-space environment resembling a large-scale experimental volume. The second is the ability to produce and store an atomic tritium source, and CENPA is one of the centers for that activity.

In the following sections, we describe in more detail a few of the elements of the experimental program at CENPA, the host laboratory for Project 8. The work would not be

*Johannes Gutenberg University, Mainz, Germany.
‡Pacific Northwest National Laboratory, Richland, WA.
§Case Western Reserve University, Cleveland, OH.
¶Massachusetts Institute of Technology, Cambridge, MA.
‖Pennsylvania State University, State College, PA.

[1] D. Asner *et al.*, Phys. Rev. Lett. **114**, 162501 (2015).

possible without the strong collaboration that is Project 8. We have also benefited from the contributions of many student volunteers.

1.9 Phase II: data-taking and tritium analysis

W. Pettus

The primary deliverable of Project 8 Phase II is a tritium endpoint spectrum, demonstrating control of systematic effects and the low backgrounds inherent to the technique. This last year saw the successful completion of data taking with the microtritium apparatus, achieving significant progress towards those goals. Two additional tritium runs were undertaken, with the high-statistics dataset concluding on March 18, 2020. Several diverse krypton campaigns were also pursued, with the final systematics run concluding on April 6.

Operations are built on a strong foundation from the 2018 campaigns, which demonstrated excellent energy resolution in shallow trap configurations, higher statistics running in deeper traps, and first tritium data ('run 1') presented at the DNP conference[1]. That limited dataset highlighted key improvement areas including optimized operating parameters, active mitigation of ^{3}He, and improved robustness of the DAQ and controls software. Improvements implemented in response to those experiences, have increased the statistics of recent runs through improved livetime and count rate. In addition, further systematic studies elucidated the subtle frequency- and trap-dependent effects in the data (Sec. 1.10).

Using the tools developed for the 2018 run, the experiment configuration parameters were re-optimized for the high-statistics tritium run. The trap configuration, operating pressure, and DAQ trigger were all modified based on newly-acquired krypton datasets to improve the count rate. Additionally, new high-resolution krypton datasets were taken to study the lineshape impacts from instrumental response and scattering (Sec. 1.11).

Significant effort was focused on the gas system this year, particularly to characterize and control the gas composition. The tritium 'run 2' in June was devoted to understanding the ^{3}He evolution in the system and the getter response after eight months in a passive state. Then in July, prompted by a failed conflat gasket, we undertook an internal review of operating procedures with the gas system and available diagnostics. Prompted by this review and with approval of the radiation safety office, the system was further modified to include an additional residual gas analyzer (RGA) adjacent to the tritium storage getter compartment. In both the final tritium and krypton data campaigns, active pumping was employed to moderate the ^{3}He levels throughout the system, with the new RGA providing critical information about the out-of-equilibrium conditions nearest the cell. These lessons learned are already being applied forward to the preliminary design of the gas system for the Phase III CRES demonstrator.

The controls and DAQ teams implemented several software upgrades to improve the livetime of the run, which will be carried forward to the operations structures used in future

[1] CENPA Annual Report, University of Washington (2019) p. 45.

phases. The DAQ software was migrated to a container deployment under the Kubernetes management system. This was primarily done to rapidly identify problematic software states and cleanly restart the software, but also affords greater version control and testing capability. The run scripting framework was also re-envisioned into a pure-python utility, allowing full feature flexibility required for the highly complicated systematics routines.

In the three-month tritium ‘run 3,’ we have achieved high livetime and collected over 4500 events (see Fig. 1.9-1). Full analysis of the tritium spectrum is ongoing, with publication planned to coincide with presentation at the summer conferences. The trying operational conditions of the COVID-19 shutdown have also highlighted the value of design choices made: Project 8 continued to run uninterrupted to finish the planned campaign with fully remote control.

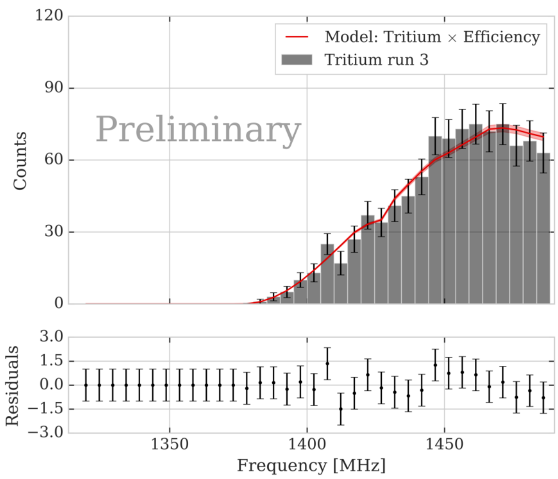

Figure 1.9-1. Preliminary tritium spectrum from a subset of the run 3 dataset. The measured frequency range, plotted after downmixing by 24.5 GHz, spans 1 keV beyond the tritium endpoint of 18.6 keV (frequency of 1368 MHz) through 2.5 keV below the endpoint. The fitted endpoint is consistent with literature and no background events are observed beyond the endpoint, validating the promise of the CRES technique.

1.10 Phase II: Background discrimination optimization and efficiency systematics studies

E. Novitski

In CRES, cyclotron radiation from an electron produces a signal that increases in frequency with time, producing characteristic “tracks” in a power spectrogram. Fig. 1.10-1 shows the first event in Project 8’s tritium data. The track and event reconstruction process detects high-power bins in Fourier-transformed data, identifies groups of these bins that are colinear in frequency vs. time to group them into tracks, and groups tracks belonging to a single electron together into an event. Next, a cut removes noise that had been incorrectly reconstructed as events. Further analysis extracts each event’s associated “start frequency” (the electron's cyclotron frequency at the time of its emission), takes into account any dependence of efficiency and start frequency precision on frequency to correct for systematic effects, and finally converts frequencies to energies to produce a spectrum.

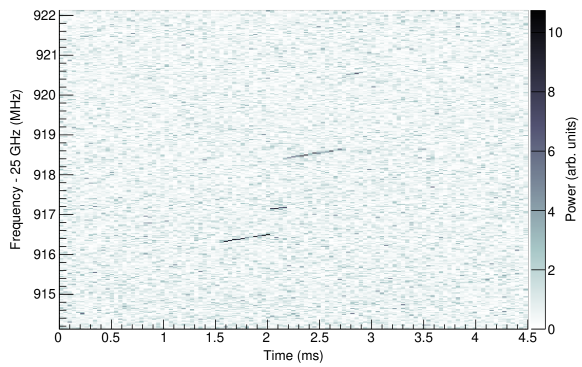

Figure 1.10-1. The first electron event identified from tritium in Project 8. The event begins at 1.5 ms. Frequency jumps between tracks are caused by inelastic collisions with gas molecules.

Improved background discrimination

The track and event reconstruction algorithm for Phase II was finalized in late 2019 after a final round of development focused on improving the cut just after the initial event reconstruction. The prior steps of the algorithm are performed with an intentionally high acceptance to yield a set of candidate events that includes as many real events as possible. These early steps exclude enough background events to avoid processing slowdown, but at this stage, many background events are still included. To remove them, a cut is performed based on three event characteristics: the number of tracks, the average power of the bins in the first track, and the number of bins in the first track (roughly, the track duration). Rather than cut on each characteristic separately, detection sensitivity and specificity are improved by classifying each event as being part of a group of events that share its number of tracks and its number of bins in the first track, and setting an average-first-track-power threshold separately for each group. The power thresholds, shown in Fig. 1.10-2, are set by studying the power distribution of false "events" in each group in control data taken without CRES electrons in the trap.

Implementing this cut reduced the false event rate by a factor of 50, while only reducing sensitivity to real tracks by 16%. The final version of the analysis produces a predicted rate of false events due to reconstruction error of less than 1 per 80 MHz data acquisition channel per 100 days, with a confidence level of 90%.

Though time and data storage contraints prevented the acquisition of an electron-free control dataset large enough to fully test this prediction, analysis of a 24-hour control dataset yielded no events. There were also no events above the tritum endpoint in a 76±3-day dataset, as shown in Fig. 1.9-1.

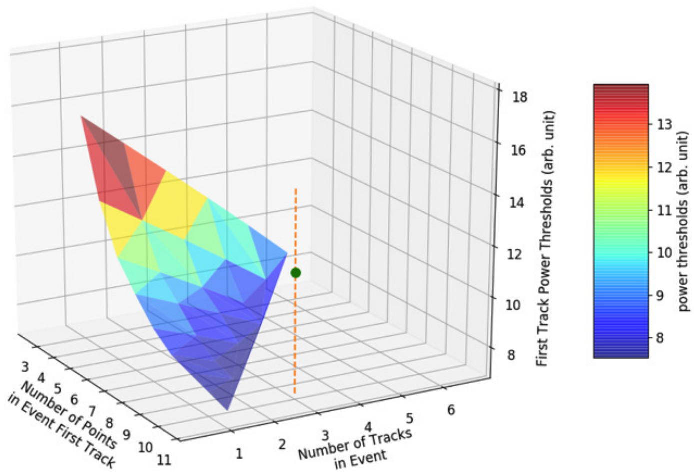

Figure 1.10-2. The surface represents the cut threshold in a 3-D parameter space corresponding to three reconstructed event characteristics. The green point is a sample candidate event that made the cut to be counted as a true event.

Systematic studies of frequency-dependent variations in efficiency

Variations of detection efficiency with frequency must be understood and corrected for in order to accurately extract the endpoint of the tritium spectrum. To explore these effects, an extra coil called the "field-shifting solenoid" surrounding the detection volume[1] was used to homogeneously shift the background magnetic field by $\pm 0.3\%$. By changing the current in this solenoid, the cyclotron frequencies of 17.8 keV electrons from ^{83m}Kr were swept through the detection frequency region corresponding to the 3.4 keV window planned for tritium datataking. Data for several frequencies are shown in Fig. 1.10-3.

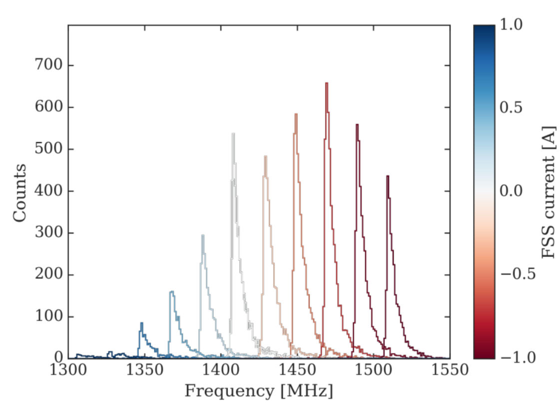

Figure 1.10-3. Counts vs. frequency-24.5 GHz for multiple ^{83m}Kr datasets taken with different background magnetic fields. The field shifts were created by changing the current through the field-shifting solenoid.

[1] CENPA Annual Report, University of Washington (2019) p. 43.

Several effects are believed to have contributed to efficiency variations. Though an RF terminator installed below the gas cell dramatically reduced reflections, it did not entirely eliminate them. Reflection from this terminator and from the lower window in the gas cell gave rise to position- and frequency-dependent interference that caused gradual changes in efficiency over the detection frequency range. Fig. 1.10-4 shows how track power changes in different trap coils as a result of this interference pattern. This effect, along with image noise from a later stage of the RF detection chain, caused a decrease in efficiency with increasing frequency. The four traps were used simultaneously in taking tritium data, making it necessary to produce a combined efficiency curve.

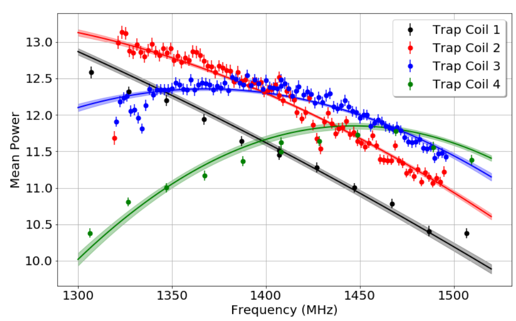

Figure 1.10-4. Measured track power vs. frequency-24.5 GHz in each individual trap (points) plotted against model from trap geometry (line with error). Because of the position-dependence of the destructive interference, each trap coil experienced a different frequency dependence of the efficiency variation of its trapped electrons. The curve shapes are predicted from the geometry of the cell and trap and agree well with the data.

In addition, a cavity-mode-like effect, from back-reflections of the TM_{01} mode of the waveguide, from the gas cell windows and other RF imperfections, is believed to have given rise to enhancement of spontaneous emission in some narrow frequency regions. This caused those electrons to lose energy faster, producing tracks whose frequencies changed more quickly (greater track "slope", e.g., at 1425 MHz in Fig. 1.10-5), which were in turn reconstructed less efficiently. The observed slope effects in these regions have been shown to explain the sharper dips in efficiency, e.g., at 1425 MHz in Fig. 1.10-6.

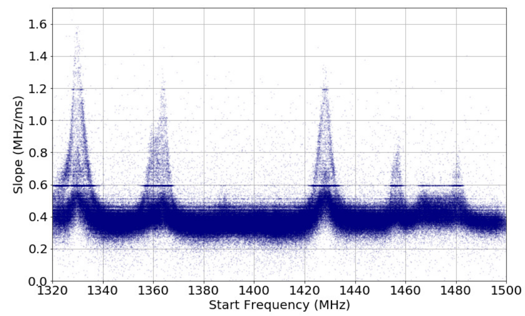

Figure 1.10-5. Track slopes vs. frequency-24.5 GHz for ^{83m}Kr data taken with different background magnetic fields.

Unfortunately, the power emitted by, and therefore the signal-to-noise ratio of and detection efficiency for, an 18.6-keV electron is not the same as that for a 17.8-keV electron in a shifted magnetic field. Therefore, it was not possible to use the raw count rates from ^{83m}Kr data to calculate relative efficiencies at different frequencies.

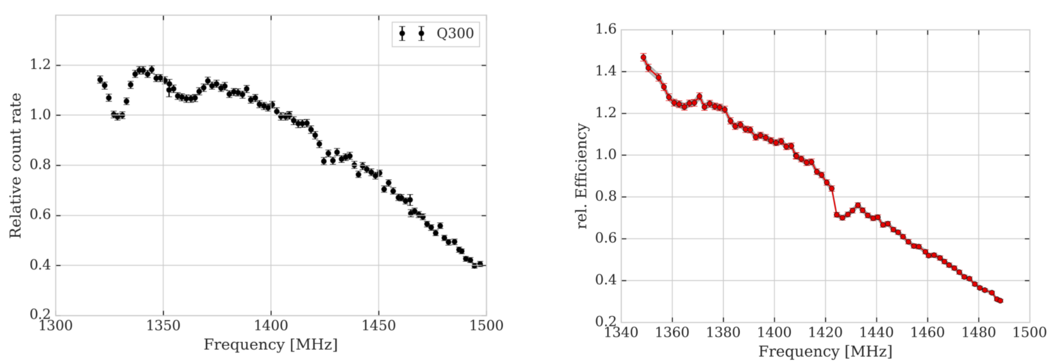

Figure 1.10-6. *Left*: Counts vs. frequency-24.5 GHz for ^{83m}Kr data taken using the field-shifting solenoid. *Right*: Derived detection efficiency for tritium data vs. frequency-24.5 GHz.

Instead, the field-shifted ^{83m}Kr data in each individual trap were analyzed to determine the distribution of track powers at each frequency. These were then adjusted to correct for the difference in power emitted by an electron of the corresponding kinetic energy. Simulated data were used to understand the effects of these corrections on detection efficiency. These results for individual traps were combined into a single detection efficiency curve. Fig. 1.10-6 compares the count rate in each ^{83m}Kr dataset with the extracted tritium efficiency prediction at that frequency.

1.11 Spectroscopy of ^{83m}Kr

A. Ashtari Esfahani

^{83m}Kr is a common calibration source for tritium endpoint measurement experiments. It decays through two sequential transitions of 32 keV and 9.4 keV. The energy of these transitions are internally converted to release electrons from the krypton's electron shells. The energy of these electrons depend on the shell to which they belonged initially. Fig. 1.11-1 shows the measurement of 32-keV conversion electron's energies from the K, L, M, and N lines of the spectrum.

The measurements shown in Fig. 1.11-1 are performed simultaneously using three channels of Phase II DAQ system. In order to achieve the high resolutions in Fig. 1.11-1 a shallow trap geometry is used. A shallow trap is one in which the disturbance of the background field is minimal by keeping the coil currents low. As a result, electrons with various radial positions and different axial motions inside the trap experience almost identical averaged magnetic fields.

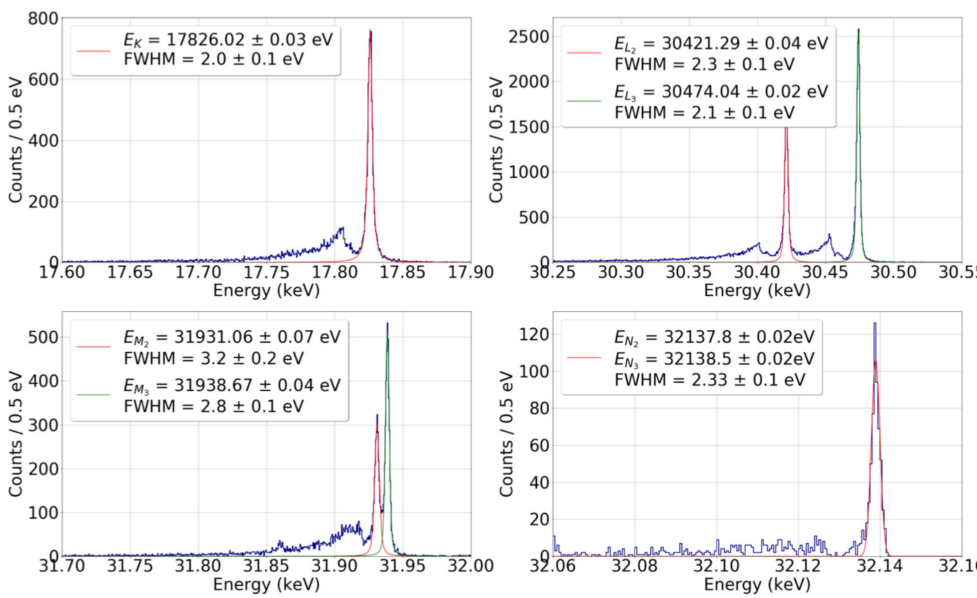

Figure 1.11-1. Energy histogram of the 32-keV conversion electrons from the K, L, M, and N lines of the ^{83m}Kr spectrum. The data is recorded in a shallow trap which is generated by running trap coil 3 at 12 mA current and trap coil 4 at 17.5 mA. The trapping field strength is $\sim 0.005\%$ of the background field in this geometry.

Although the shallow trap is an ideal geometry for high resolution measurements, its low effective trap volume makes it an undesirable choice for measuring rare events such as high energy electrons in the tritium spectrum. In these cases a deeper trap produces a higher count rate at the expense of a compromised energy resolution.

In the Phase II trap geometry, electrons with larger radii experience a lower magnetic field while electrons with larger axial reach experience a larger averaged value of magnetic field. These variations in the field result in a broadening of the krypton lines.

Knowledge of an electron's radial position and axial motion can assist us in achieving better energy resolution in the deep traps. The track power and slope provide this information.

The track slope is a measure for the total radiated power by the electron. That is because the rate of energy change manifests itself in a change in the frequency of cyclotron radiation. This change in the frequency causes the slope in the tracks.

The track slope depends on the electron's coupling to the waveguide mode. The coupling changes with the electron's radial position. Therefore the track slope also provides information about an electron's radial position. The track power also depends on the electron's coupling to the waveguide mode. Furthermore, the traveled axial distance alters its detected power through the Doppler effect [1].

Thus, track slope and power can provide information about an electron that can be used to correct for the field variations inside the trap. Fig. 1.11-2 illustrates how this procedure worked for the L line of krypton spectrum recorded in a 300 mA deep trap.

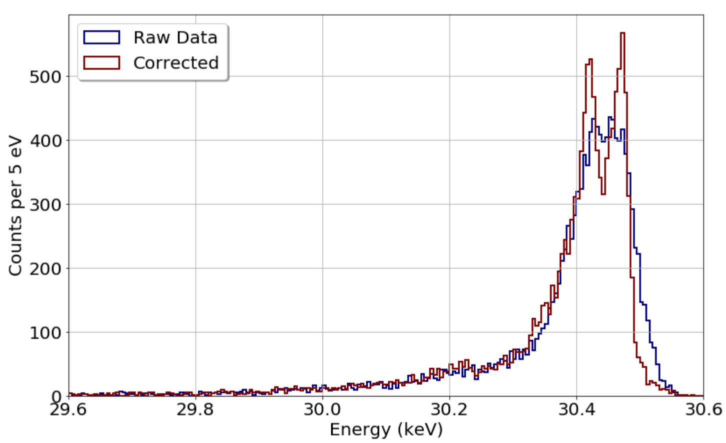

Figure 1.11-2. Energy histogram of L line of the ^{83m}Kr spectrum recorded in a 300 mA deep trap (trapping field is $\sim 1\%$ of the background field). The corrected histogram uses track power and slope to correct for the differences in the averaged magnetic field experienced by different electrons inside the trap. The doublet structure of the L line which was hidden in the raw spectrum become obvious after applying the correction.

[1] A. Ashtari Esfahani et al. (Project 8 Collaboration) Phys. Rev. C **99**, 055501 (2019).

1.12 Shakeup and shakeoff in ^{83m}Kr

R. G. H. Robertson and V. Venkatapathy*

The isotope ^{83m}Kr has been used for calibration and tests in all modern neutrino mass experiments that are based on the beta spectrum of tritium. It is conveniently produced as the daughter of 86-d ^{83}Rb and has a 1.8-hr half-life. The decay of the isomer is via 2 gamma transitions, 32 keV and 9.4 keV, which are internally converted to produce electron lines that have natural widths of only a few eV. The K-shell line at 17.8 keV is particularly useful because it is so close to the tritium endpoint at 18.6 keV and has a 2.7-eV line width.

Internal conversion lines have lower-energy satellites that are caused by shakeup and shakeoff when another electron is excited or ejected at the same time as the conversion electron. These processes modify the shape of the 'core' line, and can be important in applications that rely on the shape of the Kr line more than 20 eV from the peak. In Project 8, electrons are trapped in a weak magnetic trap and escape by scattering from residual gas molecules, often several times. The Kr conversion lines are used to develop an understanding of the resulting response function, but since the scattered intensity and shake intensity fall in the same spectral region, a quantitative description of the shake spectrum is needed. We have made use of photoionization data we obtained[1] at the Stanford Synchrotron Radiation Light source to derive the spectrum. The data have relatively low resolution by the standards of Project 8 and therefore theoretical inputs were used to assemble the basic ingredients of the two-vacancy shake spectrum. The positions and intensities of the lines were then fitted to the data to extract the spectrum unmodified by instrumental resolution (Fig. 1.12-1.) The work has been written up for publication.

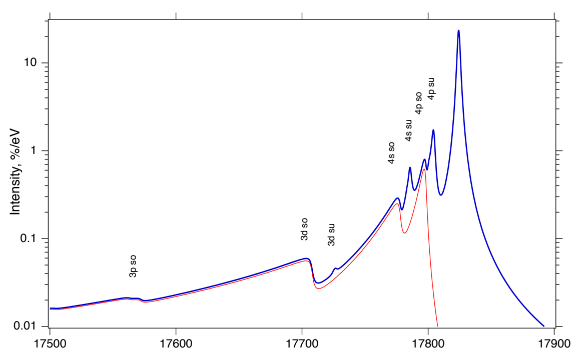

Figure 1.12-1. Spectrum of the ^{83m}Kr K-32 line showing the shakeup ('su') and shakeoff ('so') satellite structure (in blue). The fine line in red shows the shakeoff component alone.

*Tesla STEM High School Senior Volunteer, Redmond WA.

[1]D. L. Wark *et al.*, Phys. Rev. Lett. **67**, 2291 (1991).

1.13 Atomic source development

P. Doe

In order to explore beyond the 0.2 eV neutrino mass sensitivity of KATRIN, Project 8 will require an atomic tritium source, free from the uncertainties resulting from the energy excitation modes associated with a molecular tritium source.
The tritium trap for Project 8 requires to be fed by a source of $\approx 10^{15}$ atoms/s, cooled to a temperature of 0.7 K. Such a source does not currently exist. CENPA is using the apparatus, shown schematically in Fig. 1.13-1, to develop this source.

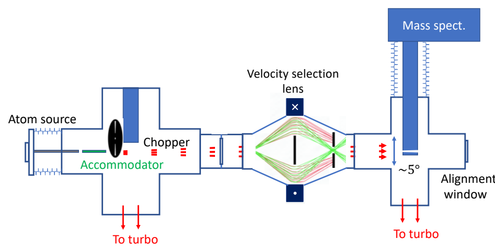

Figure 1.13-1. A schematic of the apparatus used to develop the atom tritium source..

Molecular tritium is first dissociated at temperatures of around 2000K to produce a source of approximately 10^{19} tritium atoms/s. Current commercial dissociators struggle to meet this high flux, and a novel dissociator, using an electrically heated tungsten tube to dissociate the tritium molecules, is being built by CENPA for evaluation.
With a high flux source in hand, the next step is to cool the atoms down to $\approx$30 K. This will be achieved by a cooled aluminum-'accommodator' tube. As the atomic beam passes through the tube, collisions with the walls of the cold tube cools the beam to 30 K. In order to test the efficacy of this accommodator we are using a beam chopper and time-of-flight to determine the temperature of the cooled beam. Suitable in-vacuum beam choppers are not readily available commercially and CENPA is developing its own.

The 30 K atoms must now be cooled to 0.7 K in order to be acceptable to the atomic trap. Utilizing the magnetic moment of the tritium atoms, a focusing lens and aperture system provides velocity selection to rejects hot atoms and accept atoms of the required temperature as illustrated in Fig. 1.13-1. All beam studies use a mass spectrometer optimized to mass 1 and mass 2. Scanning the mass spectrometer across the beam provides a measure of beam intensity and profile.

The apparatus shown in Fig. 1.13-2 will be used to evaluate the CENPA high flux source. Currently, for commissioning the apparatus, a commercial dissociator is being used. The apparatus will be sequentially extended to include the CENPA high flux dissociator, the beam chopper, the accommodator and velocity selection hardware for final beam cooling studies. Our goals are to complete these atomic source studies, and to provide a demonstrated design for a Phase 4 atomic source within the next two years.

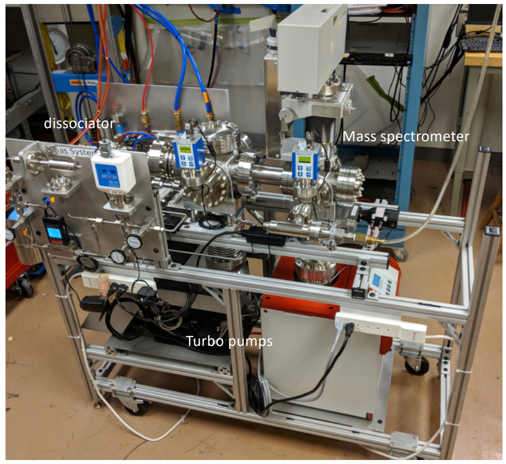

Figure 1.13-2. the source development apparatus as it currently exists.

Majorana

1.14 Status of the Majorana Demonstrator neutrinoless double-beta decay experiment

T. Burritt, M. Buuck*, J. A. Detwiler, M. Durand, I. Guinn†, A. Hostiuc, T. Mathew, D. A. Peterson, W. Pettus, N. W. Ruof, M. Stortini‡, T. D. Van Wechel, and C. Wiseman

The Majorana Demonstrator neutrinoless double-beta decay ($0\nu\beta\beta$) experiment continues data taking at the 4850 ft level of the Sanford Underground Research Facility (SURF) in Lead, SD. The experiment consists of a modular array of p-type point contact (PPC) high purity germanium (HPGe) detectors, with most detectors enriched in the $0\nu\beta\beta$ isotope ^{76}Ge (Fig. 1.14-1). The stable operation of the detector has afforded greater emphasis on analysis efforts. This last year saw publications on the multisite discrimination analysis[1] and the second $0\nu\beta\beta$ analysis[2], and preparation of a manuscript on digitizer nonlinearity correction[3].

---

*Presently at SLAC National Accelerator Laboratory, Menlo Park, CA.
†Presently at University of North Carolina, Chapel Hill, NC.
‡Presently at Los Alamos National Laboratory, Los Alamos, NM.

[1] S. I. Alvis *et al.*, Phys. Rev. C **99**, 065501 (2019).
[2] S. I. Alvis *et al.*, Phys. Rev. C **100**, 025501 (2019).
[3] N. Abgrall *et al.*, arXiv:2003.04128 (2020); *submitted to IEEE Trans. Nuc. Sci.*

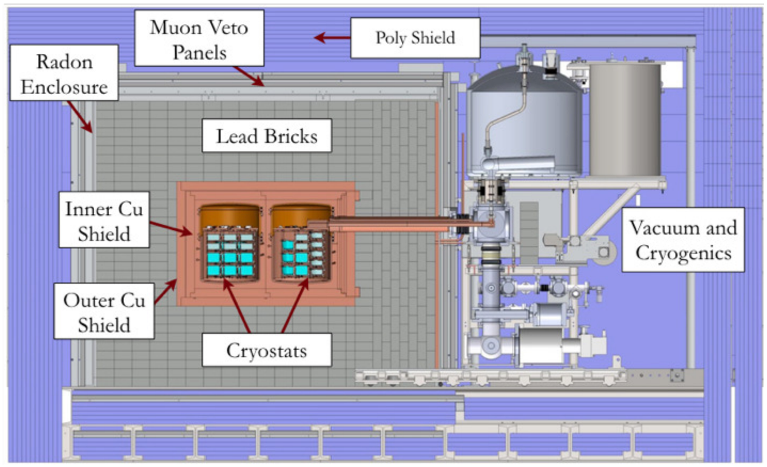

Figure 1.14-1. Schematic of the MAJORANA DEMONSTRATOR experiment. The germanium detectors (teal), enriched in the ^{76}Ge isotope of interest, are assembled with low-background materials into close-packed arrays in two cryostats inside a passive shield.

Beginning in late November, the science run was interrupted and one module opened for hardware upgrades. All the original cables and CENPA-produced connectors[1] were replaced with a new design, and the cable bundling and routing was improved. Combined, these changes have restored more of the array to working condition. Extra shielding has been installed along the crossarm to eliminate shine paths, responding to our improved understanding of the source of array backgrounds. Additionally, new enriched detectors have been produced by ORTEC in the novel inverted-coaxial geometry, whose performance will be investigated by operating as part of the DEMONSTRATOR array. These new detectors replace five original enriched PPCs, which were shipped to Italy for preliminary LEGEND-200 tests (Sec. 1.19), as well as several natural detectors. The collaboration is looking forward to an additional half-year science run through late 2021 (to begin after the COVID-19 imposed work shutdown), after which time the remaining enriched detectors will be relocated to Gran Sasso, Italy, for inclusion in the LEGEND-200 experiment.

The CENPA MAJORANA group had significant achievements in 2019. Graduate students Micah Buuck and Ian Guinn both successfully defended their Ph.D. theses last summer, and Nick Ruof passed his general exam for Ph.D. candidacy. Micah's thesis, on background modeling[2], contributed significantly to our understanding of the distribution of backgrounds in the DEMONSTRATOR and the implications for LEGEND. Ian's thesis, on double beta decay to excited states[3], obtained the most sensitive limits for these decay modes; the preliminary result was presented at the TAUP 2019 conference with peer-reviewed publication in preparation. Postdoc Clint Wiseman continues his leadership of the low-energy working group, which released new highlighted results also at the TAUP 2019 conference with publications in preparation (Sec. 1.15).

[1]CENPA Annual Report, University of Washington (2015) p. 21.
[2]CENPA Annual Report, University of Washington (2019) p. 17.
[3]CENPA Annual Report, University of Washington (2019) p. 13.

Postdoc Walter Pettus, together with former group postdoc Clara Cuesta, finished the manuscript, and saw publication of the paper, on the *AvsE* multisite event discrimination cut used in the $0\nu\beta\beta$ physics analysis. Graduate student Nick Ruof has taken over development of the AvsE analysis (Sec. 1.17), including integration of new ^{56}Co data to assess the energy dependence of the cut. Graduate student Alex Hostiuc continues his work on the DCR surface alpha rejection (Sec. 1.16). The group operates germanium detectors in the lab at CENPA, investigating key detector response characteristics (Sec. 1.18) and providing involvement for undergraduates in the project, while leveraging the technical expertise at CENPA.

The group's contributions to the project are further recognized by election to leadership positions. Jason continues service as co-spokesperson of the collaboration, being re-elected last summer. Nick and Ian were elected the two young member representatives for this year, as Walter completed his term in the same position.

1.15 Low-energy analysis for the MAJORANA DEMONSTRATOR

M. Lopez*, I. Kim†, and C. Wiseman

The MAJORANA Low-Energy Working Group has reached several significant milestones towards our first new low-energy publication since 2017. Clint Wiseman summarized this work during a contributed talk at the TAUP 2019 conference in Toyama, Japan. This work was highlighted, in the broader context of larger-scale dark matter experiments, in the plenary talk of Dr. M. Yamashita (ICRR Univ. of Tokyo), emphasizing the continued relevance of axion-like particle and hidden photon searches, as an interesting alternative to standard WIMP searches by larger-scale experiments.

The updated search for bosonic dark matter (coupling of axion-like particles to electrons) presented at TAUP takes advantage of nearly a factor 10 more enriched exposure than the 2017 paper (478 kg-d), which was based on early MAJORANA commissioning data. For this analysis, the signal rate in the low energy region has been reduced by a factor 4 (to ~0.01 cts/kg-d/keV between 20–40 keV) due to the installation of an underground-electroformed inner copper shield, and a completed outer shield. Fig. 1.15-1 shows the preliminary spectra from the enriched and natural detectors, and the enriched efficiency curve.

The Pb background is external to the detectors, and we see that the peak at 46.5 keV is wider than the expectation from our energy resolution function. In addition, we do not observe the expected accompanying line at 10.8 keV. This indicates an additional mechanism for energy degradation at the passivated surface of the detectors. The details of the mechanism are being investigated via `Geant4` and HPGe signal simulation software, and on a longer-term scale at the University of Washington by the

*University of South Dakota, Vermillion, SD.

†Los Alamos National Laboratory, Los Alamos, NM.

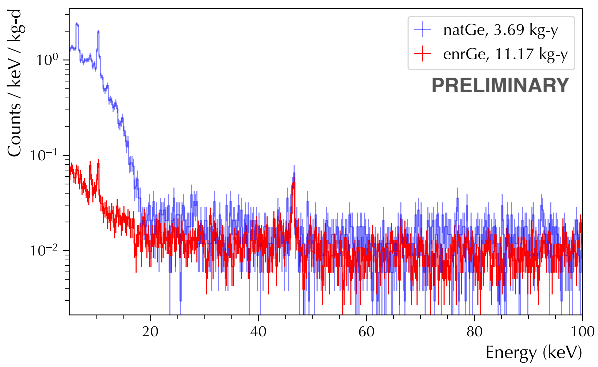

Figure 1.15-1. *Left*: The enriched and natural spectrum from Data Sets 1–6A. We observe a factor 4 reduction in backgrounds above the tritium endpoint at 18 keV over the Data Set 0 analysis. The increased exposure has also allowed us to observe a clear line from ^{210}Pb at 46.5 keV in both the enriched and natural detectors. *Right*: The combined efficiency (red) and its uncertainty (upper, cyan, lower, magenta) for the enriched detectors.

development of the CAGE internal scanning cryostat (Sec. 1.20), and additional studies with a gaseous ^{83m}Kr source on loan from the Project 8 collaboration (Sec. 1.18).

The exclusion curve for the axion-electron coupling constant g_{ae} as a function of axion mass is shown in Fig. 1.15-2. The exclusion curve was generated from open data in Data Sets 1–6A using the same unbinned profile likelihood method used in the 2017 paper (Data Set 0).

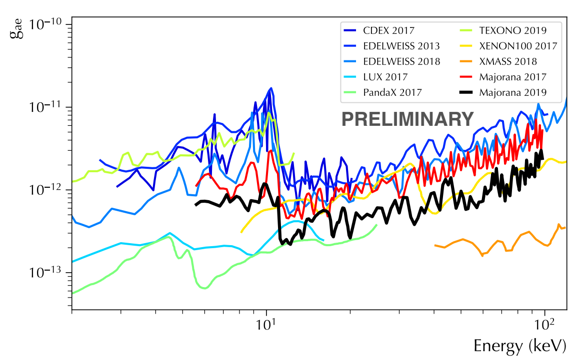

Figure 1.15-2. Exclusion limits for the Data Set 1–6A analysis (black), plotted against the previous Majorana result (red), and other current experimental limits.

To finalize the analysis presented at TAUP, the Low-energy Analysis Toolkit (LAT) is nearing completion of a software refactor that will allow us to quickly vary cut parameters, and straightforwardly include blind datasets. The three main data cleaning cuts – energy threshold, slow pulse, and high-frequency noise rejection – must be tuned for every detector after every calibration, presenting a challenge, since the Demonstrator has been in operation for several years at this point. We have completed efforts to improve the speed of the slow pulse estimation parameter, which fits each waveform to an exponentially modified Gaussian function. By rewriting the fitting code to incorporate the Numba package, we have obtained a significant speedup for this computationally intensive task. The LAT software is able to generate spectra and save event information of events passing cuts for further physics analysis, as well as provide overall and detector-specific cut efficiency curves. The analysis process must be made automatic, so that no human intervention is required when we include unblinded Data Sets. In addition, automatic routines are being developed to expedite processing of new Data Sets, and file consistency checks have been implemented.

A new method of calculating thresholds has been developed for inclusion in the current LAT analysis. The initial 2017 analysis used a software threshold of 5 keV, while the detectors routinely trigger at energies below 1 keV. We have set a goal of a 1-keV analysis for our next publication. The new algorithm compares the energy of events as evaluated by the digitizer's onboard trapezoidal filter, and the offline final energy. By finding the point at which the relationship between onboard and offline energy becomes nonlinear, and measuring the spread of the points in the linear region, we can parameterize the efficiency in terms of an error function with parameters μ, σ. Previous analyses used the same error function to parameterize the efficiency as a function of energy, but set analysis cutoffs at $\mu + 3\sigma$, allowing only signals with >99% efficiency to pass the threshold cut, with negligible uncertainty. The new algorithm takes into account the efficiency uncertainty, defining the cutoff when the uncertainty in the efficiency exceeds 10%. This allows lower analysis thresholds to be placed on each detector, increasing the effective exposure at 1 keV. This is illlustrated in Fig. 1.15-3.

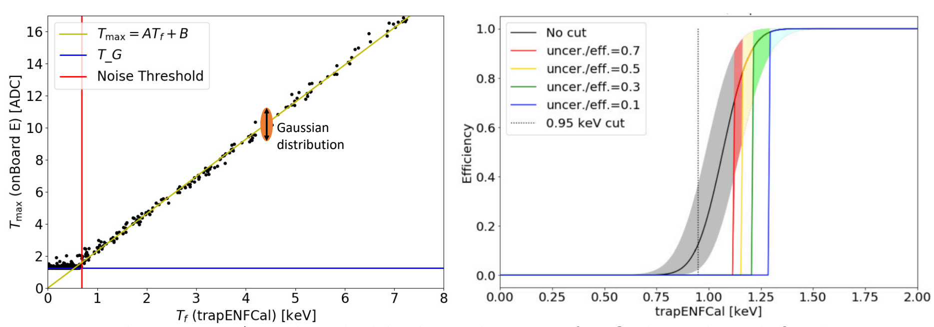

Figure 1.15-3. The new LAT threshold algorithm. *Left*: Onboard and final energies are compared. The noise threshold (where Gaussian noise-induced events become dominant) is marked in red, and the critical 50% efficiency point is at the intersection of yellow and blue lines. *Right*: Illustration of the 10% uncertainty cut (blue).

A simulation of charge buildup at the passivated surfaces of the detectors by M. Lopez (USD) has shown promise in explaining the absence of a 10.8 keV line in our spectrum from ^{210}Pb, despite the presence of the accompanying 46 keV line. By simulating a layer of surface impurities and the ^{210}Pb decay chain, we find that our data is consistent with a negative uniform surface impurity of -0.3×10^{-10} atoms / cm^2. Of course, a uniform distribution is not the only possible model for this energy degradation, but there is not yet enough background data to distinguish between different models. Once generated, the ^{210}Pb background can be included in the multi-component fit to the energy spectrum.

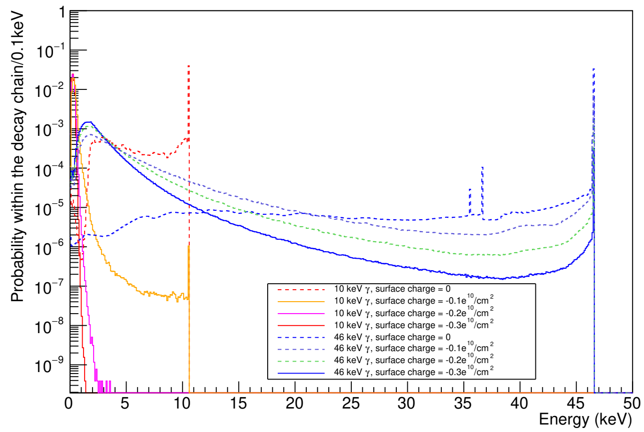

Figure 1.15-4. Simulation results from the passivated surface impurity study. A surface charge of 0 (dashed lines) is compared with a negative surface charge (solid red, solid blue), and an attenuation of the 10.8 keV line by more than 5 orders of magnitude is observed, while the 46 keV line is only reduced by two orders of magnitude.

1.16 Alpha particle discrimination in the MAJORANA DEMONSTRATOR

J. A. Detwiler, A. Hostiuc, W. Pettus, N. W. Ruof, and C. Wiseman

Reduced charge collection has been observed on the passivated surface of Germanium detectors similar to MAJORANA DEMONSTRATOR's detectors. In our experiment, events have been observed in which alphas originating on the passivated surface are significantly degraded in energy, which can result in background in the region of interest (ROI) for neutrinoless double beta decay, i.e. close to the $Q_{\beta\beta}$ value for ^{76}Ge of 2039 keV.

The delayed charge recovery (DCR) parameter is used in the MAJORANA DEMONSTRATOR in order to reject this alpha background in the attempt to achieve the necessary low background. The physical effect behind DCR is that the charge deposited by the alpha particle does not get collected all at once. Rather, some of the charge is trapped and then released slowly, on the timescale of the waveform digitization, with a characteristic shape. Specifically, the effect increases the slope of the waveform tail, appearing as extra charge. The DCR parameter in its current iteration allows for an effective rejection of background alphas while maintaining $\sim$99% of the bulk-detector events, as measured during ^{228}Th calibrations.

A new implementation of DCR, version 2.0, has been developed and is in process of being applied to data. A brief description of the new DCR calculation follows.

Using pole-zero corrected, electronics transfer-function deconvolved waveforms ensures a nearly flat-top waveform. In effect, we remove the exponential decay associated with charge bleeding from the feedback capacitor. Therefore, the distribution of "raw DCR" (δ) events in calibration is centered close to zero, with some small spread. We can use the means and widths, of Gaussian fits to this raw distribution, to create the new DCR parameter. This is done as such:

$$\text{DCR} = \frac{\delta - \alpha E}{\beta + \gamma E} \tag{1}$$

where α is the constant of proportionality between the means and the energy of the event. γ and β are the linear and constant parameters fitted to the relationship between the widths of the raw distribution and the energy of the event. See Fig. 1.16-1 for an example distribution of rawDCR and DCR.

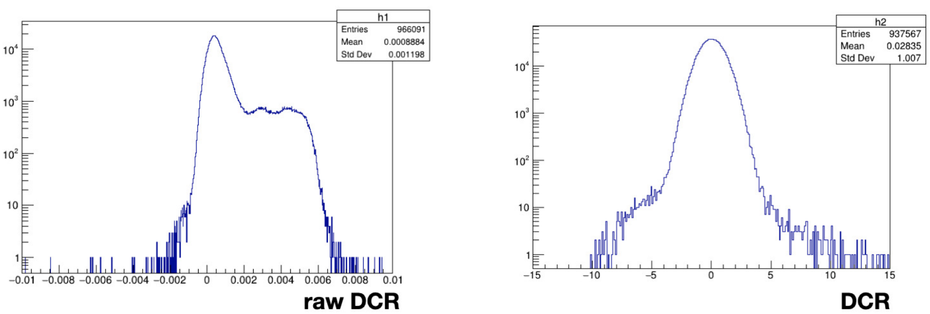

Figure 1.16-1. The aforementioned transformation from raw DCR to DCR can be seen in this plot. We notice a Gaussian shape in the middle of the distribution, with some tailing. The lower number of events on the right is due to applying a low-energy cut as well as a pulser and pile-up cut.

The DCR distribution is then well described by a dominantly Gaussian shape with a mean of 0 and a standard deviation of 1, although many detectors have some high-DCR tailing. To retain $\sim$ 99% of the bulk detector events, we can reject any events with a DCR value greater than 2.32, equivalent to a one-sided 99% cut for a Gaussian distribution. First tests in datasets DS6a and DS6b indicate that the new DCR parameter achieves the necessary efficiency; due to some high-DCR tailing the specific efficiency in these datasets are 98.42% and 98.46% (see Fig. 1.16-2), respectively. This departure from a 99% efficiency varies detector-by-detector and is the basis for the next step of the development of the DCR parameter.

The differences between the old and new DCR distributions are presented in Fig. 1.16-3. Note that, by construction, the new DCR parameter has a very similar mean and width across all detectors, so there is no need to 're-tune' the parameter such that the cut at DCR = 0 yields an acceptance of $\sim$99% for each separate calibration run. This is now handled automatically when calculating the electronics transfer-function deconvolution parameters, and when calculating the DCR parameters α, β, and γ. As such, we expect the time-stability of the DCR parameter to improve, reducing a source of systematic uncertainty.

Currently, the process described above has been done for datasets DS5c, DS6a, DS6b and DS6c, but will be completed for all Majorana Demonstrator data.

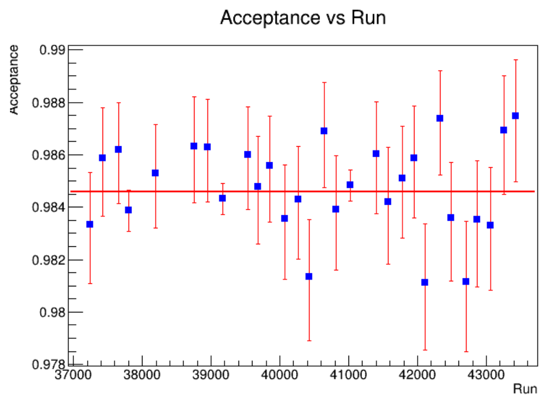

Figure 1.16-2. A look at the new DCR Stability in DS6b for all working detectors. Each point is the array-average acceptance for a weekly source calibration. The red line represents the exposure-weighted average acceptance for the cut. Uncertainties are computed using the Clopper-Pearson method. This plot indicates the time stability of the DCR acceptance in dataset DS6b.

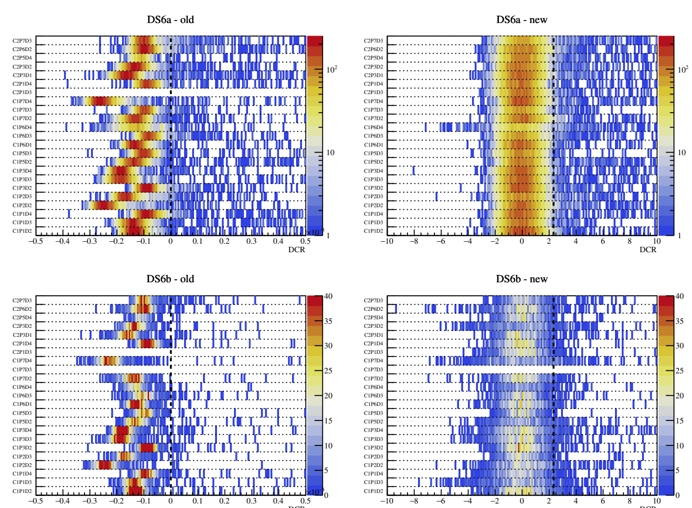

Figure 1.16-3. A first look at the new DCR parameter in datasets DS6a and DS6b, compared to the old DCR parameter.

DCR calculation version 2.1 is in development. This version will add a drift-time correction. Charge that is trapped during a regular bulk event gets released on the same timescale that DCR is being measured. Thus, we also recover delayed charge that is not associated with trapping near the passivated surface, where our alpha-contamination occurs, but rather, with trapping in the bulk. This type of trapped charge should be proportional to drift time, thus, we can estimate how much DCR we expect from this contribution. Alphas are usually events with a very short drift-time. If they only have a small amount of DCR, it might be smaller than a typical long-drift-time bulk event, but still high relative to a short-drift-time bulk event. We then look for alphas by looking at events for which DCR surpasses some corrected-DCR threshold. This effect is detector-dependent, but we foresee improvements in our ability to identify and reject alphas very close to the cut boundary.

1.17 Multi-site background rejection in the Majorana Demonstrator

M. Buuck*, J. A. Detwiler, M. Durand, I. Guinn†, A. Hostiuc, T. Mathew, W. Pettus, N. W. Ruof, M. Stortini‡, and C. Wiseman

The Majorana Demonstrator p-type point contact (PPC) detectors have multi-site rejection capability by performing pulse shape analysis on waveforms originating from the detectors. The long drift times, greater than 10us across the detector bulk, combined with the heavily localized weighting potential near the point contact, yield charge-collected waveforms with fast rising edges. Due to the waveforms' fast rise times, it is possible to distinguish waveforms with one localized event from waveforms with two or more localized events by relating the current amplitude of the waveforms to the energy deposited. A waveform originating from a multi-site event has a current amplitude that is degraded compared to a single-site event waveform's current amplitude with the same energy (Fig. 1.17-1). Since neutrinoless double-beta decay is inherently a single-site event, multi-site events can be rejected from the search.

Relating the amplitude (A) of the current pulse and the total energy (E) collected, defines the $AvsE$ pulse shape parameter for multi-site rejection.

$$AvsE = -\frac{A(E_{cal}/E_{unc}) - quad(E_{cal}, a, b, c) - exp(E_{cal}, d, \tau)}{\sigma(E_{cal}) \times s} \qquad (1)$$

Subtracted from the calibrated current amplitude is a quadratic function and an exponential function to correct for the amplitude's dependence on energy. $\sigma(E_{cal})$ is a scaling function that corrects for the width-energy dependence of $AvsE$ and s is a constant scaling factor that sets the multi-site cut at -1.

*Presently at SLAC National Accelerator Laboratory, Menlo Park, CA.
†Presently at University of North Carolina, Chapel Hill, NC.
‡Presently at Los Alamos National Laboratory, Los Alamos, NM.

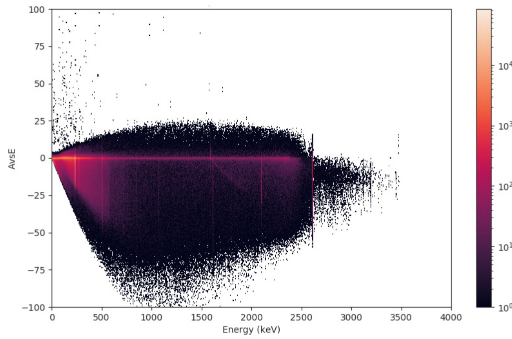

Figure 1.17-1. An AvsE spectrum for a series of long calibration runs in a ^{228}Th calibration study. A flat cut at AvsE=-1 represents a multi-site events cut, with 90% of events in the ^{208}Tl double escape peak still remaining after the cut.

The goal of the $AvsE$ parameter is to create a parameter with a flat cut that will exclude mostly multi-site events. This is done by flattening out the distribution of current amplitudes vs energy and setting the cut value where the acceptance rate at the ^{208}Tl double escape peak in a ^{228}Th calibration is 90%. A double escape peak in an energy spectrum is a population of mostly single-site events. Additional improvements, reflected in (1), have been recently added: an extra residual correction to more precisely flatten the current amplitude, and a width energy dependence correction to account for the changing width of $AvsE$ with energy. In the analysis of a ^{56}Co spectrum, it was shown that the width of the various double escape peaks is dependent on the energy, and now $AvsE$ is scaled to an empirical function that resembles the width dependence trend. The overall performance of the new $AvsE$ parameter shows a 90% acceptance for the double escape peak, 8% acceptance for the single escape peak, and 45% for the compton continuum (Fig. 1.17-2).

Figure 1.17-2. To measure the performance of the $AvsE$ parameter, the acceptance rate of three energy regions, double escape peak, single escape peak, and $0\nu\beta\beta$ compton continuum is measured for all long calibrations from the latest dataset.

1.18 Investigation of low-energy beta and gamma surface events on PPC germanium detectors

T. Burritt, J. A. Detwiler, B. Dodson, M. R. Durand, K. Hansen, T. Mathew, D. A. Petersen, W. Pettus, M. Stortini*, T. V. Wechel, D. I. Will, and C. Wiseman

Charge transport near the surfaces of HPGe detectors is difficult to characterize. Alpha and beta radiation incident on sensitive detectors surfaces result in key backgrounds for neutrinoless double-beta decay searches in Majorana and GERDA, despite showing characteristic features in their recorded waveforms that allowed for their efficient removal. The investigation of beta and gamma events at the passivated surface of the high-purity germanium (HPGe) detectors used in the Majorana Demonstrator and LEGEND is also of particular interest toward better understanding the characteristics of the detectors at the individual level, because both Majorana and LEGEND deploy many of these detectors simultaneously in an easily scalable modular approach. As high-energy betas and gammas will leave the surface region, we focus this study on the investigation of waveforms produced by low-energy betas and gammas. This also aids in our understanding of the low-energy region of the Majorana Demonstrator data. This effort is also complementary to other studies in the LEGEND experiment: the liquid argon (LAr) in which the detectors are submerged is subject to the beta decays of ^{39}Ar and ^{42}Ar, presenting a new source of surface background that must be taken into account.

In order to execute this investigation, we measure degradation in surface energy depositions using the MJ60 germanium test stand, and thereby infer the mechanisms of energy loss near the surfaces of the p-type point contact (PPC) detectors used in the Demonstrator. By recording events from the electron and gamma emissions of ^{83m}Kr, and analyzing the waveforms produced from these events, we can determine whether betas incident on the detector's passivated surface exhibit markedly different charge collection than gammas. As ^{83m}Kr decays via internal conversion, it falls through a pair of nuclear transitions with well-defined energies: first, a de-excitation of 32.15 keV, followed by a second de-excitation of 9.41 keV (with a total decay energy of 41.56 keV). These de-excitations usually proceed via the emission of monoenergetic conversion electrons with energies up to 32 keV, and sometimes with the emission of X-rays and gamma rays in the same energy range. Such low energy radiation only penetrates the first fraction of a millimeter of HPGe material, which, over most of the detector, is inactive due to the thick Li-diffused outer contact. Interactions that do result in HPGe events are predominantly near-passivated surface interactions with well-defined energies. If it is determined that these near-passivated-surface events are distinguishable from energy depositions in the bulk material, we can then produce a method to identify these events based upon a calculated parameter from the recorded waveforms. Measuring and modeling the distortion of the energy spectrum of the ^{83m}Kr

*Presently at Los Alamos National Laboratory, Los Alamos, NM.

events may also yield improved understanding of charge collection near the passivated surface. The results of this study will help inform future detector R&D efforts, and may also contribute to background rejection capabilities in Majorana and LEGEND.

The 62mm x 46mm MJ60 detector was originally a prototype for the high-purity germanium (HPGe) PPC detectors used in the Majorana Demonstrator. The detector is mounted in the central volume of a Majorana String Test Cryostat (STC) to which the ^{83m}Kr source is attached (Fig. 1.18-1). Our ^{83m}Kr source is produced as an ^{83}Rb solution adsorbed onto zeolite beads, which then decays to the metastable Kr state. Being a noble gas, the Kr can diffuse out of the material and into the rest of the system. The source we are using was produced identically to the Project 8 and ^{6}He-CRES ^{83m}Kr sources. The STC's liquid nitrogen dewar allows it to be operated at roughly 85 K, which allows the Kr to be cryopumped onto the surfaces of the detector, where it then decays. The cryostat is generally kept at a pressure of roughly 10^{-8} to 10^{-7} millibars using a vacuum turbopump, which is valved off when cryopumping the krypton, which accumulates in the cryostat.

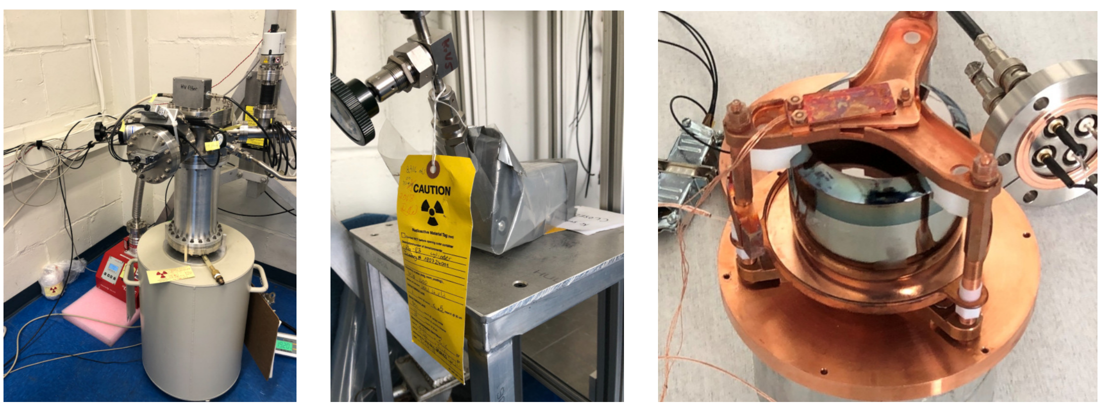

Figure 1.18-1. *Left*: The string test cryostat (STC), now in use as the MJ60 test stand. The hose extending past the right side of the image connects to our ^{83m}Kr source. *Center*: ^{83m}Kr source stabilized on the test stand. *Right*: The ORTEC PPC Prototype I (OPPI) detector in its mount, with the vacuum-side circuit visible.

Several upgrades were made to the cryostat apparatus to lower the operating temperature and decrease noise on the Ge waveform signals. The outer IR shield (the original STC shield) was removed, a bottom piece was added to the inner IR shield, and a handle was added to the cold plate. The detector was mounted to the bottom of the IR shield. Since the bottom is directly connected to the Cu cold finger and LN supply, the operating temperature of the detector decreased to 85 K from roughly 90 K prior to the upgrades. After changing the length of the junction gate field-effect transistor (JFET) source to ground cable, we were also able to install an adjustable capacitor with a lower capacitance than before (30 pF), which allowed for sharper waveforms and improved energy resolution.

In an effort to further improve the energy resolution, we also studied the effects of bias voltage. Campaign 2 was taken at a bias voltage of 1600 V, and Campaign 3 was taken at 1450 V, with lower leakage current and, thus, improved noise. A calibrated energy spectrum from data taken during this campaign is shown in Fig. 1.18-2, alongside an example background superpulse taken during Campaign 1. Additionally, we received a stronger Kr source, than the one originally used in campaign 1, from Project 8 (Sec. 1.8). In Campaign 3 we also increased the waveform length to 81.92 μs, allowing us to use a longer trapezoidal filter ramp and flat time, further improving the energy resolution.

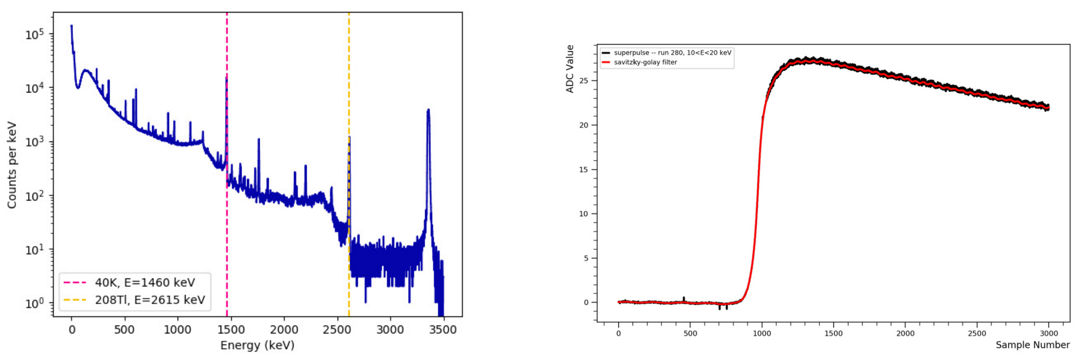

Figure 1.18-2. *Left*: Calibrated energy spectrum from Campaign 3, with the calibration peaks (^{40}K and ^{208}Tl) are marked. *Right*: An example background super pulse from the MJ60 detector.

In anticipation of future Kr data taking, the MJ60 detector is currently being replaced in the STC with the ORTEC PPC Prototype I (OPPI, one of two produced) germanium detector. With MJD/LEGEND collaborators at Los Alamos National Laboratory, in an effort to study the effects of the passivated surface on low-energy X-ray peaks, an X-ray fluorescence (XRF) source has been designed for use with a PPC detector. The fundamental design idea is to use a radioactive source in Tandem with foils to produce XRF in the range of roughly 8-70 keV, and to position these foils in a disk with holes with which the foils can be aligned. With another disk to hold the radioactive source, this allows the foil disk to be rotated such that the foil of interest can be aligned with the source. This is to be done in a manner that allows foils to be swapped without opening the cryostat (Fig. 1.18-3). The radiation of interest to stimulate emission of X-rays is bremsstrahlung: incident betas from the radioactive source create the bremsstrahlung, and the bremsstrahlung then ionizes the inner-shell electrons in the foil. During the design, attention was paid especially to energies in the Kα1 line, which has the highest rate of production. The foils to be used are included in Table 1.18-1, as well as the ideal thicknesses as determined by the simulations described below.

Prior to designing the XRF source, measurements to check the concept as well as the simulation framework were made using a Silicon Drift Detector that was sensitive to X-rays in the roughly 1-25keV region. For shielding purposes, the material closer to the source will be made of a lower-Z material (Polypropylene, PP) to shield from betas and limit bremsstrahlung, followed by a higher-Z material (tungsten, W) to block the bremsstrahlung.

Table 1.18-1. Foils to be used in the XRF source:

Foil material	Kα1 line (keV)	Thickness (μm)
Zn	8.639	80
Nb (formerly Zr)	16.615	100
Ag	22.163	80
Nd	37.361	160
Au	68.804	250

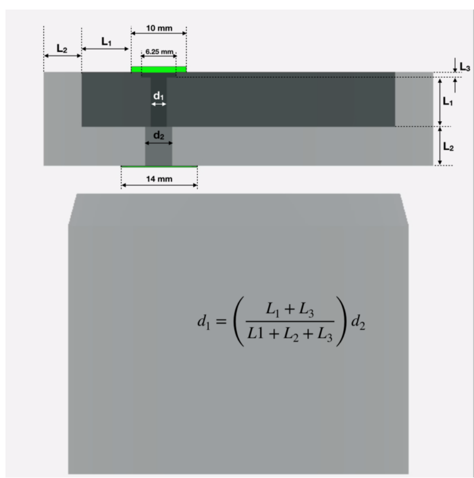

Figure 1.18-3. Sketch of the cross-section of the XRF source design. The upper geometry is the XRF source, and the lower geometry represents the HPGe PPC detector. The dark gray components are material with low Z, the light gray components are material with high Z, and the green disk at the top is the ^{99}Tc source.

In evaluating the ideal thicknesses for each foil and the optimal radioactive source and activity level, the simulation software `Geant4` was used. The simulations showed that the ideal source for this study would be ^{99}Tc, as it was shown to be low enough energy to work with the lowest Z foil, but high enough energy to still produce a sufficiently strong Kα1 peak in the highest Z foils. Together with preliminary measurements, it was determined that a low-energy beta source would be most favorable as opposed to a high-energy beta or alpha source. The design work for this study is nearly complete, and a prototype will soon be available for final refinements.

LEGEND

1.19 Status of the LEGEND neutrinoless double-beta decay experiment

T. Burritt, J. A. Detwiler, K. Hansen, A. Hostiuc, N. Lam, T. Mathew, G. Othman*, D. A. Peterson, W. Pettus, N. W. Ruof, M. Stortini†, T. D. Van Wechel, D. I. Will, and C. Wiseman

The LEGEND experiment is a program towards next-generation sensitivity to neutrinoless double-beta decay ($0\nu\beta\beta$) of ^{76}Ge. The collaboration is formed from the merger of the US Majorana (Sec. 1.14) and European GERDA collaborations, in addition to other interested parties. The phased program advances from the intermediate scale LEGEND-200 experiment to the future LEGEND-1000 experiment.

LEGEND-200 is now under construction at the Laboratori Nazionali del Gran Sasso (LNGS). It will be situated in the cryostat newly vacated by the former GERDA experiment (Fig. 1.19-1). The experiment combines the technological advances developed separately by Majorana and GERDA, as well as an increase in mass to 200 kg of germanium detectors. It will be the most sensitive experiment in the world, achieving an order-of-magnitude increase in half-life sensitivity over present experiments. Starting in January 2020, LEGEND has occupied the experimental site at LNGS for initial component and DAQ testing. Commissioning activities will intensify through late 2021 when the experiment will begin operation. The CENPA group plays a leading role in the development of the analysis framework (Sec. 1.23), which is actively tested on the data collected with our local test stands. Professor Detwiler is co-convener of the analysis working group and *ex officio* a key member on the steering committee. We are also pursuing R&D efforts to understand the surface response of the high purity germanium (HPGe) detectors, developing a local apparatus to thoroughly probe these properties (Sec. 1.20).

LEGEND-1000 is a leading candidate for a future US-led tonne-scale $0\nu\beta\beta$ experiment. It leverages the advances of the ^{76}Ge program, through LEGEND-200, to retire risks in demonstrating array scalability and achievement of background goals. It will yield an additional order-of-magnitude sensitivity to the $0\nu\beta\beta$ half-life, covering the neutrino mass parameter space allowed by the inverted hierarchy. The UW group is pursuing R&D aimed at improved LAr scintillation light collection (Sec. 1.21) and alternative HPGe detector front-end electronic readout (Sec. 1.22).

---

*University of North Carolina, Chapel Hill, NC.

†Presently at Los Alamos National Laboratory, Los Alamos, NM.

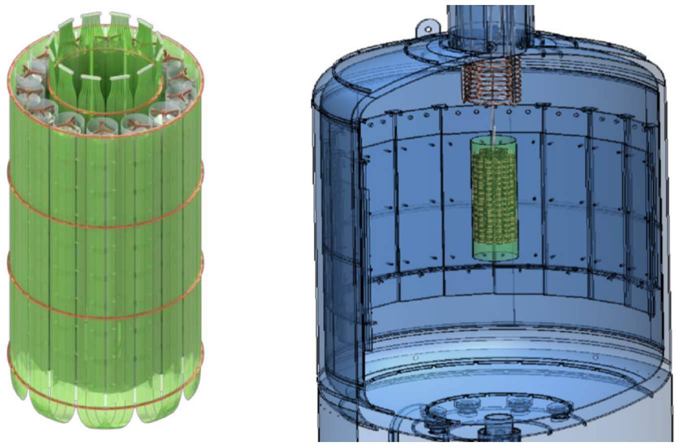

)

Figure 1.19-1. Schematic of the LEGEND-200 experiment. The HPGe detectors totalling $\sim$200 kg, enriched in the ^{76}Ge $0\nu\beta\beta$ isotope, are arranged in strings and surrounded by wavelength shifting fibers (left), then the array is immersed in a 64 m^3 liquid argon active veto (right).

1.20 Commissioning CAGE: An internal-source scanning cryostat for HPGe detectors

T. Burritt, J. A. Detwiler, T. Mathew, G. Othman[*], D. A. Peterson, W. Pettus, M. Stortini[†], T. D. Van Wechel, D. I. Will, and C. Wiseman

Majorana, GERDA, and LEGEND employ P-type point contact (PPC) high purity germanium (HPGe) detectors. In these detectors, highly pure bulk germanium is surrounded by a lithium diffused n$^+$ region, and a small p$^+$ point contact is made using boron implantation. The n+ region is kept at high voltage and electrically insulated from the p+ contact with a thin passivated layer created by sputtering amorphous germanium on the top of the detector. Radioactive signals near the surfaces of these detectors have degraded energies and have proven to be a source of unwanted backgrounds. In order to achieve LEGEND-200's background goal of 0.6 cts/(FWHM t yr), understanding and mitigating backgrounds from surface events is essential. In particular, both alpha particles from the ^{210}Pb decay chain and beta particles from the decay of ^{42}Ar can deposit energy near the surface, resulting in background in the $0\nu\beta\beta$ energy region of interest at 2039 keV. Improving detector designs and employing novel pulse shape discrimination techniques can assist in reaching the background goal.

While energy degraded events at or near the n$^+$ dead layer have been studied, the response of PPC detectors to events at the passivated surface are not as well understood. The internal-source scanning cryostat, CAGE (Collimated Alphas, Gammas, and Electrons), has been constructed at CENPA and is able to fulfill a vital role in studying detector response to these surface events. It can accomodate HPGe detectors

[*]Presently at University of North Carolina, Chapel Hill, NC.

[†]Presently at Los Alamos National Laboratory, Los Alamos, NM.

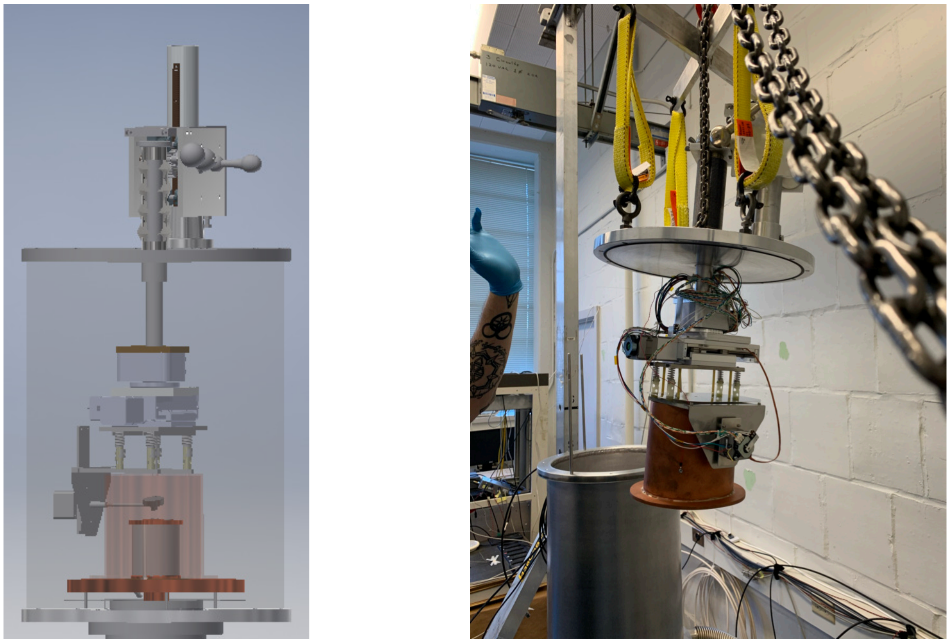

Figure 1.20-1. *Left*: Cross section of CAGE. *Right*: View of the motor assembly and IR shield.

of various sizes and use multiple collimated radiation sources to scan areas of interest on these detectors.

CAGE is a vacuum cryostat consisting of a large copper cold plate cooled by a liquid nitrogen dewar, on which the HPGe detector sits and is cooled to near-liquid-nitrogen temperatures. Its main feature is a movable copper infrared (IR) shield, which has a collimated radiation source attached to the interior. Three vacuum compatible motors are used to change the position and incidence angle of the collimated beam on the detector surface. The IR shield itself is mounted onto a linear stage that translates the shield (and consequently the source) horizontally across the detector surface. The linear stage, in turn, is mounted on a rotary stage, which changes the azimuthal position of the source beam. Additionally, the collimator holding the source is mounted within the IR shield on a third rotary motor, which allows the angle of incidence of the source beam with respect to the detector surface to be changed, as shown in Fig. 1.20-1. It is important to keep the motors above their minimum operating temperature of 0C, while allowing the IR shield and detector to remain near liquid nitrogen temperature. To accomplish this, the IR shield and collimator are insulated from their motors with spacers and a shaft fabricated from G-10—a well-known thermally insulating material. Multiple stainless steel heat shields aid in keeping the motors within operating temperatures. To move the source beam to the desired position, the IR shield is first lifted off the cold plate with a hand-cranked rack and pinion, then rotated and translated. Finally, the collimator shaft is rotated to the desired incidence angle using the second rotary motor, and the IR shield is lowered back onto the cold plate.

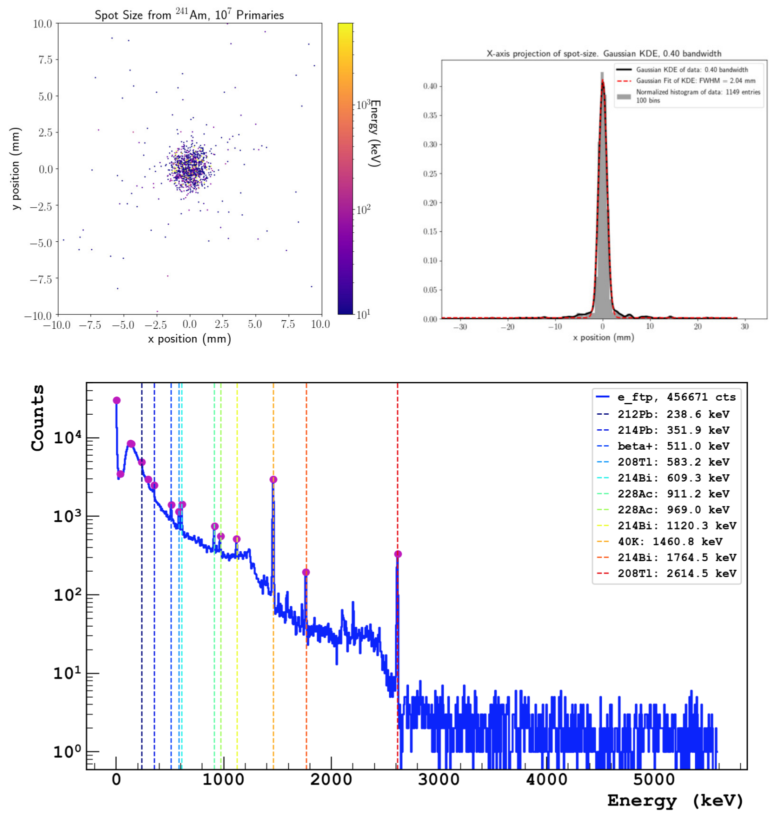

Figure 1.20-2. *Top*: Collimated beam size simulation data. *Bottom*: Initial background spectrum taken with OPPI1.

The first iteration of the CAGE cryostat was finalized and built over the summer of 2019. Multiple vacuum and cryogenic temperature tests have been conducted with operating pressures below $< 10^{-7}$ mbar and temperatures at the cold plate stabilizing at 86 K. This matches the operating temperature of the detectors operating in liquid argon in the LEGEND experiment. A new low-profile detector holder was designed and fabricated at CENPA, allowing access to most of the passivated surface of an HPGe detector. The stepper motors have been equipped with rotary encoders and limit switches to allow for absolute in situ position calibration and alignment, having passed repeatability and accuracy tests. A custom "slow controls" electronics box has been built to allow for extended data taking runs and safety interlocks. In conjunction with the slow controls box, a database and interactive PyQT5 GUI allows users to build live plots of the various sensors, and remotely bias the detector. Initial background data was taken in early December 2019 with a MAJORANA-style PPC ("OPPI1"), on loan from Los Alamos National Laboratory, and is shown in Fig. 1.20-2.

Currently, CAGE is undergoing hardware upgrades to accomodate and scan an Inverted Coaxial Point Contact (ICPC) detector. This new detector geometry will

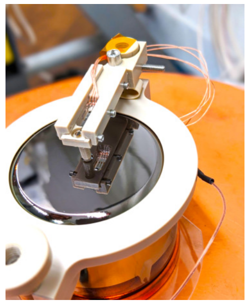

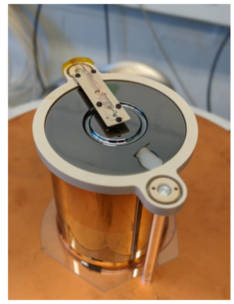

Figure 1.20-3. *Left*: OPPI1 installed on CAGE cold plate. *Right*: ICPC detector with new, lower profile detector holder.

make up the majority of detectors in LEGEND-200. A new detector mount has been made (Fig. 1.20-3), allowing the collimated beam to be placed closer to the detector for further reduction in the spot size of an ^{241}Am alpha source. Ongoing `Geant4 g4simple` simulations predict an alpha spot size of less than 3 mm for the upgraded configuration. When the CAGE upgrades are complete, we plan to take extensive scans of the passivated ditch separating the n+ and p+ contacts in the ICPC detector. These data will be analyzed to evaluate the properties of the pulse shapes and develop rejection techniques that can be applied in the LEGEND-200 experiment.

1.21 Characterization of silicon photomultipliers for LEGEND-1000

T. Burritt J. A. Detwiler, A. Hostiuc, D. A. Peterson, W. Pettus, N. W. Ruof, T. D. Van Wechel, and C. Wiseman

In LEGEND, strings of germanium detectors will be submerged in liquid argon, which acts as a cryogen for the detectors and an active-veto for the rejection of background radiation. Energy depositions in the liquid argon produce predominant photons in the vaccum ultraviolet spectrum with peak wavelength of 128 nm. The scintillation is measured by shifting the wavelengths to 400-500 nm, a region where photodetectors are sensitive, and by guiding the photons to a readout composed of silicon photomultipliers (SiPM).

In order to reach a background goal of 0.03 cts / (FWHM x t x y) or 90 times lower background than the current lowest background, LEGEND-1000 must have a higher light collection efficiency from the active-veto system. Components that contribute to the light collection efficiency are the liquid argon purity, the efficiency of the wavelength shifting fibers, and the photon detection efficiency of the SiPMs. The photon detection efficiency for SiPMs is well known at room temperature, but not well known at 87K, the temperature of liquid argon. Knowing the precise photon detection efficiency at liquid argon temperature would be crucial in the process of making an improved design for a more efficient liquid argon scintillation readout.

To determine the photon detection efficiency close to liquid argon temperature,

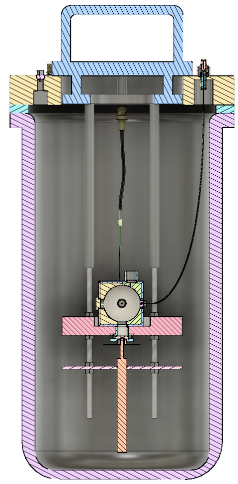

Figure 1.21-1. A cross-section view of the SiPM characterization test stand. The integrating sphere in the center of the vessel is suspended over a liquid nitrogen bath, with a SiPM mounted over the bottom port cooled by a copper cold finger. The other devices attached to the integrating sphere are a LED light source and a reference photodiode. The reference photodiode is placed on the lid of the entire test stand where the temperature is close to room temperature since that is where the responsivity is known.

a test stand is being built to characterize silicon photomultipliers at liquid nitrogen temperature (77 K). Measuring the photon detection efficiency at room temperature has been demonstrated in Figure Fig. 1.21-2. The principal set up is an integrating sphere that directs an equal amount of light to a SiPM and a calibrated reference photodiode. The light source is a green LED that continuously illuminates the integrating sphere and the photon detection efficiency (PDE) is calculated by comparing the SiPM photocurrent to the photocurrent of a reference photodiode.

$$\mathrm{PDE} = \frac{I_{SiPM-L} - I_{SiPM-D}}{G \times q_e \times \mathrm{ECF} \times R_\gamma} \tag{1}$$

I_{SiPM-L} and I_{SiPM-D} are the light and dark current of the SiPM. G is the gain, q_e is the charge of the electron, ECF is the excess charge factor which is the ratio of charge from primary dark counts to that of correlated dark counts, and R_γ is the incident photon rate on the SiPM from the LED light source.

An additional method, a photon counting method, was used by counting the number of triggered pulses in the SiPM.

$$\mathrm{PDE} = \frac{N_L - N_D}{R_\gamma} \tag{2}$$

N_L is the triggering rate under continuous exposure to the LED, N_D is the triggering rate under dark conditions, and R_γ is the total incident photon rate measured by the reference photodiode. Other calculation methods were used and will be tested when the test stand is ready for characterization at liquid nitrogen temperature, however for the room temperature demonstration the photocurrent measurement came out as the more accurate.

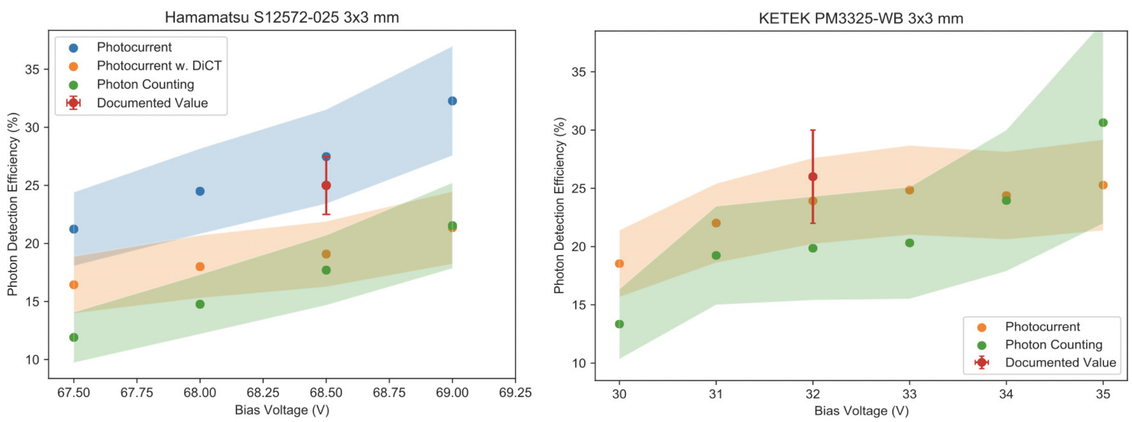

Figure 1.21-2. Photon Detection Efficiency measured for a Hamamatsu 3×3 mm SiPM (*left*) and that for a 3×3 mm KETEK SiPM (*right*). The manufactured value of the photon detection efficiency for the Hamamatsu model does not include correcting for direct cross-talk (DiCT) between neighboring pixels so blue region indicates a photocurrent method calculation without correcting for cross-talk.

1.22 Forward-biased JFET-based Option for R&D: new preamplifiers for LEGEND

T. Burritt, J. A. Detwiler, A. Hostiuc, D. A. Peterson, N. W. Ruof, T. D. Van Wechel, and C. Wiseman

The high-purity germanium (HPGe) detectors used by the LEGEND experiment are reverse-biased diodes, with small amounts of charge deposited on their p+ contact when an ionization event occurs. This charge is typically converted into an output signal by a "front-end" circuit board placed very close to the detector. In typical designs, the signal is amplified by a reverse-biased JFET. However, this configuration requires the use of either a feedback resistor or additional circuits (e.g., an optoelectronics board), to discharge the feedback capacitor. At low temperatures, the required resistance is usually on the order of GΩ, meaning the resistor generates significant electronic noise. To avoid this, and for simplicity, one can design a circuit using a forward-biased JFET. This allows the detector's and JFET's leakage current to flow through the gate-source junction. This also provides a path for continuous discharge of the feedback capacitor.

A charge sensitive preamplifier with forward biased reset is currently under testing for the LEGEND project. This will be referred to as the Forward-biased JFET-based Option for Research and Development (FJORD). The classic charge-sensitive preamplifier circuit uses a feedback resistor for stabilizing the operating point and providing a path for the detector leakage current. The forward biased reset preamplifier eliminates the feedback resistor, which is a major source of noise especially when using a detector that features low leakage current. In LEGEND, this also eliminates the need to find a low-background resistor that can survive repeated Liquid Argon (LAr) immersion, and thus represents an attractive alternative to the baseline technology[1]. This R&D project is useful for LEGEND-1000, the next generation detector.

CENPA Engineers have made changes to the test stand and the previous version of the FJORD device, to minimize the effects of external sources of noise, such as microphonics. This allows us to optimize the output (i.e. minimizing the threshold and using the optimal energy estimator) from the CAEN CoMPASS software when using a radiation source, and to characterize the performance of both low-gain and high-gain output from the CENPA built post-amp box.

Currently, a Hamamatsu S4204 dual-element Si PIN photodiode is attached to FJORD. ^{241}Am and ^{133}Ba sources are being used to test the performance of the pre-amp. Gammas from the sources are detected using the Si detector and their signals amplified by FJORD. The output signal can then be analyzed and thoroughly tested. This will allow us to evaluate the performance of the device before trying it on a Ge detector.

Furthermore, in order to test the device at Liquid Nitrogen (LN) temperature, one wants to have the pre-amp itself immersed, while the Si photo-diode detector and the radioactive sources remain outside the LN. As such, a mount for the source has been added, which enables low-temperature testing. The changes take into account that the ^{241}Am source used is very weak and necessitates being very close to the photodiode during testing. The device was subsequently re-tested in liquid nitrogen. FJORD continues to work at Liquid Nitrogen (LN) temperature.

FJORD data has been taken using a ^{133}Ba source using the DT5725 digitizer from CAEN. Good discrimination between physics and noise events has been observed. The rise-time for physics pulses is on the order of 100 ns, similar to a germanium detector, hence the silicon detector can be used as a proxy for germanium.

FJORD work continues, as we are looking at spectra and determining features, in order to understand the energy calibration needed. New tests using an ^{241}Am source (particularly, the 59.5 keV line) have been completed. These results, once understood, will be used to calibrate the CAEN CoMPASS energy output. We are currently implementing `Geant4` simulations of the apparatus, in order to validate the spectra seen during data-taking.

We anticipate testing FJORD on one of the HPGe test stands available at CENPA by the end of 2020.

[1] CENPA Annual Report, University of Washington (2018) p. 27.

1.23 Data processing for LEGEND-200

J. A. Detwiler, I. Guinn*, T. Mathew, and C. Wiseman

The LEGEND Collaboration is preparing to take its first data with LEGEND-200, a 200 kg array of HPGe detectors submerged in scintillating liquid argon (LAr), at the Gran Sasso laboratory in Italy. Wavelength-shifting fibers are coupled to silicon photomultipliers (SiPMs) in the inner volume, and the outer water tank is instrumented with PMTs to detect Cerenkov light from cosmic rays. Data from these multiple input streams will be digitized by the on-site data acquisition (DAQ) system and sent offsite to the NERSC supercomputing facility for further processing and analysis.

The collaboration is developing a set of modern software tools for the primary analysis, written primarily in Python. The primary tasks of the `pygama` software suite are to convert data from the DAQ system into a long-term storage format, run digital signal processing (DSP) algorithms, group coincident events between subsystems into events, and apply the results of energy (and other) calibrations to the physics-mode dataset. This year, we have made significant progress on developing the long-term storage format for the data, and implementing the digital signal processing framework. We have used existing small-scale HPGe test stands such as CAGE (Sec. 1.20) and characterization data for LEGEND detectors to prototype these data processing routines. Fig. 1.23-1 illustrates the suite of routines to be implemented for the processing of LEGEND data.

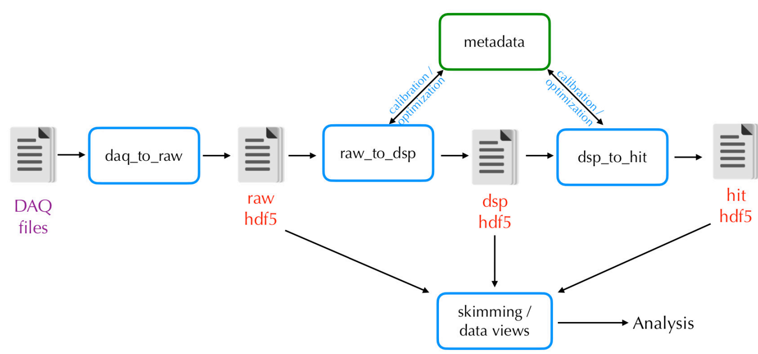

Figure 1.23-1. Routines used by `pygama` for the processing of LEGEND-200 (and related) data. Data from the DAQ is converted to a long-term "raw" storage format. Digital signal processing is run on a per-waveform basis, and necessary metadata (analysis parameters such as energy calibration constants) are saved and applied to create "hit" files. These files are then used to group data into events for the final analysis.

Most recently, `pygama` has been used to process data from the "Post-GERDA Test" (PGT), a set of data from LNGS with upgraded electronics, new detectors, and a new DAQ system, "FlashCam." Early results are shown in Fig. 1.23-2.

The long-term storage format for LEGEND-200 data is based on the HDF5 file format, a fast, extensible, and well-known specification in widespread use outside physics.

*University of North Carolina, Chapel Hill, NC.

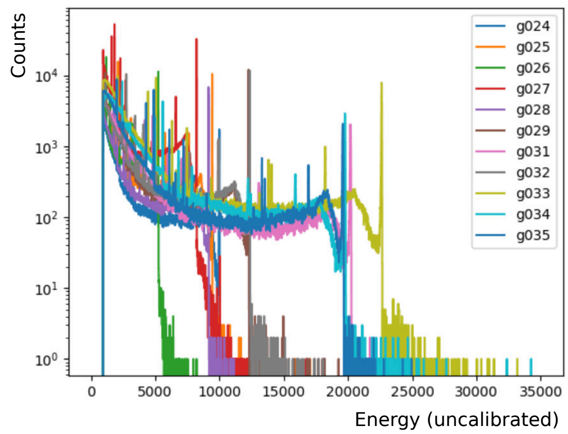

Figure 1.23-2. Energy spectra (uncalibrated) for active detectors in the post-GERDA test dataset.

The implementation uses only basic features of the HDF5 file format, to allow easy access to LEGEND files from multiple programming languages (C++, Python, Julia), and long-term preservation. The "LH5" (LEGEND-HDF5) I/O module developed for `pygama` defines structures for single-valued data (such as timestamps) and array-valued data (such as waveforms). These data are grouped by the LH5 `Table` object, analogous to a DataFrame in the `pandas` package, with columns for each single-valued datatype, and rules for association to array-valued datatypes and waveform compression.

Our tools must be able to process the full (final) LEGEND-200 dataset in a reasonable time at NERSC. Significant updates have been made to improve the speed of the data processing. The primary bottlenecks are the initial scan over binary data packets in a DAQ file (which is difficult to parallelize), and the efficient implementation of chains of DSP transforms on each waveform. We have carefully optimized the memory management of the processing codes, resulting in a `daq_to_raw` conversion speed of >100 MB/s, and a similar speed for the DSP algorithm. Using these benchmarks, we estimate that we will be able to process the full LEGEND-200 dataset using 100 cores in <2 weeks of processing time.

The development of the `pygama` software has several important near-term goals. A metadata scheme for analysis parameters will use JSON files for data subsets, with revision tracking via GitHub. The DSP algorithms will be parallelized using the `mpi4py` package to use the full processing power of the computing nodes at NERSC. Routines for energy calibration and pulse shape parameter optimizaion will be developed to handle the 150+ HPGe detectors and multiple SiPM channels. The code is on track to be ready in time for commissioning of the full LEGEND-200 array in 2021.

Selena

1.24 Measurement of the charge generation and transport properties of amorphous selenium

A. E. Chavarria, X. Li*, and A. Piers

We conducted the most precise measurement of the charge generation and transport properties of amorphous selenium (a-Se) under radiation. This study is motivated by the concept of building high spatial and energy resolution imaging detectors with a-Se for the search of neutrinoless double beta decay ($0\nu\beta\beta$) in ^{82}Se [1]. The measurement revealed excessive fluctuation in ionization charge generation above Poisson fluctuation. We concluded that this excess is due to the high electron-hole recombination probability in a-Se and the stochastic nature of energy loss process of the primary β. Impact of this result on the proposed $0\nu\beta\beta$ detector is under investigation.

As shown in Fig. 1.24-1, the detector is a single pixel consisting of a 200 μm a-Se and a 2 mm diameter cathode with a guarding ring. Holes are collected and read out from the cathode with a CMOS charge amplifier with 50 fF feedback capacitor, then further amplified for digitization. The sample and the amplifiers are hosted in a vacuum chamber which stands high voltage up to 10 kV and isolates acoustic and electromagnetic noises. Ionization signals are generated from a collimated ^{57}Co source. This setup allows us to correct for interaction depth dependence based on the signal pulse shape and the electronic noise is estimated to be $100e^-$ in RMS.

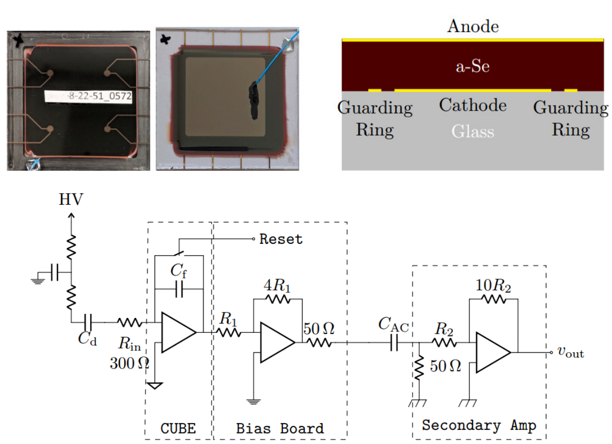

Figure 1.24-1. *Top left:* Back and top side of the a-Se sample. *Top right:* The cross section of the detectors which are the gold dots in the image shown to left. *Bottom:* The charge-readout electronics schematic.

*Department of Physics, Princeton University, Princeton, NJ.

[1] A. E. Chavarria, C. Galbiati, X. Li and J. A. Rowlands, Journal of Instrumentation, **12**(03), P03022 (2017).

A model was built to describe the average electron hole generation energy (W_{ehp}) and energy resolution behavior with drift field. We developed a `Geant4`-based simulation which suggests that this model is in compliance with data, as shown in Fig. 1.24-2. The discrepancy between this work and the result from Blevis *et al*[1] is expected because the a-Se samples contain a different dopant.

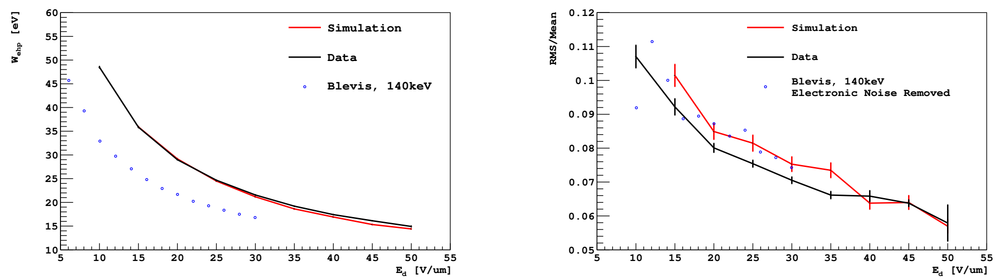

Figure 1.24-2. Comparison between data, simulation and literature[1]. *Left*: Average creation energy of an electron hole pair as a function of drift field. *Right*: Relative RMS resolution as a function of drift field. The γ energy is 122 keV.

The reason for the excessive fluctuation of collected charge resides in the fact that the energy lost by primary β through ionization is a stochastic process with discrete collisions between random free paths. The excessive fluctuations in the collected charge is caused by the strong dependence of recombination probability on the charge density along the track. Fig. 1.24-3 shows the contribution to the resolution from all the components. Note that this charge density fluctuation is related to the Landau distribution of energy lost of charged particles per unit length, thus the resolution does not scale as the square root of energy. In conventional radiation detectors like silicon detectors, this effect is not evident due to the low recombination probability.

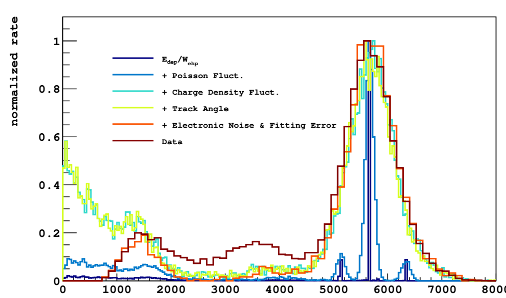

Figure 1.24-3. Example of the charge number spectrum of data taken with 30 V/μm drift field, in comparison with the decomposition of fluctuation sources from simulation.

We are currently designing the first imaging detector prototype with the CMOS chip TOPMETAL-II[2]. It is essential for the measurement of energy resolution of MeV

[1] I. M. Blevis, D. C. Hunt and J. A. Rowlands, Journal of applied physics, **85**(11), 7958-7963 (1999).

[2] M. An, C. Chen, C. Gao, M. Han, R. Ji, X. Li, ... & L. Xiao, Nuclear Instruments and Methods in Physics

β. We established the collaboration with Dr. Yuan Mei from Berkeley Laboratory, who is going to provide us with the chip. Selenium deposition will be done by the Hologic, Inc. whom we had great experiences with during previous collaborations. The TOPMETAL-II has a 72 by 72 array of 83 µm- size square pixels. Each pixel has an exposed electrode to collect charge from a-Se with extremely low noise (13.9 e^- equivalent noise charge). With a 500 µm- thick layer of a-Se, the prototype will be able to fully capture and image $\sim 1 - MeV\beta$, thus to directly demonstrate the capability of a-Se imaging detector and to further validate our model of the energy resolution.

COHERENT

1.25 Characterization of NaI(Tl) crystal scintillators for the NaI(Tl) detector subsystem for COHERENT

T. Burritt, N. Chen, J. A. Detwiler, M. R. Durand, K. Hansen, J. Librande, O. McGoldrick, D. A. Petersen, M. Stortini*, T. V. Wechel, D. I. Will, C. Wiseman

The COHERENT project is a collaborative effort to measure coherent elastic neutrino-nucleus scattering (CEνNS), a process whose precision measurement will allow searches for non-standard interactions of neutrinos with matter and a deeper study of nuclear structure. CEνNS is also clearly predicted by the Standard Model, and therefore the Standard Model may be tested via measurement of this process. CEνNS is also involved in core-collapse supernova events (Type II SNe) and therefore its study will also aid in the detection of neutrinos produced in the core collapse. Additionally, the CEνNS process provides a baseline for the background in the direct detection of dark matter. The main COHERENT experiment is based at the Spallation Neutron Source (SNS) at Oak Ridge National Laboratory in Tennessee. The sodium iodide (NaI[Tl]) group at the University of Washington is working with collaborators at Duke University to characterize roughly two tons of thallium-doped sodium iodide (NaI[Tl]) crystal scintillators, including ~120 crystals at UW, to deploy in one of the next detector phases of the multi-phase approach of the COHERENT collaboration.

The characterization effort aims to assess the performance of each crystal by identifying the ideal voltage at which each crystal's PMT base should biased such that the gain across all crystals is consistent, as well as identifying and rejecting defective crystals with some sort of damage or impurity. To characterize each NaI[Tl] crystal, we run two sets of five 10-minute trials exposing the crystal to both a Cs-137 source directly below the crystal and a Ba-133 source ~73 cm off perpendicular to the detector's side. The first set of measurements determines the voltage gain through varying the supply

*Presently at Los Alamos National Laboratory, Los Alamos, NM.

Research Section A: Accelerators, Spectrometers, Detectors and Associated Equipment, **810**, 144-150 (2016).

voltage to the PMT in 100V intervals between 600V and 1000V. The second set looks for differences in the measured energy of the Cs-137 peak by placing the Cs-137 source at five equidistant positions below the crystal. We have completed characterization of most of the crystals. Summary plots of the detector gains, Cs-137 peak widths, and Cs-137 peak energy sensitivity to source position are shown in Fig. 1.25-1. Once we complete the characterization effort, we plan to ship the crystal that pass a basic set of selection criteria to the SNS for incorporation into COHERENT.

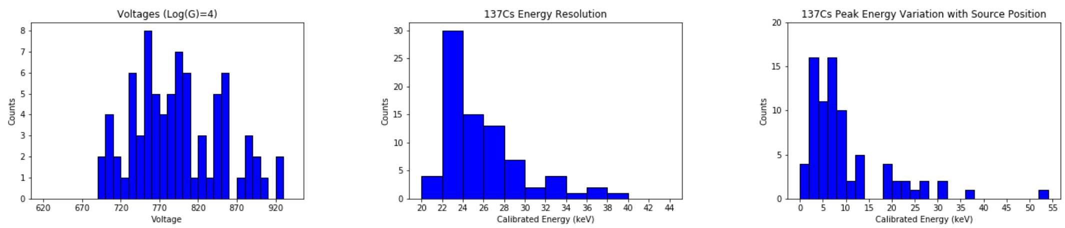

Figure 1.25-1. These plots show the gain of each of our crystals, the Cs-137 peak resolution, and the energy variation of the Cs-137 peak with source position.

The light yield of NaI scintillating crystals is sensitive to temperature. Thus temperature data are recorded and will be taken into account in the analysis. Typically there's a linear relationship between the gain and temperature, as shown for example in Fig. 1.25-2. However, many factors can cause uncertainty, including intrinsic gain differences between the bases, discrepancies in collected temperature data measured by different devices, and gain variation with respect to time. The goal of the temperature study is to analyze the uncertainty and solve any discrepancies in the collected data.

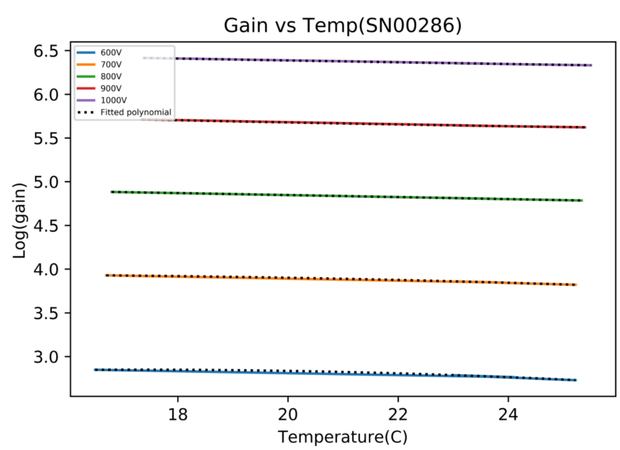

Figure 1.25-2. Linear dependence of gain on temperature in a crystal.

Another study currently being conducted in the interest of crystal characterization is measuring the absolute detection efficiency of our NaI[Tl] crystal scintillators and test our Monte Carlo models of the light collection. To measure this experimentally, a data run of standard length (10 minutes) at a bias voltage of 800 V was taken during which time the detector was only exposed to our ^{137}Cs source. A background run was then taken to be subtracted from the source run, after the detectors had had their energy scales calibrated and number of pulses scaled with respect to their relative livetimes. The final spectra for data taken when the Cs source was a standard distance from the crystal (roughly 51.50 mm) are shown in Fig. 1.25-3. Using an estimated source activity of (13109 ± 131) Bq, the absolute efficiency of our detector was calculated to be $(10.115 \pm 0.126)\%$. We are currently refining `Geant4-g4simple` simulations in order to determine our expected count efficiency to compare with that which was measured. These simulations help illuminate possible problems in the detection efficiency and allow us to calculate the efficiency degradation. At the time of writing, the final iterations of these simulations are imminent, and will likely be one of the final steps in conducting the absolute efficiency study.

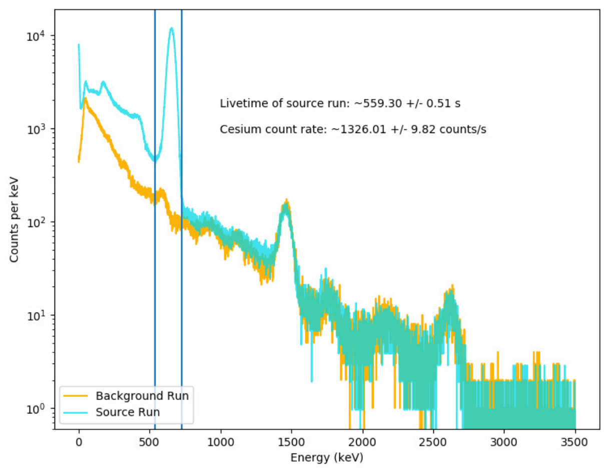

Figure 1.25-3. The energy-calibrated and deadtime-corrected detection spectra of one of our NaI[Tl] crystal scintillators with (aqua) and without (orange) our ^{137}Cs source present.

2 Fundamental symmetries and non-accelerator-based weak interactions

Torsion-balance experiments

2.1 Limits on equivalence-principle violating ultralight dark matter

E. G. Adelberger, J. H. Gundlach, C. A. Hagedorn, J. G. Lee, E. A. Shaw, and K. Venkateswara*

Searches for dark matter have been unsuccessful thus far. Popular candidates like weakly-interacting massive particles (WIMPs) and low-mass bosons called axions have yet to be found. WIMPs, in particular, have been all but excluded as a candidate by precision experiments. Focus is shifting to axions, where sensitive experiments like ADMX are searching for the Peccei-Quinn axion[1]. It also is important to look at other avenues of research. Some work has tried to infer the nature of dark matter through astrophysical evidence and some of the observations hint at the possibility of ultra-light dark matter (ULDM) with masses $m_{DM} \approx 10^{-21}$ eV/c^2. In this regime you expect to see signatures in the rotation curves of galaxies, sizes of dark matter halos, and prevalence and lifespan of globular clusters[2]. A recent paper[3] motivates torsion-balance experiments for setting limits on the mass and coupling constants of vector ULDM. One example is vector dark matter coupled to Baryon minus Lepton number (B-L). B-L is a conserved quantity in all known interactions and remains so in grand-unified and supersymmetric theories beyond the Standard Model. This makes it a well-motivated conserved charge that may have a corresponding massive gauge boson coupled to it.

We can search for a torque signal from this dark matter candidate using the composition dipole pendulum of our 8-test-body pendulum[4]. The torque on the composition dipole from this field-like dark matter would be equivalent to the torque induced by an oscillating electric field on an electric dipole. This dark matter field would oscillate at the Compton frequency of the particles, $f_{\mathrm{DM}} = m_{\mathrm{DM}}c^2/h$, with a coherent amplitude in an unknown direction in the frame of our solar system. As the Earth turns in this field the signal is modulated at the sidereal day. A previous experiment[5] searched for such a signal in a stationary apparatus. Due to the $1/f$ nature of the thermal noise from the fiber, a stationary experiment is inadequate to search for candidates of masses all the way down to the 10^{-21} eV/c^2 mass limit. To probe this limit the signal must be

*Presently at Paroscientific Inc., Redmond, WA.

[1] N. Du *et al.* (ADMX collaboration), Phys. Rev. Lett. **120**, 151301 (2018).
[2] L. Hui, J.P. Ostriker, S. Tremaine and E. Witten, Phys. Rev. D **95**, 043541 (2017)
[3] P. W. Graham, D. E. Kaplan, J. Mardon, S. Rajendran, and W. A. Terrano, Phys. Rev. D **93**, 075029
[4] CENPA Annual Report, University of Washington (2018) p. 50.
[5] CENPA Annual Report, University of Washington (2019) p. 61-62.

modulated by rotating the dipole on a turntable at a frequency that we are sensitive to over long periods of time.

Here we have analyzed a dataset that spans 40 days to demonstrate the sensitivity of our apparatus, see Fig. 2.1-1. An identical analysis of a rotating experiment was done recently with our spin pendulum[1]. We do linear fits at the turntable frequency and fit for modulations in these fit amplitudes. This type of search complements equivalence principle tests like ours[2] and the MICROSCOPE mission[3]. It would be able to determine the mass of these particles and whether they are the dark matter or a sub-component of the dark matter.

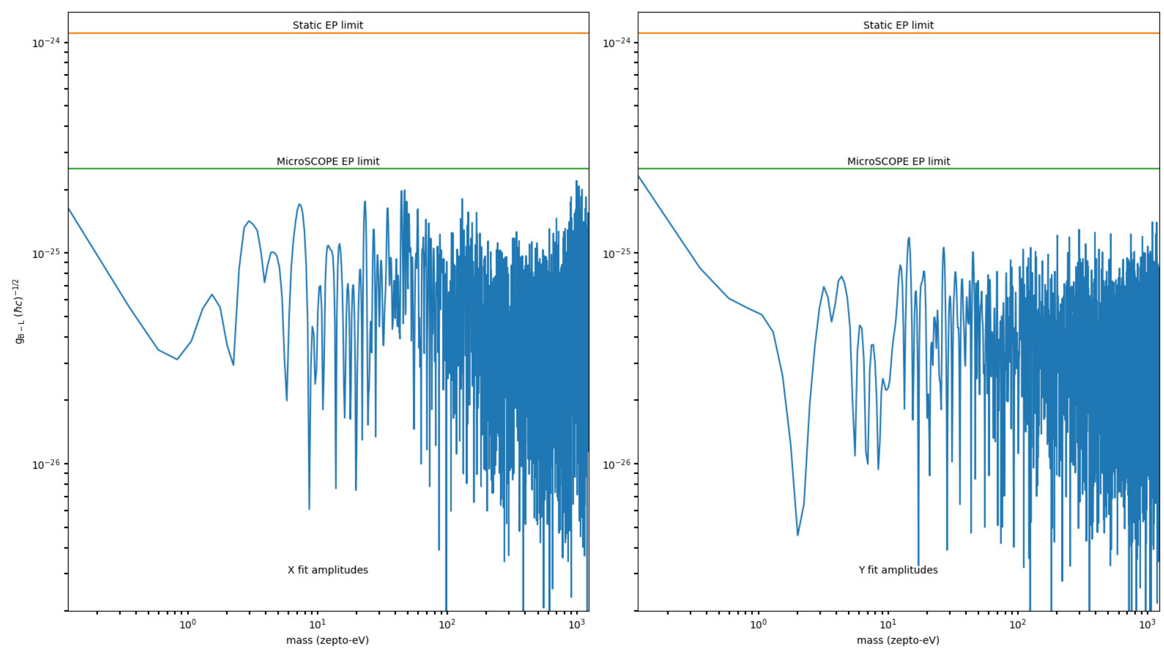

Figure 2.1-1. The X and Y fit amplitudes are fits for a dark matter signal in geocentric equatorial coordinates with charge dipole orientation blinded. This analysis is from 40 days of data at 47% duty cycle. Setting limits with this data should be able to exclude any (B-L)-coupled dark matter candidate down to the lower mass limit of 10^{-21} eV/c^2 that is of particular interest because of astrophysical observations.

[1] W. A. Terrano, E. G. Adelberger, C. A. Hagedorn, and B. R. Heckel, arXiv:1902.04246v1 [astro-ph.CO] 12 Feb 2019.
[2] T. A. Wagner, S. Schlamminger, J. H. Gundlach, and E. G. Adelberger, Class. Quantum Grav. **29**, 184002 (2012).
[3] P. Touboul *et al*, Phys. Rev. Letters **119**, 231101 (2017).

2.2 Instrumentation for the LIGO gravitational wave observatories

A. L. Lockwood, C. M. Weller, C. A. Hagedorn, M. P. Ross, and J. H. Gundlach

We developed a compact inertial rotation sensor for use on the LIGO seismic isolation platforms. The residual motion of the seismic isolation platform is predicted to decrease by a factor of ~ 20 at 0.1 Hz with the deployment of this sensor. It is expected that this increased isolation will provide a variety of benefits to the interferometer from decreased scattered light coupling to decreased noise in the gravitational wave band. The prototype is now capable of being operated remotely and will be installed on a test isolation platform in the coming months.

Additionally, we investigated the excess low-frequency noise in the LIGO optical levers. These systems are used to measure the angular motion of the LIGO optics at a broad range of frequencies. We've found that a system consisting of only an optical fiber pointed at a split photodiode exhibits similar noise as the LIGO systems. This suggests that the optical fiber is the source of the noise. We tested various unsuccessful noise-mitigation schemes: mandrel wrapping to decrease cladding modes in the fiber, using an aperture to decrease higher-order spatial modes, and mechanically securing the fiber tip.

Lastly, we continued testing a gravitational calibrator for LIGO. The calibrator consists of an aluminum rotor with six tungsten cylinders in a quadrupole and hexapole arrangement. These apply a pair of sinusoidal forces on the test mass when the rotor is spun. We predict these forces using a custom finite element calculation which can predict the force amplitudes to within 0.5%. We are assessing the capability of a series of gravitational calibration injections during LIGO's third observing run and hope to provide a secondary absolute calibration for future observing runs.

2.3 Results from the Fourier-Bessel pendulum test of the gravitational inverse-square law

E. G. Adelberger, B. R. Heckel, B. M. Iritani, J. R. Johnson, J. G. Lee, C. E. Matt, and H. E. Swanson

We completed another measurement of the gravitational inverse-square law (ISL) with the Fourier-Bessel pendulum experiment, which measures torques on a stationary torsion pendulum suspended above a rotating attractor[1]. The test-masses consisted of thin platinum foils with 18- and 120-fold azimuthal symmetries. We tested the ISL at face-to-face separations of the test-masses between 52μm and 3mm, the closest measurement to date.

We also measured an unexpected systematic effect due to the magnetic susceptibility of the test-mass materials and the residual vertical magnetic field from the earth in

[1] CENPA Annual Report, University of Washington (2019) p. 59.

the apparatus. We were able to quantify this effect through measurements taken with an exaggerated applied magnetic field. We were also excited to find that our Fourier-Bessel analysis could be applied to the magnetostatic case allowing us to predict the separation dependence of the observed effect. This additive systematic torque was nearly equivalent to a $(1.1 \pm .4)\%$ scaling of the 120ω torques.

We have excluded at 95% confidence gravitational strength Yukawa interactions with length scales $\lambda > 38.6\mu$m and set new limits between $\lambda = 8$ and 90μm, see Fig. 2.3-1. Further details may be found in our paper[1], and in John Lee's thesis[2].

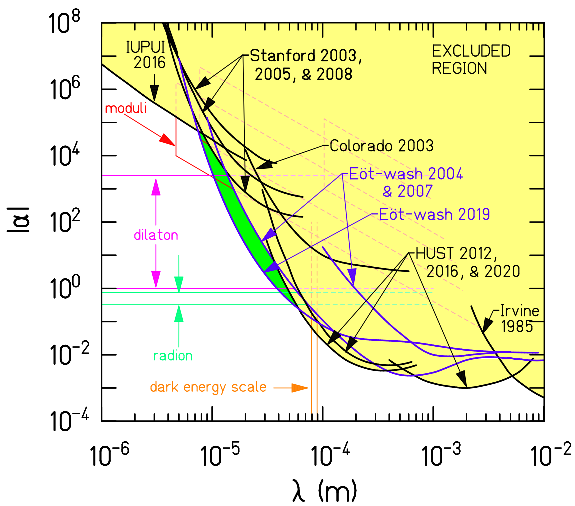

Figure 2.3-1. New 95% confidence level constraints on Yukawa interactions (λ, $|\alpha|$) from this experiment are shown as the green region.

2.4 Updates on Fourier-Bessel pendulum experiment for testing short-range gravity

E. G. Adelberger, B. R. Heckel, B. M. Iritani, J. R. Johnson, J. G. Lee, C. E. Matt, and H. E. Swanson

The Fourier-Bessel pendulum experiment tests the Inverse-Square Law (ISL) for gravity at tens of micrometers, currently placing the shortest distance limit on new forces coupling to matter at gravitational strength.

We are currently working on upgrades for the next iteration of this experiment. The vertical bounce mode of the pendulum can couple vertical seismic motion to torque, creating extra torque noise. We are developing a seismic isolation system in order to

[1] J. G. Lee, E. G. Adelberger, T. S. Cook, S. M. Fleischer, and B. R. Heckel, Phys. Rev. Lett. **124**, 101101 (2020).

[2] J. G. Lee, *A Fourier-Bessel Test of the Gravitational Inverse-Square Law,* Ph. D. Thesis, University of Washington (2020).

decrease this torque noise. This system consists of a seismometer on a platform in feedback with piezoelectrics placed beneath the experiment to counteract measured seismic motion.

Horizontal swinging motion creates additional torque noise. In order to minimize this horizontal motion we developed a new eddy current swing damper. The previous damper was ineffective with a large quality factor of $Q \approx 1000$, while our new damper is expected to have a quality factor of $Q \approx 200$. The new damper has been machined in the CENPA shop and is ready to be installed, see Fig. 2.4-1.

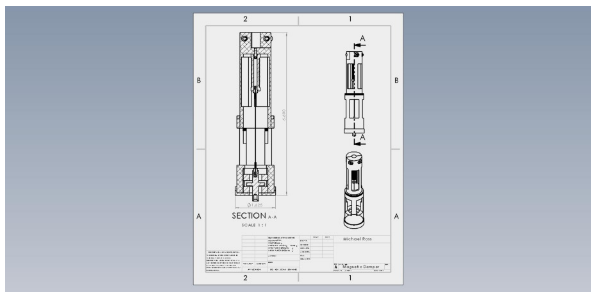

Figure 2.4-1. Short Range eddy current damper design.

Our attractor mass turntable turns at a steady rate by locking the pulse rate from the turntable rotary encoder to a reference clock signal. We developed a new feedback system to replace the previous one, which was custom built from logic integrated circuits and analog electronic components. Our new system is much simpler, implemented using an Arduino Due microcontroller. This setup also makes it easier to implement any future improvements or changes. Our improved feedback system shows decreased angle noise at the turntable frequency, and does not create any peaks at the 18th and 120th harmonics of the turntable frequency (two harmonics relevant for the gravitational test), see Fig. 2.4-2.

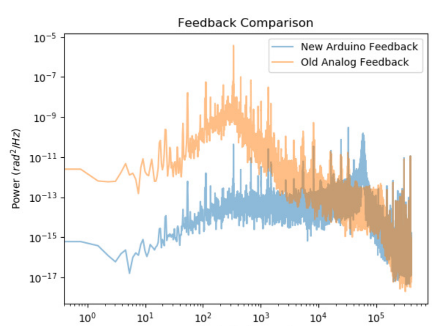

Figure 2.4-2. Improvement on turntable feedback at harmonics of turntable frequency.

3 Accelerator-based physics

3.1 Overview of accelerator-based experiments

A. García

We report on three experimental efforts using the accelerator:

- A ^{21}Ne(p,γ) experiment with the main goal of measuring the mixing ratio of the electromagnetic transition analogous to the β decay of ^{22}Na. This was performed in collaboration with groups from The University of the Western Cape, TRIUMF, and Guelph. It was successfully run over 3 months during the summer of 2019. This involved setting up 12 Ge and a pair of NaI detectors for angular distribution measurements, switching the accelerator to run in terminal-ion source mode, a dedicated program to optimize implantation of ^{21}Ne targets, and a data-taking campaign with 24/7 running for 3 months. Data analysis is under progress.

- Data analysis on extraction of little-a from laser-trapped ^{6}He continued to completion during 2019. The $\beta-\nu$ correlation coefficient was determined to ≈2% uncertainty in this pure Gamow-Teller decay. We are presently working on a publication.

- We assembled all the components for a measurement of the beta spectrum of ^{6}He using the CRES (cyclotron radiation emission spectroscopy) technique developed by the Project 8 collaboration. The main aim of the experiment is a sensitive search for tensor currents in the decays of ^{6}He and ^{19}Ne. This year we installed the superconducting solenoid and built a helium recovery system that makes use of the ADMX compressor. The magnet was cooled down and biased successfully. Preliminary measurements show that the field has adequate uniformity. We installed a cryocooler unit and set up the cooling distribution for our RF system. The daq system is running and presently undergoing tests of noise levels. Tests with an ^{83}Kr source will follow as soon as we can get back into the laboratory. We designed and tested production from a ^{19}Ne source, built on the style of the Berkeley/Princeton design. Production ($\approx 10^{9}$ ^{19}Ne atoms/s for the 10 μA beam our accelerator can deliver reliably) is short of expectations by a factor of approx. 3, but adequate for our needs.

3.2 Angular distribution of $2_1^+ \rightarrow 3_1^+$ photons in ^{21}Ne$(p,\gamma)^{22}$Na: toward solving a puzzle.

G. C. Ball*, R. Coleman†, B. Dodson, A. García, M. Huehn, M. Kamil‡, E. Kasanda†, N. J. Mukwevho‡, J. Pedersen§, V. Pesudo‡, B. Singh‡, E. Smith, M. Sung, S. Triambak‡, E. C. Vyfers‡, D. I. Will, and A. Xiong

A measurement of the $\beta - \gamma$ directional coefficient in ^{22}Na beta decay has been used to extract recoil-order form factors.[1] The data indicated the requirement of a significantly large induced-tensor matrix element for the decay, well beyond the calculated first-class contribution. This suggests either second-class currents, which would disagree with other measurements, or a problem with some of the data that were used to arrive at the conclusion.

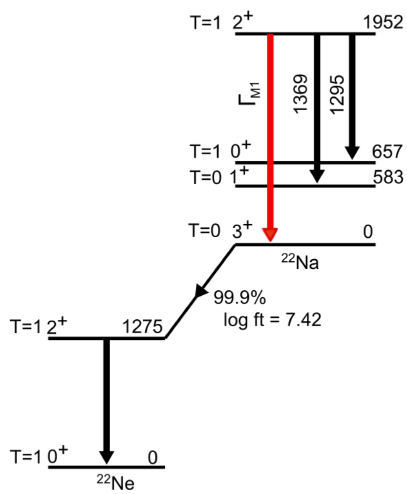

Figure 3.2-1. Decay scheme showing the 2_1^+ state. The transition of interest is highlighted in red.

The conclusion relies heavily on the weak-magnetism form factor for the decay which was determined using an unpublished value of the analog $2_1^+ \rightarrow 3_1^+$ γ branch in ^{22}Na with the further assumption that the transition was purely iso-vector M1[2]. Fig. 3.2-1 shows a decay scheme.

In order to clear up the puzzle we want to determine the mixing ratio for the $2_1^+ \rightarrow 3_1^+$ transition in ^{22}Na. During last year we dedicated a fair amount of work to:

- Developing the implantation of ^{21}Ne targets and producing the targets.

*TRIUMF, Vancouver, British Columbia, Canada.
†Department of Physics, University of Guelph, Guelph, Ontario, Canada.
‡Department of Physics and Astronomy, University of the Western Cape, Bellville, South Africa.
§Presently at Microsoft, Seattle, WA.

[1] C. J. Bowers et al., Phys. Rev. C **59**, 1113 (1999).
[2] S. Triambak et al., Phys. Rev. C **95** (2017) 035501.

Figure 3.2-2. Photo of part of the ^{21}Ne(p,γ) team in Cave 1.

- Recovering know-how to and switching the accelerator to terminal-ion-source mode, so currents of ~ 50 μA could be attained with proton beams of $\sim 0.2-2$ MeV.
- Set up a target system that could withstand the high currents (cooling with a electrically isolated water, properly measuring collimators and target currents, etc.).
- Set up a system of twelve Ge detectors, some of them Clover systems, so as to take reliable angular distributions.
- Take data during three months of the summer.

Data analysis is under progress by our South African colleagues.

3.3 Little-*a* from laser-trapped ^{6}He

Y. S. Bagdasarova, K. Bailey*, B. Graner, X. Fléchard†, A. García, R. Hong*, A. Knecht‡, A. Leredde*, E. Liénard†, P. Müller*, O. Naviliat-Cuncic§, T. P. O'Connor*, J. Pedersen¶, E. Smith, D. W. Storm, and H. E. Swanson

During last year Yelena Bagdasarova finished her Ph.D. thesis on extracting the $\beta-\nu$

*Physics Division, Argonne National Laboratory, Argonne, IL.
†LPC-Caen, ENSICAEN, Université de Caen, Caen, France.
‡Paul Scherrer Institute, Villigen, Switzerland.
§Department of Physics and Astronomy and National Superconducting Cyclotron Laboratory, Michigan State University, East Lansing, MI.
¶Presently at Microsoft, Seattle, WA.

correlation coefficient, little-a, from laser-trapped ^{6}He[1]. Many issues that needed analysis before publishing were addressed. The results show agreement with expectations based on the Standard Model and an uncertainty of $\approx 2\%$ on the correlation coefficient. Fig. 3.3-1 shows results of a fit to one of four sets of data that were used. More recently we realized that a neglected effect due to back-scattering of ions in our MCP could have significant consequences for the analysis. We are presently addressing this issue and moving on to publishing our results.

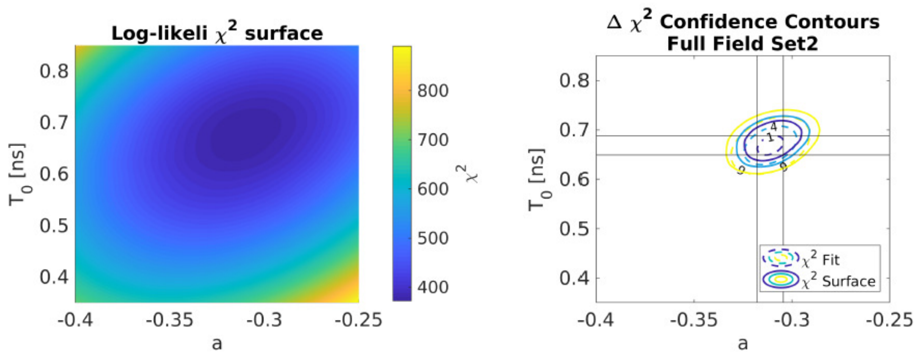

Figure 3.3-1. χ^2 surface (*left*) and corresponding $\chi^2 - \chi^2_{\mathrm{min}} = 1, 4, 9$ confidence contours (*right*) shown versus two parameters used in the fit: little-a and an offset in the ion time of flight for one of four sets of data used.

^{6}He-CRES

3.4 ^{6}He-CRES overview

A. Allen*, J. Amsbaugh, W. A. Byron, D. Combs*, R. Farrell, M. Fertl†, A. García, G. T. Garvey, B. Graner, H. Harrington, L. Hayen*, M. E. Higgins, N. C. Hoppis, K. Knutsen, D. McClain‡, D. Melconian‡, P. Mueller§, N. S. Oblath¶, J. Pedersen, G. Savard§, E. Smith, D. Stancil*, D. W. Storm, H. E. Swanson, Z. Tao, J. Tedeschi¶, B. A. VanDevender¶, F. Wietfeldt‖, A. R. Young*, and R. Zite

We are proceeding with our effort to use the Cyclotron Radiation Emission Spectroscopy (CRES) technique for accurate measurements of beta spectra in search for

*Department of Physics, North Carolina State University, Raleigh, NC.
†Johannes Gutenberg University Mainz
‡Texas A&M, College Station, TX.
§Argonne National Laboratory, Lemont, IL.
¶Pacific Northwest National Laboratory, Richland, WA.
*Department of Electrical Engineering, North Carolina State University, Raleigh, NC.
‖Department of Physics, Tulane University, New Orleans, LA.

[1]Y. Bagdasarova, University of Washington, Ph.D. Thesis, 2019.

chirality-flipping interactions. In this type of experiment one looks for a distortion of the beta spectra known as the Fierz interference. The distortion relative to the Standard Model spectra has a kinematic signature that goes inversely with the beta energy, and is directly proportional to the coupling constants of the chirality-flipping current.

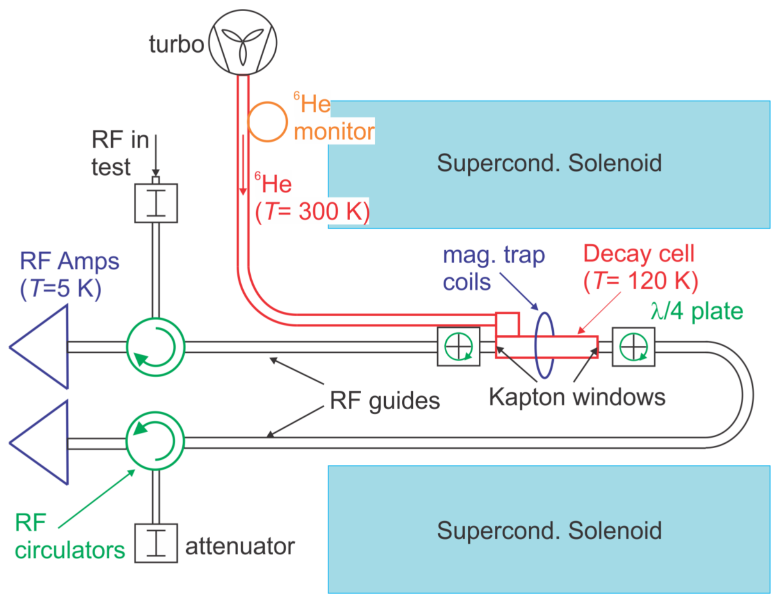

Figure 3.4-1. Sketch of RF systems for the ^{6}He-CRES experiment.

This year we assembled the necessary elements to start our exploration of the CRES technique for measuring with high accuracy the beta spectra from ^{6}He and ^{19}Ne to search for chirality-flipping interactions. The basic idea is to determine the beta energy by measuring the cyclotron frequency, which is around 20 GHz for fields of a few Tesla. Fig. 3.4-1 shows a sketch of the radio frequency (RF) systems and some of the temperature requirements for reaching the needed signal-to-noise ratio. A superconducting solenoid was brought from Argonne National Laboratory, the needed systems for recirculation of helium using the ADMX (Sec. 5.1) compressors was set up, and the magnet was cooled and biased. The uniformity of the field, without using its shimming coils, satisfies our requirements for initial testing. (Sec. 3.5) shows preliminary measurements.

In addition to the main uniform field, provided by the superconducting solenoid, we use three non-superconducting coils, producing fields of approximately a part per thousand of the main field, to trap electrons. This system, which is presently working as needed, is described in (Sec. 3.6). The cryo system required to achieve the needed temperature distributions is also working as designed, and is described in (Sec. 3.7). A non-trivial part of the CRES technique is the demand to digitize data at high rates and to guarantee accurate determination of the cyclotron frequency at the moment when the beta is emitted from the nucleus. The data acquisition (DAQ) and RF systems are described in (Sec. 3.8). In order to transport the radioactivity from the production targets, located in Cave 2, to the decay-cell, located in Cave 1, an approximately

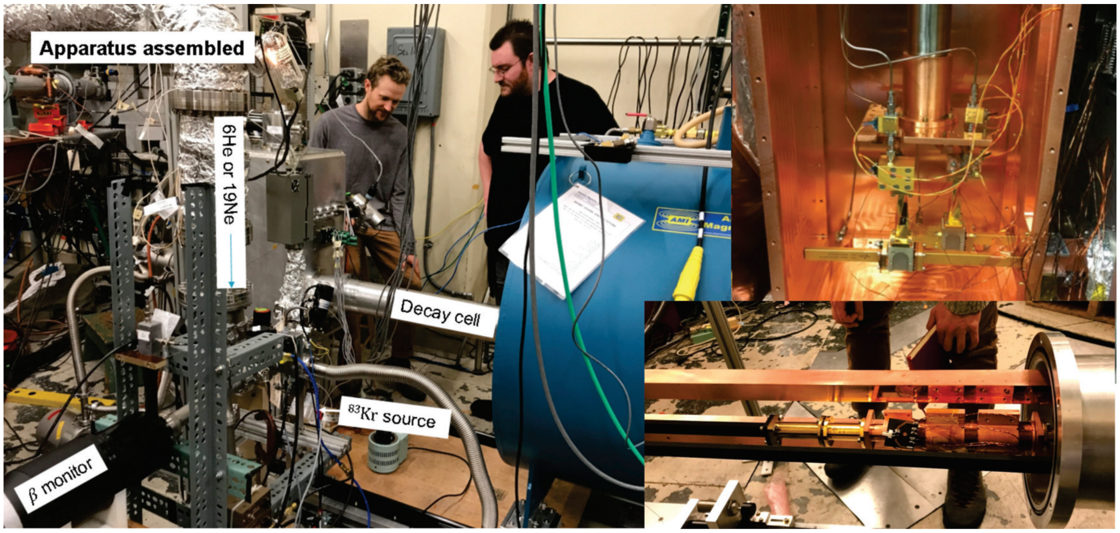

Figure 3.4-2. Photos from ^{6}He-CRES setup. *Left*: radioactive gas transport system, cryo box with nose containing decay cell, that gets inserted into magnet (blue, toward right). *Right, above*: insides of cryo box showing guides and low-noise RF amps connected to cryo-cooler. *Right, below*: decay cell and RF guides with nearby "heat bus", made of squared cross section copper bars.

6-meters long 8"-diameter SS pipe is used with a turbo pump near the decay-cell end. This is described in (Sec. 3.10). Our efforts on systematic uncertainties are only beginning and are described in (Sec. 3.9). We are developing a source of ^{19}Ne to check that the systems are working properly. This will be accomplished by comparing the spectra of ^{6}He and ^{19}Ne. If the Fierz interference exists, the spectra will show opposite signs for β^- and β^+ decays. This year we demonstrated adequate production, but more work needs to be done for improving the vacuum for using the CRES technique. More details are presented in (Sec. 3.12), (Sec. 3.13) and (Sec. 3.14).

In summary, we have assembled all the elements for looking at CRES signals. Looking forward, we plan to characterize the noise in the RF systems, and start looking at decays from the ^{83}Kr source. The vacuum manifold, which provides connections between the ^{6}He and ^{19}Ne production targets, is in place. The production rates are adequate for our needs, but more work will be needed for improving the vacuum.

3.5 Mapping of magnetic field

A. Allen[*], J. Amsbaugh, W. A. Byron, D. Combs[*], R. Farrell, M. Fertl[†], A. García, G. T. Garvey, B. Graner, H. Harrington, L. Hayen[*], K. Knutsen, D. McClain[‡], D. Melconian[‡], P. Mueller[§], N. S. Oblath[¶], J. Pedersen[‖], G. Savard[§], E. Smith, D. Stancil[*], H. E. Swanson, Z. Tao, J. Tedeschi[¶], B. A. VanDevender[¶], F. Wietfeldt[**], A. R. Young[*], and R. Zite

We are using a 1-7 Tesla AMI superconducting magnet which is now fully operational and connected to a helium recirculation system, allowing for recovery via the ADMX compressor system. We have begun the process of mapping the magnetic field within the region of interest. For this we are using a PT2025 NMR Precision Teslameter system from Metrolab. This Teslameter system achieves 5ppm absolute accuracy and 0.1 μT resolution for measurements and mappings of magnetic fields in the range 0.043 T to 13.7 T. The NMR probe is positioned within the bore using a mount which has three degrees of freedom. One of these degrees of freedom is a rotation about an axis, which is driven by a computer-controlled stepper motor. Theodolite data were taken to check the positioning of the probe provided by this mount, and there is ongoing hardware development of the probe mount to ensure the accuracy and reproducibility of these scans. Fig. 3.5-1 shows preliminary data taken at 1.5 T showing that the field is uniform to better than 53 ppm over 10 mm in the central region.

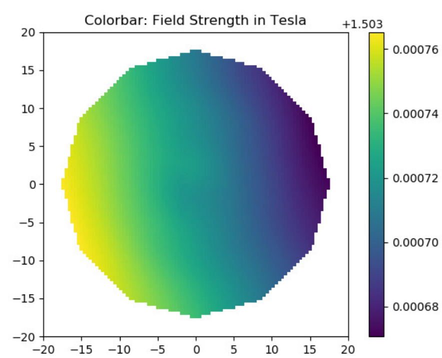

Figure 3.5-1. Interpolated magnetic field data at one slice, perpendicular to the axis of the bore, and measured with the field set to 1.5 T. The x and y axes are in mm from the bore center.

This data is then fitted to a three dimensional magnetic multipole expansion which

[*]Department of Physics, North Carolina State University, Raleigh, NC.
[†]Johannes Gutenberg University Mainz
[‡]Texas A&M, College Station, TX.
[§]Argonne National Laboratory, Lemont, IL.
[¶]Pacific Northwest National Laboratory, Richland, WA.
[‖]Presently at Microsoft, Seattle, WA.
[*]Department of Electrical Engineering, North Carolina State University, Raleigh, NC.
[**]Department of Physics, Tulane University, New Orleans, LA.

is used to determine the field at any point of interest. We expect improved uniformity once we start using shimming coils, but the field is presently adequate for beginning operations. We have also taken data on the variations of the field versus time with the magnet in persistent mode, finding that it decays by ≈18 ppm per day. This is acceptable for our operations. Detailed scans and reliable multiple fits should be completed this summer.

3.6 Trapping coils system

A. Allen*, J. Amsbaugh, W. A. Byron, D. Combs*, R. Farrell, M. Fertl†, A. García, G. T. Garvey, B. Graner, H. Harrington, L. Hayen*, K. Knutsen, D. McClain‡, D. Melconian‡, P. Mueller§, N. S. Oblath¶, J. Pedersen‖, G. Savard§, E. Smith, D. Stancil*, H. E. Swanson, Z. Tao, J. Tedeschi¶, B. A. VanDevender¶, F. Wietfeldt**, A. R. Young*, and R. Zite

In order to detect electrons using the CRES technique, electrons undergoing cyclotron motion must be trapped axially so that they live for long enough (≥ 0.1 ms) so their initial frequency can be determined. From the initial frequency of an electron its kinetic energy is deduced. For adiabatic motion the magnetic flux through the electron cyclotron orbit is conserved, which implies:

$$\frac{\sin^2\theta(t)}{B_z} = \text{Constant in time} \tag{1}$$

where $\theta(t)$ is the angle of the electron momentum relative to the magnetic field (z-axis). As a consequence the component of momentum along the field decreases as the electron transports toward a region with higher field, reaching a returning point:

$$\frac{1}{B(z_{max})} = \frac{\sin^2\theta_0}{B(z_0)}. \tag{2}$$

Thus the electrons oscillate between the points with $z = z_{max}$ and $z = -z_{max}$ (see Fig. 3.6-1). The adiabatic requirement is met in our magnetic field geometry in that the axial frequency is 10^{-3} of the cyclotron frequency; the magnetic field is effectively constant during one cyclotron period. Note that the efficiency of such a trap is independent of beta energy, which is important because we are trying to perform an accurate measurement of the spectrum.

*Department of Physics, North Carolina State University, Raleigh, NC.
†Johannes Gutenberg University, Mainz, DE.
‡Texas A&M, College Station, TX.
§Argonne National Laboratory, Lemont, IL.
¶Pacific Northwest National Laboratory, Richland, WA.
‖Presently at Microsoft, Seattle, WA.
*Department of Electrical Engineering, North Carolina State University, Raleigh, NC.
**Department of Physics, Tulane University, New Orleans, LA.

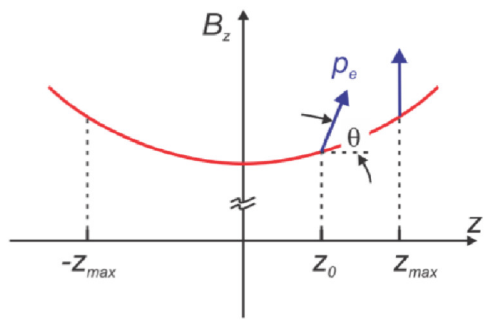

Figure 3.6-1. Schematic of electron axial trapping.

In 2019 the trap was designed, constructed, and tested. We implemented a three coil design in which the three solenoidal coils produce alternating magnetic-field polarity. The field profile created by the trap is shown in Fig. 3.6-2. When the field created by the middle coil is opposite to the main field electrons will be trapped.

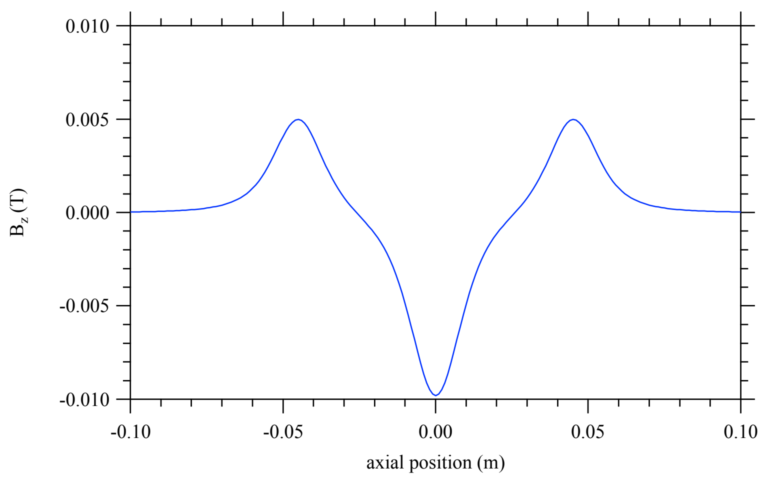

Figure 3.6-2. Axial magnetic field (T) vs axial position (m).

The trap was constructed using two clam-shell pieces that clamp around the ^{6}He decay cell (Fig. 3.6-3). The clam-shells are thermally isolated from the decay cell by G10 spacers. There is a layer of Kapton inserted between the two clam-shell pieces in order to cut down on eddy currents created when ramping the coils (Fig. 3.6-3).

Each coil was wound using 26-AWG copper-insulated magnet wire (Fig. 3.6-4). After each layer GE 7031 varnish was applied to set the wires in place and increase the heat conductivity of the coil. There are 44, 88, and 44 windings in each of the three coils respectively. With the polarity of the center coil being opposite to that of the outer two. The three coils are wired in series. For a 10^{-3} trap in a 6-T main field (our maximum field strength) we need 1.45 A in our trap coils. The maximum current rating of the wires is 4 A.

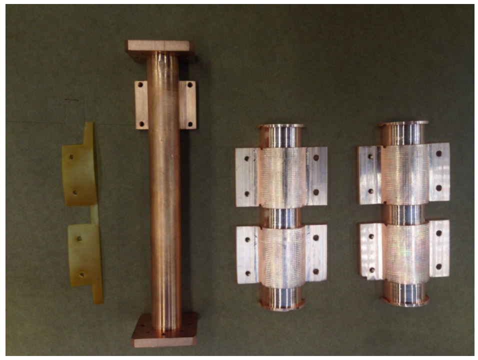

Figure 3.6-3. Component parts of the trap along with the electron decay cell (on the left).

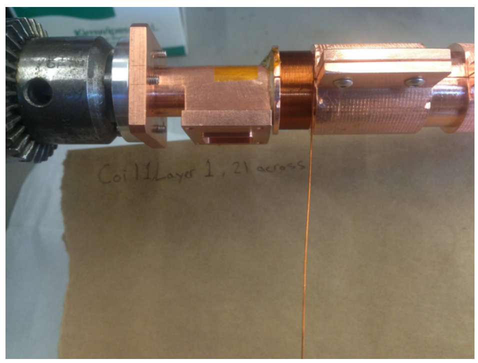

Figure 3.6-4. Winding the trap coils.

The three-coil design was motivated by the desire to empty the trapped electrons by quickly ramping the coil current down to zero. Once the trap current is at zero, the electrons collide with the Kapton windows and rapidly lose enough energy to be undetectable. With a single coil, quickly ramping the current down to zero would cause an induced EMF and associated current in the super conducting solenoid, potentially causing a quench. With the three coil design the trap has no net magnetic moment; there are 88 total turns CW and 88 total turns CCW. Therefore there is effectively no current induced in the superconducting solenoid when emptying the trap via ramping the current to zero.

Using copper braid, we have been able to get the decay cell to 110 K and the coil-form to 50 K (Sec. 3.7). We have successfully kept the decay cell above the freezing temperature of Krypton while keeping the coil-form cold to prevent run-away currents.

We have verified that we can ramp the trap current to zero in $\sim$6 ms using a KEPCO BOP 100 power supply. There is still work to be done investigating if this ramp can occur faster. If the ramping takes too long, the duty cycle for detection may be too low for us to achieve the required statistics in a reasonable amount of time. If the ramping method proves too slow, our N.C.-State collaborators will design an electrostatic trap-emptying device.

3.7 Cryo systems and measured temperature distribution

A. Allen[*], J. Amsbaugh, W. A. Byron, D. Combs[*], R. Farrell, M. Fertl[†], A. García, G. T. Garvey, B. Graner, H. Harrington, L. Hayen[*], K. Knutsen, D. McClain[‡], D. Melconian[‡], P. Mueller[§], N. S. Oblath[¶], J. Pedersen[‖], G. Savard[§], E. Smith, D. Stancil[*], H. E. Swanson, Z. Tao, J. Tedeschi[¶], B. A. VanDevender[¶], F. Wietfeldt[**], A. R. Young[*], and R. Zite

The ^{6}He-CRES experiment relies on having a signal-to-noise ratio such that we can detect a 10^{-15}-W signal. To accomplish this, cryogenic amplifiers must be kept as close to liquid helium temperatures as possible and all components that source RF noise must be as cold as reasonably achievable.

Over the past year we have installed and tested our Gifford-McMahon type cryocooler. The cryocooler is behaving as expected and does seem to be capable of absorbing 1.5 W of power at 5 K as rated. We have wrapped the majority of components, within our vacuum system, in super-insulation consisting of 6-10 alternating layers of polyester tulle and aluminized mylar. This has succeeded in significantly cutting down on the heat power, from black-body radiation, dumped onto the cryocooler. We have coupled different components to heat sinks (e.g. the copper box and copper bars) in order to fine tune their temperature. We have used silicon diodes and platinum resistance temperature detectors (RTDs) to monitor the temperatures of key components. The photonic crystal flanges we designed to thermally isolate the waveguide section closest to the cryogenic amplifiers work as expected.

The temperature distribution of the apparatus is currently satisfactory. The temperature of the terminators, amplifiers, and waveguides are sufficiently low as to satisfy our RF noise budget. The electron decay cell is just above the freezing temperature of krypton (100 K), and the copper clam-shell on which the electron trap coils are wound is cold enough to ensure there is not runaway current in the trap coils (Sec. 3.6).

Below is an overview of the current temperature distribution profile of the ^{6}He-CRES apparatus:

[*]Department of Physics, North Carolina State University, Raleigh, NC.
[†]Johannes Gutenberg University Mainz
[‡]Texas A&M, College Station, TX.
[§]Argonne National Laboratory, Lemont, IL.
[¶]Pacific Northwest National Laboratory, Richland, WA.
[‖]Presently at Microsoft, Seattle, WA.
[*]Department of Electrical Engineering, North Carolina State University, Raleigh, NC.
[**]Department of Physics, Tulane University, New Orleans, LA.

Component	Temperature	Label in Fig. 3.7-1 and Fig. 3.7-2
First Stage Amplifiers	7 K	A
Copper Box	40 K	B
Waveguide, Straight Side	87 K	C
Waveguide, U Side	67 K	C
Terminator, Straight Side	13 K	D
Copper Bars	40 K	E
Electron Decay Cell	114 K	F
Electron Trap	49 K	G

Table 3.7-1. Overview of temperature distribution for the ^{6}He-CRES apparatus.

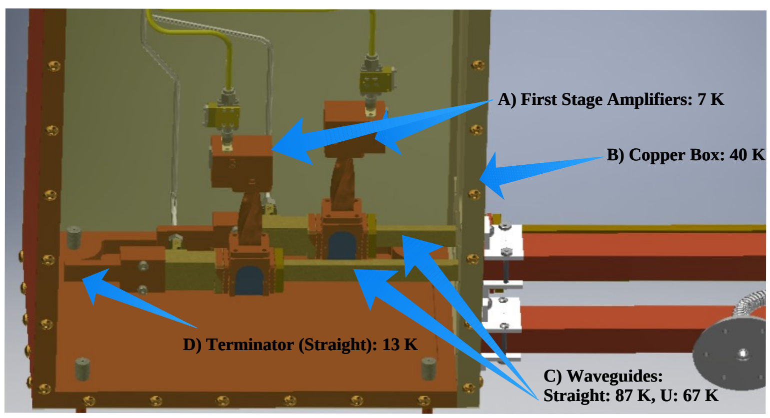

Figure 3.7-1. Temperature map of the copper box within the ^{6}He-CRES apparatus.

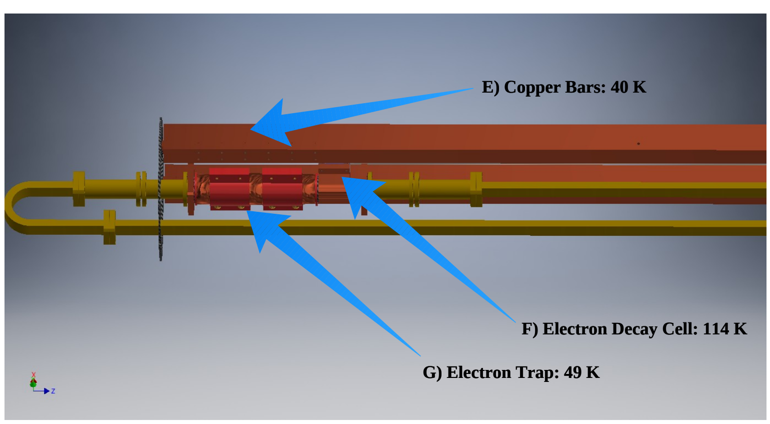

Figure 3.7-2. Temperature map of waveguide end of ^{6}He-CRES apparatus.

3.8 ^{6}He-CRES waveguide systems and data acquisition (DAQ)

A. Allen*, J. Amsbaugh, W. A. Byron, D. Combs*, R. Farrell, M. Fertl†, A. García, G. T. Garvey, B. Graner, H. Harrington, L. Hayen*, K. Knutsen, D. McClain‡, D. Melconian‡, P. Mueller§, N. S. Oblath¶, J. Pedersen‖, G. Savard§, E. Smith, D. Stancil*, H. E. Swanson, Z. Tao, J. Tedeschi¶, B. A. VanDevender¶, F. Wietfeldt**, A. R. Young*, and R. Zite

Given a raw input signal generated from the acceleration of a single electron, the amplification system of any CRES-based experiment is critical to achieving acceptable sensitivity. The microwave power coupled to the TE_{11} mode of a circular waveguide for individual beta-decay electrons is expected to be on the order of femtowatts (10^{-15} W). In the last year, our collaboration has constructed a waveguide experimental apparatus and a radio-frequency (RF) receiver chain that is capable of collecting and amplifying these low-power signals to detectable levels. In addition, we have verified that apparent noise power is within acceptable tolerances.

Parameter	18 GHz	19 GHz	20 Ghz
Cryogenic Stage Gain (dB)	63.5	63.5	63.0
Ambient Stage Gain (dB)	18.0	20.9	20.1
Thermal Noise Density (dBm/Hz)	-182.6	-182.7	-182.8
Total DAQ bandwidth (GHz)	1.8	1.8	1.8
FFT Bins	8192	8192	8192
FFT Bin Width (kHz)	220	220	220
Input Noise Power Per Bin (dBm)	-47.63	-44.89	-46.21
Input Signal Power(dBm)	-38.45	-35.64	-36.89
SNR for RMS Thermal Noise (dB)	9.18	9.25	9.32
ADC Peak Input (mVpp)	500	500	500
ADC Resolution (bits)	8	8	8
ADC Bit Noise Floor (dBm)	-50.2	-50.2	-50.2

Table 3.8-1. Summary of relevant RF receiver parameters and noise figures. All values are based on the assumption of a -120 decibel-milliwatts (dBm) (=1.0 fW) source, 1 dB or less of RF losses in the waveguide, and terminators sourcing thermal noise at 5.0 K.

The receiver is divided into two sections: the cascaded cryogenic amplifiers, which sit in vacuum at or near 5.0 K and are directly coupled to the waveguides; and the ambient temperature receiver, which sits outside the vacuum system and is responsible

*Department of Physics, North Carolina State University, Raleigh, NC.
†Johannes Gutenberg University Mainz
‡Texas A&M, College Station, TX.
§Argonne National Laboratory, Lemont, IL.
¶Pacific Northwest National Laboratory, Richland, WA.
‖Presently at Microsoft, Seattle, WA.
*Department of Electrical Engineering, North Carolina State University, Raleigh, NC.
**Department of Physics, Tulane University, New Orleans, LA.

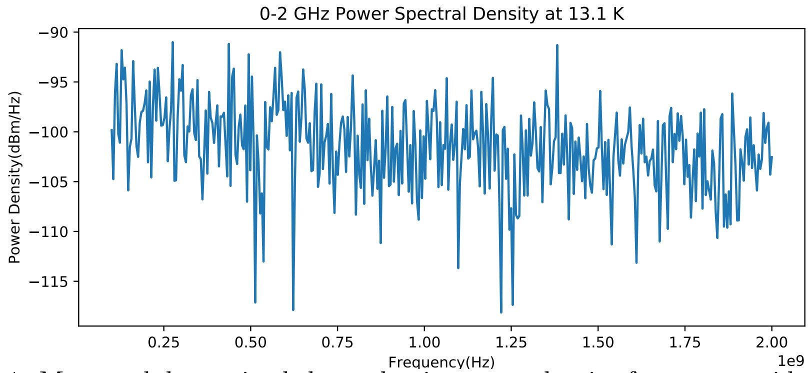

Figure 3.8-1. Measured downmixed thermal noise power density from waveguide attenuator at a temperature of 13.1 K. Signals were amplifed through the full receiver chain before being digitized; thermal noise power density is thus 81.5-84.4 dB lower than shown.

for mixing down the signal of interest from 18-20GHz to $<$ 2 GHz so that it can be digitized with 4Gs/sec analog-to-digital converters (ADCs). The cryogenic amplifiers have a characteristic noise temperature of 7.0 K when cooled to a physical temperature below 5.0 K, which is vital to achieving the input noise power density objective of -182 dBm/Hz. Thus, it is necessary to cool the primary amplifiers and lossy parts of the waveguides to near liquid-helium temperature. Table 3.8-1 gives relevant parameters for the receiver stages as well as anticipated signal and noise power levels, given reasonable assumptions of physical temperatures throughout the apparatus.

A plot of measured noise power is shown in Fig. 3.8-1. Given the 81.5-84.4 dB of gain in the system, we can expect a 1-fW electron signal to appear in the range of -36 to -38 dB at the ADC inputs. Given a 220-kHz FFT bin size and the above measured noise power density, the noise floor in a single bin should be approximately -95 dBm/Hz + 10 * log_{10}(220 kHz) = -42 dBm. We thus expect to have a reasonable signal-to-noise ratio that will enable observation of individual decay electrons. In the coming year, we expect to begin taking data on beta decay events. Our top priority will be to calibrate the system with keV-scale conversion electrons from the decay of metastable krypton gas atoms.

3.9 Estimation of systematic uncertainties

A. Allen*, J. Amsbaugh, W. A. Byron, D. Combs*, R. Farrell, M. Fertl†, A. García, G. T. Garvey, B. Graner, H. Harrington, L. Hayen*, K. Knutsen, D. McClain‡, D. Melconian‡, P. Mueller§, N. S. Oblath¶, J. Pedersen‖, G. Savard§, E. Smith, D. Stancil*, H. E. Swanson, Z. Tao, J. Tedeschi¶, B. A. VanDevender¶, F. Wietfeldt**, A. R. Young*, and R. Zite

The most difficult part of this experiment will likely be in properly evaluating systematic uncertainties. Over the last couple of years we have concentrated on the hardware and data-acquisition (DAQ) parts of the experiment, but we are starting to develop tools for systematic studies. Because the time scale of the cyclotron motion ($\sim (20\ \mathrm{GHz})^{-1}$) and the typical time required for observation of events (~ 1 ms) are so different, it is very hard to build Monte Carlo calculations that include full tracking and study issues on a from-the-bottom-up approach. We are studying issues and developing intuition using reasonable approximations. Alongside our own software, we considered the dominant uncertainties using Kassiopeia[1]. Table 3.9-1 shows a preliminary list of effects we have considered with preliminary estimations.

	Δb	
Effect	No trap	Ion trap
Magnetic field uncertainties	$\sim 10^{-4}$	$< 10^{-4}$
Wall collisions	$\sim 10^{-3}$	None
RF pickup uncertainties	$\sim 10^{-4}$	10^{-5}
Misidentification of events	$\sim 10^{-4}$	5×10^{-5}
Scattering	$\leq 10^{-5}$	$\leq 10^{-5}$

Table 3.9-1. Estimated uncertainties for the ^{6}He-CRES experiment. The "Ion trap" column indicates what could be reached in a later phase of the experiment, where an ion trap would be used to avoid distortions due to collisions with the guide walls.

As can be seen, in the present phase of the experiment, without an ion trap, a dominant source of uncertainties will be due to collisions with the walls. Electrons that are in trajectories that intersect the walls don't contribute to events, because they quickly disappear, forced back to the walls by the magnetic field. Since the fraction of electrons that hit the walls depends on their cyclotron radius, there is a strong

*Department of Physics, North Carolina State University, Raleigh, NC.
†Johannes Gutenberg University, Mainz, DE.
‡Texas A&M, College Station, TX.
§Argonne National Laboratory, Lemont, IL.
¶Pacific Northwest National Laboratory, Richland, WA.
‖Presently at Microsoft, Seattle, WA.
*Department of Electrical Engineering, North Carolina State University, Raleigh, NC.
**Department of Physics, Tulane University, New Orleans, LA.

[1] D. Furse et al., New J. Phys. **19** 053012 (2017).

correlation with energy that distorts the spectrum. In order to properly account for the distortion, one needs to determine a parameter that represents an "effective radius" of the waveguide. This parameter depends on the physical radius of the guide, as well as alignment of it with the magnetic field, and other geometry details. We don't plan to determine this parameter based on absolute measurements of the geometry, but rather by demanding that data taken at different field values, yield the same results.

Another example that we considered recently is the potential scattering of electrons from "untrapped trajectories" into "trapped" ones: electrons that may have lost energy on the Kapton foil windows may get trapped after collision with other atoms. We find the probabilities are negligible, compared to other processes.

In summary, we are starting the process of estimating systematic uncertainties in a rigorous way. Although up to the present we have concentrated mostly on hardware, we plan to invest more time in this endeavor in the near future.

3.10 Vacuum systems and connection to target

A. Allen[*], J. Amsbaugh, W. A. Byron, D. Combs[*], R. Farrell, M. Fertl[†], A. García, G. T. Garvey, B. Graner, H. Harrington, L. Hayen[*], K. Knutsen, D. McClain[‡], D. Melconian[‡], P. Mueller[§], N. S. Oblath[¶], J. Pedersen[‖], G. Savard[§], E. Smith, D. Stancil[*], H. E. Swanson, Z. Tao, J. Tedeschi[¶], B. A. VanDevender[¶], F. Wietfeldt[**], A. R. Young[*], and R. Zite

To conduct the ^{6}He-CRES experiment, it is necessary to produce and transport a sufficient amount of the radioactive gases to the decay cell. To this end, a large transport pipe, approximately 6 meters in length and 8 inches in diameter, has been attached to the ^{6}He and ^{19}Ne sources. At the end near the decay cell, the pipe is pumped by a turbomolecular (turbo) pump, in order to compress the radioactivity from the source to the decay cell.

Due to the need to minimize scattering of electrons in the decay cell, we need vacuum at approximately 10^{-7} Torr within the transport system. So far, we have only achieved vacuum at 5×10^{-6} Torr before the turbo pump. We have set up to do a full baking of the 8-inch diameter pipe. The system is all presently wrapped in heat tape, ready for baking once activites resume.

[*]Department of Physics, North Carolina State University, Raleigh, NC.
[†]Johannes Gutenberg University, Mainz, DE.
[‡]Texas A&M, College Station, TX.
[§]Argonne National Laboratory, Lemont, IL.
[¶]Pacific Northwest National Laboratory, Richland, WA.
[‖]Presently at Microsoft, Seattle, WA.
[*]Department of Electrical Engineering, North Carolina State University, Raleigh, NC.
[**]Department of Physics, Tulane University, New Orleans, LA.

On the other side of the turbomolecular pump that compresses the ^{6}He gas and sends it into the decay cell, we have a second turbo pump that is designed to establish an initial vacuum within the decay cell before running the experiment. In addition, we are using a non evaporable getter (NEG) pump to trap residual gases and keep the vacuum in the decay cell low when this second turbo pump is not running. Steps to improve the vacuum in the decay cell are being considered including the possibility of adding an ion getter pump that can pump argon.

3.11 Monitor detector for relative normalization

A. Allen[*], J. Amsbaugh, W. A. Byron, D. Combs[*], R. Farrell, M. Fertl[†], A. García, G. T. Garvey, B. Graner, L. Hayen[*], K. Knutsen, D. Melconian[‡], P. Mueller[§], N. S. Oblath[¶], J. Pedersen[‖], G. Savard[§], E. Smith, D. Stancil[*], H. E. Swanson, J. Tedeschi[¶], B. A. VanDevender[¶], F. Wietfeldt[**], A. R. Young[*], and R. Zite

Since the ^{6}He-CRES data is taken in a finite band width ($\approx 18 - 20$ GHz) that covers a small portion of the beta spectrum, we take data at different values of the magnetic field to span the whole beta spectrum. In order to *stitch together* these different parts, we use a monitor beta detector (shown in Fig. 3.4-1, right after the turbo pump, at the top of the diagram). Thus, this monitor detector has to have stability at the level required for the experiment.

We are testing the stability of a system of a Passivated Implanted Planar Silicon (PIPS) detector and digitizer to be used as a monitor for beta activity. Our initial data was taken using a ^{241}Am alpha source. In order to test its stability, we plotted the Allan Variance, which we show in Fig. 3.11-1.

[*]Department of Physics, North Carolina State University, Raleigh, NC.
[†]Johannes Gutenberg University, Mainz, DE.
[‡]Texas A&M, College Station, TX.
[§]Argonne National Laboratory, Lemont, IL.
[¶]Pacific Northwest National Laboratory, Richland, WA.
[‖]Presently at Microsoft, Seattle, WA.
[*]Department of Electrical Engineering, North Carolina State University, Raleigh, NC.
[**]Department of Physics, Tulane University, New Orleans, LA.

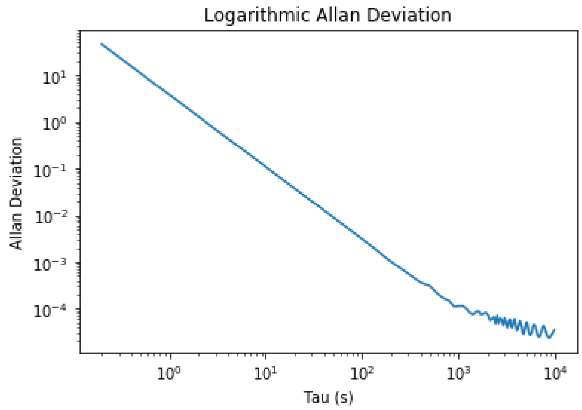

Figure 3.11-1. Allan deviation taken with a PIPS detector and a ^{241}Am source.

We observe that for the alpha source the stability of the system looks adequate, yielding better than 10^{-4} Allan deviation. Our next measurement will be with ^{90}Sr to check the stability with a system that closer resembles our needs. The PIPs Si detector (500 μm thick) will only observe a minimum-ionizing peak for the betas, making the system more sensitive to gain drifts than the ^{241}Am case.

3.12 Gas system for the ^{19}Ne source

A. García, M. E. Higgins, N. C. Hoppis, E. B. Smith, and D. W. Storm

Accurate measurements of the beta spectra from ^{6}He and ^{19}Ne could lead to the most sensitive searches for chirality-flipping interactions. This is because the effect of the chirality-flipping interactions shows as a distortion of the beta spectra that has opposite signs for β^- versus β^+ decays.[1] In addition, previous measurements[2] of the angular distribution of electrons from polarized ^{19}Ne in combination with the lifetime imply something is amiss in these measurements or their interpretation. Thus, it would be very interesting to measure the ^{19}Ne beta spectrum.

As described in last year's Annual Report[3] we plan to use the ^{19}F$(p,n)^{19}$Ne reaction with a beam from the Tandem accelerator at somewhat over 11 MeV. The source design is similar to the ^{19}Ne source developed at Berkeley[4,5] and used later at Princeton,[6] but without the difficulties related to getting polarized atoms.

[1] M. Gonzlez-Alonso, O. Naviliat-Cuncic, and N. Severijns, Prog. Part. Nucl. Phys. **104**, 165 (2019).

[2] F. P. Calaprice, S. J. Freedman, W. C. Mead, and H. C. Vantine Phys. Rev. Lett. **35**, 1566 (1975).

[3] CENPA Annual Report, University of Washington (2019) p. 83.

[4] D. Dobson, *The beta-decay asymmetry and nuclear magnetic moment of Neon-19,* Ph. D. Thesis, U. C. Berkeley (1963).

[5] D. C. Girvin, *Test of time-reversal invariance in ^{19}Ne beta decay,* Ph. D. Thesis, U. C. Berkeley (1972).

[6] M. B. Schneider, F. P. Calaprice, A. L. Hallin, D. W. MacArthur, and D. F. Schreiber, Phys. Rev. Lett. **51**, 1239 (1983).

The gas flows continuously through the target, and the activated gas passes through a cold trap to freeze out the SF_6, leaving the ^{19}Ne free to be compressed by a turbo pump. We plan to have two alternating cold traps to permit continuous operation, but so far we have only one, which we have used for tests.

In 2019 we completed and tested the gas handling system as illustrated in Fig. 3.12-1. Our first step is to remove impurities that don't freeze from the SF_6. After evacuating a storage tank (upper left of the figure), SF_6 is drawn from a supply cylinder (in the lower left of the figure) and passed through the system into the cold trap. Impurities (mainly air) are pumped out at the same time by the turbo pump. After a few hours, the trap is isolated from the target and warmed, with valves to the storage tank opened, and the cleaned SF_6 passes into the tank. This step is required because we need to maintain a good vacuum when we produce ^{19}Ne for the ^{6}He-CRES system. Typically, the storage pressure has been between 70 and 95 psi.

For our tests, we started with CO_2, which is cheaper than SF_6 and has much less impact as a green-house gas. Once we demonstrated that we could handle CO_2 successfully, we switched to SF_6.

For ^{19}Ne production, we use the cleaned SF_6 from one of the storage tanks. Supply pressure is monitored with G3, which permits readings accurate to 1 or 2 psi, and enables us to monitor the rate of gas use. (In a 50-liter tank, one bar corresponds to 2 moles of gas.) The storage regulator was set for 30 psig, and monitored on the regulator gauge, G2, to maintain 3 bars of SF_6 in the target. This density is enough to easily stop the 12-MeV proton beam in the 57-cm^3 gas target (described in last year's annual report[3]). Flow rate is controlled by the needle valve following the target and monitored on the flow meter. For protection, we installed a 50-psi pressure safety relief valve (Vsr) in the line leading to the target. To protect the accelerator vacuum system and to avoid losing all of our SF_6 in the event of a target-window failure, there is a solenoid valve (Vs) in the line to the target which is interlocked to the beamline vacuum. The flowmeter was calibrated for 3-bar SF_6 by observing the rate of pressure drop in the supply system or by noting the amount of gas passed from the cold trap into the supply cylinder after a cleaning step at constant flow rate. All the calibrations were done with 30-psig gas flow and were consistent to better than 20%.

After passing through the needle valve, the gas, which includes ^{19}Ne if the beam is on, goes to a manifold which includes V_4 and V_{11} through which the gas passes to the cold trap. The cold trap (Sec. 3.13) has a 120-psi safety relief valve. For gas-flow tests, we have run the system at around 2-mole/hr flow rate and are able to run for several hours. The target contains 6.84×10^{-3} moles at 3 bar. Thus 2-mole/hr flow rate exhausts the target in 12 s, as compared to the 17-sec half-life of ^{19}Ne. During the flow tests, V_6 and V_{10} are open, connecting the system to the turbo pump. Eventually the cold trap becomes saturated, as indicated by a rise in the manifold Pirani gauge, G_1. For the tests we did with activation (Sec. 3.14), V_{10} was closed and V_9 was open to allow flow into the counting set-up in Cave 1.

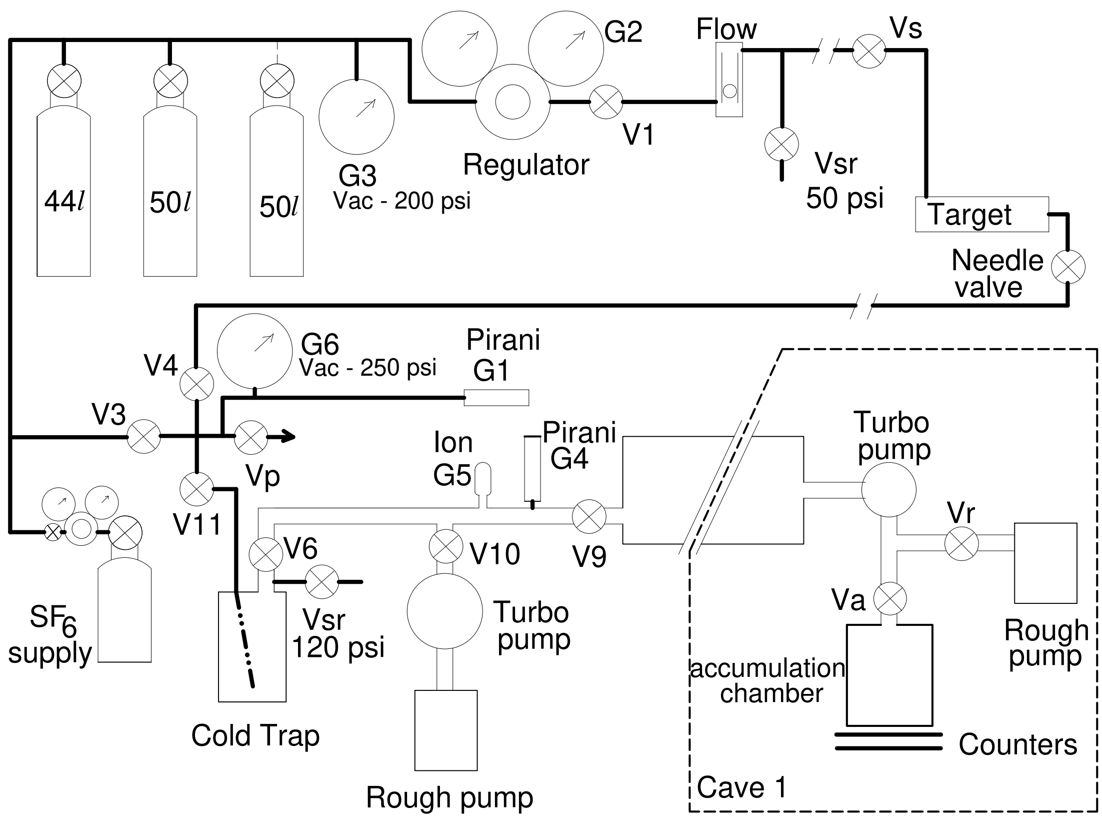

Figure 3.12-1. The ^{19}Ne gas handling system. The target and SF_6 handling system is in Cave 2, near the ^{6}He production system. Both systems connect to a 6-inch pipe running through the wall into Cave 1, where the decaying isotopes will eventually enter the ^{6}He-CRES device. The heavy lines indicate either 3/8" or 1/4" inner-diameter copper refrigeration tubing for gas transport. Two of the three gas storage tanks, 44l and 50l, are presently connected to the system.

For production tests, the ^{19}Ne and residual untrapped gases flowed into Cave 1 via the 6-inch pipe. It was compressed by the turbo pump, and cycled through the accumulation chamber for beta counting. At the beginning of the cycle both, the accumulation valve, Va, and the roughing valve, Vr, are both open. Next, Vr was closed. Gas is accumulated in the test chamber for several ^{19}Ne half-lives, and then the accumulation valve, Va, was closed. The roughing valve, Vr, was then opened to back turbo pump. We counted the activity for 10 or more half-lives (Sec. 3.14). Then, Va was opened until the end of the cycle to clean out the accumulation chamber and back the turbo pump.

We will need a significantly improved vacuum after the cold trap to use the ^{19}Ne source for the ^{6}He-CRES experiment. We do not know the vapor pressure of SF_6 at 80 K, as the published values we have found[1] only extend down to 103 K. Extrapolation indicates a value at 80 K in the 10^{-5} Torr range. We have installed a residual gas analyzer (RGA) in the test area to quantify the contents of the untrapped residual gas. Some preliminary results are described elsewhere (Sec. 3.13) in this Annual Report. Measurements with the RGA should guide us toward installing additional cryopumping or getter-pumping to remove the residual gas, without trapping the ^{19}Ne.

3.13 Progress on a cold trap for ^{19}Ne - SF_6 separation

A. García, M. E. Higgins, N. C. Hoppis, E. B. Smith, and D. W. Storm

As briefly mentioned in last year's report[2], we developed a LN_2 cooled trap to freeze SF_6 while permitting ^{19}Ne to pass through. The trap needed to tolerate both hard vacuum during freezing and 8-bar gauge when sublimating the SF_6. The initial trap, R0, was a 304 stainless steel cylindrical shell with copper baffles soldered to the bottom surface of the cylinder (Fig. 3.13-1). Our testing over the previous year has shown the freezing performance of trap R0 to be insufficient, because SF_6 ice accumulated on the top surface and egress port neck during operation. In this report we detail the modifications to our original design which have produced trap R1.

Because the top end of the R0 trap was acting as a part of the gas baffling, we took a new approach to the design of the R1 trap. Rather than soldering all of the baffles for bulk freezing and vacuum cleanup on the bottom side of the trap body, R1 bulk freezing baffles were soldered to the bottom end of the trap while the cleanup baffles were soldered to the top end (see Fig. 3.13-1). This doubles the maximum heat flux which may be sustained for a given baffle temperature, and thermally aligns the cleanup baffles in parallel with the bulk freezing baffles. The R0 cleanup baffles were in series with the bulk freezing baffles, resulting in less effective final SF_6 scavenging since they would always be at a higher temperature than the bulk freezing baffles. The ingress tube was shortened to increase the amount of SF_6 ice accumulation required

[1] https://encyclopedia.airliquide.com/sulfur-hexafluoride
[2] CENPA Annual Report, University of Washington (2019) p. 83.

to build up and block the tube hole. The ^{19}Ne egress and activated SF_6 ingress ports were also sufficiently lengthened to allow the top surface of the trap to be submerged in an excess of LN_2, providing for extended operation with the cleanup baffles cooled.

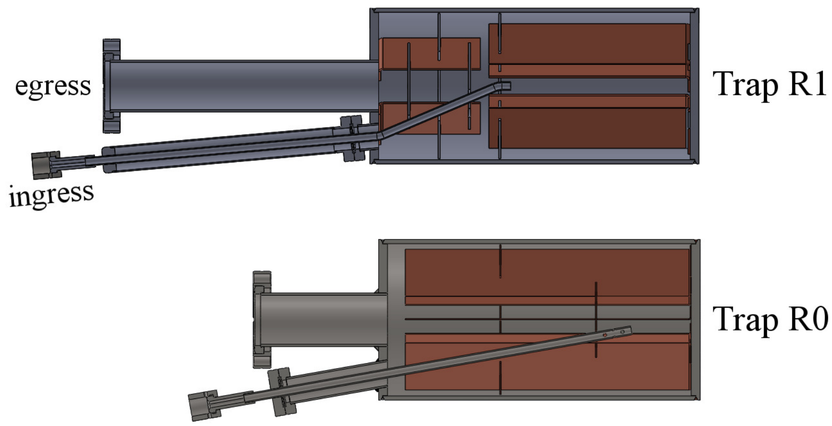

Figure 3.13-1. CAD drawing of the R0 and R1 traps. The fins within the traps are all copper. The bodies of both traps are 304 stainless steel. The fin assembly in R1 has been split with bottom fins soldered to trap bottom and top fins soldered to trap top.

These changes appear to have increased the quantity of SF_6 which the R1 trap can freeze compared to the R0 trap. Tthe most recent ^{19}Ne run occurred over the course of an afternoon, completely freezing all stored SF_6 without overfilling. However, it was also discovered that the ingress port can become plugged with frozen SF_6 if the trap is precooled for more than half an hour before flowing SF_6 . When flowing SF_6 in steady state the gas warms the ingress tube such that SF_6 ice does not accumulate.

Unfortunately, the R1 trap has not substantially decreased the vacuum system base pressure, so an SRS RGA-100 was installed to view the constituent partial pressures.

Table 3.13-1 shows the observed fractional ionization series of partial pressures corresponding to Carbon Tetrafluoride. Carbon Tetrafluoride contamination was initially suspected due to the dominant peak at 69 AMU/e, further CF_4 is a contaminant in 99.8% SF_6 on the level of 500 ppm, according to Airgas[1]. The measured m/q values correspond well to the expected ionization product ratios obtained by Dibeler and Mohler[2] for CF_4, compared to shared m/q values with other species (such as SF_6). Summing over all the fractional ionization product partial pressures of CF_4 gives a total CF_4 pressure consistent with the total measured pressure, indicating that CF_4 remediation will greatly improve system base pressure.

We do not yet have a concrete understanding of the behavior of SF_6 - CF_4 mixtures at low temperatures. Extrapolation from data in the 51st CRC handbook of Chemistry and Physics for pure CF_4 indicates that the vapor pressure near 77 K should be near

[1]Airgas, Pure Gasses Catalog, Sulfur Hexafluoride (2018).

[2]V. H. Dibeler, F. L. Mohler, J. Res. Nat. Bur. Stand. **40**, RP1853 (1948).

m/q	Pressure (Torr)	Species	Expected fraction[2]
12	6.2×10^{-7}	C^+	0.06
19	3.8×10^{-7}	F^+	0.04
25	5.5×10^{-7}	CF_2^{2+}	0.04
31	4.4×10^{-7}	CF^+	0.03
34.5	2.2×10^{-7}	CF_3^{2+}	0.01
50	1.5×10^{-6}	CF_2^+	0.09
69	9.3×10^{-6}	CF_3^+	0.73
Total	1.3×10^{-5}	CF_4	1

Table 3.13-1. Carbon Tetrafluoride species observed in the R1 trap with pumping, manifold background subtracted. The CF_4 total pressure is a supermajority of the measured net pressure.

300 mTorr[1], suggesting no CF_4 should be trapped in R1 sparing some CF_4 - SF_6 interaction. A cryopump could be modified for high conductance operation to completely scrub the remaining CF_4 after the existing cold trap. We expect to begin efforts to remediate the CF_4 issue this summer.

3.14 ^{19}Ne Production and half-life

A. García, B. Graner, M. E. Higgins, N. C. Hoppis, E. B. Smith, and D. W. Storm

In order to determine the production rate of ^{19}Ne we set up a beta decay counting system (Fig. 3.14-1). We acquired data in cycles that accounted for the ^{19}Ne half-life of approximately 17 seconds: first, allowing the ^{19}Ne to accumulate for about 3 half-lives by closing valve V_R and opening V_A; then, closing V_A, opening V_R, and counting betas for ≈ 15 half-lives; finally, opening V_A to evacuate the accumulation chamber. While the ^{19}Ne is decaying in the accumulation volume, two scintillation counters placed behind the copper foil window are used to detect coincident events.

The $^{19}F(p,n)^{19}$Ne reaction cross section[2,3] peaks at $\approx 50-70$ mb and 7 MeV. Just below 5 MeV, the reaction cross section becomes negligible. Using SRIM[4] to determine the energy profile of the proton beam as it slows in the gas, we found that ^{19}Ne production rate for a target with uniform SF_6 density, is maximized by beam

[1] R. C. Weast, CRC Han. Chem. Phys. **51**, D-146 (1970).
[2] J. D. Jenkin, L. G. Earwaker, and E. W. Titterton, Nucl. Phys. **44**, 453 (1963).
[3] S. Kitwanga, P. Lelux, P. Lipnik, and J. Vanhorenbeeck, Phys. Rev. C **42**, 748 (1990).
[4] J. F. Ziegler, M. D. Ziegler and J. P. Biersack, Nucl. Instrum. Methods **268**, 1818 (2010).

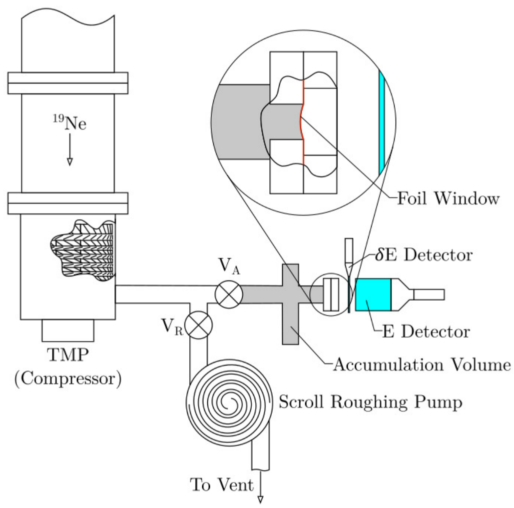

Figure 3.14-1. Diagram of the ^{19}Ne beta decay counting system. The ^{19}Ne gas is compressed by the turbo pump into an accumulation volume, which has a pair of scintillator detectors behind a copper window. We determined production and half-life by cycling valves V_R and V_A.

energies between 5 and 11 MeV. Because beam heating of the gas will unpredictably reduce target density in the neighborhood of the beam, we chose a target length of 20 cm, to provide a safety factor of 2 above cold 3-bar SF_6, and will vary target pressure to permit trimming of the low energy tail of the beam. Using the data from Jenkin et al.[1], we find an 11-MeV proton beam, stopping in the gas, should produce 1×10^{-4} ^{19}Ne atoms/s per incident proton. Kitwanga[3], however, reports a thick target production of 3×10^{-4} atoms/s per incident proton. The former value is adequate for our requirements. For reference, our Tandem accelerator can deliver ≈ 10 μA of 11-MeV protons in a stable fashion. With an estimation of the beta efficiency of our scintillators of $\approx 0.35\%$, and a measured current on the Faraday cup of ≈ 200 nA, we find a yield at our counting station of $\approx 1.4 \times 10^{-5}$ atoms per incident proton (Fig. 3.14-2). Using our measured values for the gas flow and pumping speed, we conclude that the ^{19}Ne in the target should take, at minimum, about a half-life to move to the decay counter. We are a factor of approximately 3 short of the prediction based on the data[1]. We still need to investigate variations of production yields versus target pressure.

There has been recent interest in an accurate determination of the ^{19}Ne half-life[2,3,4]. As a byproduct of our work, we can determine this half-life. In order to perform a fit to our half-life data, there are a series of crucial steps that must occur. First, the data must be separated so each cycle has its own decay count curve. Within each curve,

[1] J. D. Jenkin, L. G. Earwaker, and E. W. Titterton, Nucl. Phys. **44**, 453 (1963).
[2] S. Triambak et al., Phys. Rev. Lett. **109**, 042301 (2012).
[3] L. J. Broussard et al., Phys. Rev. Lett. **112**, 212301 (2014).
[4] C. Fontbonne et al., Phys. Rev. C **96**, 065501 (2017).

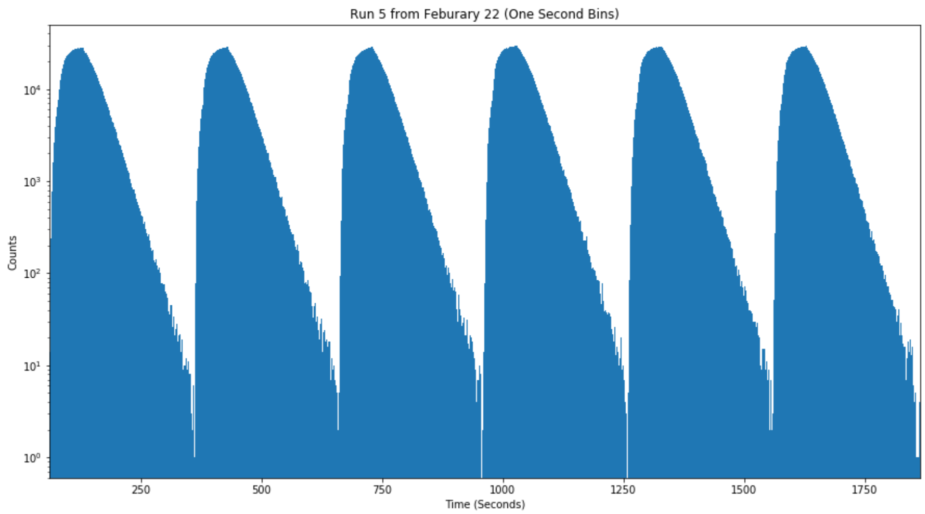

Figure 3.14-2. Plot of decay counts/second for a run with 6-accumulation cycles.

there are periods when counts record while the decay volume is being populated with ^{19}Ne, and there are periods when counts drop to zero discontinuously due to the decay volume being opened to the scroll pump. The former can be seen in Fig. 3.14-2 as the ramp up before the peak in each cycle. Only the counts from times after the time of maximum (peak) counts and before the discontinuous drop to zero are selected for fittings. The data is fit to a model for exponential decay with non-paralyzable deadtime given by:

$$M_i = \frac{\ln\left(\left|\frac{DN_0 e^{-\lambda T_{i-1}} + BD + 1}{DN_0 e^{-\lambda T_i} + BD + 1}\right|\right) + BD\lambda(T_i - T_{i-1})}{(BD^2 + D)\,\lambda} \tag{1}$$

Here M_i is the number of measured counts for each bin with time range $T_i - T_{i-1}$, B is the background rate, and D is the deadtime per accepted event, and λ is the decay constant.

We are presently working on analysis of the data, assuming all cycles have common D, and some cycle-dependent parameters (initial rate, background rate). We have plans to determine the deadtime, D, with independent measurements and look for rate-dependent gain shifts that could affect the extraction of the half-life λ, and ultimately the half-life, $T_{1/2} = \ln(2)/\lambda$.

4 Precision muon physics

MuSun

4.1 Muon capture and the MuSun experiment

D. W. Hertzog, P. Kammel, E. T. Muldoon, D. J. Prindle and R. A. Ryan*

Muon capture provides a powerful tool to study properties and structure of the nucleon and few nucleon systems as predicted by effective theories (EFT) founded on Quantum Chromodynamics. Our program focuses on capture from the simplest of all muonic atoms, namely the theoretically-pristine muonic hydrogen (MuCap experiment) as well as muonic deuterium (MuSun experiment). Our collaboration has pioneered a novel active-target method based upon the development of high-pressure time-projection chambers (TPC) filled with hydrogen/deuterium gas.

One of the most interesting topics for muon capture in the few-body sector is the family of two-nucleon weak-interaction processes. In these reactions only a single unknown low energy constant (LEC) enters the theoretical description up to the required order, which characterizes the strength of the axial-vector coupling to a four-nucleon vertex, the two-nucleon analog to g_A for the nucleon. This family contains muon capture on the deuteron, $\mu + d \to n + n + \nu$, together with astrophysics reactions of fundamental interest, in particular, pp fusion, which is the primary energy source in the sun and the main sequence stars, and the νd reactions, which provided the evidence for solar neutrino oscillations at the Sudbury Neutrino Observatory (SNO). The extremely small rates of these processes do not allow their quantitative measurement under terrestrial conditions; they can only be calculated by theory, with information derived from the more-complex three-nucleon system. MuSun plans to determine the rate Λ_d of muon capture on the deuteron to 1.5%, where Λ_d denotes the capture rate from the doublet hyperfine state of the muonic deuterium $1S$ state. Current experiments are at the 6-10% level and the most precise one disagrees with the latest 1% theory calculation by more than 3-sigma. The LEC will be determined at the 20% level, i.e. 5 times better than what is presently known from the two-nucleon system.

The MuSun experiment, shown in Fig. 4.1-1, uses the so-called "lifetime method". The disappearance rate, $\lambda_{\mu d}$, of negative muons in an active deuterium target is measured. The capture rate is then determined as the difference $\Lambda_d \approx \lambda_{\mu d} - \lambda_{\mu^+}$, where λ_{μ^+} is the precisely known positive muon decay rate[1]. Muons pass through the entrance detectors to stop in a deuterium target TPC. Decay electrons are detected in two cylindrical wire chambers and a 16-fold segmented scintillator array. The lifetime is

*Presently at Helion Energy, Redmond, WA.

[1] V. Tishchenko et al., *Phys. Rev.*, D87(5):052003, 2013.

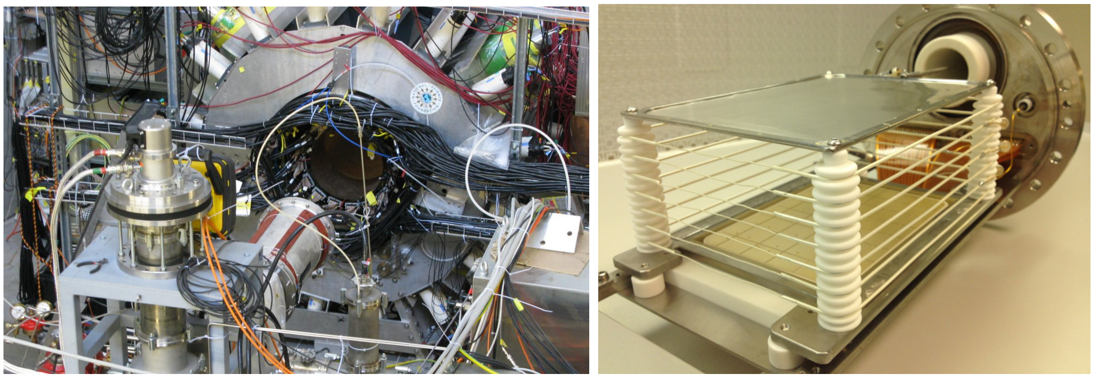

Figure 4.1-1. MuSun detector. *Left*: detector overview, showing cryosystem, TPC vessel and electron detector. *Right*: cryogenic-time projection chamber developed at CENPA.

determined from the measured time difference between the fast muon entrance detector and the decay electron scintillator array.

A key aspect for achieving the required precision was the development of a new cryogenic high-density TPC operating with ultra-pure deuterium. Three dimensional tracking in the TPC eliminates most muon-stops in wall material. Muon transfer to impurity elements, where capture occurs with a much higher rate than in deuterium, is suppressed by keeping the gas contamination at the 10^{-9} level. The target conditions (T = 31 K and density 6.5% of liquid-hydrogen density) are optimized to allow an unambiguous extraction of Λ_d, independent of muonic atomic-physics complications that occur after muons stop in deuterium, such as dd-fusion reactions catalyzed by the muons[1]. The high gas density implies that the cryo-TPC has to be operated as an ionization chamber without signal amplification in the gas and that drift voltages of 80 kV are required.

After final hardware upgrades MuSun collected the full statistics of 1.4×10^{10} events in two main production runs R2014 and R2015, followed, in 2016, by a shorter systematics run. MuSun is a high statistics/high precision experiment, which needs supercomputer resources to analyze the several hundred TB of primary and processed data (provided by an XSEDE[2] grant). The UW team led the development of the staged analysis framework and maintains it. We upgraded the MuSun Monte Carlo to a well-tuned and indispensable analysis tool, and run large production sets (D. Prindle). The analysis of the high quality R2014 data is well documented in the Ph.D. thesis of R. Ryan, March 2019, which provides the most comprehensive report on the MuSun experiment. Expanding on this work, we have fully developed a data driven approach to constrain one of the most difficult systematics, the so-called *fusion interference* caused by the overlap of muon-catalyzed fusion events with the incoming muon track in the TPC, and applied it to both R2014 and R2015. This analysis is supported by large scale

[1] P. Kammel and K. Kubodera, *Ann. Rev. Nucl. Part. Sci.*, 60:327–353, 2010.

[2] The Extreme Science and Engineering Discovery Environment is supported by the National Science Foundation.

Monte Carlo simulations which, after adapting our production chain to the new Rocks cluster at CENPA, reach a simulated statistics commensurate with the full statistics of the experiment. A highlight of last year was the unblinding of the μ^+ dataset collected in MuSun. The good agreement found with the muon lifetime, measured with the dedicated MuLan experiment mentioned above, verifies essential aspects of MuSun's technique and is encouraging towards the final analysis of the ten-time higher statistics of negative muon data, which determines the muon capture rate. Up to now, MuSun has mainly used its scintillator barrel for electron detection, without fully employing its electron tracking detector. Although the tracker allows for directional cuts and can dramatically reduce beam related background, some aspects of this more complicated detector system were not fully understood. During last year, E. Muldoon largely resolved these issues and developed an improved version of the tracking code. This will provide an additional powerful tool to investigate subtle systematic effects.

4.2 Fusion Interference

D. W. Hertzog, P. Kammel, E. T. Muldoon, D. J. Prindle and R. A. Ryan*

One of the most challenging systematic effects in the MuSun experiment is a slight misreconstruction in the TPC which can occur when the incoming muon track overlaps with those of nuclei produced by muon-catalyzed fusion. We call this systematic *fusion interference*. After the muons stops in D_2, there is a ∼6% probability for formation of a muonic molecule $dd\mu$, which spontaneously fuses its deuterons into the two branches (^3He+n) or $(p+t)$ with an energy release of several MeV. The time distribution of the sequence - fusion followed by muon decay - differs from the purely exponential muon decay distribution (which includes all events regardless of the occurence of a fusion process). Thus, reconstruction losses which apply only to events with fusions have to be kept small or corrected for, as a 1% loss of those events corresponds to a 6 Hz systematic shift of the $\mu + d$ capture rate Λ_d extracted from MuSun.

The main cause for misreconstruction is illustrated in Fig. 4.2-1. After the muon stops, the created electron cloud drifts down to the anode with $v_d = 5\,\text{mm}/\mu s$. If a fusion product is emitted shortly after the muon stopped, its track can overlap with the drifting electron column, thus generating an apparently contiguous track when arriving on the anode reconstruction plane. The most dangerous recoil is the 3 MeV proton from $(p+t)$, as it has a long range of 13 mm, just short of the TPC's pad size. In this case, the tracking algorithm can erroneously add the proton track to the muon track. If that happens at a fiducial volume boundary, the muon stop point can be reconstructed outside, even if the true stop lies inside the fiducial boundaries. Applying fiducial volume boundaries on the muon stop is a key part of the experiment, to suppress stops in wall materials. There capture proceeds with much higher rates than in deuterium, which has one of the smallest known capture rates among all elements.

*Presently at Helion Energy, Redmond, WA.

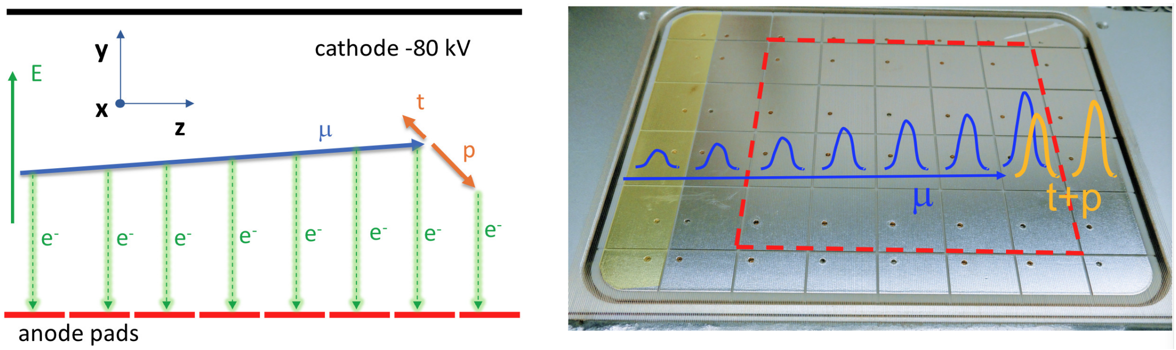

Figure 4.2-1. *Left*: A fusion process, following a muon stop, can overlap with the drifting electron cloud from the muon, resulting in a joined muon-fusion track. *Right*: Sketched signals on top of the real TPC grid and anode pads illustrate how the combined track can be misreconstructed outside of the fiducial plane (red dashed rectangle). The first row used for shaping the muon stop distribution is shaded in yellow.

The CENPA group invested significant effort in optimizing the tracker to be less prone to these errors. Nevertheless corrections are required. Although a full MC simulation of the experiment has been developed by D. Prindle and others, because of subtle differences between data and simulation model, data driven correction methods were developed. As the TPC volume is of rectangular shape, fusion losses can occur on all boundaries in X (horizontal), Y (vertical) and Z (beam direction). However, basic understanding as well as detailed simulations indicate that the dependence of these losses on the fusion time is nearly independent of the boundary at which they occur. Thus the systematic time shift is simply proportional to the number of fusions lost at a particular geometry defined by analysis cuts. The cut dependence of the number of fusions per muon is measured precisely with the high resolution TPC. Alternatively and more directly, albeit at as loss of statistical power, one can directly fit the time distribution for different analysis cuts to estimate the impact of the various boundaries.

The question remains, how one can vary the analysis cuts to study different fiducial boundaries, given the relatively spread out muon stopping distribution. The first TPC row, which intersects the incoming muon beam, provides a powerful tool for those studies (c.f. R. Ryan's Ph.D. thesis). The signals in this row are protected from fusion interference, as only stops starting with the 3rd row are accepted in the main analysis and fusion protons from those stops cannot reach the first row. This allows for shaping the muon stopping distribution in X and Y by cuts on X-pads and drift time, respectively, and in Z by dE/dx requirements on the first row. Thus the strategy is to change the muon stop distribution in one dimension, while keeping the other dimensions unchanged. That works very well as shown by the examples in Fig. 4.2-2. Because the muon distribution is narrowed only in one dimension at a time, sufficient statistics remain for meaningful fits.

We plan to further suppress fusion interference by removing fiducial volume cuts

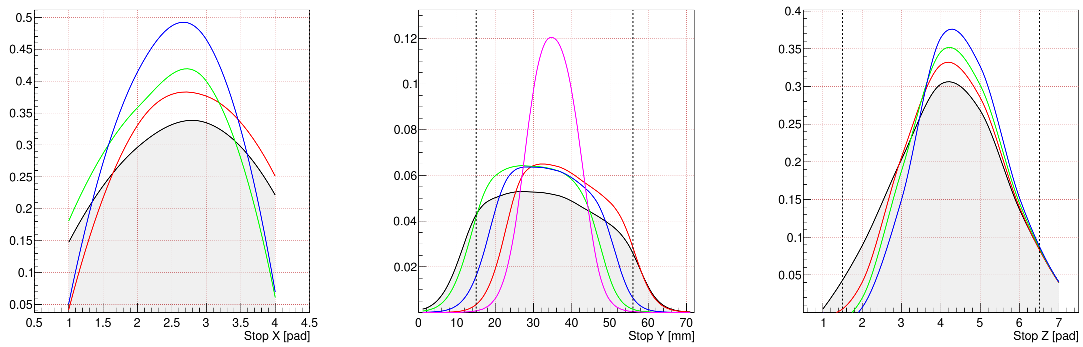

Figure 4.2-2. Normalized stopping distributions in X,Y and Z shaped by cuts on the first TPC row. As examples, the center panel shows how the vertical stopping distributon can be shifted or narrowed to reduce the muon population close to the fiducial boundaries, while in the right panel muon stops are reduced at the chamber entrance (Z=2) while keeping the exit population at Z=7 constant. The gray shaded area indicates the nominal cuts used in the final analysis.

in X and Z downstream, where there are mainly thin potential wires in the muon's pass. The small fraction of muon capture on these elements can be monitored and corrected for based on observed capture neutrons, as developed by E. Muldoon. While discrepancies between the various methods at the sub-percent level cannot be avoided, the combination of all these method should allow us to finalize these corrections and assess their realistic error, which currently is estimated to be below 10 Hz.

4.3 Electron tracking in MuSun

D. W. Hertzog, P. Kammel, E. T. Muldoon, D. J. Prindle, and R. A. Ryan*

The MuSun experiment has two separate detector systems for monitoring decay electrons. The electron scintillators (eSCs) are a barrel of sixteen scintillator bars which provide the precise timing needed for the experiment. The electron proportional chambers (ePCs) are a pair of concentric cylindrical wire chambers which detect the electron position and allow for reconstruction of the electron track. In principle the eSCs alone are sufficient for the MuSun lifetime measurement, and much of the preliminary MuSun analysis uses this approach. However, without the directional information of the ePCs there is a relatively high sensitivity to background beam electrons, which have a somewhat complicated time dependence of their own[1]. As we work towards a final result, we would like to use the ePC tracking to ensure we select clean decay electrons and

*Presently at Helion Energy, Redmond, WA.

[1]CENPA Annual Report, University of Washington (2019) p. 93.

greatly reduce the sensitivity to beam backgrounds. Several additional systematic issues may also be addressed using the additional directional information, including wall stops and fusion interference.

Incorporating the ePCs into the analysis has been a longstanding challenge, producing a large shift in the observed lifetime relative to measurements with the eSCs alone. The bulk of this discrepancy has now been traced back to an early cut in the low-level electron tracking code which attempted to detect sparks in the wire chambers by looking for large numbers of wires being triggered. A bug in the application of this cut led to the time-dependent deletion of electron track information without effecting the eSCs or the rest of the event, naturally causing a large distortion in the observed lifetime. However, further examination revealed that a smaller discrepancy still occurs even after re-implementing this spark flag correctly, with ePC cluster size somehow correlated with the lifetime. This issue as well as other concerns about the reliability of the low-level electron tracking prompted a thorough code review and re-write.

Each ePC consists of a set of anode wires sandwiched between two cathode layers. The first phase of analysis treats these layers separately, grouping nearby wire triggers into clusters. The most obvious challenge in this step comes from pickup in the pre-amps which can produce a feedback loop causing continuous ringing in either an individual wire or an entire sector of sixteen wires sharing a pre-amp card. This ringing can last for tens of microseconds and makes it impossible to determine whether there were any real hits on those wires. An extra pre-processing step has been added to detect these periods and filter them out, removing around one percent of events. Improvements have also been made to how wires are assigned to clusters to minimize sensitivity to noise in unrelated wires.

Another challenge is how to handle abnormally large clusters, given that cutting them has undesired time dependent effects. However, these large clusters are not well localized and cause problems for the tracking if they are not removed. While extremely large clusters are rare, to reach the MuSun precision goal we must be very careful to avoid introducing any time dependent bias. To solve this problem, clusters above a size threshold are subdivided until all clusters fall below the threshold. This fragmentation procedure allows later tracking phases to select the sub-clusters which are most consistent with the other electron detectors, reflecting the uncertainty in position. There is also the added benefit of potentially separating pairs of real electrons which are close enough to be clustered together. Information about the size of the clusters is saved to allow for more sophisticated studies later on.

The second analysis phase involves matching clusters from each of the three wire planes. Because the planes are arranged at different angles, their overlap determines the positions of ePC hits in the Z and ϕ dimensions. Ideally all hits should be triple coincidence with overlapping clusters from all three planes, but about five percent of the matches only have two planes. Many of these are due to particularly noisy wires which were masked out at a hardware level to avoid overwhelming the DAQ, leaving areas which can never see triple coincidences. The tracking code has now been made aware of this masking, and will check whether two fold coincidences overlap with masked regions. Other changes to this step mainly involve somewhat looser cuts and being careful to accept all cluster combinations as possible hits rather than making any assumptions.

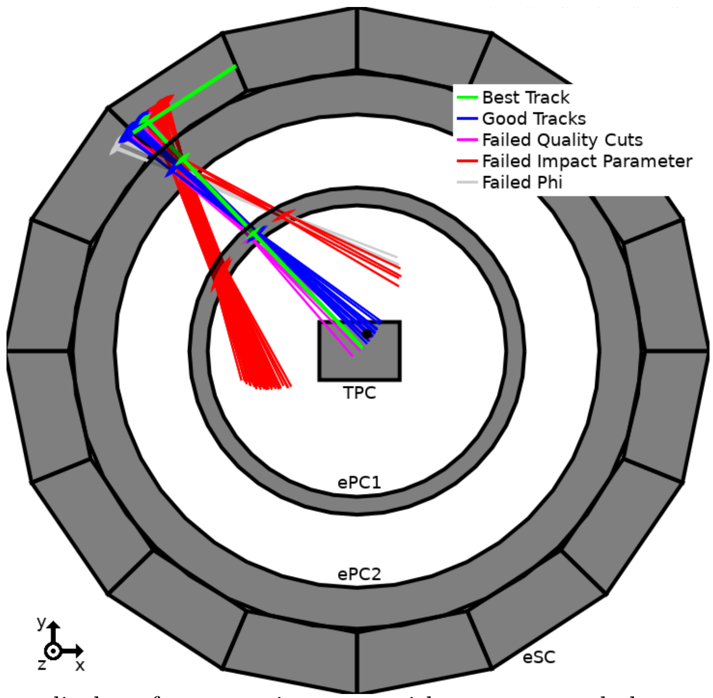

Figure 4.3-1. Event display of a rare noisy event with reconstructed electron track candidates, color coded by track quality. The main detectors involved in the reconstruction are the TPC, electron tracking chambers (ePC) and the scintillator barrel (eSC).

The last stage of the analysis forms tracks in 3D using hits in the two ePCs and the eSCs. The basic strategy here is to first make tracks out of every plausible combination of ePC hits, and then find the best matching track for each eSC hit. Originally this simply used the angular agreement with the eSC, but this is not very useful in distinguishing tracks intersecting the same scintillator panel. The new cluster fragmentation and looser cuts produce some rare events (such as the one in Fig. 4.3-1) with up to hundreds of track candidates, requiring a more sophisticated selection algorithm. Several criteria are now used, including the agreement with the eSC in angle, Z position, and time, the proximity to the beam axis, and cluster quality information from the previous analysis stages. These cuts are all calibrated to be rather loose, as shown in Fig. 4.3-1 where clearly spurious tracks are rejected but most of the central group are accepted as good tracks.

Finally, a second strict filtering step reduces the remaining tracks to a single best track. In order to check if the choice of best track has inadvertently introduced some bias, we actually produce several best tracks with alternate criteria. Verifying that the lifetime is insensitive to the precise electron definition is an important consistency check and will help demonstrate the reliability of the new tracking scheme. In addition to making the tracking more reliable, this update also makes new information about the cluster size and quality available in the analysis output, allowing us to study their effects on the lifetime fits and any correlation with other parameters. A full analysis pass is currently underway, and we will soon see the first high statistics results using the revised tracking.

4.4 Monte Carlo framework and studies

D. W. Hertzog, P. Kammel, E. T. Muldoon, D. J. Prindle, and R. A. Ryan*

We have previously described the MuSun Monte Carlo[1] and running large samples on the cenpa-rocks cluster[2]. In brief, we have a detailed `Geant` description of the MuSun detector. We generate one muon at a time according to the beam profile. The Monte Carlo has a complete desciption of μ^- kinetics in deuterium including $\mathrm{dd}\mu \rightarrow \mathrm{p} + \mathrm{t} + \mu$ (pt fusion) which happens for about 3% of events. The `Geant` output is passed through a detector response program producing raw data output which is then analyzed by the standard MuSun analysis chain producing lightweight trees used for the final lifetime analysis. When running on the cenpa-rocks cluster we run the chain in sequence, storing all files locally on each node to minimize network usage and saving only the lightweight tree and log files to permanent storage. A typical job takes about a week of real time resulting in 3.5×10^9 fiducial volume muon stops. The saved output takes about 13 TB of storage space that we copy to the ranch.tacc.utexas.edu tape archive, keeping the lightweight trees (3 TB) on local disks for analysis on cenpa-rocks. The 2014 and 2015 data taking runs collected 10^{10} fiducial volume stops. Generating that many Monte Carlo events takes about three weeks of real time.

In one recent Monte Carlo analysis we characterized pt fusion mergers with the muon track. The muon ionization drifts downward at 5 mm/μs and, if a pt fusion happens early enough, our clustering algorithm merges it with the muon cluster. This is important because a merged pt fusion can change the reconstructed muon stop position, sometimes moving it across a fiducial volume boundary. This will change the measured muon lifetime; we need to characterize the pt migration effect at the 10^{-3} level to have an acceptably small change in the muon lifetime. In Fig. 4.4-1 we show the pt fusion time for all events (green line in left panel) and the subset of events in which the muons stops are migrated into the fiducial volume from downstream (blue line). It is easier to see the time structure of the migration events by taking the ratio, which we call the η function, shown in the right panel. When the pt fusion happens in the first $\sim 2\mu$s our clustering algorithm always merges the pt and muon clusters while if the fusion happens after $\sim 5\mu$s the clusters are never merged. For intermediate times

*Presently at Helion Energy, Redmond, WA.

[1] CENPA Annual Report, University of Washington (2018) p. 79.
[2] CENPA Annual Report, University of Washington (2019) p. 95.

the merging depends on the proton (with a range of 13 mm) or triton (range of 0.8 mm) travelling downward and catching up with the muon ionization.

PT induced upstream migration happens when the proton or triton crosses the pad row boundary and merges with the muon ionization, giving the upstream pad ("stop pad") enough energy to be tagged as a stopping muon. We find the η function depends on the muon track slope $Y' \equiv dY/dZ$. The latest fusion that can merge does so with the highest Y of the track in the "stop pad". For upward going muons, $Y' > 0$, this highest point is at the downstream edge of the "stop pad" which is close to the actual muon stop Y. For $Y' < 0$ the highest point is at the upstream edge of the "stop pad" and the Y difference between this point and the muon stop depends on the muon track slope. The pt fusion can be delayed by the drift time corresponding to $\delta Y = \delta Z \times Y'$ and still merge. This is shown in Fig. 4.4-2 where we plot the η function for three narrow ranges in Y'. Tracks near maximum Y' (blue) are close to the same as tracks with $Y' = 0$ (red). In contrast tracks with $Y' < 0$ (green) extend to sginificantly later times. In the left panel we show the η functions while in the right panel we see that we can charcterize each function with three times; the time there is always a merger, the time the triton causes a merger, and the time the proton causes the merger.

To make use of this analysis with real data we replace the use of pt truth information with an energy cut selecting muons with overlapping pt. In Monte Carlo data the two are interchangeable but the energy cut can be applied to data. To determine lifetime sensitivity to pt fusion migration we remove various fractions of fusion events matching the expected slope distributions of the migration events. Applying this to real data we can calibrate the sensitivity of our lifetime determination due to fusion induced muon migration.

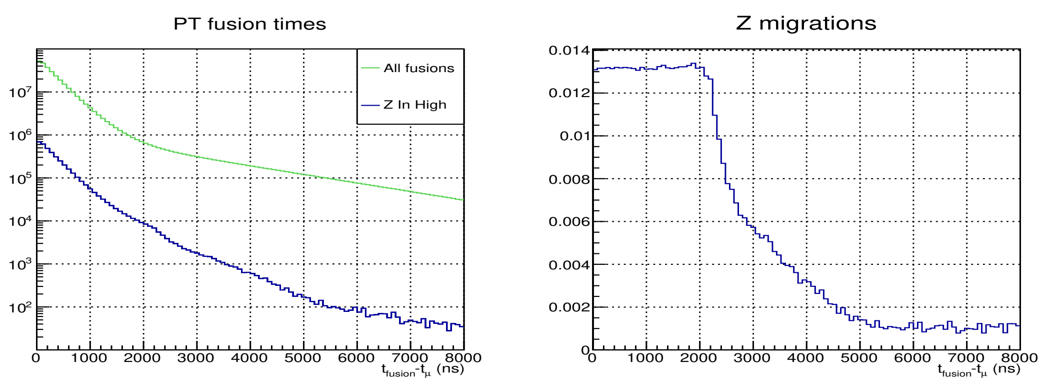

Figure 4.4-1. The left panel shows the fusion time for all pt fusions (green) and for events migrating into the fiducial volume from downstream (blue). The right panel right shows the ratio. For the first $\sim 2\mu$s the pt and muon are always merged and after $\sim 5\mu$s they are never merged. At intermediate times merging depends on the proton and triton directions.

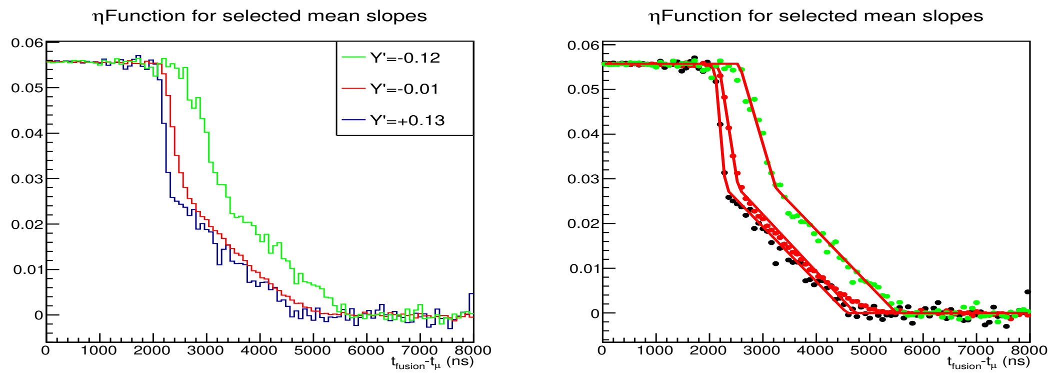

Figure 4.4-2. The left panel shows the angular dependence of pt fusion merging. We have scaled the vertical axis to compare shapes more easily. We determine the slope of the muon, $\mathrm{Y}' = \mathrm{dY}/\mathrm{dZ}$, using the reconstructed muon track, and the fusion time from the Monte Carlo truth information. We find that all muons with $\mathrm{Y}' > 0$ have a very similar time dependence but for $\mathrm{Y}' < 0$ it takes longer to separate fusions from the muon track. The panel on the right shows how we can characterize the merging fractions.

4.5 Measuring the positive muon lifetime with MuSun

D. W. Hertzog, P. Kammel, E. T. Muldoon, D. J. Prindle, and R. A. Ryan*

In each of the 2014 and 2015 data collection periods, an additional week of data was taken with the beam polarity reversed. A total of 1.2×10^9 positive muon-positron pairs were collected in 2014, and an additional 1.5×10^9 were collected in 2015. Besides serving as a consistency check by comparing the unblinded result to the μ^+ lifetime, which has been well measured by the MuLan collaboration, complicated systematics such as muon catalyzed fusion are not present with positive muons and the data can be used to study more subtle effects.

One challenge which is absent in the negative muon data but must be considered with positive muon data is muon spin rotation (MuSR) effects. Positive muons which stop in the TPC do not undergo capture, and decay via

$$\mu^+ \rightarrow e^+ \nu_e \bar{\nu}_\mu. \tag{1}$$

In the case of the $\pi E1$ beamline at PSI, the muons are strongly polarized in the direction of the beam, designated as the Z-direction. Due to parity violation in the weak interaction, the positrons emitted after the decay are strongly correlated to the muon spin. In the presence of any magnetic field, the muon spin will precess leading to a time dependent observation of positron intensity for a given detector location. In order to better quantify this effect, MuSun employs saddle coils on either side of the TPC to apply a fixed magnetic field of approximately 40 Gauss in the X direction. The geometry of the eSC hodoscope relative to the applied MuSR field can be seen in figure Fig. 4.5-2. Primarily, the magnetic field from the saddle coil is applied in the positive X direction, perpendicular to the muon polarization in Z. This transverse field effect is expected to dominate. However, any small polarization along the X axis due to misaligned beam elements, or a slight misalignment of the field coils could also lead to a precession in the plane perpendicular to the beam direction, referred to as a longitudinal effect.

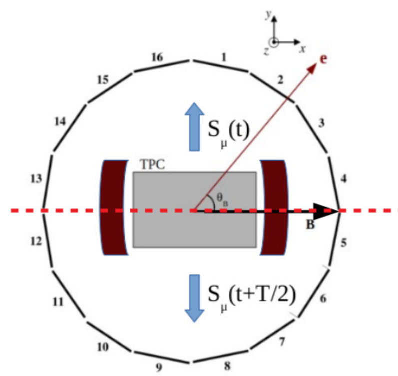

Figure 4.5-1. Cross section of the MuSun eSC hodoscope looking upstream. The muons arrive predominantly polarized in the Z direction, coming out of the page. The spin direction shown in blue precesses in the Y-Z plane, and flips every half period, denoted by T above. The red dashed line separates the upper and lower halves of the detector.

The effect of MuSR on the decay histograms is enhanced in asymmetry histograms, created by looking at the difference in counts versus time for specific detector halves. The difference in the number of counts versus time in the upper (segments 4-13) and lower (segments 5-12) halves is used to quantify the transverse MuSR effect, and can be seen in figure Fig. 4.5-**??**. A fit of this histogram, shown in red, quantifies the frequency and relaxation of the MuSR oscillation.

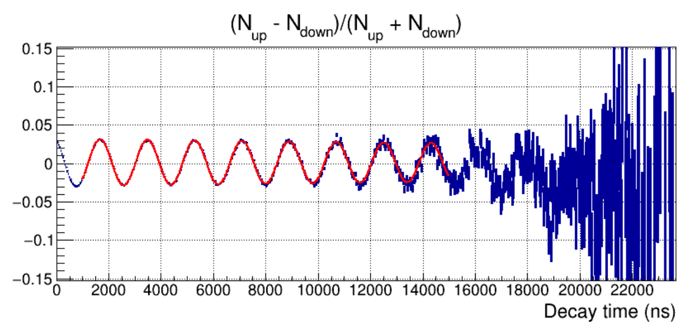

Figure 4.5-2. The number of counts in the upper and lower halves of the eSC hodoscope, as depicted in Fig. 4.5-2, versus time normalized to the full decay distribution enhances the transverse MuSR effect. The fit, shown in red, is used to extract the MuSR oscillation frequency and relaxation.

This fast periodic oscillation is present in any lifetime histogram, but is easily decoupled from the exponential component of the fit. The effects of the transverse field are accounted for by including sinusoidal terms with the frequency and relaxation parameters established above in the full $\mu+$ fit function. A similar asymmetry histogram, comparing the left and right halves of the detector, is used to quantify the longitudinal MuSR effects. An unexpectedly fast longitudinal relaxation is observed, which is likely related to muonium formation but is not fully understood. Unlike the transverse effect, this longitudinal component does not easily decouple from the exponential fit. However, the effect of this longitudinal relaxation on the final lifetime fits was studied in detail, and ultimately a larger systematic error was applied to account for this effect.

Systematic sources of error also present in the μ^- datasets, including electron track interference and a time dependent background, were also quantified. As a final consistency check, scans of the fit parameters as a function of eSC segment, electron Z position, muons stop position within the TPC, and fit start time, were used to check the robustness of the fit and the final results.

After the detailed analysis of both μ^+ datasets with a hardware and software blinding offset applied had been completed and all sources of statistical and systematic error had been quantified, the data was unblinded. The software offset allowed for the unblinding of the μ^+ dataset without unblinding the full μ^- datatset. The difference between the rate obtained and PDG value is shown for each dataset and the combined final result in figure Fig. 4.5-3. The final combined result differs from the PDG value by $14\,s^{-1}$, within the allowed uncertainty of $22\,s^{-1}$. This consistent result is an important step toward unblinding the full MuSun μ^- datasets.

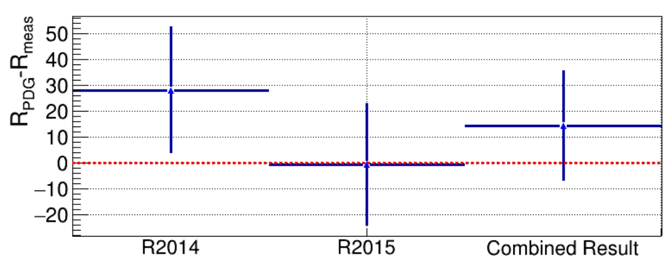

Figure 4.5-3. Comparison of the unblinded mu+ rates for each MuSun dataset and the combined result. The Y axis displays the difference between the obtained rate and PDG value. Both datasets and the combined result are consistent with the PDG value within error.

g-2

4.6 Overview of the Muon $g-2$ experiment

H. Binney, M. Fertl, A. T. Fienberg, A. García, J. B. Hempstead, D. W. Hertzog, Z. Hodge, P. Kammel, J. Kaspar, K. S. Khaw, J. LaBounty, B. MacCoy, R. E. Osofsky, and H. E. Swanson

The Muon $g-2$ experiment is in a most active period of its life cycle. We have been simultaneously taking data 24/7 throughout the long, yearly Fermilab accelerator operations calendar, analyzing the last aspects of the Run-1 data set and preparing publications, starting production and analysis for Run-2, developing preliminary work for the Run-3 analysis, and working on summer 2020 upgrades and special beam-off measurements. Our group remains central to this work, as will be evident in various accompanying articles to this Chapter. Here, we highlight UW efforts, but emphasize that the $g-2$ Collaboration has approximately 200 members who are working creatively and with dedication toward the overall success of determining the muon's anomalous magnetic moment to very high precision.

At the time of this writing, Run-3b, along with all Fermilab accelerator operations, was abruptly terminated owing to the COVID-19 crisis. At that time, the data being collected were in rather ideal conditions. In particular, the recently upgraded kicker was, for the first time, finally capable of centering the incoming muons within the magnetic storage ring volume. J. Kaspar and CENPA shops played a vital role in this success. We have also helped understand a most peculiar transient magnetic field perturbation that occurs every time the electrostatic quadrupoles are energized just prior to beam arrival. The effect reduces the magnetic field within the quadrupole regions and, if unaccounted for, could lead to an incorrect deduction of the anomalous magnetic moment, a_μ, which is inversely proportional to the measured magnetic field. The transient effect was only able to be noticed because of the electronics developed at CENPA that allows for synchronizing the pulsed NMR probe DAQ sequence with respect to timed accelerator operations. E. Swanson was critical in developing a model of the transient field effect and, together with Kaspar and other $g2$ collaborators, they mapped the effect in the storage ring to enable a correction and establish an uncertainty well enough for publication of the Run-1 data. The work will continue in the coming summer to improve the mapping and to possibly develop a mitigating fix. Interestingly, this same effect was present – but unnoticed – at Brookhaven during the E821 experiment. Fortunately, our estimates of its impact on a_μ for them, and for us, are relatively small.

One of the most intriguing systematic challenges we have in Run-1 was driven by the fact that 2 out of 32 HV resistors in the quadrupole system exhibited RC time much longer than the $5\,\mu$s design. This led to a slower-than-planned rise to full voltage of the quadrupole plates and caused the beam vertical mean and RMS to move slightly during storage. As co-led by K.S. Khaw (now a professor at Shanghai), such a beam motion can introduce a phase shift owing to a correlation in between phase and detector acceptance inside the storage volume. If unaccounted, it can lead to an incorrect extraction of a_μ from the measured precession frequency, ω_a. This is the largest remaining systematic uncertainty we are evaluating and a tremendous amount of work has been done by many people in the collaboration to understand the effect. The good news is that the resistors were replaced prior to Run-2 and Run-3, so the problem naturally has gone away.

These "bad resistors" had one more important consequence. The Run-1 muon loss rate, defined as muons that escape the ring during the nominal measuring period, was 10 times higher than in Run 2 or Run 3. The case, again, is believed to be the unstable beam spatial distribution, and also possibly a strong radial field. H. Binney led a data-driven and analysis campaign to measure the effect on a_μ. She describes this work in a separate article where the conclusion is that there is only a net small perturbation to the muon precession frequency from this effect in Run 1.

J. Hempstead has begun detailed analysis of the Run 2 precession frequency including, along with others in our group, much of the behind-the-scenes calibration and data-base work required to initiate the physics production pass. He developed the calibration methods critically required for all data analyzers. The first look at Run-2 precession data looks quite good. The well-behaved data were obtained under better conditions compared to Run 1. There are many subtle systematics in Run 1 and he has completed a variety of studies to help in the phase-dependent acceptance and for the ongoing question of the need for a subtle residual gain (or slow) term effect in the precession analysis. One interesting detector effect, is how do the detectors respond to two nearly adjacent pulses in time? In a report herein, you will learn of a nice laboratory setup to study this effect.

Two reconstruction programs are used to process the precession data. J. LaBounty completed a detailed study comparing UW's Recon-West (RW) to Cornell's Recon-East (RE) on an event by event basis, thus teasing out small differences and leading to an overall greater confidence in the analysis. These reconstruction methods are central to all event-based analyzers groups. He also has been studying calorimeter and tracker coincident events, another critical check on how the instrumentation performs and reports results.

B. MacCoy's IBMS system is now complete. As described in a separate article, it images the incoming beam as the accelerator operators try to thread it through the back leg of the storage ring, and through the very narrow corridor of the inflector magnet. The IBMS system – now consisting of 3 imaging planes – provides a spatial and temporal snapshot at the entrance to the storage ring, just in front of the inflector, and at the exit from the inflector.

Newly arrived Postdoctoral Scholar Z. Hodge started work at Fermilab helping with operations, and then taking on the challenges of upgrading the MIDAS DAQ to its next version (mandated by an overall linux version upgrades at Fermilab). He has also been working on Tracker-Calorimeter matching as he begins to explore the large $g-2$ data set and its analysis possibilities.

Finally, here we mention the exceptional work done by our recent Ph.D. recipients A. Fienberg and R. Osofsky, who analyzed the Run-1 muon precession frequency (ω_a) and the average magnetic field (ω_p), respectively. Both of them developed significant analysis software and led teams of analyzers in the Run-1 data sets. Their pioneering work is being built on by others. They are both now in new positions elsewhere conducting exciting research.

Experiment and Collaboration

Before turning to the technical aspects of $g-2$, we remind the reader of the physics motivation and basic experimental technique. Muon $g-2$ is a special quantity because it can be both measured and predicted to sub-ppm precision, enabling the comparison to be a measure of possible New Physics: $\Delta a_\mu^{\rm New} \equiv a_\mu^{\rm Exp} - a_\mu^{\rm SM}$. As a flavor- and CP-conserving, chirality-flipping, and loop-induced quantity, a_μ is especially sensitive to new physics contributions[1]. The $g-2$ test compares measurement to the Standard Model prediction, so the question is, "what is the SM prediction?". To that end, a world-wide group of theorists has been actively working together to develop a recommended SM value, incorporating the many approaches and data set inputs to determine the critical hadronic contributions. In September, (DH) co-hosted the most recent Workshop of this group, which was held at UW's Institute for Nuclear Theory. A White Paper is forthcoming with the summary recommended[1] SM value, along with supporting chapters.

For the time being, we quote the most recent SM update[2] which gives

$$\Delta a_\mu^{\rm New} = [270.5 \pm 72.6] \times 10^{-11} \quad 3.7\,\sigma. \tag{1}$$

The persistent discrepancy between experiment and theory continues to fuel speculative models of new physics. While tension exists with respect to many of the most popular interpretations such as supersymmetry (SUSY) for which no evidence has been seen, there remain many new-physics scenarios. Some can address the muon anomaly and suggestive additional experimental "anomalies", such as the $g-2$ for the electron – now in opposite sign discrepant to the SM – and various lepton universality violation indications from B-mesons decays.

[1]http://www.int.washington.edu/PROGRAMS/19-74W/

[1]A. Czarnecki and W. J. Marciano,"The muon anomalous magnetic moment: A harbinger for new physics,"Phys. Rev. D **64**, 013014 (2001); D. Stockinger, "The Muon Magnetic Moment and Supersymmetry," J. Phys. G **34**, R45 (2007).

[2]A. Keshavarzi, D. Nomura and T. Teubner, Phys. Rev. D 97, 114025 (2018)

The muon anomaly is proportional to the ratio ω_a/ω_p, where ω_a is the anomalous precession frequency of the muon spin in a magnetic field and ω_p is a measure of that average magnetic field determined using proton nuclear magnetic resonance (NMR).

Our UW group is involved in the ω_a and the ω_p measurements, and in critical beam-dynamics systematic studies. We have designed and built a significant array of hardware tools and reported on these in previous Annual Report articles and in many technical publications. During the past year, we have distributed the UW work to maintaining and improving our hardware and software contributions to the experimental operations tasks, while focusing the rest of our efforts on the analysis of the Run-1 data and preparations for Run-2 analysis (where major changes to the offline software were needed).

The E989 Collaboration exceeds 200 collaborators, drawn from more than 30 institutes in 7 countries. D. Hertzog continues as Analysis Coordinator. K.S. Khaw transitioned from Co-Coordinator of the six Precession Analysis efforts to co-leading the Phase-Acceptance Task Force. A. Fienberg led our precession analysis and R. Osofsky led the "Bloch" Field Analysis. As mentioned, J. Hempstead served as Detector Coordinator throughout Run-2. Those duties are being shared this year by a rotation of H. Binney, J. LaBounty, and B. MacCoy. We discuss the three major working areas within the $g-2$ Collaboration's analysis organization: Beam Dynamics, Field, Precession below. Our group is involved in all of these teams at various levels.

The work of the Beam Dynamics team begins with understanding the muon beam delivery into the storage ring, then moves to characterizing the beam's storage properties. B. MacCoy, who built three precision hodoscopes that image the beam as it enters the storage ring, has worked closely with simulation experts to help tune the incoming beam for optimal storage. Her detectors provide a real-time view for upstream accelerator operations that ensure stable conditions. As mentioned, J. Kaspar, following his stints as Run Coordinator and otherwise storage ring hardware expert, worked to improve the three kicker systems. The focus was on a redesign of the HV feedthrough and cabling system, both which had limited performance owing to sparks and cable burnout. The improvements were finally realized recently in the second half of Run-3, a milestone moment with stored, centered beam. Many members of our group have been working in the analysis aspects of Beam Dynamics, related to Run-1. This includes H. Binney's work on Muon Losses and significant work by many of us on the ongoing Phase-Acceptance systematic study. D Hertzog has been leading the writing of a comprehensive Beam Dynamics Systematics paper to accompany the anticipated Run-1 PRL in the coming months.

The Field team is divided into two groups that track the field 24/7 between trolley runs, where the entire field is measured *in situ* every few days. Magnetic field measurements involve mapping the storage volume field every few days with a measurement trolley calibrated by an absolute water probe and transferring that calibration to 378 fixed probes mounted outside the storage volume that are sampled every 1.4 seconds.

All measurements use high resolution pulsed proton NMR. Two teams named after distinguished NMR researchers Bloch and Purcell were formed and R. Osofsky took the lead in the Bloch team. The Bloch strategy was to pin the field seen by fixed probes to trolley values obtained as it passed by their locations and then evolve the field that would have been seen by the trolley at later times using differences in sequential fixed probe measurements. There were a number of challenges that had to be overcome. The trolley itself has a magnetic signature that affects fixed probe readings. Trolley measurements take of order two hours to complete and have to be corrected for field drift when averaging the field over azimuth. The geometry of fixed probes is not ideal for extracting a multipole decomposition of the field and in addition they incompletely sample the ring in azimuth. Each team met these challenges independently and developed their own analysis algorithms to interpolate the field between trolley runs. An un-blinded comparison of a small subset of Run-1 data gave the teams confidence they had each captured the essence of determining trolley equivalent field multipoles from fixed probe measurements. All of Run-1 has now been analyzed by both teams and recently unblinded, a continuous field map of the storage ring volume will be available to convolute with the muon distribution. In a bit of serendipity, at Rachel's thesis defense Statistics Department Professor E. Thompson questioned her use of a random walk model to describe the growth in uncertainty of the field interpolation following a trolley run and recommended using a Brownian Bridge instead. This builds in the condition that the uncertainty vanishes at the times of the beginning and ending trolley runs that bracket the measurement period. The covariance using this process is half of the variance given by the random walk model bringing the uncertainty more in line with our design error budget.

The Precession team for Run-1 consists of six quasi-independent analyses. Four are built from the UW-based West Coast reconstruction products that create positron time and energies from struck calorimeter crystals. A. Fienberg wrote this software and carried out the extraction of the muon precession frequency for all of the Run-1 independent data sets. These results were compared to others in a blinded fashion while individual groups improved their own studies. In February of 2020, a complete unblinding within groups was performed and, just like last year's sample unblinding, all groups presented consistent results with respect to one another. One of the remarkable features of the collective analyses is the small systematic uncertainties. Three different pileup methods had been developed and all indicated that the detectors, electronics, and analysis protocols would easily keep pileup well below the design goals. One of the more challenging problems was control of gain. Because the temperature varied significantly, and the SiPMs used to read out the crystal calorimeters were tied to ambient room air, real gains varied by up to 40% during Run-1. Given that the goal is to keep the day to day gains at 1% or better, and the in-fill early-to-late gain instability is required to be no worse than a few parts in 10^4, much attention was devoted to both the laser-based calibration system and to the gain-correction routines. The work has been successful, however, there remains a small mystery that could either be gain related or beam-dynamics related, which can introduce some 10's of ppb shift in the precession frequency if it is repaired by ad-hoc functions. We are working on this issue, even though it is well below the statistical uncertainty for Run-1, which is in the range of 400 - 500 ppb.

Going forward, we will be looking at Run-2 data soon to see how the bad resistor repair impacts various beam dynamics issues and possibly the need to add a slow residual change to the fit function, by gain or other means. In Run-3, the MC-1 building temperature system was finally brought up to the design specification and thus, with rock-stable temperatures for the first time, both the magnet stability and detector gain stability are much improved. That coupled to the fact that the muon distribution is finally stored centrally, is very promising for this much larger data sample.

In the articles that follow, the reader will find a variety of specialized efforts team members have led. It is but a small sample of the actual work accomplished of course, but should provide a flavor for the variety of UW work.

4.7 Phase-momentum correlation systematic uncertainty

H. Binney

Muons in the storage ring can hit aperture-defining collimators and lose momentum, spiraling inward. These lost muons are depleted from the storage ring before decaying. Some lost muons hit the calorimeters, passing through several in succession and depositing a well-known amount of energy in each one. A clean lost muon signature can be distinguished from the decay positron spectrum by requiring a triple coincidence in adjacent calorimeters with a known time separation and energy.

The triple coincidence spectrum does not contain an absolute lost muon scaling, because the calorimeter acceptance is unknown. The absolute scaling is instead derived from an ω_a fit, which includes a term to account for lost muons that multiplies the overall normalization so that

$$N_0 \to N_0 \left(1 - K_{loss} \int_0^t \exp(t^{'}/\gamma\tau_\mu) L(t^{'}) dt^{'}\right), \tag{1}$$

where K_{loss} is the scale parameter, $\gamma\tau_\mu = 64.4\mu s$ is the time-dilated muon lifetime, and $L(t)$ is the triples spectrum described above. The cumulative loss fraction, as determined in the UW analysis for the four Run-1 datasets is shown in Fig. 4.7-1.

Lost muons can induce a systematic uncertainty if the lost population has a different phase than the stored population. The basic form of the ω_a fit function is

$$N(t) = N_0 e^{-t/\tau}[1 - A\cos(\omega_a t - \phi)], \tag{2}$$

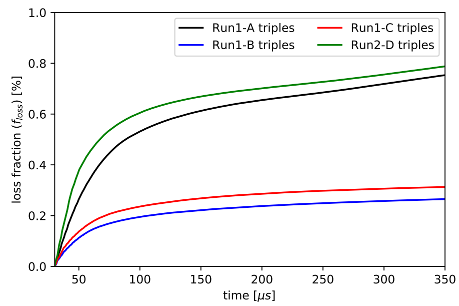

Figure 4.7-1. Preliminary cumulative muon loss fraction from the nominal 30 μs fit start time for each of the four Run-1 datasets. The curves are derived from the UW precession fit analysis.

where ϕ, the average spin phase at injection, is assumed to be a constant. If it is not constant, a Taylor expansion of $\phi(t)$ results in a shift $\Delta\omega_a = \frac{d\phi}{dt}$.

One possible way for lost muons to cause $\phi(t)$ is if there is a correlation between spin phase of the muons and their momentum, and if muons with a certain momentum are lost more often. This will result in a change over the fill to the average momentum of the stored muon population. A phase-momentum correlation is predicted in by end-to-end simulations, but because lost muons don't preserve any of their phase or momentum information when they are measured, the effect is not directly measurable in normal running conditions.

We were able to arrive at a data-driven approach to this systematic uncertainty. We took two sets of measurements: the first to determine the phase-momentum correlation empirically, and the second to map out the momentum dependence of the lost muons.

For the first measurement, we changed the field of the magnetic storage ring so that different portions of the incoming momentum distribution would be selected. Then, we performed a ω_a fit for each field setting to extract the phase. This allowed us to compute a phase-momentum correlation of $10 \pm 1.6 \frac{mrad}{\%dp/p}$. A comparison to simulation is shown in Fig. 4.7-2 showing good agreement.

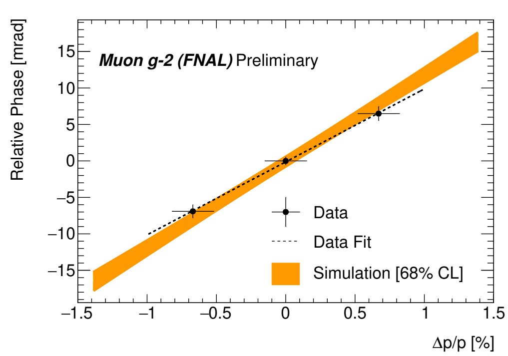

Figure 4.7-2. Comparison of the simulated and measured phase-momentum correlation.

The second part of the measurement involved using upstream collimators to select different portions of the momentum distribution and then measuring the lost muon spectrum for each distribution. The biased momentum distributions and some sample corresponding lost muon spectra can be seen in Fig. 4.7-3, where "1/5 CTAG low" means that the beam intensity has been reduced by 1/5, biasing the momentum distribution to the low momentum side. The triples spectrum plot indicates that high and low momentum muons are lost with different probabilities with time-dependent behavior throughout the fill. These 8 distributions were used to parameterize an analytical loss model function, whose form was motivated by simple simulation phase space studies. The black curve in Fig. 4.7-3 (left) is an example of a calculated loss probability function.

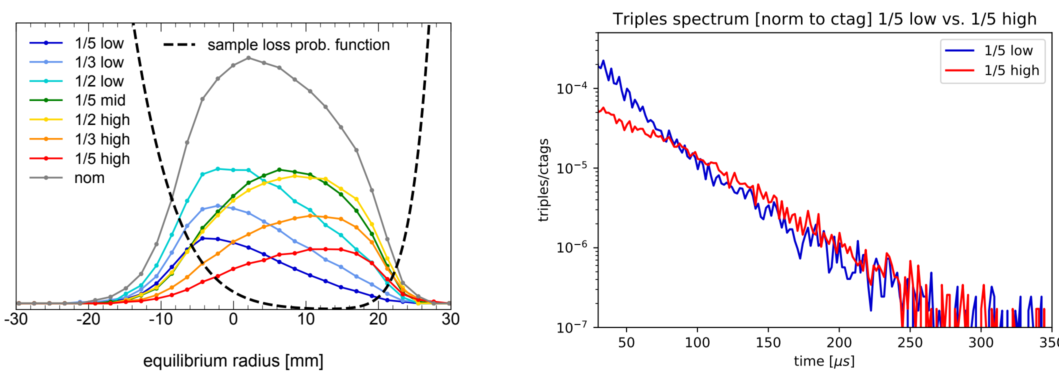

Figure 4.7-3. *Left*: measured momentum distributions, scaled to intensity, resulting from the use of upstream collimators to bias the distribution. The black dashed line is a sample calculated loss probability function. *Right*: Corresponding sample triples spectra for the most extreme momentum distributions showing that the lost muon behavior is dependent on momentum.

In practice, what is needed is a time-dependent muon loss probability function $l(t)$, which will be applied to the nominal momentum distribution to yield the time-dependence of the average momentum of the stored muons. That information is readily translated into the average spin phase of the stored muons, $\phi(t)$ using the phase-momentum correlation discussed above. $l(t)$ is determined by fitting the 8 distributions over an increasingly longer time range from the fit start time $t_s = 30\,\mu$s. At each time t, the fit is performed using 8 equations of the form

$$\int_{R_{min}}^{R_{max}} F(x)_i l(x,t)dx = \frac{1}{\mathrm{C_i}} \int_{t_s}^{t} \exp(t'/\gamma\tau_\mu) L(t')_i dt', \tag{3}$$

where i runs from 1 to 8 for each of the special runs. R_{min} and R_{max} represent the minimum and maximum possible radii of the stored muons. $F(x)_i$ is the measured intensity of the fast rotation distribution for that run as a function of the equilibrium radius, normalized to 1. $\gamma\tau_\mu \approx 64.4\,\mu$s is the time-dilated muon lifetime. $l(x,t)$ is the empirical loss function as a function of time and radius, to be determined in the fit.

$L(t')_i$ is the measured integrated triples spectrum (for example, Fig. 4.7-3, right) and is integrated from the fit start time to t. The extra term $\exp(t'/\gamma\tau_\mu)$ is included in order to follow the convention of the muon loss term in the decay positron fit function, as expressed in Eq. 1. The normalization by C_i, the total number of positrons measured in that dataset, ensures that the 8 special runs can be correctly compared.

An analytic form of $l(x,t)$ is assumed in order to perform the fit. From simulations, $l(x,t)$ is expected to peak near the edges of the storage distribution, as muons that have a high or low equilibrium radius are more likely to be lost. Several forms of $l(x,t)$ with this qualitative behavior were compared, including a sum of two Gaussians and a piecewise sum of two parabolas. The same analytic form was used throughout the fill and the fit parameters allowed to vary with time to account for the changing behavior of the lost muons.

At each time, the remaining stored distribution $F_{curr}(x,t)$ is calculated using the equation

$$F_{curr}(x,t) = F_0(x) - f_{loss}\frac{F_0(x)l(x,t)dr}{\int_{R_{min}}^{R_{max}} F_0(x)l(x,t)dr} \tag{4}$$

$F_0(x)$ is the fast rotation distribution of the full physics dataset, normalized to 1, and represents the radial distribution of the stored muons at the fit start. The second term represents the total muons that have been lost up to that time, scaled by the fractional loss correction $f_{loss}(t)$ which emerges from the decay positron fit, as seen in Fig. 4.7-1.

The average radius of the stored distribution is then extracted at each time from $F_{curr}(x,t)$. This average radius can be converted into momentum units. The average dp/p of the stored distribution is converted to ϕ using the measured phase-momentum correlation. The $\phi(t)$ determined by this method for one dataset is shown in Fig. 4.7-4.

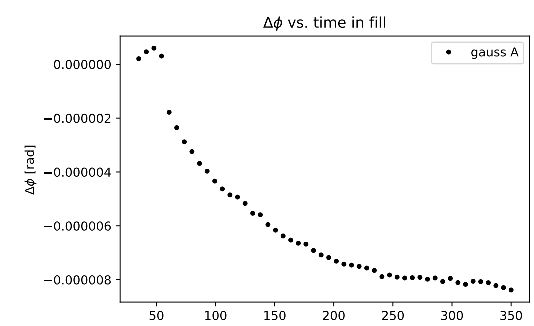

Figure 4.7-4. Calculated vs. time for a double Gaussian form loss probability function.

$\Phi(t)$ is parametrized using a high degree polynomial function, which is used to generate a set of points based on the 5-parameter decay positron fit function Eq. 2. A fit is then performed on the generated points using $\phi(t) = \phi_0$, as is assumed in the physics analysis, with all parameters allowed to float. The bias to ω_a is extracted by comparing the input ω_a value to the value extracted from fitting with a constant ϕ.

This procedure is performed on every dataset using the momentum distribution and $f_l oss$ functions for that dataset. It is also repeated using a variety of candidate fit functions for $l(r, t)$.

This procedure results in a bias to ω_a of < 40 ppb. Because the statistical uncertainty for Run 1 is 400-50 ppb, this systematic uncertainty is under control for Run-1. For future higher-statistics datasets, the muon loss rate will be lower, reducing the size of this effect.

4.8 Storage ring magnetic field transients at muon injection

M. Fertl*, D. W. Hertzog, J. Kasper, B. MacCoy, and H. E. Swanson

Fixed probes sample the complete ring field every 1.4 seconds and are therefore only able to track field variations occurring more slowly than the 1/3 Hz Nyquist frequency limit imposed by this rate. The sheer size of the magnet and the controlled thermal environment within the experimental hall keeps actual field variations from the magnet itself well within this limit. The fixed probe system has been shown to track the average magnetic field over time with an uncertainty of less than 100 ppb. We were however motivated by concerns about possible field transients from the accelerator complex to develope a method to improve the frequency response.

Muons are injected into the ring in 2 groups of 8 bunches synchronized with the 1.4 second accelerator cycle period. Bunches are separated by 10 milliseconds (ms) with bunch durations lasting 0.7 ms. Tracking the field over these times requires a frequency response of kilohertz which is well beyond the real time capabilities of the fixed probe system. However any periodic field waveform stationary within the accelerator cycle period can still be measured by varying start times of measurements relative to the start of each cycle and assembling a time series from the results. This takes many cycles to complete and requires correction for field drift. Random field fluctuations over this period would appear as noise. The pulsed NMR system has an inherent sample rate of around 50 kHz with a readout system that averages from 20 to 200 samples per measurement depending on the length of the free induction decay (FID) analyzed. Stepping these measurements along the bunch regions has the necessary frequency response and provides essentially a moving average over any periodic time dependent field waveform in that region.

We used this approach on fixed probe measurements. There are 84 cycles of 60

*Johannes Gutenberg University, Mainz, DE.

Hz in the 1.4 second period and both 60 and 120 Hz were observed in the spectra. The known 30 Hz from the accelerator was not observed. Fixed probes located in vacuum chambers with electrostatic quadrupoles saw field oscillations with periods corresponding to muon bunch spacing while those in other chambers did not. The quads are pulsed for each muon injecction. These oscillations continued beyond the 8 muon bunches consistent with some mechanical resonance in the quad structure ringing down. A number of models were proposed to generate magnetic fields from motions due to electrostatic forces on the charged quadrupole plates. Accelerometers placed on the quadrupole support structure verified that motion resulted from the high voltage pulse on the quadrupole plates. The next step was to make field measurements within the quadrupoles themselves as the vacuum chamber walls attenuate higher frequency field transients at the location of the fixed probes.

NMR probes were sealed in vacuum compatible Peek tubes and placed along the center line between quadrupole plates where the potential when charged is at a minimum. A pulse generator provided timing signals in the absence of accelerator beam. The quads were ramped to their nominal 18.2 kV with a pulse rate of 100 kHz to match normal running conditions. The Q3-L waveform from scanning over the first group of 8 bunches in is shown in black on the left in Fig. 4.8-1. The vertical grey lines show when the quads are pulsed to constrain the muon trajectory in the ring. Peak-to-peak field oscillations inside the quad are 600 ppb while the blue curve shows the field measured by fixed probes which is consistent with eddy current attenuation in the vacuum chamber. The plot on the right zooms in on the 4th bunch during the time these muons are circulating in the ring (also shown in grey). While in the quad muons in this bunch are precessing in a field that is 150 ppb lower than that provided by fixed probe tracking.

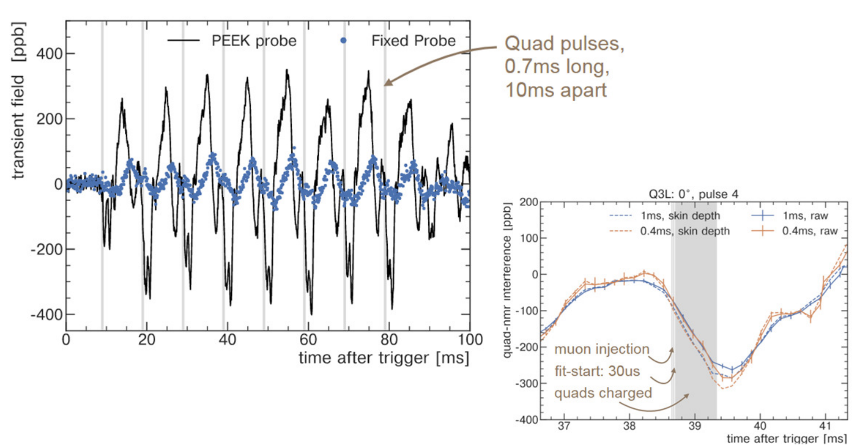

Figure 4.8-1. Magnetic field measured in the center of electrostatic quadrupole Q3-L. Grey lines in the left plot show when quads were pulsed on to focus muon trajectories. The field desends rapidly when quads are charged as shown in the zoomed in plot on the right.

We have made these measurements in the 4 short quads and one half of each of the 4 long quads. Each quad structure has a slightly different resonant frequency and when driven at 100 Hz by quad pulsing, resonates with a different phase relative to the driving phase. Even though the peak-to-peak amplitude of field oscillations in the different quads is very similar, the phase of oscillations at the time of muon injection can be different. Nonlinear restoring forces can also shift the phase as the resonant amplitude builds over the group of bunches. Consequently and fortunately field transients in the different quads tend to cancel each other.

The average transient field offset from all bunches measured is -15 ppb. Since this was measured in Run 3, given the sensitivity to quad structure resonances and the lack of knowledge about mechanical stability, we estimate the uncertainty on this result to dominate its value for Run 1 and possibly Run 2 publications. We will be mapping this effect over the complete extent of the quadrupoles with considerably smaller uncertainties for the Run 3 publication and beyond.

4.9 Characterizing beam injection with the inflector beam monitoring system

P. Kammel and B. K. H. MacCoy

The muon injection into the $g-2$ storage ring is one of the most critical and complex elements in the muon delivery concept. The muon beam enters through strong fringe fields and the narrow inflector aperture (18 mm × 56 mm), which results in a mismatch between the transmitted beam phase space and the ring acceptance. The Inflector Beam Monitoring System (IBMS), designed and constructed at CENPA, is the primary diagnostic tool to continuously monitor the beam profile at injection. Two IBMS modules (IBMS1 and IBMS2) were installed in Run 1, and a third module (IBMS3) was installed in Run 2.

IBMS1 and IBMS2 consist of two planes of 16 scintillating fibers (SciFis) each, oriented in the horizontal and vertical directions. IBMS3 consists of just one plane of 16 vertical SciFis. Each 0.5 mm diameter fiber is coupled to a 1 mm^2 silicon photomultiplier (SiPM). The signals are read out with low-noise programmable gain amplifiers and transported by micro-coax cables to the waveform digitizers. Each 16-SiPM-channel readout board fits onto one 16-fiber detector plane, with each channel reading out one SciFi.

As shown in Fig. 4.9-1, IBMS1 is the upstream-most IBMS module, positioned just outside the yoke hole bore into the ring magnet. IBMS2 is positioned 2 m into the 100 mm diameter yoke hole bore, just upstream of the inflector entrance. IBMS3 is the downstream-most module, positioned 1 m downstream of the injection point (inflector exit aperture) inside the storage ring vacuum chamber. Its vertical fibers provide horizontal beam profiles, which contains the most important injected beam information. IBMS3 is inserted for dedicated beam studies and retracted for normal production running using a vacuum feedthrough linear micrometer. Detector geometry was optimized for the expected beam profile at each position (Fig. 4.9-2).

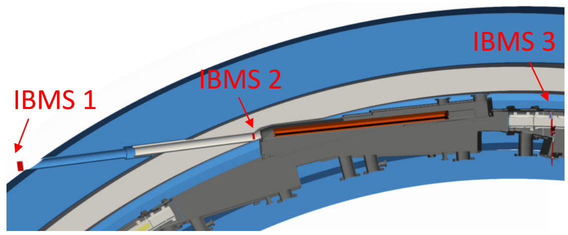

Figure 4.9-1. IBMS1/2/3 locations are shown in a top view segment of the ring.

During the summer before Run 3, a campaign to survey the position of IBMS3 in the ring was completed. IBMS3 was uninstalled and its internal geometry was measured with a laser scannner at the Fermilab metrology shop. Before uninstallation and again after reinstallation, external fiducials were measured by laser tracker to register the detector geometry in the ring. The position of IBMS3 (for both Run 2 and Run 3) is now known to better than 0.5 mm, with a repeatability better than 50 µm provided by limit switches.

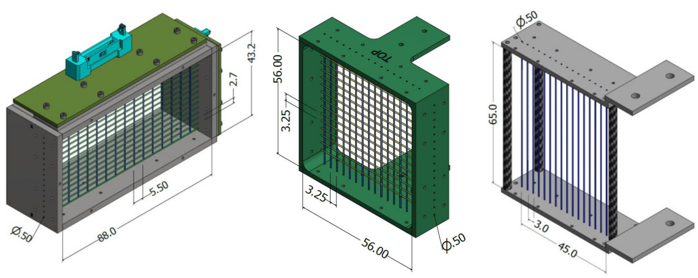

Figure 4.9-2. IBMS1 (*left*), IBMS2 (*center*), and IBMS3 (*right*) geometries designed for the beam shape at each detector position.

In Run 2, several dedicated IBMS3 beam studies were performed. First, IBMS3 was inserted into the injected beam to measure its spatial profile. Beam profiles measured at all three IBMS detectors are shown in Fig. 4.9-3.

IBMS3 was inserted into the injected beam for a horizontal beam steering study, in which the currents of two upstream horizontal dipole magnets were scanned to control the horizontal trajectory of the beam. This type of scan is periodically performed to optimize injection and muon storage (typically with IBMS3 not inserted to avoid interfering with the stored beam). In this study, muon storage efficiency was measured simultaneously with the injected beam profiles at each point in the scan. Injection efficiency at IBMS3 relative to IBMS2 is compared with muon storage efficiency, and the injection trajectory for each dipole current setting is characterized by the beam position at each detector in Fig. 4.9-4.

IBMS measurements can also help tune Monte Carlo simulations. Several software

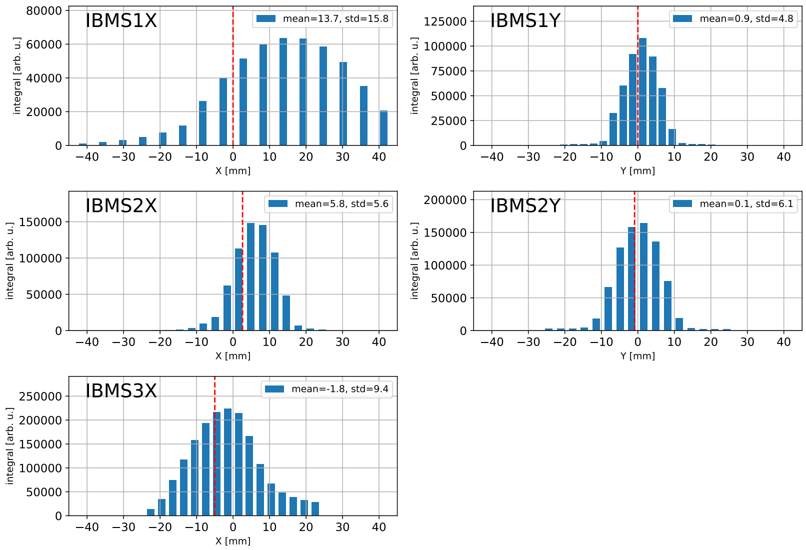

Figure 4.9-3. Spatial beam profiles for IBMS1, 2, & 3 in Run 2. X profiles (left) are horizontal (+X = radially in) and Y profiles (right) are vertical (+Y = up). For reference, red dashed lines indicate the nominal beamline at each detector position

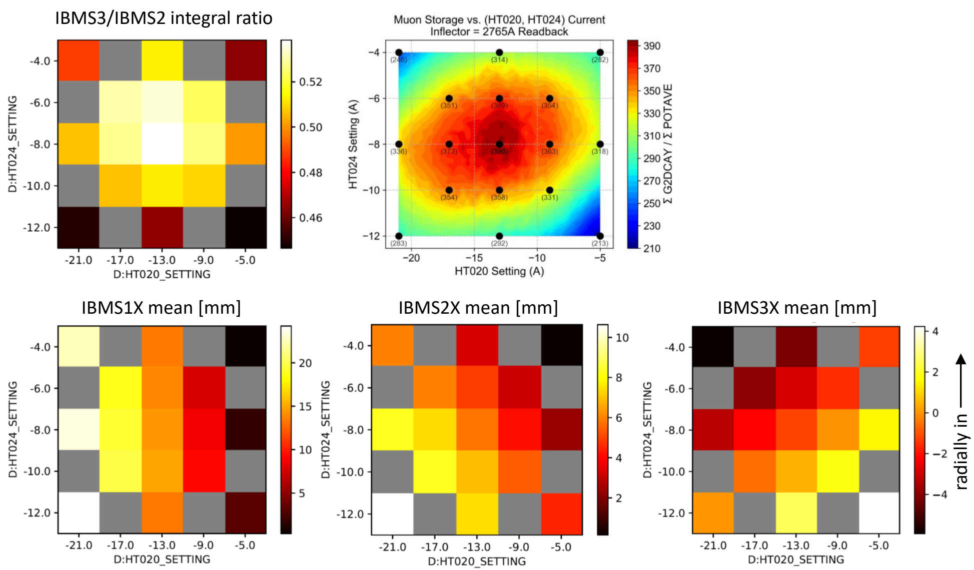

Figure 4.9-4. IBMS3 beam integral normalized to IBMS2 vs horizontal dipole current setting (top left) provides a proxy for inflector throughput. Points not covered in the scan grid are shown in gray. Muon storage efficiency (top right) is maximized near the same point as the inflector throughput, as expected. IBMS1, 2, & 3 horizontal beam position vs dipole current setting (bottom row) maps the trajectory change as a function of dipole current. Position is relative to detector center, with +X = radially in.

packages with different capabilities allow results to be cross-checked. The simulations have not reached complete agreement with each other and with the experimental data on a few key parameters such as stored beam radial distribution and lost muon distribution. IBMS measurements of the full injection trajectory can be used to tune beam injection in these simulations. Implementation of IBMS detectors in the different simulation packages is in progress.

4.10 Lab tests of the nanosecond-level gain recovery function for the Muon $g-2$ SiPMs

J. B. Hempstead

The problem

The muon's anomalous precession frequency ω_a is measured through use of calorimeters to record the hit times and energies of decay positrons. When a minimum energy cut is applied, a clear oscillation appears in the number of decay events seen versus time after beam injection. One way to directly pull the measurement of ω_a is to introduce a time-in-fill energy bias. A sample mechanism for this would be if the detectors misreport the energy of a particle hit immediately (within tens of nanoseconds) following a separate hit. The rate of pileup events such as this changes through the fill, coherently across every fill. Thus, a correction must be made to the energy of the second pulses in these scenarios.

Each of the twenty-four calorimeters in the $g-2$ experiment consists of 54 lead fluoride crystals read out by large-area silicon photomultipliers (SiPMs). Each SiPM has approximately 57 000 binary-response pixels. When a pixel fires, there is an associated recovery time as the depleted charge is restored. A positron hitting a calorimeter produces Cherenkov light in the crystals as it showers. The light then uniformly fills the face of the SiPM. The number of pixels fired from a pulse goes approximately as

$$N_{\text{fired}} = \epsilon N_\gamma \frac{N_{\text{available pixels}}}{N_{\text{total pixels}}}.$$

Following a large pulse, the number of pixels available to fire recovers exponentially. The energy report for a pulse is proportional to the number of pixels fired, so the energy scale following a positron hit also recovers exponentially. By knowing the number of pixels fired in (or somewhat equivalently energy of) the first pulse, it should be possible to correct the second pulse's energy.

It is possible to measure the gain of a SiPM (ratio of output pulse to number of pixels fired) using the photostatistics properties of the system. By changing the amount of light reaching the SiPM in a controlled way, the variance of output signals can be plotted versus the mean. The linear term of this relationship is the gain.

In the experimental hall, an impressive laser system distributes light to the 1296 calorimeter channels. Using a clever triggering system, the nanosecond-level effect detailed above can be measured. Correction functions can be constructed and implemented into data reconstruction. However, when the functions were measured they seemed to disagree with the predicted pulse reduction based on number of pixels firing.

Lab setup

While the laser system in the experiment is great for large-scale tests of the calorimeters, it is not ideal for understanding the SiPMs at a granular level. So far, the nanosecond-level effect has been described as only arising from pixel depletion. The oft-quoted lore has been the effect is too fast to involve electronics crosstalk between the pixels. To test this, the two pulses can be spatially separated on the face of the SiPM. Should the effect remain, there's clearly some electronics component.

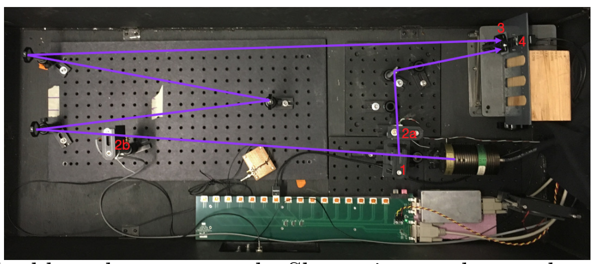

Figure 4.10-1. The double pulse test stand. Shown in purple are the two separate beam paths with a $\Delta t = 10\,\mathrm{ns}$. Some key aspects are as follows: 1) a 50:50 beam splitter, 2) shutters that can be used to block the a) first pulse and b) second pulse, 3) a removable and rotatable physical divider to separate laser pulses on the SiPM face, and 4) the SiPM being tested.

In the lab at CENPA, two separate beam paths were constructed to the SiPM. The time difference between the two paths is approximately 10 ns, enough to see the effect but not so short to make analysis overly difficult. Fast, controllable shutters were placed in each beam path. Data was taken in a pattern of $A, B, A+B$, with A and B corresponding to the short and long beam paths. A physical barrier was sometimes placed between the two beams to separate the light from the two pulses on the face of the SiPM. The whole setup can be seen in Fig. 4.10-1.

Analysis and results

For each running condition, the overall intensity of the laser light was varied to facilitate estimating the number of pixels fired. The average pulse shape for each type of event was constructed, as can be seen in Fig. 4.10-2. The average A pulse is subtracted from the average $A+B$ pulse and compared to the average B pulse. This gives a measure of the relative gain drop due to the A pulse.

The main focus of this study was determining the effect of a possible electronics effect causing a larger than expected gain drop. When the barrier was placed between

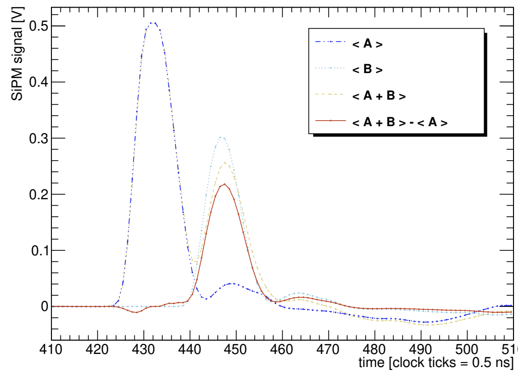

Figure 4.10-2. Average SiPM pulse shapes. The three types of events are shown as well as a reconstruction of the second pulse from the double pulse events. This is done by taking the average $A+B$ pulse shape and subtracting the average A pulse shape. A ratio of the red, solid pulse to the cyan, dotted pulse gives a measure of the relative gain following the first pulse.

the two beam paths, the gain drop effectively disappeared (see Fig. 4.10-3). The SiPM appears to act as if it has ≈10 000 pixels instead of ≈57 000. Other effects have been studied including the bias voltage, programmable gain setting, and operating temperature. The cause of the unexpectedly large gain drop is unknown, though the lab tests performed validate the correction functions constructed from the laser data taken *in situ*.

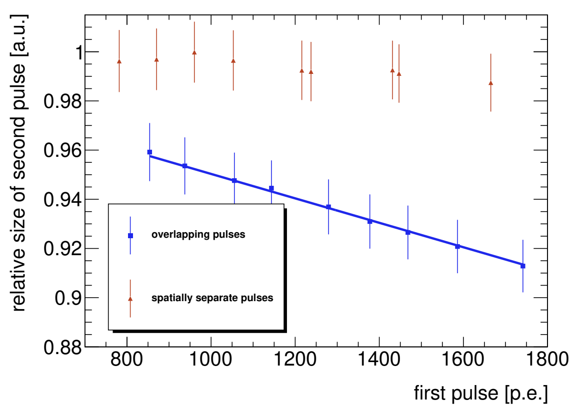

Figure 4.10-3. Relative gain drop vs. pixels fired in first pulse. The data taken with both pulses diffused over the full SiPM shows the known gain drop. The shown fit fixes the pixel recovery lifetime to that found in the experiment, while letting the total number of pixels float. The fit finds ≈10 000 total pixels rather than the expected ≈57 000. When the two pulses are separated on the face of the SiPM, the effect goes away. This indicates the recovering pixel mechanism is correct, though the amplitude is not well understood.

4.11 Run 2 ω_a analysis snapshot

H. Binney, A. T. Fienberg, J. B. Hempstead, D.W. Hertzog, J. Kaspar, K. S. Khaw, J. LaBounty, and B. MacCoy

Nearline

The nearline is the intermediate level data analysis system for the Muon g-2 experiment, providing near real-time feedback on the data being taken with basic calibrations and quality control. A number of upgrades and improvements to the nearline were undertaken in preparation for Run 2 [1]. These included upgrading to the latest version of the $g-2$ software, streamlining the configuration files to make debugging easier, and increasing the percentage of data that the nearline was able to process in near real time. Throughout the run, these improvements enabled the nearline to process an average of 35 percent of the data within 2 hours of it being taken. This means that we are able to inform systematic studies in near real-time, and provide feedback for optimum run conditions going forward. This is compared to the $\mathcal{O}$(6 month) turnaround on the final production files. Trend plots of various beam parameters were created from this data, and a new webpage for shifters to monitor was implemented.

For certain systematic runs where additional statistics were required, the nearline analyzers were run on the Fermigrid in order to process 100 percent of the data. The study preformed in Section 4.7 was performed entirely with nearline data, as were many others over the course of Run 2. Scans of kicker timings, quad settings, and beam injection parameters were also analyzed using nearline data.

Dataset Definitions

Run 2 data taking took place between March and July of 2019. In that period, there was a significant amount of time devoted to systematic studies and long periods of beam-off time (when laser-only data is often taken). In order to prioritize the production of physics-quality data, we defined a series of datasets which excluded these periods. We also analyzed a number of different experimental parameters to ensure that conditions were consistent throughout each of the datasets we defined. These could then be processed first to allow the extraction of ω_a to proceed in parallel to analysis of systematic studies. Many systematic studies can also be done to the required precision with Nearline data, and so there is no need to allocate limited computing resources to processing this data in full.

There are a number of constraints placed on the creation of these datasets to ensure that we can extract ω_a (and ultimately a_μ) accurately. Some of the most pressing are:

[1] CENPA Annual Report, University of Washington (2019) p. 117.

- The dataset should be bounded on each end by a trolley run, so the magnetic field the muons are in is well known throughout.
- The magnet should not have been power cycled within a dataset.
- The dataset should not contain a mix of different experimental parameters (kicker/quadropole settings, beam tuning, etc.).
- The dataset should not contain any systematic runs.
- The dataset should be as large as possible, to maximize statistical precision.

The first 4 items on this list are all in tension with the final one, and so the process becomes an optimization problem. In total, we created 8 datasets of various sizes which represent 669 hours of production quality data taken over 54 unique days. The datasets, plotted over a subset of the parameters considered, are shown in Figure Fig. 4.11-1.

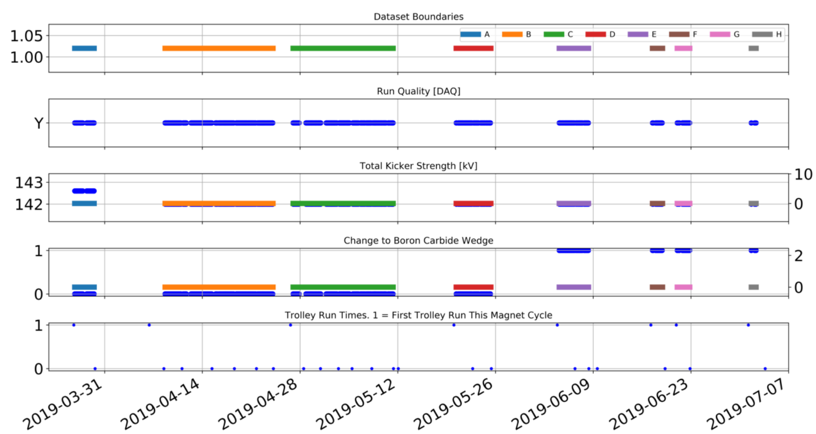

Figure 4.11-1. The date ranges covered by the various datasets overlayed on of some of the main parameters which defined them.

Run 2 Data Production

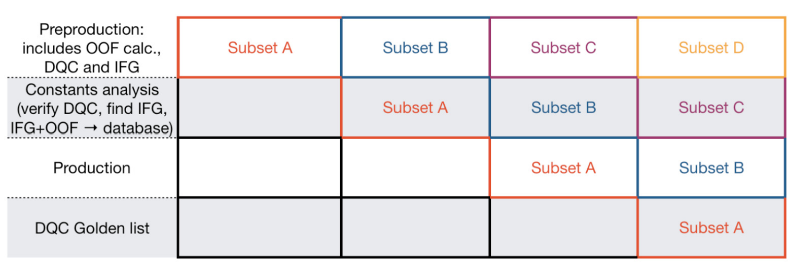

Figure 4.11-2. A diagram showing a single dataset progressing through the various stages of the $g-2$ data production.

All of the work described in Section 4.11 is designed to be an input to the production of the Run 2 data production team. In contrast to Run 1, where we processed each dataset from raw data to final production quality in one batch before moving on to the next dataset, we have implemented a rolling production structure for Run 2. For a single dataset, the stages (roughly speaking) are:

1. Pre-production: Computing a number of gain corrections to correct for temperature drifts and other detector effects. Determining which data files contain good subruns and should proceed to the second stage of production. Producing preliminary histograms to analyze the stability of various parameters vs. run number.
2. Corrections Analysis: Computation of corrections to the detector systems on a fill-by-fill basis. Inserting these constants into the production database for use in the next stage.
3. Full production: Using the constants produced in the previous step, produce the dataproducts necessary for a full analysis.
4. Final Data Quality Control: From the production files, constructing a list of the 'good' runs/subruns/fills to be used in the final ω_a analysis.

Because the work in each one of these stages is effectively independent, breaking up this production into stages allows us to parallelize this process. The corrections for dataset A can be computed while dataset B is actively in the pre-production stage (see Figure Fig. 4.11-2). The other major upgrade from Run 1 is the introduction of the production database. Previously, many of the constants used for gain correction or energy calibration were stored in configuration files. Therefore when these constants needed to be changed there was a high potential for human error. Now all constants are uploaded to the database with a well defined 'interval of validity', and the correct values are chosen automatically by the $g-2$ software at run time.

Verification of Data Integrity

During Run 1, muon data was taken at approximately 50% of the rate predicted in the Muon g-2 Technical Design Report (1100 CTAG/fill[2] vs. 550). However, even with this reduced rate we were close to exceeding the rate at which we could save data to Fermilab long-term tape storage. In preparation for Run 2, where a higher data rate would be realized, a number of measures needed to be taken in order to reduce the amount of data saved to disk per detected positron. One way this was accomplished was by truncating the calorimeter islands to only record crystals involved in a positron shower. Each calorimeter is made up of 54 PbF_4 crystals arranged in a 9x6 grid.

[2] 1 CTAG = 1 positron detected in the calorimeters with an energy $\geq 1700\ MeV$.

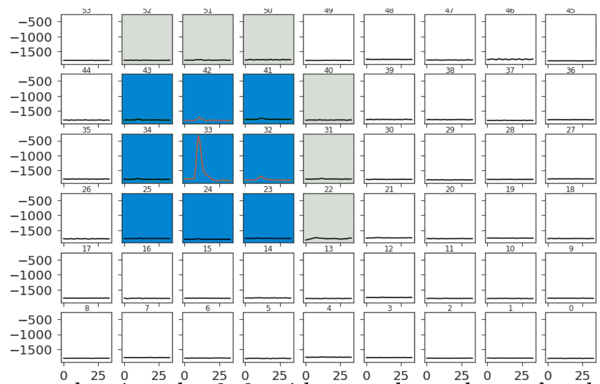

Figure 4.11-3. A diagram showing the 3x3 grid around an above threshold crystal. Only those crystals highlighted in blue and grey would be read out in the Run 2 configuration, rather than all 54.

During Run 1, each time a pulse above a certain threshold was detected in *any* crystal, waveforms from all 54 crystals were read out and stored to disk. Considering that only 14% of the calorimeter is included in the average cluster, this is a massive waste of space. So for Run 2, we altered the readout so that only crystals in a 3x3 grid around an above threshold pulse would be saved (see Figure Fig. 4.11-3). This resulted in a drop in the total data rate of $\approx 25\%$, and so was an indispensable tool in letting us meet our data rate goals.

One concern with this approach is that we might be throwing away crystals which, while below the threshold for island chopping, have some amount of positron energy deposited in them. This would lower the reconstructed energy from these islands and could therefore introduce a bias in the analysis of ω_a. This is especially true if this effect differs from early to late within a single fill (for example if there is a gain sag in the electronics chain which changes our effective chopping threshold). If such an effect were found, we would have to actively compensate for it by changing our chopping threshold throughout the fill to match the observed sag or compensating for the sag in the data during analysis.

In order to test the effect this might have on the Run 2 data, we implemented the truncation scheme artificially in the Run 1 data. Before the clustering stage of the reconstruction, we inserted a filter that removed any crystals which did not fall into the aforementioned 3x3 grid. We then re-performed the clustering with the same parameters as the original Run 1 data. After passing both of these through the full ω_a analysis chain, including a correction for the different levels of pileup and muon loss between the two datasets, we found a difference of 2.7 ppb in the blinded proxy for ω_a) between the two fits. All parameters aside from the number of counts and the $g - 2$ asymmetry measured by the calorimeter were consistent with one another, but both of these differences were expected. Based on this, we concluded that there was no measurable effect from implementing this truncation procedure, and the Run-2 data collection proceeded with this scheme in place.

5 Dark matter searches

ADMX (Axion Dark Matter eXperiment)[1]

5.1 Overview of the ADMX Experiment

C. L. Bartram, T. Braine, R. Cervantes, N. Crisosto, N. Du, S. Kimes*, G. Leum, L. J Rosenberg, G. Rybka, and J. Yang

The Axion Dark Matter eXperiment (ADMX) is an implementation of the axion haloscope experiment first put forward by Pierre Sikivie, to search for axion dark matter in the galactic halo[2]. Since it moved to CENPA in 2010, ADMX has undergone a series of upgrades including the integration of ultra low-noise quantum amplifiers and a dilution refrigerator. These upgrades have made ADMX the most sensitive axion haloscope, capable of searching for the most promising theoretical models for axion dark matter in the mass range from 650-800 MHZ (2.81-3.31 μeV).

The "strong CP problem" came about from the observation that Quantum Chromodynamics (QCD) appears to conserve CP (charge times parity) symmetry, despite containing a CP-violating term. The amount of CP violation in QCD is parametrized by a phase, θ, in the QCD Lagrangian. Experiments have placed strong upper limits on neutron electric dipole moment, which limit the amount of CP violation possible in QCD to $\theta < 10^{-10}$ [3]. Because CP-violation in the strong interaction would be fed by CP-violation in weak interactions, θ is predicted to be of order unity. The discrepancy between the predicted value for θ and experimental limits requires a fine tuning of the Standard Model, and has become known as the "strong CP problem".

A solution to the strong CP problem put forward by Peccei and Quinn introduces a new $U_A(1)$ symmetry to the Standard Model which promotes θ to a dynamical field which naturally relaxes to zero[4]. This additional symmetry is spontaneously broken, producing a new particle known as the axion[5,6]. It was realized that an axion with a mass between 1-100 μeV would make an ideal candidate for 100% of the dark matter within the Universe.

ADMX searches for dark matter axions in the local galactic halo through the use of an axion haloscope. The axion haloscope, first put forward by Pierre Sikivie[2],

---

*Presently at Microsoft, Seattle, WA.

[1]ADMX is supported by the DOE Office of High-Energy Physics and makes use of CENPA resources by recharge to the cost center.

[2]P. Sikivie, Phys. Rev. Lett. **51**, 1415 (1983).

[3]C. Abel et al., Phys. Rev. Lett. **124**, 081803 (2020).

[4]R.D. Peccei and H. Quinn, Phys. Rev. Lett. **38**, 1440 (1977).

[5]S. Weinberg, Phys. Rev. Lett. **40**, 223 (1978).

[6]F. Wilczek, Phys. Rev. Lett. **40**, 279 (1978).

consists of a microwave resonant cavity inside a magnetic field. Due to the large De Broglie wavelength of the cold dark matter axions, 100 m, relative to the size of the experiment, the axion can be treated as a field driving the electromagnetic field inside cavity. As the haloscope travels through the galactic dark matter halo, the axion field couples to the magnetic field, producing photons with frequency $f = E/h$, where E is is the total energy from the axion rest mass and a small kinetic energy term. The two benchmark models for the axion are the Kim-Shifman-Vainshtein-Zakharov (KSVZ)[1,2] and Dine-Fischler-Srednicki-Zhitnitsky (DFSZ)[3,4] model. The DFSZ axion is especially compelling for its implementation into Grand Unified Theories, but it a factor of 3 times more weakly coupled to photons than the KSFZ model. At present, ADMX is the only axion haloscope to achieve sensitivity to the well-motivated DFSZ axion.

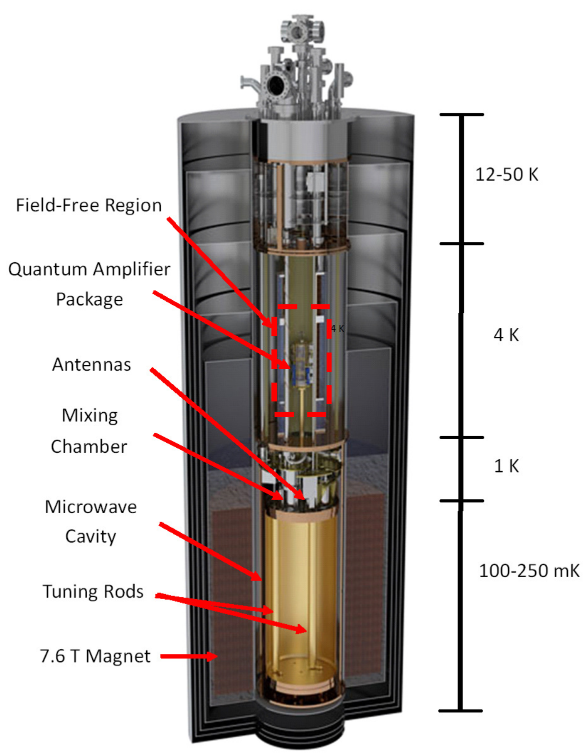

Figure 5.1-1. Cut-away model of the ADMX cryostat and experimental insert. The cavity is placed in the bore of a superconducting solenoid magnet and tuned with two tuning rods. Power from the cavity is extracted by antennas and amplified by a Josephson parametric amplifier, which is kept in the field free region.

ADMX, shown in Fig. 5.1-1, consists of a 136 liter cylindrical copper cavity of a 7.6 T superconducting solenoid magnet. Two copper-plated rods extend the length of the cavity and can be positioned between the center and walls of the cavity to tune

[1] J.E. Kim, Phys. Rev. Lett. **43**, 103 (1979).

[2] M.A. Shifman, A.I. Vainstein, and V.I. Zakharov, Nucl. Phys. **B166**, 493 (1980).

[3] M. Dine, W. Fischler, and M. Srednicki, Phys. Lett. **B104**, 199 (1981).

[4] A.R. Zhitnitsky, Sov. J. Nucl. Phys. **31**, 260 (1980).

the resonant frequency of the cavity. During data taking, room temperature stepper motors coupled to the cavity tuning rods via a cryogenic gearbox are actuated to tune the resonant frequency of the cavity. The expected power when the cavity frequency is tuned the same frequency as the photon produced from the axion is

$$\begin{aligned}P_{\text{axion}} = 2.2 \cdot 10^{-23}\ \text{W}(\frac{V}{136\ \text{L}})(\frac{B}{7.6\ \text{T}})^2(\frac{C}{0.4}) \\ \cdot(\frac{g_\gamma}{0.36})^2(\frac{\rho_a}{0.45\ \text{GeV cm}^{-3}})(\frac{f}{740\ \text{MHz}})(\frac{Q}{30000}).\end{aligned} \tag{1}$$

where V is the volume of the cavity, B is the magnitude of the external magnetic field, g_γ is the model dependent axion-photon coupling, ρ_a is the local dark matter density, f is the frequency of photon, Q is the loaded quality factor of the cavity, and C is the form factor of the cavity.

C, the form factor reflects the amount of overlap between the electric field of the cavity mode and the external magnetic field. In the case of the ADMX cavity, the optimal form factor was observed with TM_{010} mode. Over the range explored in this run, the average form factor was of order 0.4 (when convolved with the solenoid B-field).

The signal top noise ratio for ADMX is dictated by the Dicke-Radiometer equation as follows,

$$\frac{S}{N} = \frac{P_{axion}}{k_B T_{sys}}\sqrt{\frac{t}{b}} \tag{2}$$

where P_{axion} is the power of the axion signal, t is the amount of the time the signal is integration time, b is the detection bandwidth, and T_{sys} is the system noise temperature. In the case of ADMX, the system noise is dominated by thermal Johnson-Nyquist noise, equal to the sum of the physical temperature of the cavity and the noise temperature of the amplifiers. With the integration of a dilution refrigerator to cool the experiment and quantum amplifiers to reduce the amplifier noise, ADMX is able to achieve an unprecedented level of sensitivity to axion dark matter. Since it was delivered to CENPA in 2010, ADMX has searched for and excluded both benchmark models of axion dark matter in the mass range of 680-800 MHz (2.66 to 3.31 μeV)[1,2] over the course of several runs.

In the most recent run published in 2020[2], ADMX utilized a Josephson parametric amplifier to search for axion dark matter between 680-800 MHz (2.81-3.31 μeV). During this run, the solenoidal magnet was ramped to a field of 7.6 T. Improvements to the dilution refrigerator and thermal linkages within the experiment cooled the cavity to 130 mK, compared with 150 mK observed in previous runs. Due to a thermal disconnect between the quantum amplifiers package and cavity, the Josephson parametric amplifier

[1]N. Du et al., Phys. Rev. Lett. **120** 151301 (2018).
[2]T. Braine et al., Phys. Rev. Lett. **124** 101303 (2020).

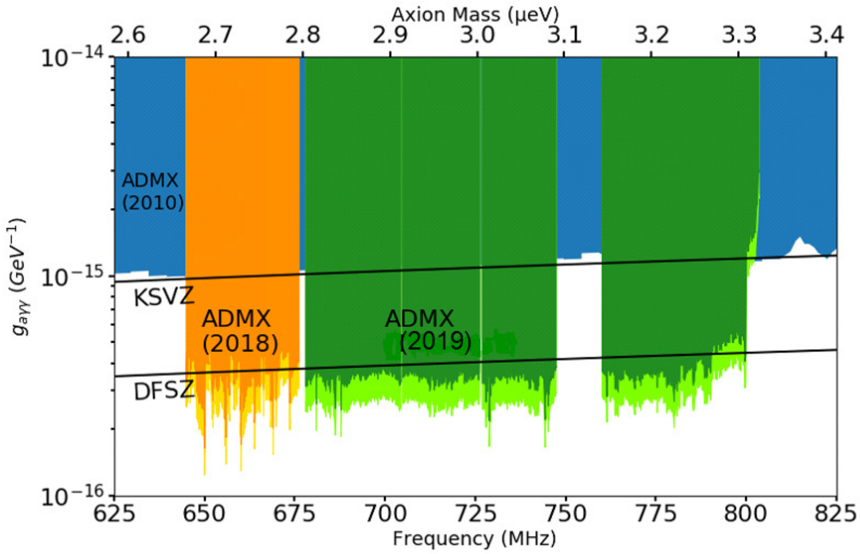

Figure 5.1-2. 90% confidence exclusion on axion-photon coupling as a function of axion mass for the Maxwell-Boltzmann (MB) dark-matter model and N-body model.

is hotter, at a temperature of about 230 mK. In addition, the run marked the first successful implementation of a blind synthetic axion injection scheme into ADMX. This system was used to both monitor the health of the amplifier receiver chain of the experiment and to blindly inject axion-like signals into the experiment that could be flagged at axion candidates by the down-stream analysis. While no real axion signals were observed over the course of the run, ADMX was able to exclude both benchmark models of the axion for axion masses between 680-800 MHz (2.81-3.31 μeV) to 90% confidence for models where the axion is 100% of the dark matter in the galactic halo, as shown in figure Fig. 5.1-2.

ADMX has undergone a number of upgrades to enable the continued search for axion dark matter in higher mass ranges. In September 2019, ADMX began another run searching for axion dark matter from 800-1020 MHz (3.31-4.22 μeV) using a JPA that is operable at higher frequencies. This run uses the same resonant cavity used in previous runs of ADMX but with two larger diameter tuning rods to allow the experiment to scan at higher masses. In addition, ADMX now utilizes a redesigned quantum amplifier package to improve the thermal connection between the cavity and quantum amplifiers. Both are shown in figure Fig. 5.1-3. The redesigned amplifier package has reduced the physical temperature of the quantum amplifiers from 230 mK in previous runs to 130 mK in this run. This has reduced the total system noise temperature to an average of 280 mK, further improving the already unprecedented sensitivity of ADMX.

Following completion of this current run, ADMX will continue to search for higher mass axions. Up to 2 GHz, ADMX will utilize the same cavity with modified rod

Figure 5.1-3. (*Left:*) The quantum amplifier package being used by ADMX in 2020. The smaller form factor reduces heating from stray thermal contact in the experiment, reducing the temperature of quantum amplifiers. (*Right:*) The cavity being used by ADMX in 2020. The larger diameter rods allow the experiment to reach higher frequencies.

geometries. For frequencies between 2-4 GHz, a multi-cavity system has been developed and is currently undergoing testing. In addition, R&D projects for resonators up to 10 GHz are currently underway. These future searches will probe even more deeply into the well-motivated yet unexplored axion parameter space, and a discovery of the axion could be made at any moment.

5.2 Higher-frequency axion searches with Orpheus

R. Cervantes, P. Mohapatra, and G. Rybka

The ADMX Orpheus experiment aims to search for axion-like particles with masses approaching 100 μeV/c^2. Orpheus consists of a dielectric-loaded Fabry-Perot resonator. It operates at a high-order mode to increase the mass range while keeping the detection volume high. The open design reduces dissipation in the cavity walls, thus increasing the quality factor. Alumina plates are placed every fourth half-wavelength in order to suppress the electric field that is anti-aligned with the external magnetic field, increasing the resonator's coupling to the axion.

From March 2019 to March 2020, we have designed and fabricated a cryogenically compatible Orpheus resonator. The cryogenic engineering was difficult because there are a lot of moving parts. Machining tolerances must be maintained even after thermal

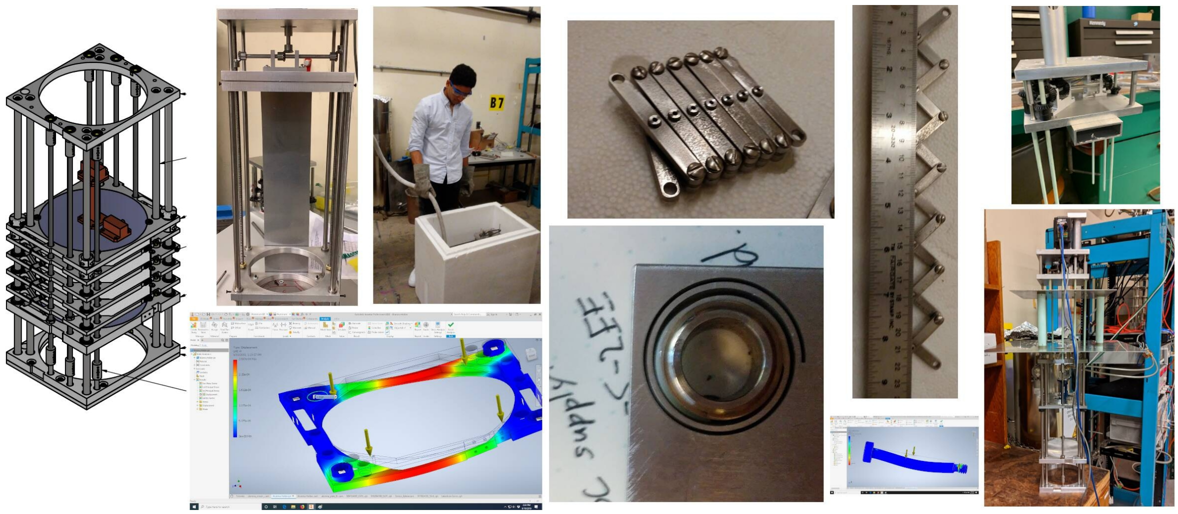

Figure 5.2-1. Prototyping various mechanical designs. Stress simulations were also performed to identify any possible points of failure.

contractions. The structure must also have enough flexibility to operate even if thermal contractions cause slight misalignments. To maintain the same machining tolerances after cooling, the structure is made mostly of the similar materials. Vertical shafts are made of stainless steel and horizontal plates are made of aluminum. However, similar materials that slide against each other causes galling. To prevent galling, a silver coating is applied to bearing surfaces. To account for slight misalignments after contraction, spiral flexures are placed around bushings. Finite element analysis to identify possible points of failure. Figure Fig. 5.2-1 shows the prototyping at various stages of development.

We have developed a gearbox that moves 3 plates independently of each other. Each motor controls 2 co-rotating threaded rods that move the plates up and down. It has proven to run smoothly, even when the resonator structure is submerged in liquid nitrogen (LN2). The scissor jacks were also successfully tested in LN2.

We have developed the software stack. Our software stack uses a combination of Docker containers, Kubernetes, Dripline, and Grafana to monitor and control the experiment remotely.

DAMIC

5.3 Dark matter searches with DAMIC at SNOLAB

A. E. Chavarria, P. Mitra, A. Piers, and outside collaborators*

DAMIC (Dark Matter in CCDs) at SNOLAB is a low-noise, low-threshold dark matter experiment located 2 km underground in the Vale Creighton Mine near Sudbury, Ontario. The experiment consists of a tower of seven science-grade, 675-μm thick, fully depleted silicon charged coupled devices shielded by layers of electroformed copper, ancient and regular lead, and polyethylene. DAMIC at SNOLAB operates with extremely low levels of electronic noise (< 2 e$^-$), leakage current ($< 5 \times 10^{-4}$ e$^-$pix^{-1}day^{-1}), and background rate ($<$ 11 counts kg^{-1}day^{-1}keV$_{\mathrm{ee}}^{-1}$), yielding a search for dark matter candidates in the form of weakly interacting massive (WIMPs) or hidden-sector dark matter particles.

The WIMP parameter space spans orders of magnitude in mass. The 50 eV$_{\mathrm{ee}}$ threshold in DAMIC CCDs allows for a sensitive search from $1 - 10$ GeV/c^2. To search for a potential WIMP signal over background, we developed a comprehensive background model by performing an extensive `Geant4` simulation of our entire detector geometry, fitting 48 spectral templates–including bulk and surface templates–between $6-20$ keV$_{\mathrm{ee}}$, and extrapolating the fit below 6 keV$_{\mathrm{ee}}$ for the backgrounds in the WIMP search region of interest. We have also put considerable effort into understanding all the detector effects, including an unknown charge collection efficiency on the backside of the CCD, and integrating these effects into our search profile likelihood function. While the final stages of the analysis are still ongoing, the DAMIC Collaboration presented preliminary results on the WIMP search at the April 17th Fermilab Colloquium; we expect a publication on the results to follow shortly.

Additionally, if there exists a dark photon capable of mixing with real photons, it is possible to have a dark matter candidate of much lower mass ($\mathcal{O}$(MeV)) scatter off a weakly bound electron and deposit enough energy to excite electron-hole pairs in the CCD. We set limits on this form of dark matter by examining the pixel distribution (Figure 1) of four CCDs with the lowest dark current and searching for a contribution above the known noise sources (dark current and electronic). This search method resulted in the best direct detection limits on the DM-electron scattering cross section (Figure 2) for masses between 0.6 and 6 MeV/c^2 and the dark photon kinetic mixing parameter between 1.2 and 9 eV/c^2.

*DAMIC Collaboration.

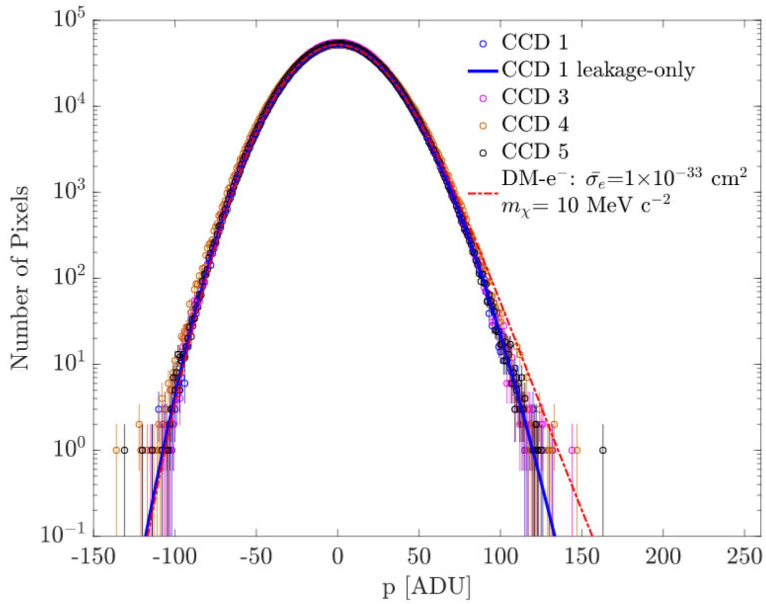

Figure 5.3-1. Pixel values from the four CCDs selected for the DM-electron scattering analysis. The best fit leakage-only model for CCD 1 is shown in the solid blue line, while the expectation for a characteristic dark matter candidate with $m_\chi = 10$ MeV/c^2 and $\sigma_e = 1 \times 10^{-33}$ cm^2 is shown in the dashed red line.

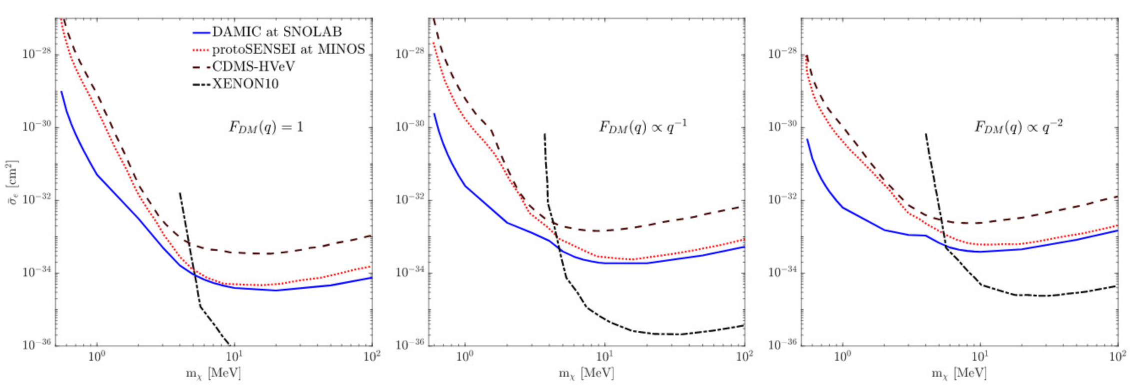

Figure 5.3-2. 90 % Upper limits on the dark matter-electron scattering cross section for different dark matter form factors.

5.4 Upgrade of DAMIC at SNOLAB

A.E. Chavarria, M. Huehn, M. Kallander, D. Peterson, T. D. Van Wechel, and outside collaborators*

We are leading the installation of our new 24 megapixel "skipper" CCDs with single-electron response (Sec. 5.6) in the DAMIC cryostat at SNOLAB. The purpose of this upgrade is to measure with higher energy and depth resolution the population of events observed in our previous search for weakly interacting massive particles (WIMPs) with conventional CCDs (Sec. 5.3). A direct comparison between conventional and skipper CCDs in the same background environment will provide a reliable benchmark as we transition to DAMIC-M.

Fig. 5.4-1a shows the design of the CCD holder for the two new CCDs. The holder will be machined from commercial high-purity copper that has been stored underground for over three years, sufficiently long for most cosmogenic radioactive contaminants to have decayed away. Fig. 5.4-1b shows how the new copper structure attaches to the existing cold finger in the DAMIC cryostat.

We will reuse the existing radiation shield, vacuum and cryogenic systems but the electronics will be upgraded to handle skipper CCDs. We designed and fabricated new front-end electronics and a vacuum feed through board. For CCD control and readout, we will use Fermilab's new Low Threshold Acquisition (LTA) board [1]. Installation of the new CCD system is scheduled for mid-2020.

a) b)

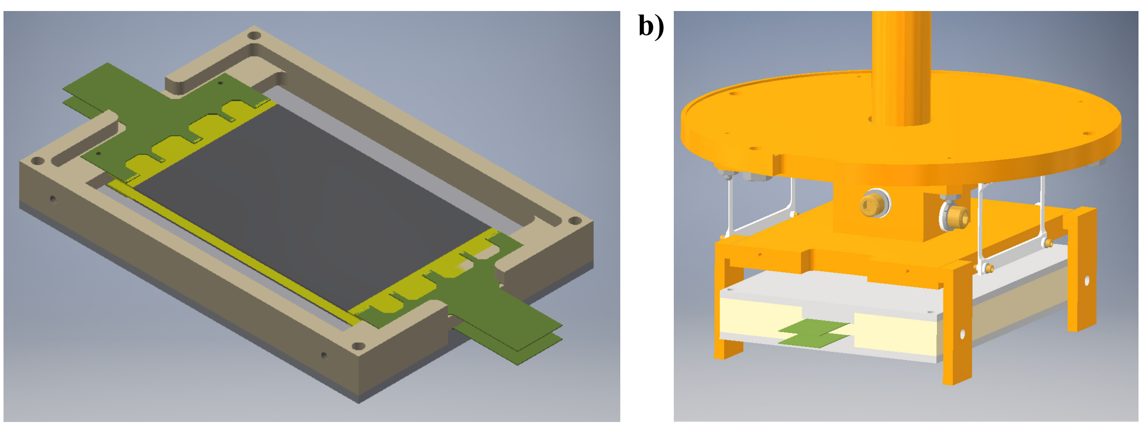

Figure 5.4-1. a) Copper holder for two 24-megapixel "skipper" CCDs to be installed in DAMIC at SNOLAB. The CCD area (gray) and the flex cables that carry the CCD signals (green) are also shown. b) Mechanical connection of the new CCD holder to the existing copper cold finger in the DAMIC cryostat.

*DAMIC Collaboration.

[1] G. Cancelo *et al.*, arXiv:2004.07599 (2020).

5.5 DAMIC-M detector design

J. Amsbaugh, T. Burritt, A.E. Chavarria, S. D'Ambrosia, M. Kallander, and outside collaborators*

We continue the design of the DAMIC-M detector, which will search for the interactions between dark matter particles and ordinary silicon atoms with unprecedented sensitivity [1]. DAMIC-M will consist of a tower of fifty CCDs with single-electron response deployed in an ultra-low-radiation environment in the Modane Underground Laboratory (LSM) in France [2].

Fig. 5.5-1a shows a preliminary design of the DAMIC-M cryostat. The CCD tower is housed inside an infrared shield made from electroformed copper (labeled "4"), which is cooled by a cold plate welded to an L-shaped conventional high-purity copper cold finger (labeled "33") that serves as a thermal connection to a liquid-nitrogen heat exchanger (not shown). The detector weight is supported on the bottom of the cryostat by a quartz disc (labeled "5"). An ancient lead disc with negligible ^{210}Pb activity (labeled "10") shields the detector tower from γ radiation emitted by the components above it. Additional lead shielding around the cryostat (not shown) stops environmental radiation. Detailed simulation activities are ongoing to determine the optimal dimensions of the copper cold finger and the internal lead shield to achieve adequate thermal performance (CCD operating temperature of 100 K) and sufficiently low background from natural radioactivity (0.1 events per keV per kg-day), respectively.

We have also progressed in the design of the CCD modules that stack up to make the CCD tower. We completed the mechanical and thermal testing of the copper trays that will hold the CCDs. The final trays will be fabricated from high-radiopurity electroformed copper, which will be grown in a cylindrical mandrel, cut open and then flattened to a plate. We reproduced this flattening procedure starting with a tube of conventional high-purity copper and machined some prototype trays. The trays were then cooled in a liquid-nitrogen bath and their surface flatness was measured while cold and after returning to room temperature. No evidence of warping back to the original cylindrical shape was observed, which suggests that the proposed flattening procedure is adequate.

We are also exploring the use of connectors and cables from Axon [3] to carry the signals for the DAMIC-M CCDs. Axon cabling components are an attractive substitute for the traditional flex cables used for CCDs because of their demonstrated low radioactivity. Fig. 5.5-1b shows our design of a CCD package using high-radiopurity Axon wire-bonding connectors and Picocoax cables. We submitted our design proposal to Axon and we expect to test this new CCD package later in 2020.

*DAMIC-M Collaboration.

[1] CENPA Annual Report, University of Washington (2019) p. 142.
[2] N. Castello-Mor (DAMIC-M Collaboration), Nucl. Instrum. Methods Phys. Res. **A958**, 162933 (2020).
[3] Axon Advanced Interconnect Solutions, Montmirail, France (`www.axon-cable.com`).

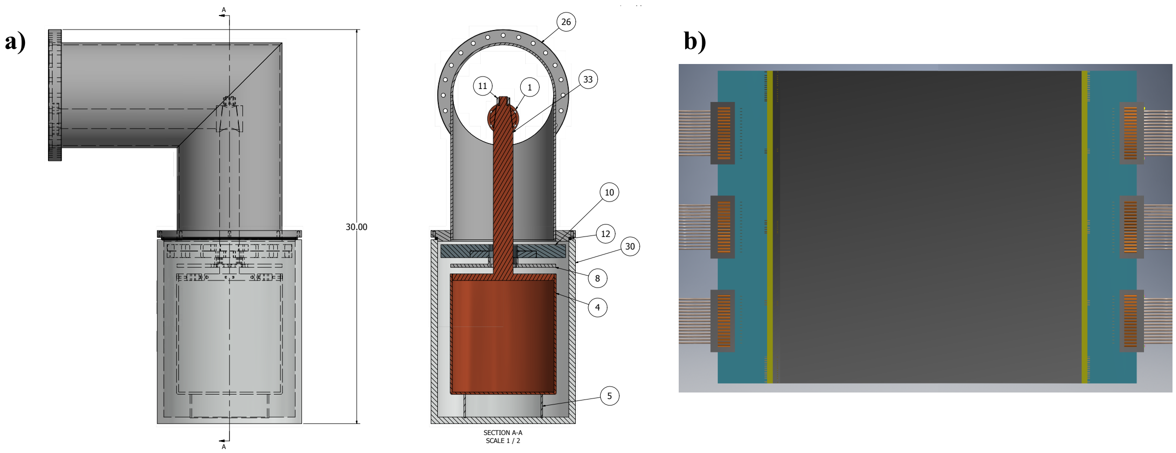

Figure 5.5-1. a) Preliminary design of the DAMIC-M cryostat. The CCD tower will be housed within the infrared shield labeled "4." See text for details on other components. b) CCD package with the Axon cabling option. CCD signals are carried by six bundles of Picocoax cables with wire-bonding connectors on one end. The wire-bonding connectors are glued on a silicon pitch adapter (teal) that distributes the signal lines to match the CCD (dark gray) wire-bonding pads.

5.6 DAMIC-M CCD testing and characterization

A. E. Chavarria, S. D'Ambrosia, M. Huehn, M. Kallander, P. Mitra, D. Peterson, A. Piers, T. D. Van Wechel, R. Zhang, H.T. Gaensbauer, and outside collaborators*

The DAMIC-M (DArk Matter In CCDs at Modane) is an experiment to search for dark matter using charge-coupled devices (CCDs). The experiment will be located at the Modane Underground Laboratory (LSM) in France. The DAMIC-M CCDs employ a skipper output stage which enables them to make repeated non-destructive measurements of the number of electron hole pairs in the silicon to achieve an unprecedented resolution of single electron-hole pairs. DAMIC-M is the first experiment what will use 675-μm thick CCDs with such a resolution and a low dark current. The DAMIC-M group at CENPA is responsible for the development of the packaging of the detector as well as the testing and characterization of the skipper CCDs. The packaging apparatus was developed at CENPA by J. Amsbaugh and M. Kallander. The front end electronics to operate the CCDs were developed and fabricated by D. Peterson and T.D. Van Wechel. The hardware of the controller is from Astronomical Research Cameras, programmed fully at CENPA by P. Mitra.

The new packaging and testing laboratory for DAMIC-M at CENPA is now fully operational and so far has been used to package 30+ CCDs for the experiment. The different kinds of CCDs packaged are listed in Table 5.6-1. Fig. 5.6-2 shows a fully

*DAMIC-M Collaboration.

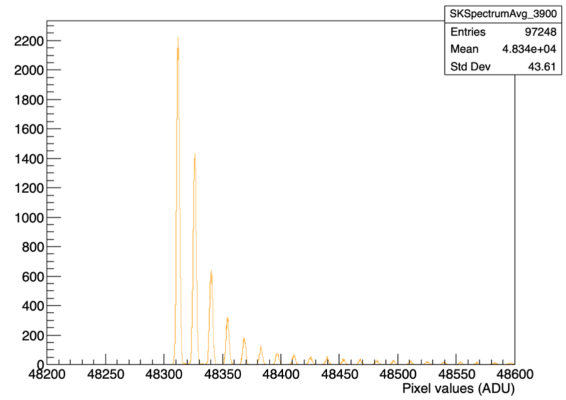

Figure 5.6-1. A histogram of an image taken with a skipper CCD at CENPA. The pixel values correspond to the number of electron-hole pairs that make up the pixel. Discrete values show a single electron-hole pair resolution.

Dimensions (pixels)	Amplifier Description	Quantity Packaged
4000 $\times$ 2000	DESI	8
1000 $\times$ 4000	Skipper	4
1000 $\times$ 6000	Skipper	8
6000 $\times$ 4000	Dual (Skipper and DESI)	4

Table 5.6-1. List of CCDs packaged at CENPA for the DAMIC-M testing and characterization.

packaged 6000 $\times$ 4000 pixel CCD. CENPA is also in charge of providing the packaged test CCDs and the software infrastructure to operate them to the rest of the collaboration. In accordance, CENPA has provided CCDs, infrastructure and support to:

1. Kavli Institute of Cosmological Physics at University of Chicago
2. Pacific Northwest National Laboratory in Richland WA
3. Laboratoire de Physique Nucléaire et de Hautes Énergies at Sorbonne Université in Paris, France
4. Instituto de Física de Cantabria at the University of Cantabria in Santander, Spain
5. Physik-Institut, Universität Zürich in Zurich, Switzerland
6. Universidad Nacional Autónoma de México, Mexico City, Mexico *Software infrastructure only*

The 1000 $\times$ 6000 pixel skipper CCDs packaged at CENPA (Laboratory located in PAB B-059) were used to obtain images with resolutions of 0.07 electron-hole pairs at the University of Chicago, LPNHE Paris and at CENPA using the software infrastructure and the charge movement algorithm developed at CENPA (See Figure Fig. 5.6-1). It was demonstrated at CENPA that electron-hole pairs in such CCDs can be measured non-destructively up to 16,000 times. At present, the control algorithm is being modified to improve the dark current from the CCDs. The packaging lab at CENPA will also be used to prepare science-grade CCDs for a demonstrator run of DAMIC-M. The packaging lab will also be used to prepare science-grade CCDs for the upcoming upgrade of the DAMIC setup at SNOLAB (Sec. 5.4) and a first DAMIC-M demonstrator setup to be installed in LSM later in 2020. For this purpose, the cleanroom is being reconditioned to better than class 1000 by M. Kallander and M. Huehn in collaboration with PNNL.

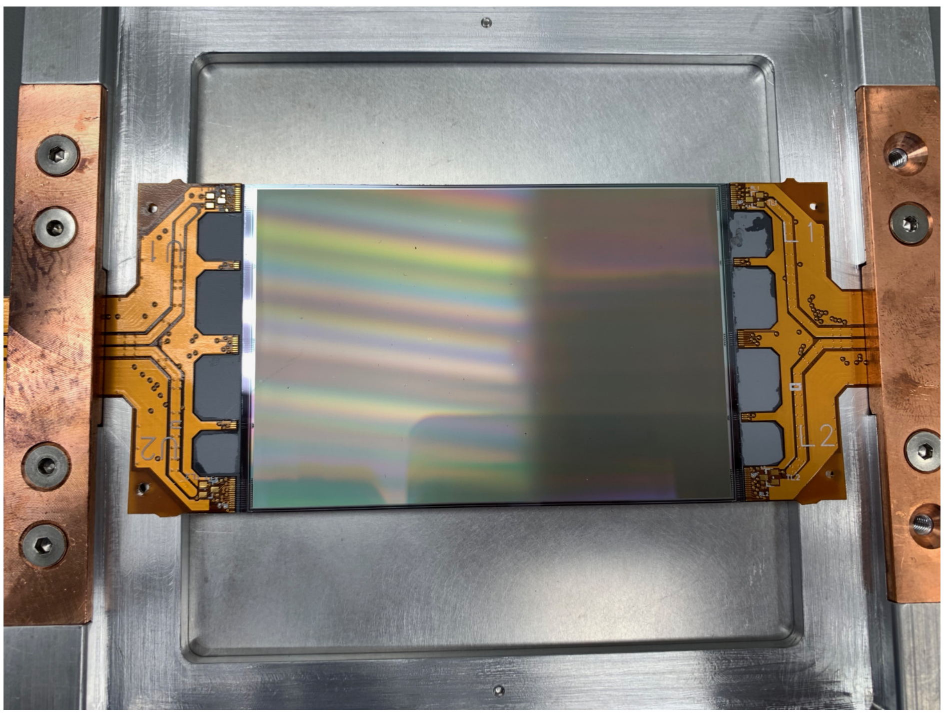

Figure 5.6-2. A fully packaged 6000 × 4000 pixel dual amplifier CCD.

A second clean-room is being prepared at CENPA (located at the NPL building) for DAMIC-M CCD characterization and as a test bed for the electronics. It will be a class 10000 cleanroom. A second test chamber has been built for this purpose. The chamber consists of a cryostat from Kurt Lesker, a CCD electronics control system from Astronomical Research Cameras, Inc. and a cryocooling solution designed by M. Huehn. The test setup is fitted with two resistance-temperature devices (RTD sensors). The control algorithm from the previous chamber was adopted to cool or heat a CCD package at 3 °C per minute to bring a CCD down to the cryogenic conditions essential for its operation or up to room temperature for maintenance. The system is now operational and awaits installation and integration inside the new cleanroom.

5.7 Measurement of the activation rate of cosmogenic ^{3}H in silicon on the surface

J. Amsbaugh, A.E. Chavarria, P. Mitra, A. Piers, and outside collaborators*

Tritium (^{3}H) produced in the bulk silicon of CCDs by cosmic rays can be a problem for the DAMIC-M experiment because the signals from the low-energy β particles constitute an irreducible background for the dark matter search. Tritium will accumulate in the silicon crystal starting when the ingot is pulled, throughout wafering and CCD fabrication, until the final devices are brought to the Modane Underground Laboratory (LSM). To successfully plan the construction of the DAMIC-M experiment, we are measuring the activation rate of cosmogenic ^{3}H in silicon to determine the maximum time that the CCD silicon can spend on the surface before ^{3}H decays become a limiting background for the experiment.

In September 2018, we irradiated three 8-megapixel CCDs at Los Alamos Neutron Science Center (LANSCE) [1]. The neutron flux was tuned to mimic the cosmic-ray energy spectrum but with much higher intensity (Fig. 5.7-1a). We acquired dark images with the irradiated CCDs to perform spectroscopy of the β particles detected in the bulk silicon of the devices and measure the ^{3}H decay rate. By scaling the quantity of ^{3}H activated in the CCD by the relative neutron fluence, we can obtain the cosmogenic activation rate.

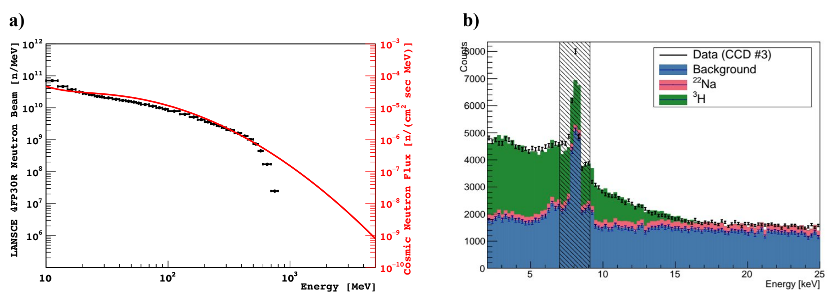

Figure 5.7-1. a) Comparison between the energy spectrum of the LANSCE neutron beam used for CCD irradiation and the cosmic neutron flux. b) Fit to the energy spectrum of β particles in the irradiated CCD data with Monte Carlo templates that include a realistic model of the degraded CCD response.

Over the past year, we focused on understanding several important systematic effects in our experiment. One notable complication is that a significant fraction of the tritons produced in the bulk silicon have sufficient kinetic energy to be ejected out of the thin (0.68-mm-thick) CCDs. Likewise, a fraction of tritons produced up the beam, e.g., in the thin aluminum covers protecting the CCDs, are implanted in the devices.

*R. Bunker, R. Saldanha, and H.M. Tsang (Pacific Northwest National Laboratory); A. Matalon, P. Privitera, and R. Thomas (The University of Chicago); S. Elliott (Los Alamos National Laboratory).

[1] CENPA Annual Report, University of Washington (2019) p. 143.

We performed a series of `Geant4` simulations with various nuclear physics models to evaluate these fractions and estimate a suitable correction to the measured ^{3}H decay rate to obtain the number of tritons produced in the bulk silicon of the devices. A second challenge was the simulation of the response of the CCDs, which degraded significantly because of the intense irradiation. For example, charge transfer efficiency in the CCD pixel array deteriorated, while the dark current increased [1]. Thus, we had to model these instrumental effects and incorporate them in the templates used to fit the energy spectrum of the observed β particles. Fig. 5.7-1b shows a recent fit to the CCD data spectrum with the latest templates, demonstrating clear spectral evidence for ^{3}H decay.

Data analysis is almost finalized and we expect to publish soon our results for the cosmogenic activation rate of ^{3}H in silicon.

[1] K. Dawson *et al.*, IEEE Trans. Nucl. Sci. **55**, 1725 (2008).

6 Education

6.1 Use of CENPA facilities in education and coursework at UW

B. W. Dodson

CENPA remains a cornerstone of UW physics education, involving undergraduate and graduate students in a wide range of applied methods in modern physics experimentation and general lab safety. CENPA's variety of on-site operations and off-site experiment collaborations offer UW students unique opportunity to make meaningful contributions to physics research and engineering.

Students involved in CENPA research receive specialized training mandated through laboratory PI's and UW's Environmental Health & Safety (EH&S) training programs[1] (Sec. 6.3). Student researchers are immersed in collaborative efforts, earning essential academic abilities in group cooperation and science communication. Access to the electronics shop, student machine shop, chemistry and a variety of other laboratory spaces gain students advantageous skills relevant in engineering and technical industries. CENPA has also sustained a continued presence in UW curriculum since 2011 with a graduate-level laboratory course on nuclear physics with special interest in accelerators and radiation detection, PHYS 575/576 *Radiation: Sources, Detectors and Safety* (Sec. 6.2).

We also offer educational group tours to interested schools and organizations adapted for a range of grade levels to inspire interest in experimental physics, especially in young visitors (Fig. 6.1-1). Historically, tours have encouraged visiting students to get further involved in CENPA research activities— notably visitors from the Conference for Undergraduate Women in Physics[2] (CUWiP, January 2019) have since joined CENPA research collaborations.

Figure 6.1-1. Scout BSA Troop 90 of Everett visit CENPA as part of earning their Nuclear Science Merit Badge.

[1] Environmental Health & Safety, https://ehs.washington.edu/training

[2] Conference for Undergraduate Women in Physics, https://www.aps.org/programs/women/workshops/cuwip.cfm

6.2 Accelerator-based lab class in nuclear physics

B. W. Dodson, A. García, E. B. Smith, and D. I. Will

As part of UW physics evening master's program, CENPA hosts *PHYS 576 Radiation: Sources, Detectors and Safety*[1]. Consisting of lectures and lab sessions, PHYS 576 offers accessible and uniquely engaging education in nuclear theory, research, and application in the local workforce. Emphasis on relevant applied methods of nuclear physics experimentation supports professional development for students already working or interested in growing aerospace and technical industries. (Fig. 6.2-1).

Figure 6.2-1. PHYS 576 Autumn 2019 Lab Group A. Working professionals enroll in PHYS 576 for development in their technical fields.

Laboratory sessions collectively offer each student hours of hands-on experience with experimental equipment including the Van De Graaff accelerator, an array of particle detectors, nuclear instrumentation electronics, and data acquisition systems (Fig. 6.2-1).

Lectures are 90 minutes once a week followed by 90-minute small group lab sessions. Supported by professional engineers, the following list of subjects are covered:

1. The atomic nucleus. Basic nuclear physics, nuclear energy, orders of magnitude.
2. Attenuation of photon radiation. Solid state detectors (Ge and Si).
3. Ranges of ions and electrons. The weak interaction. Radioactivity, radiation damage, and health risks (α, β, γ, and neutron activity).
4. Counting statistics.
5. Deciphering a mystery γ spectrum measured using a Ge solid-state detector. Gauging the level of radioactivity and assessing health risks.

[1] PHYS 576, Radiation: Sources, detectors, and Safety, https://phys.washington.edu/courses/2019/autumn/phys/576/b

6. 9 megavolt Tandem accelerator operation, duoplasmatron ion source function, and ion beam optics. Tuning beam through our own Tandem Van de Graaff accelerator.
7. Rutherford back-scattering (RBS) spectra measured by scattering accelerated protons off of foil targets and into Si solid-state detectors. Deciphering a mystery spectrum to determine the material contents of a mystery foil (Fig. 6.2-2 *Left*).
8. Fission and fusion. Nuclear reactors, nuclear astrophysics (nucleosynthesis in stars).
9. Basics of the Shell Model. Approximate predictions using simple models, using quantum numbers, predicting decay rates.
10. Searching for new physics with ^{6}He.
11. Nuclear Resonance. Resonance energy of ^{27}Al(p,γ)^{28}Si nuclear reaction determined by irradiating an aluminum target with accelerated protons and detecting the resulting γ's in a high purity germanium (HPGe) solid-state detector (Fig. 6.2-2 *Right*).
12. Tour of Seattle's Boeing accelerator facilities. A glimpse of accelerator science in the modern workforce.

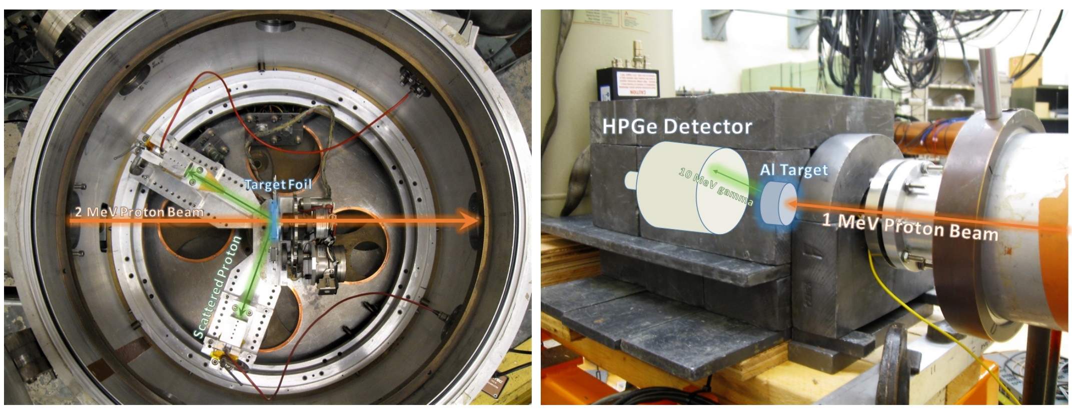

Figure 6.2-2. *Left*: RBS setup indicating 2-MeV protons (orange) incident on a thin foil target yielding back-scattered protons (green) detected in Si solid-state detectors. *Right*: ^{27}Al(p,γ)^{28}Si nuclear resonance setup indicating 1 MeV incident protons (orange) incident on Aluminum target yielding resonance emission γ's (green) detected in an HPGe solid-state detector.

Students are uniquely guided through experimental problem solving, represented most recently in Autumn quarter 2019 when engineering staff upgraded experimentation configuration to better demonstrate ^{27}Al(p,γ)^{28}Si nuclear resonance energy as described (Fig. 6.2-2 *Right*). Observance of emerging and disappearing peak resonance gammas via scanning incident proton energy was shrouded by protons backscattering off of the aluminum foil target and interacting with surrounding aluminum housing. At a certain energy threshold, backscattered protons traveled some depth into the thick aluminum housing before reaching resonance energy– resulting in a cascade of gammas undisguised from the intended target. Extrapolating from learned RBS concepts, students were able to identify the physics at play. Ultimately this issue resolved by shielding the path to exposed aluminum with a copper washer, the idea being any resonance in copper would be discernible enough to the ^{27}Al(p,γ)^{28}Si resonance energy.

6.3 Student training

J. F. Amsbaugh, B.Ẇ. Dodson, G. T. Holman, D. R. Hyde, D. A. Peterson, E. B. Smith, T. D. Van Wechel, and D. I. Will

CENPA instills a high standard of student training in all laboratory and research operations. Completion of general and specific laboratory safety classes mandated through EH&S[1] training programs are required for code-enabled building access. Further access to machine shops, chemistry laboratories, and general experimental laboratories requires specialized, hands-on training from professional CENPA staff and faculty.

Students involved in CENPA research and engineering efforts receive dynamic instruction in a wide range of technical subjects such as CAD design and simulation software, safe machining, cryogenic fluids (safety, liquefaction, dispensing, delivery, and transport), electrical power (high voltage, high current systems), compressed gases (safe handling, application), vacuum technology, hoisting and rigging, high magnetic fields, nuclear instrumentation, radiation detection and measurement, radiation safety, and radioactive sources (Fig. 6.3-1).

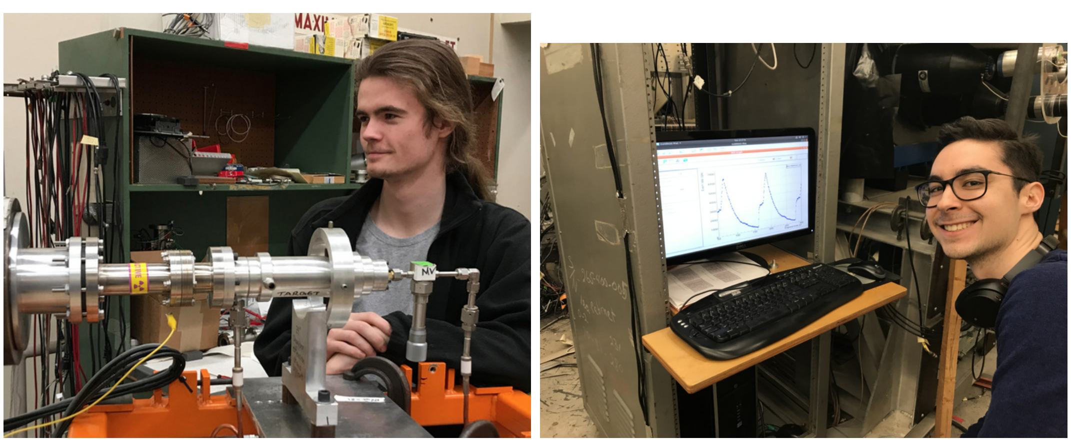

Figure 6.3-1. Undergraduate students Noah Hoppis *(left)* and Michael Higgins *(right)* display their own engineered experiment setup and data acquisition station for ^{19}Ne cold trap (Sec. 3.13). CENPA students get unique opportunity to forefront all aspects of experiment coordination, design, build, data acquisition, and data analysis.

[1]Environmental Health & Safety, https://ehs.washington.edu/training

The CENPA student machine shop widely encourages students, engineers and faculty alike to be trained in machine shop safety and specialized machine tool operation. Detailed and documented training is offered weekly from a retired staff instrument maker and is required for each specific piece of equipment. Notably available for general use includes lathes, milling machines, drill presses, saws, grinders, a metal sheer and breaker, hand tools, and various power tools. Additional instruction is given for the use computer-aided fabrication machines for more complicated parts; namely our Southwestern Industries CNC milling machines (a TRAK KE 2-Axis and a TRAK DMPSX2P 3-Axis), along with our KERN HSE large format laser cutter system (purchased with UW Student Technology Fee (STF) grant).

The CENPA electronics shop is a shared workspace staffed with highly experienced engineers available to assist students with soldering, wiring, and the use of basic electrical and electronic components for their application and general education. More specialized training and instruction in Electronic Design Automation software for producing prototype Printed Circuit Boards (PCBs) and utilization our UV ProtoLaser (purchased with STF grant) is provided to any upon request. Any trained UW student desiring to fabricate prototype PCBs for their research project is welcome to use the ProtoLaser.

Central and historic to the spirit of CENPA, engineers encourage students to receive operational training of our 9-MegaVolt FN Tandem Van de Graaff accelerator (Sec. 7.1) and duoplasmatron ion source. Undergraduate and graduate students learn the theory and mechanisms of ion beam generation, megavolt potentials beam optics, tuning the ion beam through the accelerator, and transporting the beam to an experimental target. Trained students are qualified to operate the accelerator for their research and serve as crew operators during sustained 24-hour experiment runs for other research efforts.

7 Facilities

7.1 Van de Graaff accelerator and ion-source operations and development

B. W. Dodson, K. W. Fitzsimmons, K. Hansen, G. C. Harper, M. E. Higgins, N. C. Hoppis, M. A. Huehn, J. Pedersen*, D. A. Peterson, E. B. Smith, T. D. Van Wechel, and D. I. Will

This annual reporting period had extensive operation of the Ion Sources DECK Direct Extraction Ion Source (DEIS) for implantation, and likewise of the Tandem accelerator in TERMINAL ION SOURCE (TIS) mode. TIS mode has not been utilized since 2010, and required extensive learning and work by engineering staff. We successfully implanted $^{21}Ne^{+}$ into 9 Ta targets, $^{22}Ne^{+}$ into 3 Ta targets, and $^{20}Ne^{+}$ into 2 Ta targets. The Tandem accelerator was entered a total of 5 times: twice for configuring the accelerator for TIS mode, once to configure the accelerator back to TANDEM mode, and twice to refill the supply of hydrogen gas for TIS.

On April 16, 2019, the Tandem accelerator tank was closed after having been open since November 11, 2018. The weeks in April were spent configuring the Tandem to operate with an internal source of positive $^{1}H^{+}$ ions and able to provide these 1 MeV ions at a nominal current of 50 uA to targets in the 30-degree left (30L) beam line of CAVE 1 for the $^{21}Ne(p,\gamma)^{22}Na$ (or Ne-21) experiment. The normal TANDEM mode operation would not be able to deliver more than 10 uA.

At its core, the TIS mode consists of an rf plasma ion source installed in place of the stripper foil mechanism normally mounted on the side of the stripper box of the Tandem TERMINAL, which is the midpoint between the two accelerating columns that is charged to high positive voltages. The ion source has a quartz plasma tube externally strapped with 2 copper electrodes attached to an rf oscillator coil, but 180-degrees out of phase with each other. Hydrogen gas is leaked into the vacuum environment of the quartz tube at an end that is biased positive causing $^{1}H^{+}$ in the plasma to be extracted out the other end. The tube is positive biased with respect to the TERMINAL, providing acceleration of the $^{1}H^{+}$ into the stripper box. An Einzel lens structure between the tube and box provides focusing. A bending magnet using permanent magnets to steer the beam into the accelerator center-line, and horizontal and vertical electrostatic steerers were installed in the stripper box, whose input aperture was removed to allow better vacuum pumping of the gas leak source. The high voltage (HV) power supplies (PS), isolation transformer, and bottles of hydrogen gas are all installed in the TERMINAL. Control and sense signals from the TERMINAL computer are connected, gas connections made, and all vacuum and gas connections leak checked.

The $^{1}H^{+}$ emitted by the TIS have about 13 keV energy, and would normally be

*Presently at Microsoft, Seattle, WA.

entering an accelerator column section, tube #3, that is built to accommodate ions of 100's or 1000's of keV using a design called spiral inclined plane. Ions are accelerated by the electric field between adjacent column planes at different potentials. Such an accelerating tube will have a low transmission for 13 keV ^{1}H$^+$, so this approximately 10' long tube #3 was removed and replaced by a tube with straight planes, which is required for ions being accelerated from order 10 keV to several MeV. The accelerator column preparation, uncoupling, re-coupling, aligning, and passing through the tank portals of these 10' long, heavy, fragile tubes required a team of people.

Additionally, the correct shorting together of many of this first accelerating planes of tube #3 and the last approximately 3/4 of spiral incline planes of tube #4 was required to achieve the maximum transmission of 1 MeV ^{1}H$^+$ out of the Tandem accelerator. Shorting of adjacent accelerating planes was achieved by placing ball bearings between the field hoops connected to the planes. Planes are normally separated by column resistors that allow adjacent planes to be at different voltages producing an electric field between the planes. The second Tandem tank entry was performed to remove some of the plane shorting ball bearings of the first planes of tube #4 to increase the total high energy (HE) column resistance, which allows the TERMINAL charging system to provide enough current to maintain a nominal 1 MV while extracting nominal HE cup current of 75 uA yielding nominal 50 uA currents on target. The exact ball bearing placements are recorded.

Learning to produce a TIS plasma and extract large currents of ^{1}H$^+$ from it took several days to master and more was learned over the many weeks of operation. Detailed operation parameters and qualitative understandings were recorded. Configuration of the Tandem accelerator to TIS mode required approximately 10 days of tank entry.

The more than 2 full months, June and July, of almost continuous TIS operation of the Tandem accelerator providing beam for the Ne-21 experiment required third and fourth Tandem tank entries, each to install twin cylinders of about 150 psig each of hydrogen gas to supply the TIS.

Configuring the Tandem accelerator back to TANDEM mode operation required a fifth Tandem tank entry with 20 days of work. Developing a method for proper alignment of the TERMINAL steerer plates and stripper foils shield box entry & exit collimators with the axis of the stripper foil frames center and tube #3 axis (i.e. accelerator z-axis) was particularly critical, as there was nothing recorded previously. The method was thoroughly documented this time.

Coincident with the 2 months of Tandem TIS operations, the Ion Source DECK and DEIS performed nearly continuous implantation of Ta targets with 50 or 45 keV isotopes of Ne. The 24V DC motor of the DEIS gas leak valve drive failed due to substantial drag of the planetary gear reducer unit caused by aged grease, which caused a 24V DC PS to fail as well. The gear reducer unit was disassembled, cleaned, lubricated with lithium grease, and re-assembled. A new motor was installed, and the 24V DC PS was replaced, which is also the PS for the leak valve position read back potentiometer. The Extract electrode HV PS failed, requiring a temporary HV PS to be installed with modified signal controls and modified output coax cable socket.

During the annual reporting period from April 1, 2019, to March 31, 2020, the Tandem Pelletron chains operated 1165 hours, the sputter-ion-source (SpIS) operated 0 hours, and the duoplasmatron direct-extraction-ion source (DEIS) operated 844 hours. Additional statistics for accelerator operations are given in Table 7.1-1. Tandem accelerator produce beams of ions originating from the DEIS included 10 MeV $^{2}H^{+}$ for the ^{6}He-CRES ^{19}Ne experiment, nominally 1 MeV $^{1}H^{+}$ for the $^{21}Ne(p,\gamma)^{22}Na$ experiment and PHYS 576 class, and 2.0 MeV $^{1}H^{+}$ for the PHYS 576 class.

ACTIVITY SCHEDULED	**DAYS SCHEDULED**	**PERCENT of TIME**
Nuclear-physics research, accelerator	69	18.9
Ion implantation	32	8.8
Development, maintenance, or crew training	108.5	29.7
Grand total	209.5	57.4

Table 7.1-1. Tandem Accelerator Operations April 1, 2019, to March 31, 2020.

7.2 CENPA Instrument Shop

T.H. Burritt and J.H. Elms

The CENPA Instrument shop supports the experiments of this group, and outside users. We are requested to do rush jobs and work with all levels of staff, facility, and students. We make designs and fabricate. Some examples of the parts we produce are below.

The CENPA Instrument shop is manned by highly skilled instrument makers with decades of experience working in the research environment. Tom Burritt supports faculty, staff and students, gives advice and suggestions and makes sure what they want is feasible and cost effective. He works in designing and fabrication of ultrahigh vacuum systems, cryogenic components equipment operating in high magnetic fields, high and low voltage applications, hydraulics, and gas handling systems and mechanical devices. Jim Elms is our primary CNC operator wizard, welder and mechanical genius. Together we solve mechanical problems and give CENPA the ability to be a leading force in Physics. In addition to supporting CENPA we also machine parts for other groups at the University. The Astronomy department has asked for our help to get parts made for them. Some notable fabrications are shown in the images below.

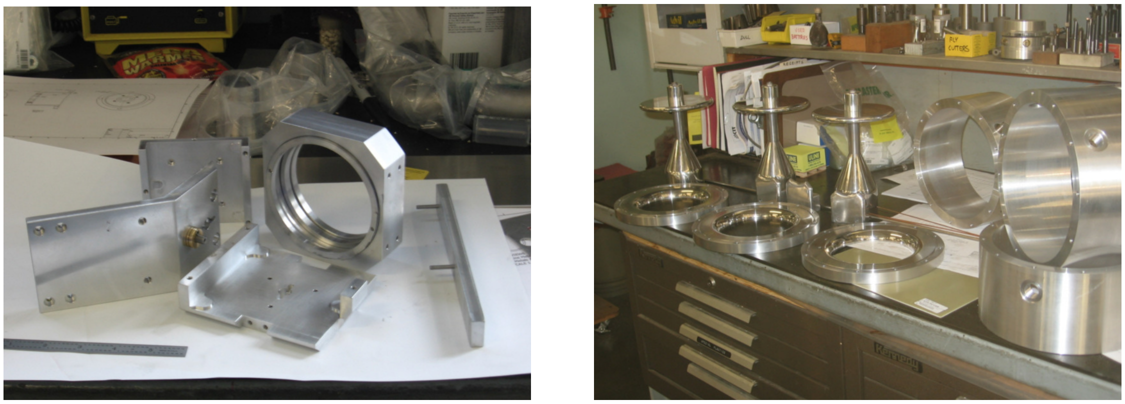

Figure 7.2-1. *Left*: Lens mount for Astronomy Department. *Right*: High-voltage components high polished for $g-2$.

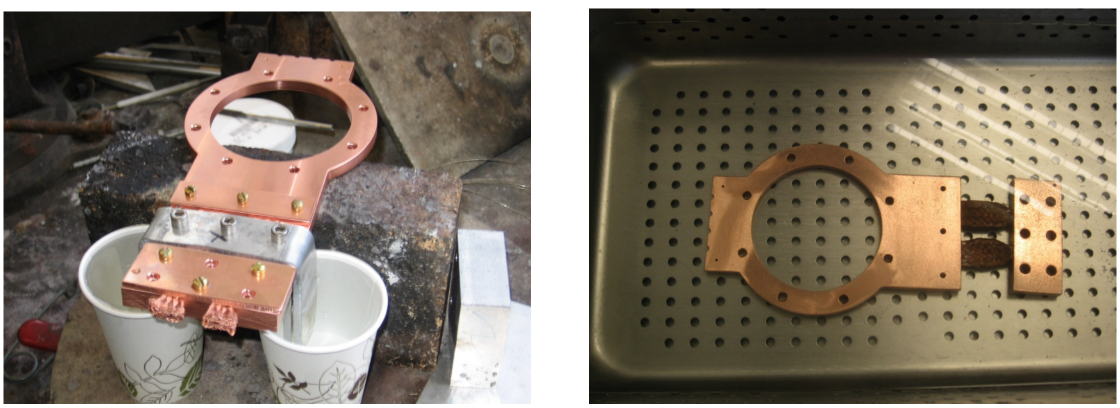

Figure 7.2-2. Soft solder to copper braid set up and cleaning for ^{6}He-CRES.

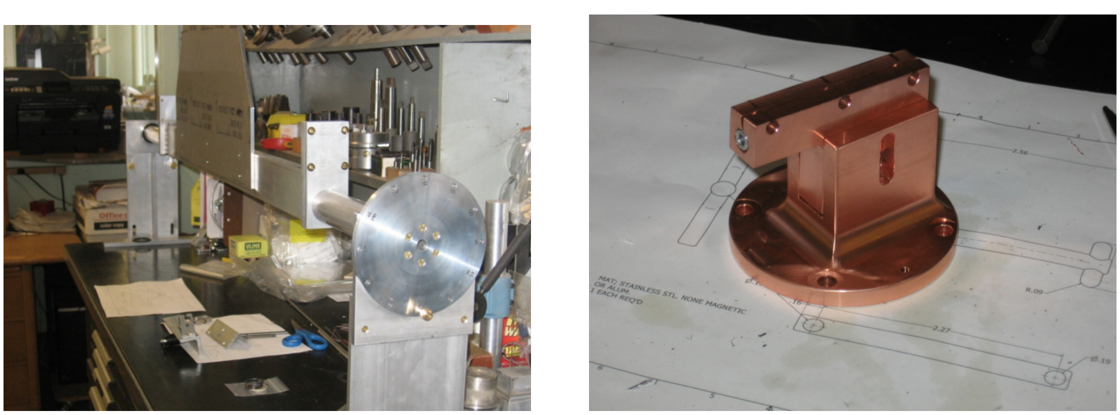

Figure 7.2-3. Field-mapping device and atomic-source cold-finger aperture for Project 8.

Figure 7.2-4. *Left*: Redesign and assembly for Orpheus. *Right*: New design set up for testing germanium crystal for LEGEND.

7.3 CENPA electronic shop

D. A. Peterson and T. D. Van Wechel

The electronics shop is responsible for the design and construction of new laboratory electronic equipment as well as the maintenance and repair of existing CENPA electronics. Projects undertaken by the electronics shop in the past year include the following:

1. Re-design, layout and construction of the $g-2$ kicker magnet power supply. Three units were constructed. Fig. 7.3-1

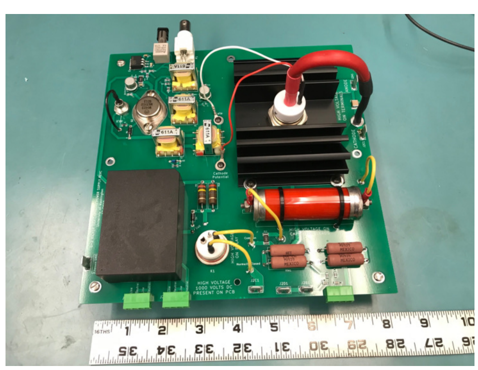

Figure 7.3-1. $g-2$ kicker magnet power supply.

2. A GHz bandwidth calibrated noise source was designed and constructed for testing of the ^{6}He-CRES DAQ system (Fig. 7.3-2)

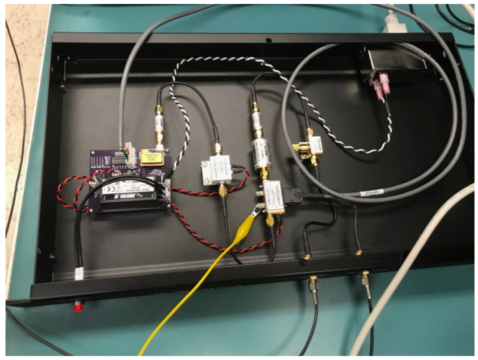

Figure 7.3-2. ^{6}He-CRES noise source.

3. Construction of DAMIC-M signal/power breakouts, cables, adapters and CCD battery bias supplies (Fig. 7.3-3).

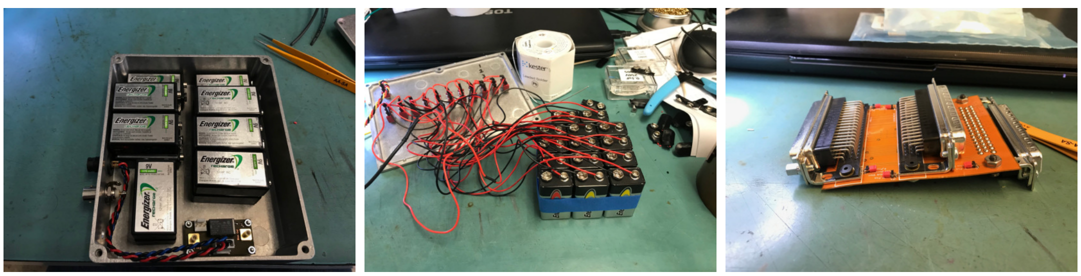

Figure 7.3-3. *Left and Center*: CCD battery bias supplies. *Right*: Vacuum-side polyimide flex adapter board for 6Kx4K CCDs.

4. Designed and constructed a five-channel amplifier for silicon photo-multiplier evaluation for the LEGEND project (Fig. 7.3-4)

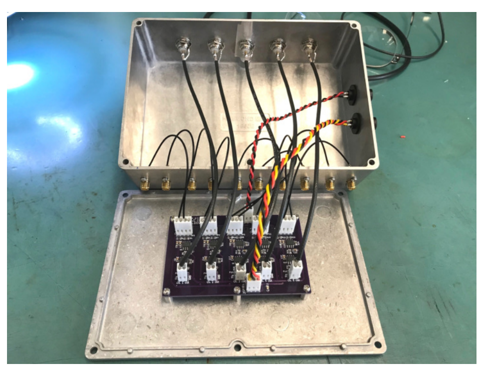

Figure 7.3-4. LEGEND five-channel amplifier.

5. Layout and construction of a system for LEGEND/CAGE that monitors temperature and turbo pump pressure along with decoding the serial-peripheral interface (SPI) readout of rotary/linear source position encoders (Fig. 7.3-5).

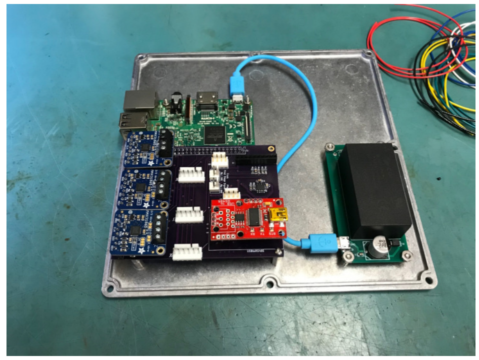

Figure 7.3-5. LEGEND/CAGE interlock/encoder readout.

7.4 Laboratory safety

B. W. Dodson, G. T. Holman, E. B. Smith, and D. I. Will

We continued safety compliance tracking and facility access policy.

We manage our current users (we generally have 150 active staff, faculty, students, postdocs, visitors, etc.) in our online user list (also known as "telephone list"). Once added to the telephone, the use will gain access to training and access to facility via door code. General visitors, collaborators, etc. sign in/out at the front office and must be escorted. The following is the general order of events:

1. Safety orientation - prior to adding user to telephone list (and hence gaining door code), the supervisor must walk the new user around the facility pointing our evacuation, personal protection equipment (PPE), first aid, fire extinguishers, automated external defibrillator (AED) - mounted in front lobby, etc.

2. Both user and supervisor will then sign the orientation paperwork and we file that paper copy in front office.

3. Front office administrator then adds user (with photo) to telephone list on website. In addition, the signed orientation document is saved in the users personnel file.

4. All CENPA users must complete generalized training, while others need specific based on their lab hazards. These training requirements are selected on the web page for each user.

5. A scheduled weekly task checks safety completion compliance as follows.

    - For each user/uwnetid, a required-training user array (user_array)is created based on the per-user safety requirements.
    - The EH&S database is queried directly for uwnetid and pushed onto array stack (training_array).

- For each entry (based on EH&S unique Master CourseID key) in (training_array), if it is in (user_array) that entry is removed from (user_array).
- There is some data massaging, for example training is checked "if current".
- The resultant array, is that user's required training still outstanding.
- If (user_array) is not empty, an email is generated to user with list of outstanding training requirements.
- If (user_array) is empty, training is completed and no email is sent to user.

6. Brittney Dodson completed Crane Rigging and Signal Person certification and is qualified to now train all personnel in crane and hoisting operation.

7. We continued to dispose of unused chemicals. This year we removed over 200 dated chemicals though EH&S hazardous-waste pickup.

8. Work continues in the Eöt-Wash Lab to carefully remove and decontaminate the decommissioned Rot-Wash spindle that contained Depleted Uranium (DU) bricks which have since been shipped to Pacific Northwest National Laboratory. The remaining spindle parts and surrounding housing are disassembled and bagged for radioactive waste disposal, or thoroughly decontaminated for retention, recycle, or waste.

9. Doug Will provided much assistance to the UW Radiation Safety Office (RSO) in collecting CENPA radioactive sources, placing in standardized containers, and identifying the containers with UW RSO UPC serial number sticker. A catalog spreadsheet of the serial numbered sources will be used to greatly improve CENPA source tracking.

7.5 Laboratory computer systems

G. T. Holman

CENPA is a mixed shop of Windows 7, 10, Mac OS X, and various Linux distributions. Windows 10 is installed on new workstations, but we are still running some Windows XP systems for data acquisition, DOS 6 on accelerator controllers, and an embedded Win 98 for a mechanical shop mill. As with every year, the IT focus was directed toward server consolidation, network security, process documentation and removal of redundant processes. We continue to utilize Xen virtualization for Autodesk Vault versions, ELOGs, wikis, collaboration calendars, and document servers. The CENPA website and research group web pages run on a Drupal 7 web framework. The NPL mail server still provides NPL presence but all email is relayed to UW e-mail hardware. Workstations connect to the UW delegated organizational unit (OU), which mostly removes the need to run a dedicated domain or LDAP server.

Two Dell 510 20-TB servers (Lisa and Marie) continue to offer user storage, print server capability, and improved backup policy. Linux, Windows, and Mac workstations are backed up to the 20-TB Marie raid farm, which is backed up offsite using UW Trivoli backup service. Lisa runs the Crash Plan Pro backup application which supports all operating systems and provides differential and encrypted backups. Whereas workstations rely on Crash Plan Pro for backups, all servers utilize rsnapshot. Marie provides 20 TB for research, user, and shared group data.

The NPL Data Center (NPLDC) provides legacy infrastructure supporting high-performance scientific-computing applications.

7.6 Building maintenance, repairs, and upgrades

I. Boeckstiegel, B. W. Dodson, E. B. Smith, and D. I. Will

During the 2019 calendar year, 175 work orders (WOs) were placed for the North Physics Laboratory buildings which house the CENPA research facility. For the Van de Graaff Accelerator Building, 79 total WOs included the following: 46 Preventive Maintenance/Repair/Alterations WOs (PM/R/Alts) by Facilities Services; 32 Service/Repair WOs (S/R) by CENPA staff; and 1 Alterations WOs (Alts) by CENPA staff. For the Cyclotron Building, 54 total WOs included the following: 40 PM/R/Alts WOs by Facilities Services, 14 S/R WOs by CENPA staff, and 0 Alts WOs requested by CENPA staff. For the CENPA Instrument Shop, 42 total WOs included the following: 35 PM/R/Alts WOs by Facilities Services, 7 S/R WOs by CENPA staff, and 0 Alts WOs by CENPA staff.

1. Water hammer in the hydronic heating system.

There has been a water hammer in the hydronic heating system for the Van de Graaff Accelerator Building high bay setup area and adjacent offices. This problem still has not been solved.

2. Replacement of fluorescent lamps with LED lamps.

An effort is ongoing to replace any failed fluorescent lamp fixtures (i.e. failed lamp ballasts), both indoor and outdoor, with LED lamp fixtures and lamps. The outdoor lights under the eaves are being preemptively replaced with LED fixtures and lamps at UW Electricians availability.

3. Two problems converged this year: the front sidewalk was so badly buckled as to be a trip hazard, and the water main beside the sidewalk failed.

The water main leak repair under the CENPA front lawn has been completed. During the repair, concrete sidewalk was removed. The area has been temporarily filled in with compressed gravel to allow walking, but will eventually be finished with a poured concrete surface.

4. Multistack Maglev (TurboCor) Chiller.

The Multistack Maglev chiller with FlexSys control system in RM 154, which provides chilled water for CENPA, is presently inoperable due to the differential water pressure sensor of chilled water input and output experiencing 100+ psig pressures, that are above of the sensor's 100 psig limit, which causes the sensor to output a value below the acceptable operating limit of the control system. UW Refrigeration Group has placed an order for a sensor with a 250 psig limit. However, there remains a question as to why the chilled water input and output pressures have climbed to values above 100 psig, such as a failure of the chilled water make-up regulator to maintain an appropriate base pressure of the chilled water system.

UW Refrigeration consultants visited CENPA, investigated the chilled water system, and are developing a proposal for an improved chilled water system. The improved system would use a Variable Frequency Drive (VFD) controlled chilled water pump motor, pressure sensors, and various automatic control valves.

5. Condenser water cooling tower fan.

UW Refrigeration will have UW Electricians install "Cool Blue" electrical line filters on the power feeds to the Condenser water cooling tower fan to reduce the high pitched noise that can be heard at certain fan motor drive frequencies, and which are indicative of wasted energy and possible destructive vibrations. If these line filters do not reduce the high pitched noise, an present Variable Frequency Drive (VFD) for the fan motor would be replaced with an updated VFD.

6. Office, laboratory and hallway floors were cleaned and waxed.
7. Windows and blinds were cleaned.

8 CENPA Personnel

8.1 Faculty

Eric G. Adelberger[1]	Professor Emeritus
Alvaro Chavarria[1]	Assistant Professor
John G. Cramer[1]	Professor Emeritus
Jason Detwiler	Associate Professor
Peter J. Doe	Research Professor
Sanshiro Enomoto	Research Associate Professor
Martin Fertl[2]	Research Assistant Professor
Alejandro García	Professor
Gerald Garvey[1]	Affiliate Professor
Jens H. Gundlach[1]	Professor
Blayne R. Heckel[1]	Professor
David W. Hertzog	Professor; Director
C. D. Hoyle[1,3]	Affiliate Assistant Professor
Peter Kammel	Research Professor
Jarek Kaspar	Research Assistant Professor
Peter Mueller[1]	Affiliate Professor
Diana Parno[1,4]	Affiliate Assistant Professor
R. G. Hamish Robertson	Emeritus Professor
Leslie J Rosenberg[1]	Professor
Gray Rybka[1]	Associate Professor
Derek W. Storm[1]	Research Professor Emeritus
Robert Vandenbosch[1]	Professor Emeritus
Krishna Venkateswara[1,5]	Acting Assistant Professor
John F. Wilkerson[1,6]	Affiliate Professor

[1]Not supported by DOE CENPA grant.
[2]Departed June 30, 2019. Associate Professor, Gutenberg University, Mainz, DE.
[3]Affiliated faculty, Humboldt State University, Arcata, CA.
[4]Affiliated faculty, Carnegie Mellon University, Pittsburgh, PA.
[5]Departed August 1, 2019. Currently Director of R&D at Paroscientific Inc., Redmond, WA.
[6]Affiliated faculty, University of North Carolina, Chapel Hill, NC.

8.2 CENPA external advisory committee

Robert McKeown[1]	Jefferson Laboratory
Daniel McKinsey[1]	UC Berkeley
Michael Ramsey-Musolf[1]	University of Massachusetts, Amherst

8.3 Postdoctoral research associates

Chelsea Bartram[2]	Benjamin LaRoque[2,3]
Nicole Crisosto[2,4]	Pitam Mitra[2]
Aaron Fienberg[5]	Elise Novitski
Brent Graner	Walter Pettus
Charlie Hagedorn[2]	Rachel Ryan[4]
Zachary Hodge[6]	Menglei Sun
Megan Ivory[7]	Clint Wiseman
Kim Siang Khaw[8]	Jihee Yang[2,9]

8.4 Predoctoral research associates

Ali Ashtari Esfahani	Joshua La Bounty
Yelena Bagdasarova[10]	John Lee[2,11]
Hannah Binney	Ying-Ting Lin[12]
Thomas Braine[2]	Brynn MacCoy
Micah Buuck[10]	Eris Machado[13]
William (Drew) Byron	Ethan Muldoon
Raphael Cervantes[2]	Rachel Osofsky[14]
Nick Du[2]	Alexander Piers[2]
Ian Guinn[15]	Michael Ross[2]
Madeleine Hanley[16]	Nicholas Ruof

[1] CENPA External Advisory Committee formed January 2014.
[2] Not supported by DOE CENPA grant.
[3] Departed March, 2020.
[4] Departed January, 2020.
[5] Departed August, 2019.
[6] Arrived March, 2020. Currently working on location at Fermilab.
[7] Departed May, 2019.
[8] Departed September, 2019.
[9] Arrived January, 2020.
[10] Graduated July, 2019.
[11] Graduated March, 2020.
[12] Graduated December, 2019.
[13] Departed December, 2019.
[14] Graduated December, 2019.
[15] Graduated June, 2019.
[16] Departed June, 2019.

Heather Harrington	Erik Shaw[1]
Jason Hempstead	Jermaine Wegner[1,2]
Alexandru Hostiuc	

8.5 Undergraduates

Yifei Bai	Gravity	Hagedorn, Advisor
Carson Blinn	Gravity - New Wash/Dark EP	Hagedorn, Advisor
Lars Borchert	Muon g-2	Hertzog, Advisor
Ningyi Chen	COHERENT	Detwiler, Advisor
Jeff Chrisope	LPKF	Peterson, Advisor
Samuel D'Ambrosia	DAMIC	Mitra, Advisor
Jake Dougherty	Neutron Detection	Smith, Advisor
Madison Durand	COHERENT, Project 8	Detwiler, Advisor
Fernando Eizaguirre	ADMX	Rybka, Advisor
Katherine Evans	HPGe Gamma Detector	Smith, Advisor
Callum Farrell	Majorana	Detwiler, Advisor
Roland Farrell	^{6}He	Garcia, Advisor
Sean Fell	ADMX	Rybka, Advisor
Hans Gaensbauer	DAMIC	Chavarria, Advisor
Jonathan Gort	Project 8	Pettus, Advisor
Jan Graefje	ADMX	Rybka, Advisor
Michaela Guzzetti	ADMX	Rybka, Advisor
Keira Hansen	COHERENT	Detwiler, Advisor
Michael Higgins	^{6}He-CRES	Garcia, Advisor
Noah Hoppis	^{6}He-CRES	Garcia, Advisor
Adit Jain	ADMX	Rybka, Advisor
Dinggan Jin	Ne21pg	Garcia, Advisor
Jared Johnson	Gravity	Hagedorn, Advisor
Joshua Johnson	LPKF	Peterson, Advisor
Emily Joseph	Gamma Ray Spectroscope	Smith, Advisor
Claire Komori	ADMX	Rybka, Advisor
Cedric Kong	LPKF	Peterson, Advisor
Hima Korandla	ADMX	Rybka, Advisor
Kavic Kumar	Eot-Wash	Gundlach, Advisor
Alyssa Lee	ADMX	Rybka, Advisor
Jocelin Liteanu	Majorana	Detwiler, Advisor

[1]Not supported by DOE CENPA grant.
[2]Arrived January, 2020.

Alexandra Lockwood	Gravity	Hagedorn, Advisor
Nicole Man	ADMX	Rybka, Advisor
Cayenne Matt	Gravity	Hagedorn, Advisor
Olivia McGoldrich	COHERENT	Detwiler, Advisor
Parashar Mohapatra	ADMX	Rybka, Advisor
Julian O'Leary	Radiation Monitoring	Detwiler, Advisor
Axl O'Neal	HPGe Gamma Detector	Smith, Advisor
Nicholas Orndorff	Gravity - Eot Wash	Hagedorn, Advisor
Yujin Park	ADMX	Rybka, Advisor
Elliott Phillips	Project 8	Fertl, Advisor
Daniel Primosch	ADMX	Rybka, Advisor
Matthew Stortini	^{6}He	Garcia, Advisor
MinJung Sung	^{6}He	Garcia, Advisor
Courtney Symmes	COHERENT	Detwiler, Advisor
Zhizhong Tao	^{6}He-CRES	Garcia, Advisor
Colin Watson	Radiation Monitoring	Detwiler, Advisor
Colin Weller	LIGO/Gravity	Hagedorn, Advisor
Emilee Wurtz	DAMIC	Chavarria, Advisor
Zachary Wuthrich	Majorana	Detwiler, Advisor
Mingxun Xie	Ne21pg	Garcia, Advisor
Anni Xiong	^{6}He-CRES	Garcia, Advisor
Katrina Yang	Formula	Peterson, Advisor
Ruoyu Zhang	DAMIC	Chavarria, Advisor
Leo (Zining) Zhu	ADMX	Rybka, Advisor
Brooke Ziegenhagen	DAMIC	Mitra, Advisor
Regan Zite	^{6}He	Garcia, Advisor

8.6 Visitors and volunteers

Gordon Ball	Ne21pg Visitor
Gwen Bayarbaatar	KATRIN Visiting Volunteer
Doug Beck	Visitor
Christian Boutan	ADMX Visitor
Daniel Bowring	ADMX Visitor
Jay Briggs	COHERENT Volunteer RA
Raahul Buch	Volunteer RA ^{6}He
Nicholas Buzinsky	Visiting RA Project 8
Alexander Cable	LPKF Visitor
Aaron Chou	ADMX Visitor
Robin Coleman	Ne21pg Visiting RA
Edward Daw	ADMX Collaboration Member
Pierre Fountaine	^{6}He-CRES Undergraduate Intern
Shanti Garman	LPKF Visitor

Julieta Gruszko	MJD/LEGEND Visiting Postoc
Patrick Harrington	Visiting RA ADMX
Jeremy Hartse	Project 8 UW Visitor
Mohamed Kamil	Ne21pg Visiting RA
Eva Kasandra	Ne21pg Visiting RA
Felix Keil	Visiting RA $g-2$
Cedric Kong	LPKF Visitor
Yasuo Kuga	LPKF Visitor
Erik Lentz	AMDX Visiting Postoc
Rachel Leu	Formula Undergraduate
Xinran Li	Selena Visiting RA
Alec Lindman	Project 8 Visiting RA
Xiayu Linpeng	LPKF Visitor
Ndinanyi Justice Mukweveo	Ne21pg Visiting RA
Gulden Othman	Visiting RA LEGEND
Lisa Pellerin	LPKF Visitor
Mitchell George Perry	ADMX Visiting RA
Bhivek Singh	Visitor Ne21pg
Andrew Sonnenschein	ADMX Visitor
Matthew Sorensen	LPKF Vistor
William Soyars	ADMX Visitor
David Tanner	ADMX Visitor
Jonathan Tedeschi	He-6 CRES Visitor
William Terrano	Gravity Visiting RA
Catriona Thomson	ADMX Visiting RA
Smarajit Triambak	Beamline Project Visitor
Steven Troy	Working with Eric Smith, Teaching Associate
Matthew Turner	Eot-Wash, Laser Volunteer
Esmond Craig Vyfers	Ne21pg Visiting RA
Talia Weiss	Project 8 Visiting RA
James Whitehead	LPKF Visitor
Fred Wietfeldt	He-6 CRES Visiting Professor
Nathan Woollett	ADMX Visitor
Nathan Yang	LPKF Visitor
Jihee Yang	ADMX Visiting Research Associate
Andrew Ziegler	Project 8 Visiting RA

8.7 Administrative staff

Ida Boeckstiegel	Office Administrator
Samuel Hoffman[1]	Fiscal Specialist
Pamela Rhodes[2]	Fiscal Specialist
Libby Wang[3]	Fiscal Specialist
Joseph Wang[4]	Fiscal Specialist

8.8 Professional staff

John F. Amsbaugh[5]	RS/E4	Engineering, vacuum, cryogenics design
Tom H. Burritt	RS/Engr Sr	Precision design, machining
Brittney Dodson	RS/E1	ADMX safety officer, engineering
Gary T. Holman	Associate Director	Computer systems
Michael Huehn	RS/E1	DAMIC and Project 8
Matthew Kallander	RS/E Assistant	DAMIC and Project 8
Seth A. Kimes[3]	RS/E2	ADMX Dilfridge, Liquifier
Grant H. Leum	RS/E1	ADMX Liquifier
Joben R. Pedersen[3]	RS/E2	Accelerator, ion sources
Duncan J Prindle	RS/E4	Muon research, Cluster admin
Eric B. Smith	RS/E3	Accelerator, ion sources
H. Erik Swanson	RS/EP	Precision experimental equipment
Timothy Van Wechel	RS/E4	Analog and digital electronics design
Douglas I Will	RS/Engr Sr	Cryogenics, ion sources, buildings

8.9 Technical staff

James H. Elms	Instrument Maker
David A. Peterson	Electronics Technician

[1] Front office temp Jan-Mar., 2020.
[2] Front office temp Sept-Nov., 2019.
[3] Departed June, 2019.
[4] Front office temp Nov-Dec., 2019.
[5] Retired March, 2020.

8.10 Part-time staff and student helpers

David R. Hyde	Student shop manager
Greg Harper	Accelerator engineering, consultant
Hendrik Simons	Instrument maker
Kyle Fitzsimmons	Lab Tech 1
Brandon Iritani	Lab Tech 2
Kris Knutsen	Lab Tech 1
Dylan Soh	Undergraduate Research Assistant (URA)
Madeline Walters	URA
Henry Gorrell	URA
Jonathan Gort	URA
Kiera Hansen	URA
Michael Higgins	URA
Timothy Mathew	Lab Tech 1
Matthew Stortini	Lab Tech 1
Yadi Wang	URA
Sierra Wilde	URA

9 Publications

Publications and presentations with a date of 2019 or 2020 are included below. Some entries from early 2020 may therefore also appear in the 2019 Annual Report.

9.1 Published papers

[1] K. Altenmüller et al., "Gamma-induced background in the KATRIN main spectrometer", The European Physical Journal C **79** (2019), DOE Supported.

[2] B. Aharmim et al., "Measurement of neutron production in atmospheric neutrino interactions at the Sudbury Neutrino Observatory", Phys. Rev. D **99**, 112007 (2019), DOE Supported.

[3] M. Aker et al., "Improved Upper Limit on the Neutrino Mass from a Direct Kinematic Method by KATRIN", Phys. Rev. Lett. **123**, 221802 (2019), DOE Supported.

[4] A Ashtari Esfahani et al., "Locust: C++ software for simulation of RF detection", New Journal of Physics **21**, 113051 (2019), DOE Supported.

[5] B. Aharmim et al., "Cosmogenic neutron production at the Sudbury Neutrino Observatory", Phys. Rev. D **100**, 112005 (2019), DOE Supported.

[6] Y.-T. Lin et al., "Beta Decay of Molecular Tritium", Phys. Rev. Lett. **124**, 222502 (2020), DOE Supported.

[7] A. Anastasi et al., "The laser-based gain monitoring system of the calorimeters in the Muon $g-2$ experiment at Fermilab", JINST **14**, P11025 (2019), DOE Supported.

[8] K. S. Khaw et al., "Performance of the Muon $g-2$ calorimeter and readout systems measured with test beam data", Nucl. Instrum. Meth. **A945**, 162558 (2019), DOE Supported.

[9] A. A. Esfahani et al., "Electron radiated power in cyclotron radiation emission spectroscopy experiments", Phys. Rev. C **99**, 055501 (2019), DOE Supported.

[10] A. A. Esfahani et al., "Cyclotron radiation emission spectroscopy signal classification with machine learning in Project 8", New J. Phys. **22**, 033004 (2020), DOE Supported.

[11] S. I. Alvis et al., "Search for neutrinoless double-β decay in ^{76}Ge with 26 kg yr of exposure from the Majorana Demonstrator", Phys. Rev. C **100**, 025501 (2019), DOE Supported.

[12] S. I. Alvis et al., "Multisite event discrimination for the Majorana Demonstrator", Phys. Rev. C **99**, 065501 (2019), DOE Supported.

[13] J. G. Lee et al., "New Test of the Gravitational $1/r^2$ Law at Separations down to 52 μm", Phys. Rev. Lett. **124**, 101101 (2020).

[14] T. Braine et al., "Extended Search for the Invisible Axion with the Axion Dark Matter Experiment", Phys. Rev. Lett. **124**, 101303 (2020), DOE Supported.

[17]X. Sun et al., “Improved limits on Fierz interference using asymmetry measurements from the Ultracold Neutron Asymmetry (UCNA) experiment”, Phys. Rev. C **101**, 035503 (2020).

9.2 Papers submitted or to be published

[18]M. Aker et al., *First operation of the KATRIN experiment with tritium*, 2019, DOE Supported.

[19]R. G. H. Robertson and V. Venkatapathy, “Shakeup and shakeoff satellite structure in the electron spectrum of $^{83}\mathrm{Kr}^{m}$”, (2020), DOE Supported.

[20]N. Abgrall et al., “ADC Nonlinearity Correction for the MAJORANA DEMONSTRATOR”, (2020), DOE Supported.

9.3 Invited talks at conferences

[21]W. C. Pettus, *Background Rejection through Pulse Shape Discrimination in the* MAJORANA DEMONSTRATOR, Invited plenary, Mazurian Lakes Conference on Physics, Piaski, Poland, Sept. 2019, DOE Supported.

[22]W. C. Pettus, *Prospects for Next-Generation Neutrino Mass Sensitivity with Project 8*, Invited talk at INT-20-1a Workshop: Neutrinos from the Lab to the Cosmos, Jan. 2020, DOE Supported.

[23]X. Li, *High resolution selenium imaging detector for neutrinoless $\beta\beta$ decay*, CPAD instrumentation frontier workshop, Madison, Wisconsin., 2019, DOE Supported.

[24]E. Novitski, *Cyclotron Radiation Emission Spectroscopy for measuring neutrino mass and searching for chirality-flipping interactions*, invited, Paul Scherrer Institut, Switzerland: 5th International Workshop on the Physics of Fundamental Symmetries and Interactions – PSI2019, DOE Supported.

[25]P. Mitra, *Single electron charge resolution with the first prototypes of DAMIC-M skipper CCDs*, Invited talk, Kavli Institute of Cosmological Physics, University of Chicago, 2019.

[26]A. Garcia, *Cyclotron radiation detection to search for new physics, NSCL*, at MSU, invited seminar, 2020, DOE Supported.

[27]B. Graner, *Radio Spectroscopy for Nuclear Physics*, Contributed talk, Institute for Nuclear Theory workshop: Fundamental Symmetries Research with Beta Decay, Seattle, WA, 2019.

[28]P. Kammel, *Muon Capture in Hydrogen and Deuterium as a Probe of the Weak Axial Current*, invited, ELBA2019 - Lepton Interactions with Nucleons and Nuclei, Elba, Italy, June, 2019, DOE Supported.

[29]P. Kammel, *Baseline Concept for New Experiment*, invited, NuMu2019 workshop, Villigen, Switzerland, October, 2019, DOE Supported.

[30]P. Kammel, *Muon Capture and Neutrino Scattering*, invited, INT Program: Fundamental Symmetries Research with Beta Decay, Seattle, WA, November, 2019, DOE Supported.

[31]R. Ryan, *MuSun: Analysis of the First Production Dataset*, invited, Physics of fundamentalSymmetries and Interactions -PSI2019, Villigen, Switzerland, October, 2019, DOE Supported.

[32]R. G. H. Robertson, *The direct road to neutrino mass*, Invited talk, Symposium, Looking for ν physics on Earth and in the Cosmos, Berkeley, CA, 2020, DOE Supported.

[33]D. Hertzog, *Status of the muon g-2 experiment at Fermilab*, INT Workshop on g-2 Hadronic Contributions, Sept. 2019.

[34]D. Hertzog, *Status since the 2015 Long Range Plan*, IUPAP Meeting, London, Aug. 2019.

9.4 Abstracts and contributed talks

[35]W. C. Pettus, *Background Rejection through Pulse Shape Discrimination in the* MAJORANA DEMONSTRATOR, Contributed talk, APS-DNP meeting, Crystal City, VA, Oct. 2019, DOE Supported.

[36]R. Cervantes, *Orpheus: Extending the ADMX QCD Dark-Matter Axion Search to Higher Masses*, Contributed talk, APS April meeting, Denver, Co, 2019, DOE Supported.

[37]C. Wiseman, *Low Energy Rare Event Searches with the* MAJORANA DEMONSTRATOR, TAUP2019: 16th International Conference on Topics in Astroparticle and Underground Physics, Toyama, Japan, 2019, DOE Supported.

[38]E. Novitski, *Phase II of the Project 8 neutrino mass experiment using Cyclotron Radiation Emission Spectroscopy*, Crystal City, VA: 2019 Fall Meeting of the APS Division of Nuclear Physics, DOE Supported.

[39]N. Hoppis, *Development of a* ^{19}Ne *Source in Search of Chirality Flipping Interactions*, North American Particle Accelerator Conference, 2019, DOE Supported.

9.5 Reports, white papers and proceedings

[40]W. C. Pettus, “Overview of Project 8 and Progress Towards Tritium Operation”, J. Phys.: Conf. Ser. **1342**, In proceedings of TAUP 2017, 012040 (2020), DOE Supported.

[41]C Wiseman (MAJORANA Collaboration), “A low energy rare event search with the MAJORANA DEMONSTRATOR”, Journal of Physics: Conference Series **1468**, 012040 (2020).

[43]V. Cirigliano, A. Garcia, D. Gazit, et al., “Precision Beta Decay as a Probe of New Physics”, arXiv1907.02164 (2019), DOE Supported.

9.6 Seminars

[44]W. C. Pettus, *Weighing a Ghost: The Quest to Measure the Neutrino Mass*, University of North Carolina - Chapel Hill, Physics and Astronomy Colloquium, Jan. 2019.

[45]W. C. Pettus, *Backwards is Better: Next-Generation Detectors for Nuclear Physics*, University of North Carolina - Chapel Hill, Physics and Astronomy Chalk Talk, Jan. 2019.

[46]W. C. Pettus, *Searching for the WIMP Modulation with the COSINE-100 Dark Matter Experiment*, University of Washington, CENPA Seminar, June 2019.

[47]W. C. Pettus, *Weighing a Ghost: The Curious Case of Neutrino Mass*, IIT Physics Colloquium, Aug. 2019.

[48]W. C. Pettus, *Weighing a Ghost: Horizons on Neutrino Mass Probes from Nuclear Experiment*, Fermilab Wine & Cheese Seminar, Aug. 2019.

[49]W. C. Pettus, *Project 8: Towards the Atomic Tritium Future of Neutrino Mass Measurement*, University of Wisconsin, NPAC Seminar, Sept. 2019.

[50]W. C. Pettus, *Weighing a Ghost: Horizons on Neutrino Mass Probes*, University of Wisconsin, Special NSCL/FRIB Seminar, Sept. 2019.

[51]W. C. Pettus, *LEGEND in the Making: The ^{76}Ge Program for Neutrinoless Double Beta Decay*, Yale University, NPA Seminar, Oct. 2019.

[52]W. C. Pettus, *Weighing a Ghost: The Quest to Measure the Neutrino Mass*, Indiana University, Physics Research Seminar, Jan. 2020.

[53]W. C. Pettus, *The Ghostly Neutrino: A ν Lens for Studying the Universe*, Hillsdale College, Physics Research Seminar, Feb. 2020.

[54]W. C. Pettus, *Chasing Ghosts: A Decade on the Dark Side of the Universe*, Sanford Underground Research Facility, Research Seminar, Feb. 2020.

[55]W. C. Pettus, *Weighing a Ghost: The Quest to Measure the Neutrino Mass*, Temple University, Physics Seminar, Feb. 2020.

[56]C. Bartram, *A Search for CPT-Violation in Ortho-Positronium*, University of Washington, CENPA Seminar, June 2019.

9.7 Ph.D. degrees granted

[57]Y. Bagdasarova, "A measurement of the e-$\bar{\nu}_e$ angular correlation coefficient in the decay of ^{6}He", http://hdl.handle.net/1773/44887, PhD thesis (University of Washington, Department of Physics, July 2019).

[58]M. Buuck, "A Radiogenic Background Model for the MAJORANA DEMONSTRATOR", http://hdl.handle.net/1773/44889, PhD thesis (University of Washington, Department of Physics, July 2019).

[59]I. Guinn, "The Search for Double-Beta Decay to Excited States in 76-Ge using the MAJORANA DEMONSTRATOR", http://hdl.handle.net/1773/44888, PhD thesis (University of Washington, Department of Physics, June 2019).

[60]J. Lee, "A Fourier-Bessel Test of the Gravitational Inverse-Square Law", http://hdl.handle.net/1773/45542, PhD thesis (University of Washington, Department of Physics, Mar. 2020).

[61] Y.-T. Lin, "The Tritium Recoil-Ion Mass Spectrometer Experiment", http://hdl.handle.net/1773/45253, PhD thesis (University of Washington, Department of Physics, Dec. 2019).

[62] R. Osofsky, "Magnetic Field Determination for Run 1 of the Fermilab Muon $g-2$ Experiment", http://hdl.handle.net/1773/45255, PhD thesis (University of Washington, Department of Physics, Dec. 2019).

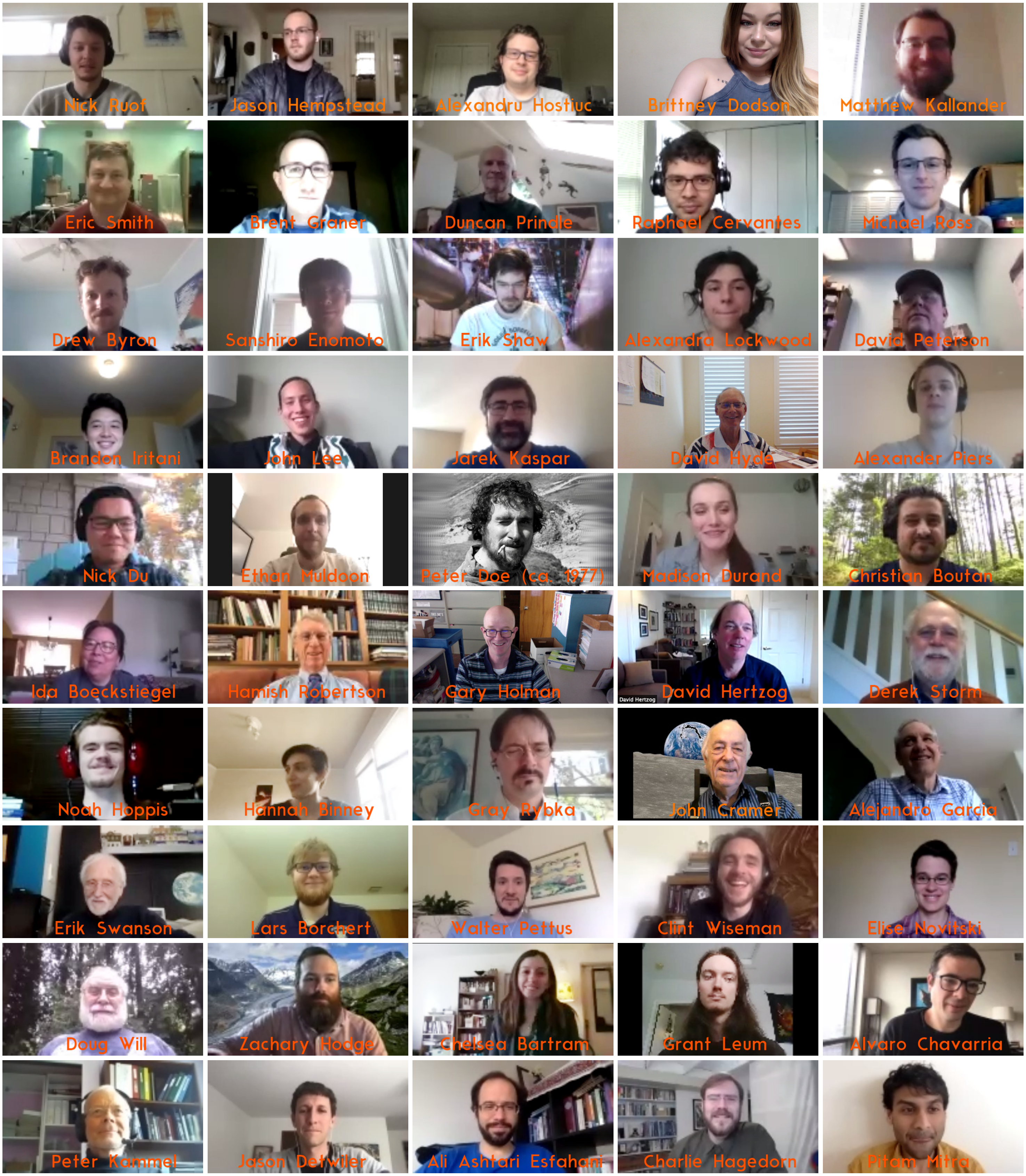

CENPA Group ZOOM Photo 2020